Annual Research Journal

Electrical Engineering
Research Experience for Undergraduates

Vol. I (2003)

PENN**S**TATE

Department of Electrical Engineering
University Park, Pennsylvania

EEREU Annual Research Journal

Ruyan Guo (editor)
W. Kenneth Jenkins (co-editor)
Bo Wang (associate-editor)

NSF EE REU Site Program Contact

Table of Contents

Research Articles

NSF EEREU Faculty and Staff Members

Faculty Mentors
Prof. Amar Bhalla
Prof. Sven Bilen
Prof. Craig Grimes
Prof. Ruyan Guo, Co-Director
Prof. Heath Hofmann
Prof. Ken Jenkins, Co-Director
Prof. I. C. Khoo
Prof. Mike Lanagan
Prof. John Mitchell, Seminar Chair
Prof. Victor Pasko
Prof. Joan Redwing
Prof. Jeff Schiano
Prof. Srinivas Tadigadapa
Prof. Kenji Uchino

Prof. Andy Lau, Ethics Workshop Chair
Prof. David Salvia, Resource Coordinator
Ms. Amy Freeman, Director, Minority Program

Administration and Coordination
Mrs. Linda Becker

2003 NSF EE REU Scholars, Projects, and Mentors

REU Scholars and Home Institutions	Research Project	Faculty Mentor
George Li *Rutgers University*	Exploration of lead-free composition materials for tunable filter applications	Prof. Amar Bhalla
Daniel Dobrin *University of Illinois, Chicago*	Power System Modeling for LionSat	Prof. Sven Bilen
Christine Smit *University of Maryland*	Data collection and analysis of high frequency damped oscillation waves	Prof. Craig Grimes
Elric Von Eden *University of Maryland*	Detecting Pyroelectric Response upon Modulated Infrared Radiation	
Amanda Skrabut *Penn State University*	Electromechanical Properties of Piezoelectric Thin Films by Optical Interferometry	Prof. Ruyan Guo
Vanessa Morales *Penn State University*	Ferroelectric and Microscopic Properties of PZT Single Crystal Thin Films	
Ran Chang *University of Maryland*	MATLAB Finite Element Analysis for Electromechanical Systems	Prof. Heath Hofmann

REU Scholars and Home Institutions	Research Project	Faculty Mentor
"Rosa" Xiao-Shan Tao Cornell University	AC Field Modulation of Stimulated Orientational Scattering Effect in nonlinear liquid crystal	Prof. I. C. Khoo
Dean Kissinger Penn State University	Photorefractivity of Carbon Nanotube Doped Nematic Liquid Crystals	
Lance Haney Mercer University	Properties of Nickel as Ring Resonators in the Microwave Frequency Range	
Calvin Leiter Penn State University	Microwave Measurements	Prof. Mike Lanagan
Michael Ellis Bucknell University	Software/Hardware Diagnostics For Testing Rocket Payload Electronics	Prof. John Mitchell Prof. C. Croskey
Mark Lininger Penn State University	Studies of Electromagnetic Fields in the Atmosphere	
Adeel Haroon Penn State University	Visualization and Analysis of Simulated Atmospheric Gravity Wave Data	Prof. Victor Pasko
Scott Kiefer Penn State University	Schumann Resonances and the Earth-Ionosphere	

iv

REU Scholars and Home Institutions	Research Project	Faculty Mentor
Mark Colgan *Bucknell University*	Adaptive Equalization for Acoustic Stereo Effect	Prof. Ken Jenkins
Richard Bemben *Virginia Tech*	Electrical Characterization of Doped Silicon Nanowires Grown in Anodized Aluminum Membranes	Prof. Joan Redwing
Bonnie Hammond *Cedarville University*	Detection of Explosives and Biological Warfare Agents using Nuclear Quadrupole Resonance	Prof. Jeff Schiano
Bryan Martin *Western Michigan University*	Labview-based Instrumentation for a MEMS Biosensor for Sensitivity Improvement	Prof. S. Tadigadapa
Zachary Harmany *Penn State University*	Demonstration Models using Microelectromechanical Devices	
Thomas Plummer *Univ. Miami*	Micro Piezoelectric Ultrasonic Motor Optimization	Prof. Kenji Uchino

NSF EE REU 2003 Summer Program
Weekly Scientific Seminar

Department of Electrical Engineering
Pennsylvania State University, University Park, PA 16802

Room 101 EE East, 11:00 am – 12:00 noon, Thursdays
Seminar Chair: **Prof. John Mitchell** (jdm4@psu.edu)

(Followed by **REU Weekly Ethics Workshop,** 12:30-1:30pm)

Date	*Topic*	*Speaker*
June 5, 2003	Sensors using Micro and Nanoscale Structures	Srinivas Tadigadapa
June 12, 2003	Lightning-related Transient Luminous Events in the Middle Atmosphere	Victor Pasko
June 19, 2003	Introduction to Micromechatronics	Kenji Uchino
June 26, 2003	Micro-Management: A BS is Not Enough	Jeff Schiano
July 3, 2003	Electrodynamic Tethers for Propulsion: Past, Present, and Future	Sven Bilén
July 8, 2003	What do Star Wars Jedi, Lasers & Liquid Crystal Have in Common?	I. C. Khoo
July 17, 2003	Signal Processing	Robert Nickel
July 24, 2003	What's Next? Graduate School, of Course!	Ken Jenkins
July 31, 2003	(NSF EE REU Symposium 8:30 am – 4:00 pm Nittany Lion Inn)	REU Students

NSF EE REU 2003 Summer Program
Weekly Ethics Workshop

Department of Electrical Engineering
Pennsylvania State University, University Park, PA 16802

Room 101 EE East, 12:30 pm –1:30 pm, Thursdays
Workshop Chair: **Prof. Andrew Lau** (andylau@psu.edu)

Weekly	Workshop Topic Addressed	Faculty Leader
Week 1	PSU Science, Technology, and Society Program Faculty presentation Introduction to Ethical Concepts and Making a Life in Engineering and Science	
Week 2	The Basis and Scope of Professional Responsibility- Privacy, Ethical and Legal Judgments, Types of Moral Problems	Prof. Andy Lau
Week 3	Central Professional Responsibilities of Engineers – The Responsible Conduct of Research	Prof. Kenji Uchino
Week 4	Responsibility for Research Integrity	Prof. Sven Bilen
Week 5	The Responsibility of Investigators for Experimental Subjects	
Week 6	The Responsibility for the Environment and Public safety	Prof. Kenneth Jenkins
Week 7	Fair Credit in Research and Publication	
Week 8	Intellectual Property in Engineering Practice	
Week 9	(Final Mini Symposium - REU program Student Presentation on Research Experience)	

2003 NSF EE REU Bi-Weekly Field Trips and Industry Sponsors

Sound Technology, Inc.
State College, Pennsylvania

Philips, Inc.
Reedsville, Pennsylvania

Northrop Grumman Corp.
Electronic Systems
Linthicum, Maryland

Sullivan Park Research Center
Corning Inc., Corning, New York

Murata Electronics North America,
State College, Pennsylvania

State of The Art, Inc.
State College, Pennsylvania

MESSAGES FROM EEREU SITE CO-DIRECTORS

Dear 2003 EE REU Scholars:

On behalf of all faculty and staff members of our REU program, and the members of the Electrical Engineering Department, we would like to take this opportunity to thank you for participating in the 2003 Summer REU in Electrical Engineering, at University Park Campus, Penn State University.

It is the first year that the Department of Electrical Engineering is hosting the National Science Foundation sponsored REU-Site activities. It has been our hope that your experience with us this summer will enhance your knowledge and understanding of the scope of electrical engineering research and contribute to the development of your academic goals.

While you have spent most of your time in the laboratory this summer, we hope you have also taken the advantage of the many special opportunities we offered as well.

The ***Weekly Scientific Seminar*** series aimed to let you hear leading researcher/scientists at Penn State discussing their current research, and to broaden your view on the research frontier. We hope you found the ***field trips*** we arranged for you to visit prominent local, national and international industrial research sites interesting and valuable. We trust that you were involved in debate and analysis on real ethical problems in engineering research in our "***Weekly Workshop on Ethics in Science and Research.***"

Although not all the research projects can be completed within the limited time, we hope your work have made a significant contribution to the research topic you were working on. We are proud of you as we prepare this volume of "***Annual Research Journal***" to document your research findings.

We hope that experiences such as this summer's research make graduate school appear more attainable and attractive to you. As you return to your home institutions to continue your academic endeavors, we hope that you will choose to enter graduate school in pursuit of an advanced research degree; and we do encourage you to give serious consideration for graduate studies at Penn State.

Our best wishes to all of you for a productive academic year and success as you pursue long term career goals.

Prof. Ruyan Guo and Prof. Ken Jenkins,
Co-Directors of the NSF EE REU Site,
Department of Electrical Engineering,
Penn State University

NSF EE REU SYMPOSIUM

Time	Sessions and Topics	Chairs and Speakers
8:30-8:55 am	**Symposium Registration**	Linda Becker
8:55 – 9:00 am	**Welcome**	Kenneth Jenkins
9: – 10:15 am	**Session I** Session Chairs:	Bilen/Mitchell
9:00 – 9:15	Magnetoelastic Resonance Sensor Simulation	Christine Smit
9:15 – 9:30	MATLAB Finite Element Analysis for Electromechanical Systems	Ran Chang
9:30 – 9:45	Power System Modeling for LionSat	Daniel Dobrin
9:45 – 10:00	Software/Hardware Diagnostics for Testing Rocket Payload Electronics	Michael Ellis
10:00 – 10:15	Adaptive Equalization for Acoustic Stereo Effect	Mark Colgan

10:15 – 10:30 am coffee break

Time	Sessions and Topics	Chairs and Speakers
10:30 – 11:45 am	**Session II** Session Chairs:	Grimes/Tadigadapa
10:30 – 10:45	Resonance Characteristics for MEMS Cantilever Structures	Zachary Harmany
10:45 – 11:00	Micro Piezoelectric Ultrasonic Motor Optimization	Thomas Plummer
11:00 – 11:15	Electrical Characterization of Doped Silicon Nanowires Grown in Anodized Aluminum Membranes	Richard Bemben
11:15 – 11:30	Ferroelectric and Microscopic Properties of PZT Single Crystal Films	Vanessa Morales
11:30 – 11:45	LabView-Based Instrumentation for a MEMS Biosensor for Sensitivity Improvement	Bryan A. Martin

12:00 – 1:00 pm Lunch break

NSF EE REU SYMPOSIUM (cont.)

1: – 2:15pm	**Session III**	Session Chairs:	Bhalla/Schiano
1:00 – 1:15	Detection of Explosives and Biological Warfare Agents using Nuclear Quadrupole		Bonnie Hammond
1:15 – 1:30	Photorefractivity of Carbon Nanotube Doped Nematic Liquid Crystals		Dean Kissinger
1:30 – 1:45	AC Field Modulation of Stimulated Orientational Scattering (SOS) Effect in Nonlinear Liquid Crystal (NLC)		Xiao-Shan Tao
1:45 – 2:00	Pyrooptic Response of PMN-PT Crystal upon Near-IR Radiation		Elric Von Eden
2:00 – 2:15	Electromechanical Properties of Piezoelectric Thin Films by Optical Interferometry		Amanda Skrabut

2:15 – 2:30 pm coffee break

2:30 – 4:pm	**Session IV**	Session Chairs:	Pasko/Lanagan
2:30 – 2:45	Sprites		Mark Lininger
2:45 – 3:00	Visualization and Analysis of Simulated Atmospheric Gravity Wave Data		Adeel Haroon
3:00 – 3:15	Schumann Resonances and The Earth-Ionosphere Waveguide		Scott Kiefer
3:15 – 3:30	Microwave Measurement		Calvin Leiter
3:30 – 3:45	Exploration of Lead-Free Composition Materials for Tunable Filter Applications		George Li
3:45 – 4:00	Properties of Nickel as Ring Resonators in the Microwave Frequency Range		Lance Haney

4:00 pm Adjournment – Concluding Remarks   Ruyan Guo

MAGNETOELASTIC RESONANCE SENSOR SIMULATION

Christine E. Smit*
(Craig A. Grimes, Faculty Mentor)
Department of Electrical Engineering
Pennsylvania State University, University Park, PA 16802

*Undergraduate student of
Department of Electrical and Computer Engineering
University of Maryland
College Park, MD 20742

ABSTRACT
   Magnetoelastic resonance sensors are modeled as second-order underdamped systems with two information-bearing parameters: the resonant frequency and the damping ratio. The response of the system is made up of the steady-state response and the transient response. In the time domain, signals can be analyzed using frequency counting or FFTs. In the frequency domain, signals can be analyzed by sweeping the frequencies and measuring the strengths of the responses. Currently, a microcontroller based instrumentation board[1] has been created to interrogate the sensor and calculate the damping ratio and resonant frequency using frequency sweeps and frequency counting. However, lack of memory and computational speed prevents the board from being able to perform an FFT.
   This project extends the previous work[1] by creating two simulations: one simulation of the current board using frequency counting and frequency sweeps and one simulation of a board currently under development that uses an FFT. The simulation of the current board is used to compare the real-world sensor data with the theoretical model. The simulation of the board under development is used to determine if the FFT could better analyze the data.

INTRODUCTION
   Magnetoelastic sensors are wireless, passive sensors and can be used to measure any environmental parameter that changes the resonant frequency of the sensor[2]. The resonant frequency of the sensor changes as a function of many factors including size, temperature, mass loading, and the viscosity and density of the surrounding liquid[2].

Magnetoelastic sensors may be interrogated using magnetic fields. If a time-varying magnetic field is applied to a magnetoelastic sensor, the sensor will mechanically vibrate. Vibration in the sensor will in turn launch a time-varying magnetic field that can be remotely detected[2].

Because these sensors can be modeled as second-order damped oscillation with a single degree of freedom[1], one method for determining the resonant frequency of the sensor is to analyze the transient response of the system. A driving frequency is used to excite the sensor at a known frequency. When the driving frequency is stopped, the transient response can be recorded. This transient response will be a damped oscillation of the form

$$x(t) = Ae^{-\zeta \omega_n t} \cos(\omega_d t - \phi), \tag{1}$$

where A is the amplitude, ζ the damping ratio, ω_n the natural frequency of undamped oscillation, ω_d the frequency of the transient oscillation, and ϕ the phase angle. The frequency of the transient response and the natural frequency are related by the formula

$$\omega_d = \sqrt{1 - \zeta^2}\, \omega_n \,. \tag{2}$$

If the damping ratio is small ($\zeta \ll 1$), $\omega_d \approx \omega_n$ and the frequency of the transient response can be taken as the resonant frequency, ω_d[1].

A second method for determining the resonant frequency involves sampling the transient response and taking an FFT. The magnitude squared of the transient response will be

$$G(\omega) = \frac{c}{\omega^4 + (4\zeta^2\omega_n^2 - 2\omega_n^2)\omega^2 + \omega_n^4} \tag{3}$$

in the frequency domain, where c is a constant scaling factor that does not affect the overall shape of the response. The location of the peak and width of the peak are related to ω_n and ζ. Thus, ω_n can be calculated

$$\omega_n \approx \omega_{mx}, \tag{4}$$

where ω_{mx} is the frequency for which $G(\omega)$ takes on its maximum value. The damping ratio can be calculated from the width of the peak,

$$\zeta \approx \frac{\Delta\omega}{2\omega_n},$$ (5)

where $\Delta\omega$ is the width of the peak at half the maximum value of $G(\omega)$. Although $G(\omega)$ is not band-limited, it tapers off quickly away from the resonant frequency. So, minimal aliasing occurs if the sampling frequency of the transient response is high.

Previously, a microcontroller based instrumentation board was created to interrogate a sensor system and to determine the resonant frequency using frequency counting and frequency sweep techniques. The board runs short bursts of oscillating current through a coil to create a magnetic interrogation signal. Each burst excites the sensor. When the burst is over, the sensor continues to vibrate for a short time, causing a magnetic field that in turn creates a voltage (faraday's law) in a pick-up coil. The board analyses this response voltage to calculate the resonant frequency, ω_n.

This work deals with creating a simulation of the board's sensor interrogation scheme and calculation of the sensor's resonant frequency, ω_n. A close correlation between simulated and real results will help to validate the principals on which the board was built. This work also extends the previous work by simulating a board that uses an FFT to calculate ω_n and the damping ratio, ζ.

EXPERIMENTAL DESCRIPTION
Simulink Sensor Model

A simulation of the sensor excitation and transient response capture was created using MATLAB's Simulink. The simulation runs a short excitation burst through a second-order system model for the sensor,

$$H(s) = \frac{\omega_n^2}{s^2 + 2\zeta\omega_n s + \omega_n^2} \ .$$ (6)

If the frequency of the excitation burst is close to the resonant frequency, a large transient response is captured (see Fig. 1).
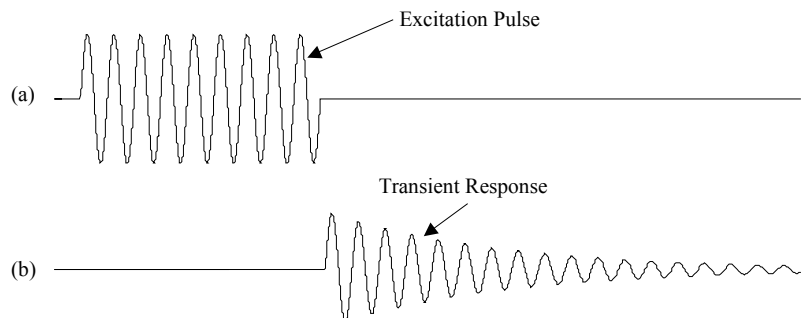
Figure 1: Illustration of the transient response of a sensor. Plot (a) shows the excitation pulse that starts the sensor vibrating. Plot (b) shows the transient response after the excitation pulse stops.

Microcontroller Based Instrumentation Board Simulation

Once the sensor has been excited and the transient response recorded, frequency counting is used to determine the strength of the transient response. A comparator is set to switch when the input voltage is zero. A counter is set to increment on the falling edge of the comparator, effectively counting one zero each cycle. When the envelope of the transient response reaches a pre-set cutoff voltage, the comparator stops switching (see Fig. 2).
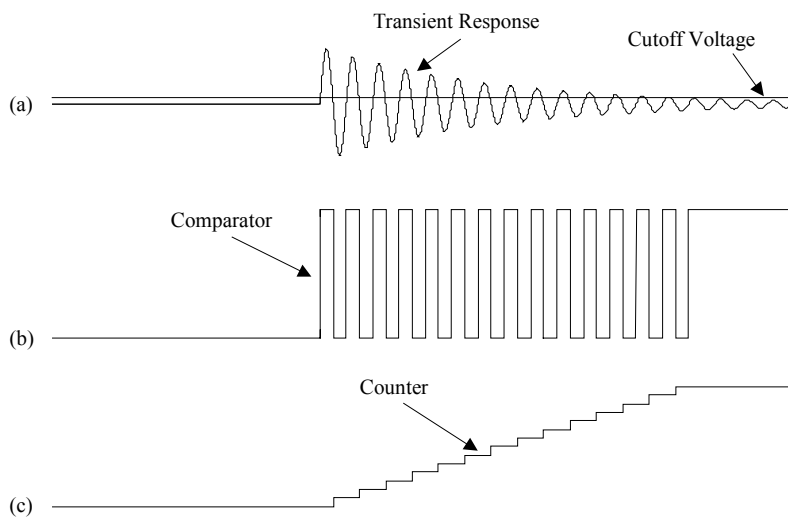
Figure 2: Illustration of the zero-counter. Plot (a) shows the transient response of the sensor after an excitation pulse. The cutoff voltage is used to stop the comparator. Plot (b) shows that comparator, which flips between 0 and 1 every time it detects zero volts in the transient response.

4

This comparator is shutoff when the envelope of the transient response hits the cutoff voltage. Plot (c) shows the counter, which increases by one on every falling edge of the comparator.

To simulate a frequency sweep, multiple excitation frequencies are used in succession (see Fig. 3). The sensor's transient response increases when the excitation frequency gets close to the sensor's resonant frequency. Because the transient response is larger, the transient response reaches the cutoff voltage (see Fig. 2) later and more zeros are counted. So, the resonant frequency of the sensor is

$$\omega_n = \omega_{zero\ mx} \tag{7}$$

where $\omega_{zero\ mx}$ is the excitation frequency for which the most zeros are counted.
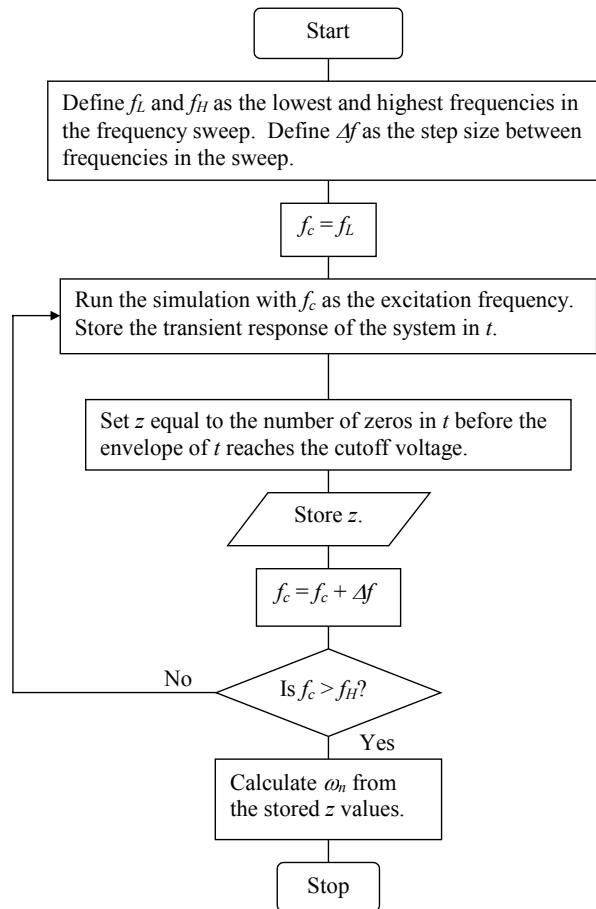
Figure 3: Flowchart of the instrumentation board simulation code.

5

FFT Board Simulation

Once the sensor has been excited and the transient response sampled and recorded, an FFT is taken of the transient response. The resonance frequency and damping ratio are then calculated from the FFT (see Eq. 4, Eq. 5). To simulate a frequency sweep, multiple excitation frequencies are run sequentially (see Fig. 4).
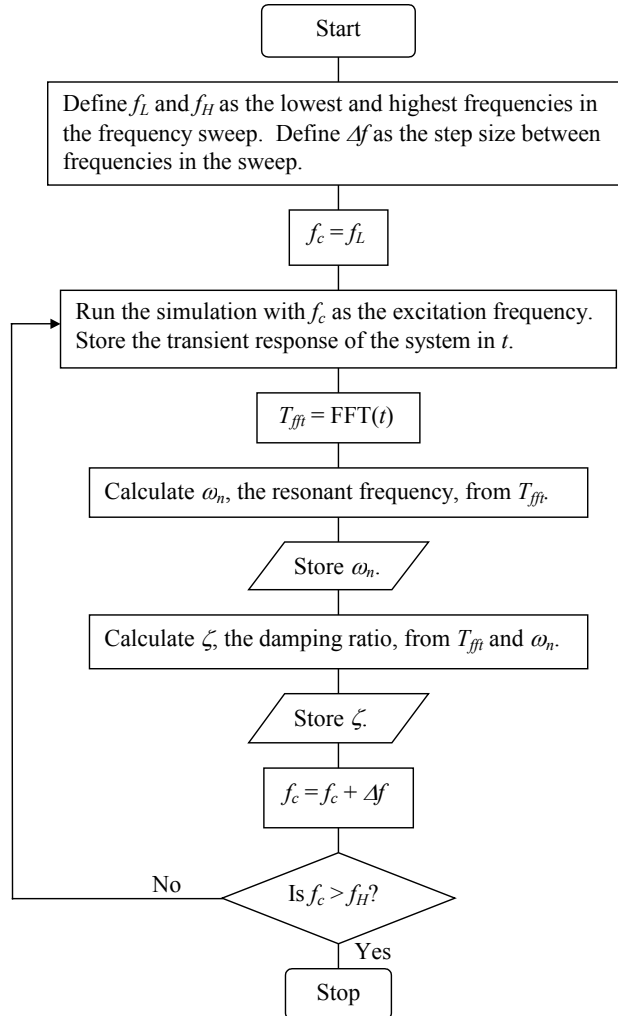

Start

Define f_L and f_H as the lowest and highest frequencies in the frequency sweep. Define Δf as the step size between frequencies in the sweep.

$f_c = f_L$

Run the simulation with f_c as the excitation frequency. Store the transient response of the system in t.

$T_{fft} = \text{FFT}(t)$

Calculate ω_n, the resonant frequency, from T_{fft}.

Store ω_n.

Calculate ζ, the damping ratio, from T_{fft} and ω_n.

Store ζ.

$f_c = f_c + \Delta f$

No

Is $f_c > f_H$?

Yes

Stop

Figure 4: Flowchart of the FFT board simulation code.

To test the simulation against the real data obtained from the interrogation board, a frequency sweep is run on the instrumentation board. The frequency with the most zeros counted on the board is then used as the resonant frequency, ω_n, in the system model for the sensor (Eq. 6). The board does not currently measure the damping ratio because the board's software is in the process of being

6

updated. So, the damping ratio is estimated by hand. The simulation is then run using the same frequencies as the board and the simulation results are compared with the board's results. Also, the FFT board simulation is run to calculate the resonant frequency and damping ratio.

RESULTS
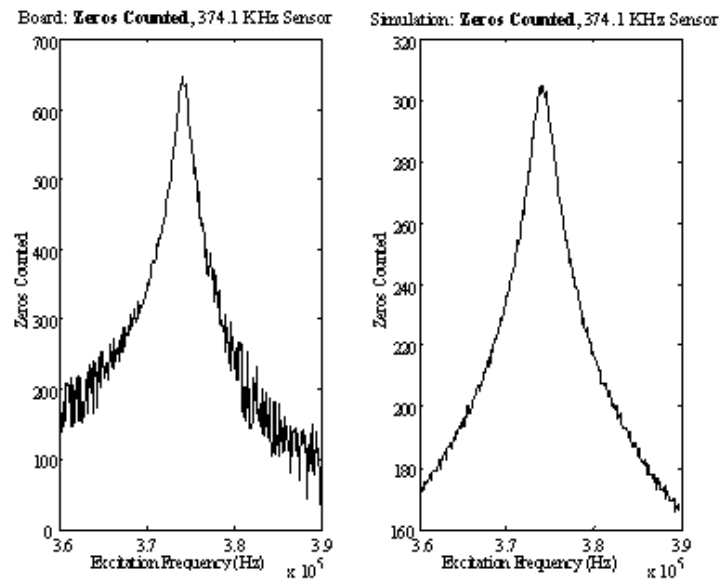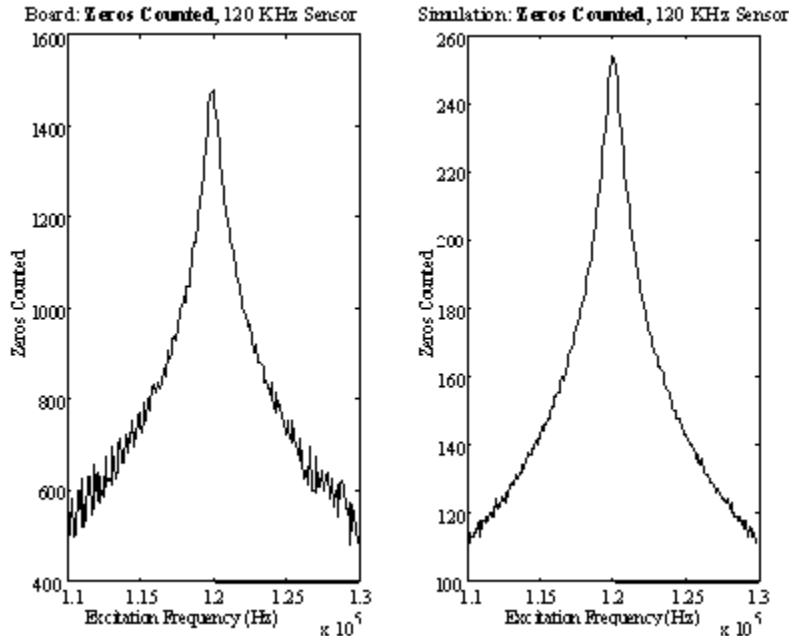Instrumentation Board Zero Counts and Simulated Zero Counts

Figure 5: Illustration of the zeros counted during a frequency sweep of a 120 KHz sensor. The plot on the left shows the number of zeros counted by the instrumentation board[1] at each frequency in the sweep. The plot on the right shows the number of zeros counted by the MATLAB simulation of the instrumentation board.

Figure 6: Illustration of the zeros counted during a frequency sweep of a 374.1 KHz sensor. The plot on the left shows the number of zeros counted by the instrumentation board[1] at each frequency in the sweep. The plot on the right shows the number of zeros counted by the MATLAB simulation of the instrumentation board.

The number of zeros counted in the simulation is much smaller than the number of zeros counted on the instrumentation board (Fig. 5, Fig. 6) because the board uses several counters, which are added together. Adding the counters together helps to reduce noise. The current SIMULINK model has no noise. Since the resonant frequency is calculated based on the location of the maximum point on the graph and not on the actual maximum value, no extra counters were needed**.**

There are two interesting phenomena that show up in both the real and simulated zero counts (Fig. 5, Fig. 6). First, when the system is driven by frequencies that are far away from the resonant frequency, the number of zeros counted does not increase or decrease in a smooth fashion. Second, the absolute maximum point of the 374.1 KHz sensor graph is difficult to decipher because there are several peaks (Fig. 6).
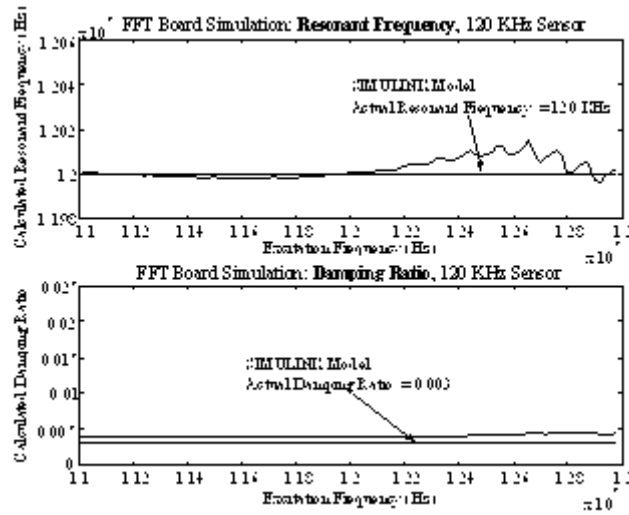
Simulated FFT Board Results

8

Figure 7: Illustration of simulated FFT board calculations during a frequency sweep. The modeled sensor has a resonant frequency of 120 KHz and a damping ratio of 0.003. The top plot shows the calculated resonant frequency and the bottom plot shows the calculated damping ratio.
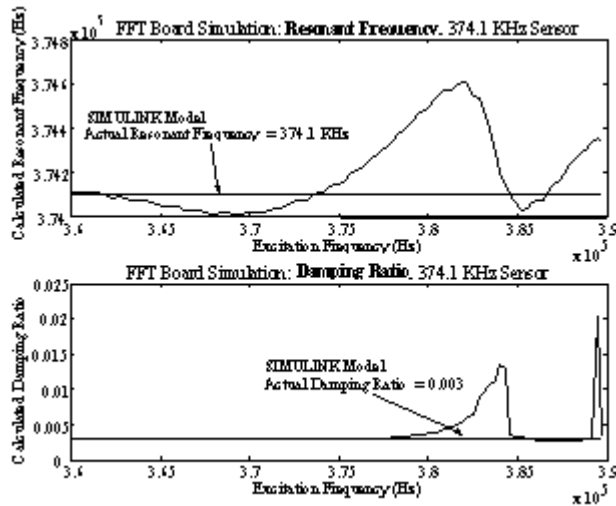

Figure 8: Illustration of simulated FFT board calculations during a frequency sweep. The modeled sensor has a resonant frequency of 374.1 KHz and a damping ratio of 0.003. The top plot shows the calculated resonant frequency and the bottom plot shows the calculated damping ratio.

DISCUSSION

It is interesting that the simulated, noise-free environment creates what looks like noisy signals (right-hand plots: Fig. 5, Fig. 6). The number of zeros counted fluctuates quite rapidly away from the peak value and the peak itself is not

9

smooth. So, at least some of the fluctuation in the data from the instrumentation board must be inherent to the mathematical model of the system.

In the simulated FFT system, the calculated resonant frequency remains fairly steady over a wide range of frequencies (top plots: Fig. 7, Fig. 8). So, if this system were implemented, finding the resonant frequency would be relatively simple. Since the calculated damping ratio can fluctuate quite significantly when the driving frequency is far from the resonant frequency (bottom plot: Fig. 8), the system would first have to find the resonant frequency and then drive the system with that resonant frequency to find the damping ratio.

Obviously, two sensors by themselves cannot give statistically significant data. These experiments should be run many times with many different sensors. Also, a formula for calculating the number of zeros you should expect to see for a given driving frequency, resonant frequency, and damping ratio should be developed to explain the fluctuations in the simulated zero-counter.

SUMMARY

The simulation shows that some fluctuation in the number of zeros counted during a frequency sweep is inherent to the mathematical model of the system and not the result of noise. Also, a system using an FFT may hold certain advantages because such a system can pick out the resonant frequency of a sensor even when the driving frequency is quite far from the resonant frequency.

REFERENCES

1   K. Zeng, K. G. Ong, C. Mungle, and C. A. Grimes, "Time domain characterization of oscillating sensors: Application of frequency counting to resonance frequency determination," *Review of Scientific Instruments*, **73** (12) 4375-4380 (2002)

2   C. A. Grimes, C. S. Mungle, K. Zeng, M. K. Jain, W. R. Dreschel, M. Paulose, and K. G. Ong, "Wireless Magnetoelastic Resonance Sensors: A Critical Review," *Sensors*, **2002** (2) 294-313 (2003).

FINITE ELEMENT ANALYSIS FOR ACTUATOR WITH MSM MATERIAL

Ran Chang*
Faculty Mentor: Heath Hofmann
Department of Electrical Engineering
Pennsylvania State University, University Park, PA 16802

*Undergraduate student of
Department of Electrical and Computer Engineering
University of Maryland, College Park, MD 20742

ABSTRACT

In this report, I analyzed several different designs of an actuator containing material shape memory (MSM) material using the Finite Element Method. This MSM material is extremely active and they can develop and produce shape changes in a magnetic field [1, 2, 3]. Actuators made from MSM are expected to achieve higher performance and to replace conventional electromagnetic devices in many applications [2]. In the analysis the procedures involved are to run simulations of various designs of an actuator using Maxwell SV, to build up the model for the actuator using the built-in functions and graphical capabilities of MATLAB and to modify the finite element code being developed in order to obtain the maximum strength of the magnetic field intensity and magnetic flux density MSM of the actuator. This analysis is necessary because a certain value of the magnetic field intensity is required to utilize MSM as well as other criteria mentioned in discussion. Finally, results obtained are presented and some major conclusions are drawn.

INTRODUCTION

In this project at Penn State University I aided in the development of finite element code, written in MATLAB, to analyze an electromagnetic device, an actuator. The design of the actuator is of great interest because parts of it are made from Magnetic Shape Memory materials, or also known as MSM. Magnetic shape memory materials are a special kind of active alloys that produce rapid shape changes in a magnetic field due to its high theoretically achievable strain [3]. Magnetically controlled shape memory materials are a new way to produce motion and force. Accordingly, the largest magneto-strain effects were achieved

in Ni-Mn-Ga ferromagnetic shape memory alloys which strains up to 6% [1]. Due to its fast response in magnetic field and gigantic field-induced strain, MSM are expected to have enormous potential in the design and utilization of an actuator. In the study of this project, the finite element method is used in the examination of MSM in the actuator through using the built-in functions and graphical capabilities of MATLAB.

The goal of this project is to explore different designs of an actuator which provides a certain magnetic flux density within MSM to utilize magnetic shape memory material to its maximum strain. Two methods are used to achieve this goal. One method uses the finite element commercial software, Maxwell SV, to simulate various dissimilar actuator designs and to compare the results of the different designs in order to select an optimal model which minimizes the size of the actuator. Another method builds up the model selected from the simulations in Maxwell SV through programming in MATLAB and modifies the two-dimensional finite element simulator in MATLAB code in order to calculate the magnetic field intensity and the magnetic flux density in MSM of the actuator.

EXPERIMENTAL DESCRIPTION
Software
- ❖ MATLAB, an interactive software as well as an extremely useful tool used in engineering and scientific applications, is used in the finite element analysis of electromagnetic finite element to relieve the workload of finite element analysis to a significant extent.
- ❖ Maxwell SV, a powerful and accurate software for two-dimensional, electromagnetic, and electrostatic-field simulation, is especially intended and applicable for my studying of the different designs of electromagnetic component, the actuator.

Mathematical tool
- ❖ Electromagnetic finite element analysis (FEA) is a numerical method of solving Maxwell's equations for a specific and complicated engineering problem by discretizing or subdividing the problem space into a "mesh" of finite sized elements of simple shape, applying boundary conditions, and generating large systems of equations which must then be solved.

Finite element formulation
- ❖ $KA=J+J_m$ (1)

Where:
K: Stiffness matrix
A: Magnetic vector potential (MVP)
J: Current density generated by windings
J_m: Magnetization current density of hiperco and MSM material

<u>*Object*</u>
❖ Actuators are devices that impose a condition on a system.

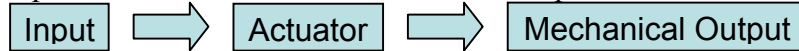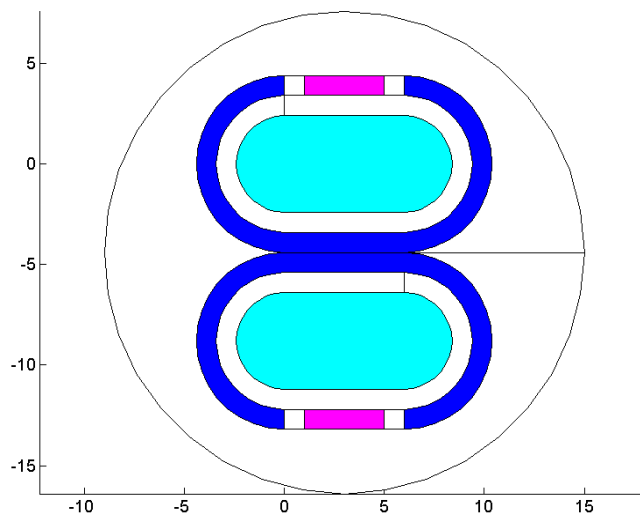|	
Electrical	Force
Magnetic	Displacement
Thermal	Torque
Optic	Speed

Input ⇨ Actuator ⇨ Mechanical Output

Actuator examples:
❖ Motors (which impose a torque)
❖ Force heads (which impose a force)
❖ Pumps (which impose either a pressure or a fluid velocity)

Figure 1. One of the actuator designs used and analyzed in MATLAB.

o Cyan-Windings <Copper>
o Blue-Hiperco <High permeability>
o Purple-Magnetic shape memory (MSM) <special alloys produce shape changes in a magnetic field due to its high theoretically achievable strain>

13

Table I. Properties of MSM compared with other actuator materials. [2,3]

	Multi-layered Piezo	Magnetostrictive Terfenol-D	MSM (ni-Mn-Ga)
Control Field	Electric	Magnetic	Magnetic
Max. strain ε (μm/mm), linear	1.25	1.6	100
Work output, $\sigma \times \varepsilon$ (MPa × μm/mm)	25	112	300
Resistivity (Ω-m)	10^{10}	58×10^{-8}	80×10^{-8}
Relative permeability	1	3-10	1.5-40
Max. energy density (kJ/m^3)	18.5	27	90
Field strength for max. strain	2 MV/m	240 kA/m	400 kA/m

Mathematical equations
Maxwell's Laws

$$\nabla \cdot B = 0 \tag{2}$$
$$\nabla \times H = J \tag{3}$$
$$\nabla \times E = -\partial B / \partial t \tag{4}$$

Constitutive Law

$$B = \mu_0 H + \mu_0 M = \mu M \tag{5}$$
$$J = \sigma (E + v \times B) \tag{6}$$

Where:
M: Magnetization
J: Magnetization current density
E: Electric field intensity
H: Magnetic field intensity
B: Magnetic flux density
μ_0: Permeability in the air

RESULTS

Maxwell SV

Figures 2-11 illustrates the effect that the size of the MSM material has on the actuator.

Figure 2. MSM length=36mm.
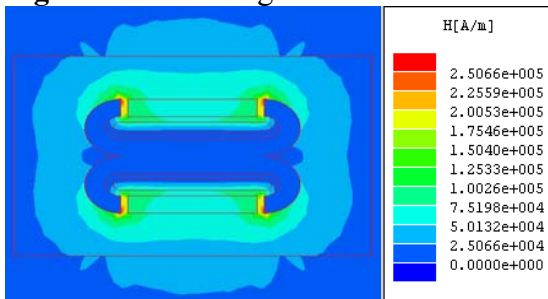
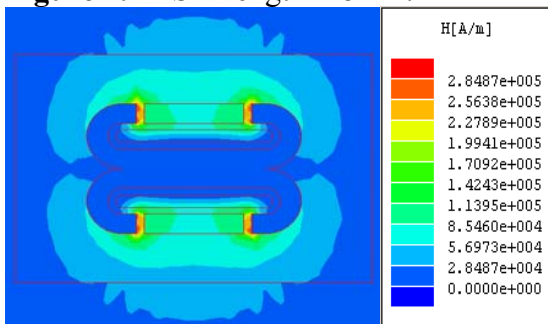**Figure 3.** MSM length=32mm.
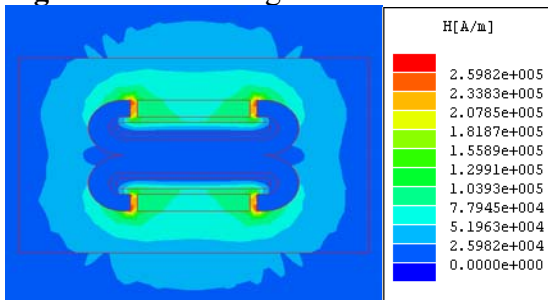
Figure 4. MSM length=28mm.
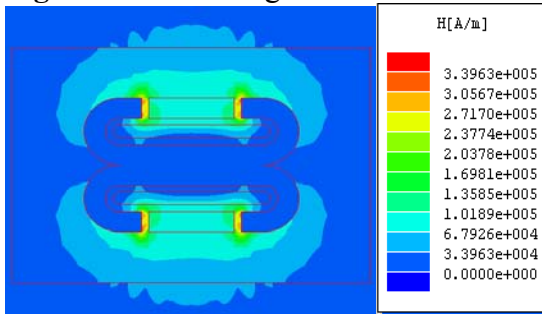
Figure 5. MSM length=24mm.
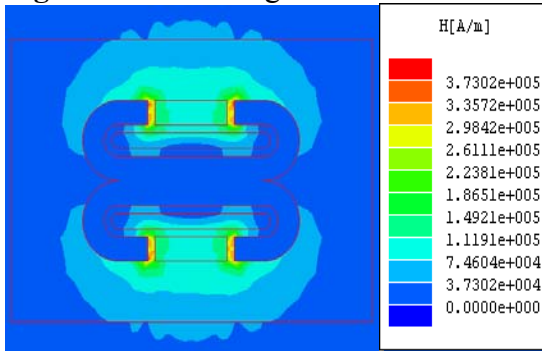

Figure 6. MSM length=20mm.
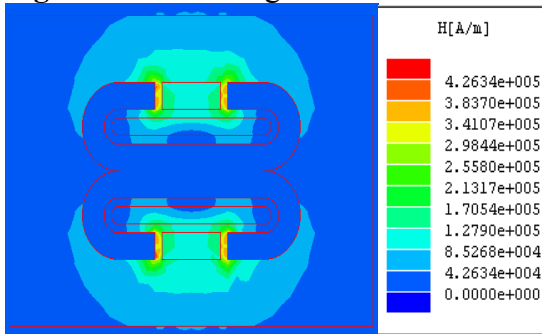

Figure 7. MSM length=16mm.
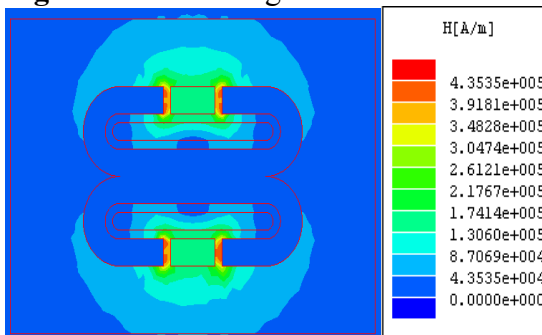

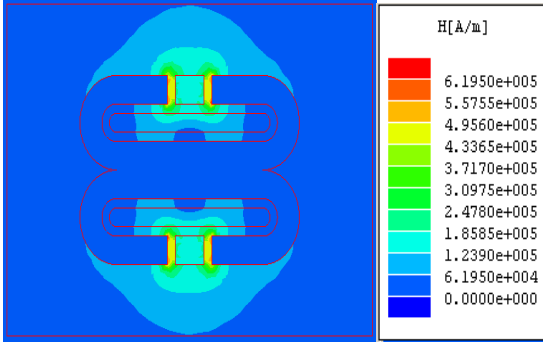**Figure 8.** MSM length=12mm.

Figure 9. MSM length=8mm.
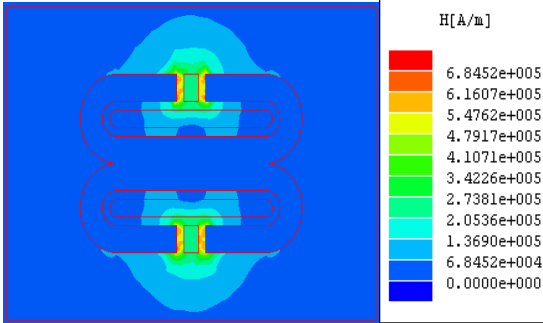

Figure 10. MSM length=4mm.
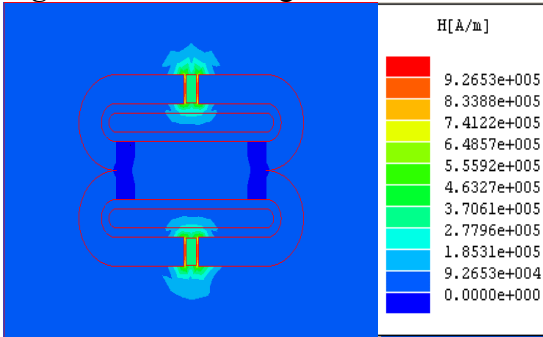

Figure 11. MSM length=2.6mm.

**Table II.** Lengths of MSM and the correspondent maximum and minimum H-field and the [1]Delta H-field.

Length of MSM (mm)	Max. H-field (A/m)	Min. H-field (A/m)	Delta H-field (A/m)
36	8.30E+04	6.77E+04	1.53E+04
32	9.08E+04	7.33E+04	1.75E+04
28	1.01E+05	8.05E+04	2.05E+04
24	1.12E+05	8.99E+04	2.21E+04
20	1.24E+05	1.03E+05	2.10E+04
16	1.41E+05	1.21E+05	2.00E+04
12	1.61E+05	1.44E+05	1.70E+04
8	1.89E+05	1.70E+05	1.90E+04
4	2.34E+05	2.06E+05	2.80E+04
2.6	3.68E+05	3.54E+05	1.40E+04

[1]Delta H-field is the difference of the maximum and minimum H-field.

**Graph 1.** There is not a definite trend between the length of MSM and the uniform distribution of MSM.
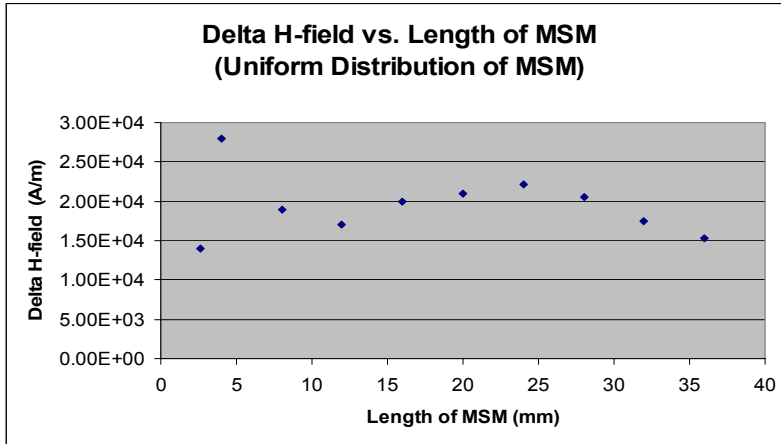
Graph 2. As the length of MSM material increases, the maximum and minimum H-field within MSM decreases exponentially.
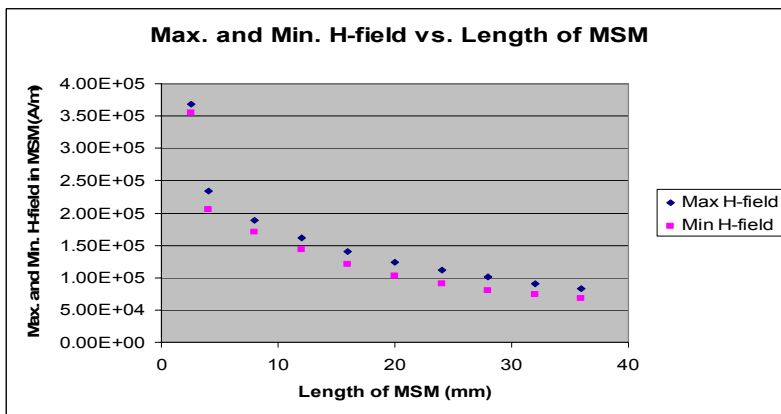
Graph 3. A linear relationship is found between MSM mass ratio and the length of MSM. As the length of MSM increases, so does MSM mass ratio.
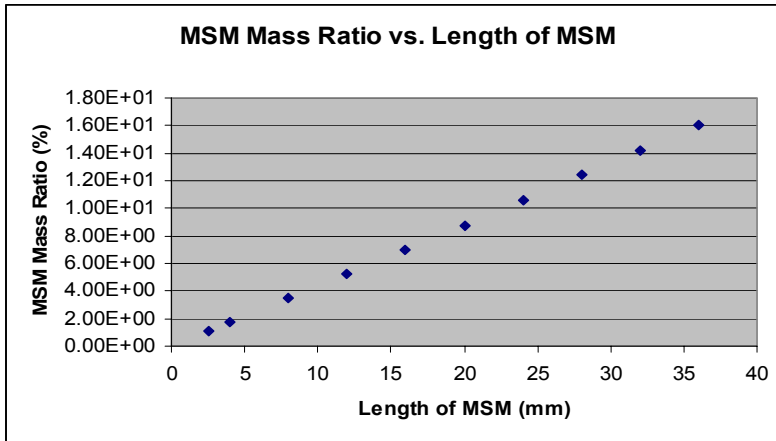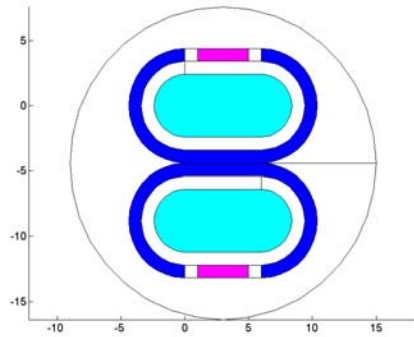

Graph 4. Saturation point is observed in MSM H-field by varying the current density in Cu.
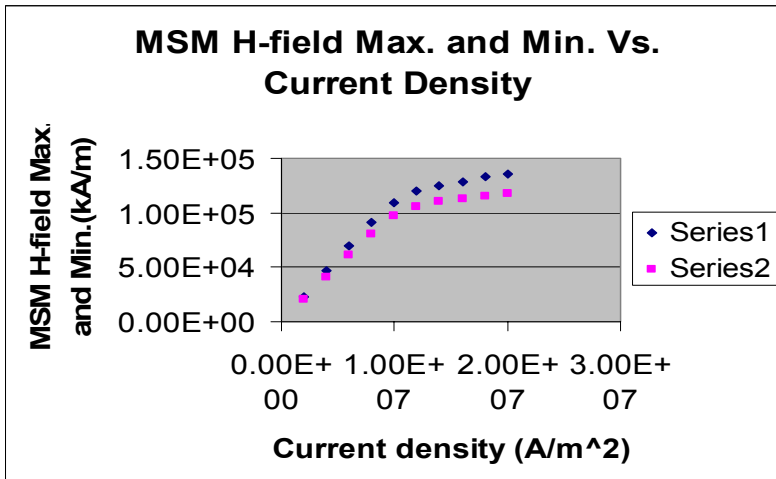
MATLAB

1. Build up the physical model. **Figure 12.**

2. Get the initial mesh. **Figure 13.**
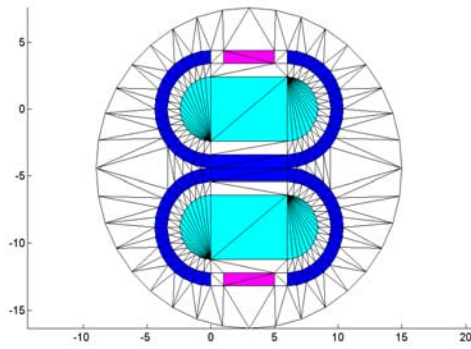
3. Refine the mesh to a smaller degree. **Figure 14.**
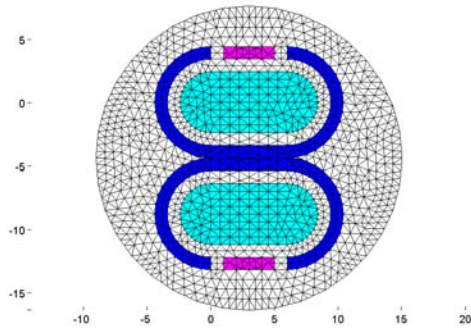
4. Recognize the boundary nodes. **Figure 15.**
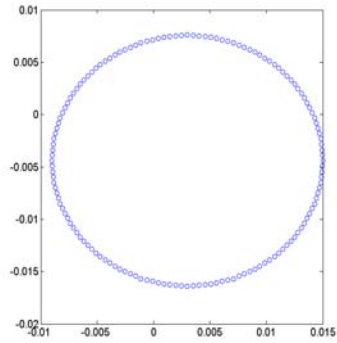
5. Organize the global matrix of the finite element method done in MATLAB programming.

6. Static analysis: solve for the solution of the problem.
   H-field **Figure 16**.

Figure 17. Maxwell SV simulation of an actuator design which is also built up and analyzed in MATLAB with the exact dimensions.

21

DISCUSSION

Through analysis in programming and simulations from MABLAB and Maxwell, respectively, the key to this study is to analyze the results from the simulations 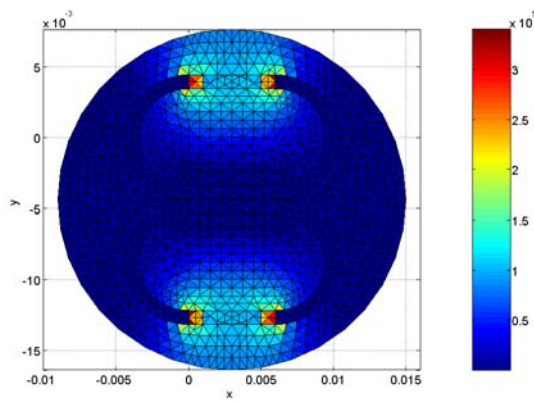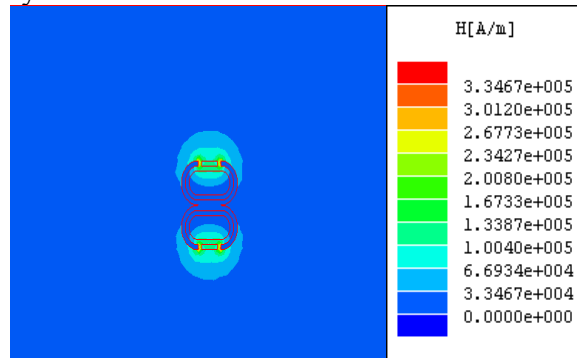to obtain a compact design of an actuator which provides magnetic field intensity (H-field) of 400kA/m in magnetic shape memory (MSM), high mass ratio in MSM, uniform H-field distribution in MSM and less leakage of H-field within MSM.

A magnetic field strength of 400kA/m is required in MSM in order for it to achieve its maximum strain. According to Maxwell SV simulations of various designs, it is observed that the figures that are horizontally stretched shape and contain relatively small area of MSM closely spaced from the hiperco material satisfy a magnetic field strength of 400kA/m within MSM. This conclusion for an optimal design of an actuator which satisfies a magnetic field strength of 400kA/m is a very general one. I believe that more simulations of different designs need to be done in order to obtain a more specific and accurate result in concluding an optimal actuator design.

For the calculation of MSM mass ratio among all the materials, an optimal design of an actuator requires that MSM contain the most ratio in mass possible. This is because more mass ratio of the magnetic shape memory material produces a greater shape change in MSM through the magnetic field due to its strain. This stain yields to a larger mechanical work done in the MSM material. According to Graph 3, the length of MSM is linearly proportional to the MSM mass ratio. Therefore, a greater area of MSM is desired in producing a higher mechanical work.

It is essential that there is a uniform H-field distribution in the MSM materials of the actuator because a non-uniform distribution of H-field within MSM may cause internal stress. Not only can the internal stress generate an ineffective and futile result, it could also possibly lead to a breakage within MSM. To avoid such phenomena, careful consideration must be taken in choosing the volume of MSM in the actuator. From looking at the Graph 1, the lower the delta H-field the more uniform of the H-field is distributed within MSM. So graph 1 demonstrates that there is not a definite relationship between the length of MSM and delta magnetic flux density.

The leakage of H-field, or electromagnetic interference, is observed from Maxwell simulations of different designs of actuators. An electromagnetic interference is a serious environmental issue for it can interfere with nearby electronic equipment. Thus an important criterion in a good design of an actuator is to have least leakage of the magnetic flux density possible. It is observed in the results that the length of MSM is closely related to the leakage of H-field. Looking at figures 2-11, we notice that the leakage of H-field decreases as the length of MSM decreases.

Moreover, one of the actuator designs, figure 17 simulated in Maxwell SV is built up in MATLAB shown in figure 16. Note that the magnitude of H-field in

figure 17 using Maxwell SV simulation and the magnitude of H-field in figure 16 using MATLAB are 3.3467e5A/m and approximately 3.4e5A/m, respectively. Thus these results validate its accuracy.

CONCLUSION

Mainly, the focus of my research is based on the effect in which the lengths of MSM and the current density in copper have on the overall design of the actuator. It is not sufficient in choosing the best design of an actuator because there are many other aspects to the actuator that needs to be studied. Therefore, I believe further analysis needs to be studied and examined for future experiments.

In summary, the four criteria researched and discussed are crucial to obtain an optimal design of an actuator which best utilizes MSM. For the two methods used, Maxwell SV is easier to manipulate in providing a faster result of H-field while MATLAB has more capabilities in producing further analysis on the actuator. (I.e. work, energy…) Very interestingly, the criteria discussed in obtaining an optimal design create paradoxes where a greater length of MSM yields to a higher MSM mass ratio and work done in its strain, yet it also creates a greater leakage of the magnetic flux density.

ACKNOWLEDGEMENT

REFERENCES

[1]   K. Ullakko, "Magnetically Controlled Shape Memory Alloys: A New Class of Actuator Materials", J. of Material Engineering and Performance **5** (1996), 405-409.

[2]   K. Ullakko, J.K.Huang, V.V.Kokorin and R.C. O'Handley, Scripta Mater. 36, 1133, (1997).

[3]   A. Likhachev, K.Ullakko, "Quantitative Model of Large Magnetostrain Effect in Ferromagnetic Shape Memory Alloys", EPJdirect B2, 1999.

[4]   R. O'Handley. Modern Magnetic Materials: Principles and Applications. John Wiley & Sons, USA, 2000, p.470.

[5]   R. Tickle, R.D. James, T.Shield, M.Wutting, V.V.Kokorin, "Ferromagnetic Shape Memory in NiMnGa System", IEEE Transaction on Magnetics, Vol.35 (1999), No.5.

[6]   A. Sozinov, A.A. Likhachev, N. Lanska, K. Ullakko, "Giant magnetic-field-induced strain in NiMnGa seven-layered martensitic phase", Applied Physics Lett. Vol 80 (2002), No.10, 1746-1748.

[7]   F. Brailford, Physical Principles of Magnetism. D.Van Nostrand Company, London, 1966, p.74.

[8]   John P. Wolf. The Scaled Boundary Finite Element Method. John Wiley & Sons Ltd, 2003, p.12-25.

[9]   Tirupathi R. Chandrupatla and Ashok D. Belegundu. Introduction to Finite Elements in Engineering. Prentice-Hall, 1991.

[10] John R. Brauer. What Every Engineer Should Know about Finite Element Analysis. Marcel Dekker, 1993.

POWER SYSTEM MODELING FOR LIONSAT

Daniel Dobrin*
(Dr. Sven Bilén, Faculty Mentor)
(Dr. Charles Croskey, Faculty Mentor)
Department of Electrical Engineering
Pennsylvania State University, University Park, PA 16802

*Undergraduate student of
Department of Electrical and Computer Engineering
University of Illinois at Chicago
Chicago, IL, 60607-7050

ABSTRACT

This paper describes different methods for transferring, in the most efficient way, power from the solar cells to the battery system, and from the battery system to all loads of LionSat.

Since overcharging a battery can cause damage to the battery, this paper describes/analyzes different DC-DC converters that will not just reduce/regulate the voltage, but at the same time perform efficiently, giving the best performance. DC-DC power converters are used in many applications, including power supplies for laptop computers, office equipment, as well as spacecraft. The input to a DC-DC converter is a varying voltage source. In the case of a spacecraft, the input to a DC-DC converter depends on the orientation of the solar panels with respect to the sun. Therefore, the job of the DC-DC converter is to produce a constant output voltage, having a magnitude that is different than the input.

The following paper will mention converters such as: buck (decreases voltage magnitude), boost (increases voltage magnitude), buck-boost (increases/decreases voltage magnitude), series-connected boost converter (SCBC), etc. Different topologies of DC-DC converters are examined in order to achieve the desired function and efficiency.

Furthermore, after charging the battery system to the maximum capacity, power must be transferred to all loads (e.g., micro-controller, communication) of the satellite. The load power must also be transferred in an efficient manner and be controlled at the same time. Not enough power delivery to satellite components

can result in mission failure. Therefore, the paper describes/analyzes converter topologies that will deliver an average of 10 watts of power.

INTRODUCTION

The power system for LionSat is responsible for providing the electric power for the components of the spacecraft. It is composed of a power source (solar cells), a power storage facility (batteries), as well as power conversion and distribution equipment. The satellite systems that need power include: microcontroller, ion thrusters, etc. These systems total an average power of 10 W.

To provide LionSat with the necessary power, a generation system is needed. There are several generation systems that could be used, but LionSat uses solar panels. Solar panels are used in missions where power must be generated beyond the capabilities of battery cells. Solar panels produce electrical power, with voltage determined by the cell technology and current available by the level of incident light. Solar cells can either be sun-tracking or fixed. Using sun-tracking arrays has the benefit of being more efficient, since it allows the maximum array area to be targeted at the sun at all times. If the solar cells are fixed then they can be distributed on non-tracking panels or around the body of the spacecraft. Using fixed solar cells gives less efficiency in the use of the solar cells [3, 5].

Solar cell efficiency determines how much electrical energy is converted from light by the solar cells. Since different solar panel technology could be used, the choice for LionSat is between Silicon and Gallium-Arsenide. The current technology of choice for most satellites is Gallium-Arsenide. Thus far, the choice for LionSat is currently toward Gallium-Arsenide.

Furthermore, when the satellite is away from the sun, eclipsed, the batteries will store the power needed. Therefore, batteries come into use during eclipse periods, or to meet short term power peaks. Rechargeable batteries in LionSat are used to meet the power requirements that can not be covered by solar panels. However, since mass is of importance (30 kg maximum) for LionSat, Nickel Cadmium batteries are being considered. A specific Nickel Cadmium battery being considered is Sanyo N-4000DRL, since this is recommended by the NS-3 program[1]. Charging time for Nickel Cadmium is about one hour for fast charge at a nearly complete level of discharge. Most of the charging systems use the Peak Power Tracking (PPT) method or the Direct Energy Transfer (DET) method for recharging batteries and providing power. To ensure longer battery life, the battery must be completely discharged once in a while through a relay resistor circuit.

EXPERIMENTAL DESCRIPTION

The purpose of this research/experiment is to analyze various topologies to provide an efficient power system for LionSat. The analysis is done using the

---

[1] Battery type/specification provided by AFRL Internal Cargo Unit User's Manual, UN-0001, Revision-July 2003.

Virtual Test Bed software. Developed by Dr. Roger Dougal and others at the University of South Carolina, The Virtual Test Bed (VTB) is software for "prototyping of large-scale, multi-technical dynamic systems. It allows proof-testing of new designs prior to hardware construction [4]." By simulating different models of power systems using Virtual Test Bed, results (tables, graphs, etc.) are compiled to develop the desired and efficient power system for LionSat. Virtual Test Bed has the capability to also output a 3D simulation of the constructed system.

Figure 1. Snapshot of the 3D visualization simulation

By providing a virtual simulation of the system that was constructed, it helps in giving the designer/developer a better understanding of how the final system works.

Converter Topologies and Characteristics (DC-DC)

In order to convert the input voltage into the required output voltage, certain approaches have to be taken.

In general, two approaches exist for converting one voltage into another voltage. The first approach, "time-continuous with dissipative element ($V_{in} > V_{out}$ only)," is used to convert a high voltage to a low voltage. The second approach, "time-discrete with energy-storage element," is used for both types of conversion; high to low and low to high. The energy-storage element can be inductive or capacitive. More information on the two approaches, capacitive voltage converters and inductive voltage converters, can be found in the literature; see, for ex., [1].

Working with DC-DC converters requires certain important characteristics to be taken into consideration: weight, size, fault tolerance, efficiency, power quality, and reliability. There are different DC-DC converters that can regulate the magnitude of a dc voltage, but the most common types used are briefly described below.

Buck Converter: The buck converter reduces the magnitude of the dc voltage, and has a conversion ratio of

$$M(D) = D \qquad\qquad (1)$$

where D is the duty cycle.

Boost Converter: The boost converter increases the magnitude of the dc voltage, and has a conversion ratio of

$$M(D) = 1 / (1 - D) \qquad\qquad (2)$$

Buck-Boost Converter: As the name might already suggest, this converter increases or decreases the magnitude of the dc voltage. At the same time, the converter changes the voltage polarity.

Cuk Converter: Constructed with inductors in series with the converter input and output, the converter is identical to the buck-boost converter.

SEPIC: Single-ended primary inductance converter can increase or decrease the magnitude of the dc voltage without changing the voltage polarity. It has a conversion ratio of

$$M(D) = D / (1 - D) \qquad\qquad (3)$$

SCBC: Developed at the NASA Glenn Research Center using isolated DC-DC buck converters, the series connected boost converter adds a bypass connection to the DC-DC converter [2].

Other types of DC-DC converters use a combination of the above and other technologies, such as PWM, controllers, intelligent control, etc. Since some of the basic converter topologies mentioned above do not provide isolation between the input and output, they are often not used in their basic format. To provide isolation and at the same time multiple voltage outputs of different polarities, a transformer is used. Transformers can create better converter efficiency by making proper choices in the transformer turns ratio. Also, when a transformer is inserted into a converter, the transformer will operate at the converter frequency. Higher frequencies decrease size and weight of a transformer.

DISCUSSION

Designing a power management and distribution (PMAD) system for LionSat requires an understanding of the satellite mission and issues as reliability, size, efficiency, energy balance, etc. Creating the power system for LionSat requires making choices between the options one has in designing the electrical power system. Hyder et al. [3] provide a good description of the electrical power system options that one has to work with. However, in this section I am concentrating on some preliminary choices for LionSat.

Since LionSat is a small satellite, the electrical power system will be

centralized. The size of the satellite and the low power demand of the payloads (average of 10 W), does not require the distribution of electrical lines over long distances. The energy distribution system is DC distribution as opposed to AC distribution.

To transfer energy and provide the most power from the solar cells, LionSat can use direct energy transfer (DET) or a peak power tracker (PPT). From all the readings I have done, a DET system generally provides higher efficiency and lower cost for many, but not all, systems. The basic idea behind DET is to regulate any excess power from the arrays using linear or switching shunt. In order to investigate the operation and performance of shunting, a DET power system using sequential shunting, as shown in Figure 2[2], could be studied. Using sequential shunting reduces power loss since the transistor is operated as a switch. Pulse width modulation controls the transistor based on the bus voltage, reference voltage, and error signal. A PPT system provides lower efficiency since it requires adding extra components, but might be more efficient for LionSat. From readings I have done, the PPT system can have an advantage in low Earth orbit missions, and missions that need the maximum power at end-of-life. A PPT system also provides a higher overall efficiency at lower mass for systems with moderate or low power requirement. Figure 3 shows a buck converter being controlled by PPT in order to draw the maximum power from the solar array.

As previously mentioned, a transformer incorporated in the LionSat converter is needed to provide DC isolation between input and output. Having isolation will help reduce electromagnetic interference in LionSat. However, there are several choices between converters with transformers. Some of these choices are: half-bridge, full-bridge, flyback, forward, and others. From all these choices, the flyback converter is the one that is mostly used for low power requirements. The low power requirement is a power that is less than 100 watts. The flyback converter is based on the buck-boost topology, and therefore has almost the same conversion ratio; with the exception of a factor n (number of turns ratio).

$$M(D) = (n)(D) / (1-D) \qquad (4)$$

A new and efficient technology that is now available to LionSat is the series connected boost converter (SCBC). The SCBC makes use of isolated buck converters for controlling the boost given to the DC-DC converter input voltage. One, probably major, advantage provided by the SCBC is the ability to use an off the shelf DC-DC converter, and regulate more power than the converter can regulate on its own. If the SCBC can regulate more power, it means that the efficiency for the output power in LionSat can be above 90%[3]. However, the fact that it boosts the input voltage and helps increase the output power causes a problem for LionSat. Even though the efficiency is increased, the output power

---

[2] Refer to the Virtual Test Bed website [4].
[3] Refer to reference [2].

might be greater than the needed LionSat power requirement.

RESULTS/DATA

All data/results are preliminary as of July 15, 2003 (estimated), and serve as a step toward a final power system design. The data is subject to change based on improvements and changes made by future teams working on the LionSat power system. Table I[4] gives approximations of power usage for LionSat.

Table I. Power usage approximations as of July 15, 2003

ITEM	DUTY CYCLE	VOLTAGE (V)/ CURRENT (mA)	PEAK POWER (mW)	AVG. POWER (mW)
Magnetometer	100%	+5 / 30 -5 / 30	300	300
RF Probe	15%	+5 / 78 -5 / 22 +15 / 50 -15 / 62	2180	327
Transmitter	4%	12 / 500	6000	240
RF Power Amp	4%	+5 / 500	2500	100
Command Receiver	100%	3.3 / 33 +15 / 30	558.9	558.9
Magnetic Torquer	5%	+5 / 600	3000	150
ACS Computer	5%	3.3 / 650	2145	107.25
Main Computer	100%	3.3 / 650	2145	2145
GPS	100%	3.3 / 150	495	495
Microthruster	5%	12 / 2500	30000	1500

SUMMARY						
	3.3v	+5v	-5v	12v	+15v	-15v
Average power (mW)	2856.2	458.5	166.5	1740	563	140
Peak load if all on (mW)	4893.9	6040	260	36000	1200	930

TOTAL Avg. Power	
Without converter loss	5.92315 W
With 75% converter loss & 85% regulation	9.2912 W

[4] Developed by Dr. Charles Croskey in Electrical Engineering at Penn State University, University Park.

Figure 2. Schematic diagram of a simplified DET power system
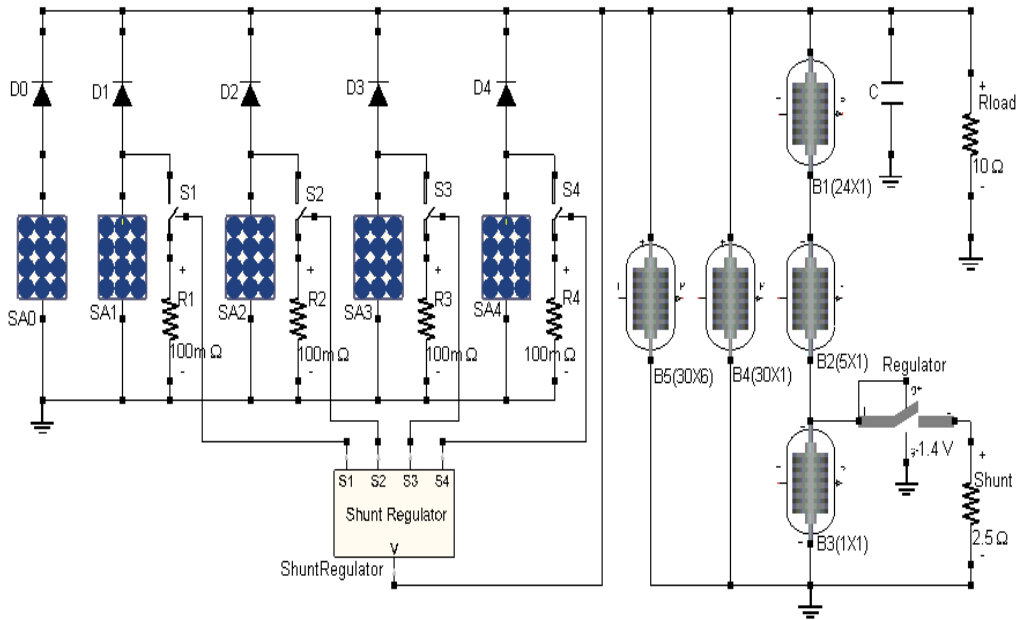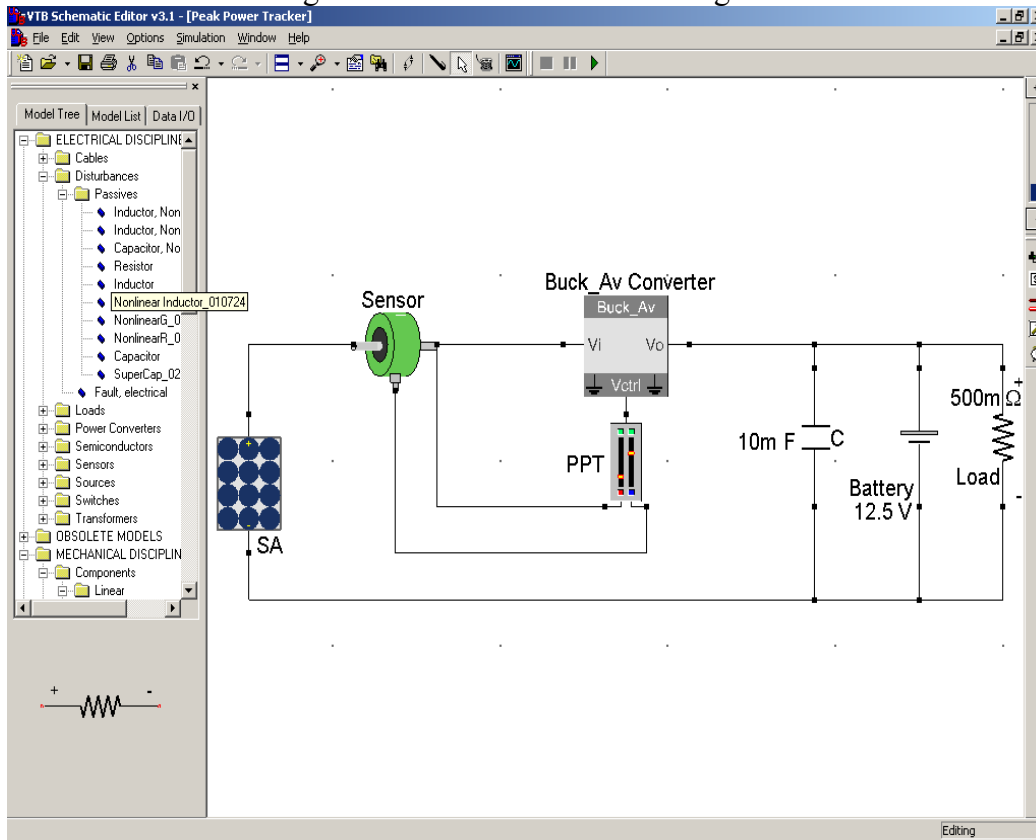

Figure 3. Peak Power Tracker Diagram

The sample satellite system given in VTB and shown in Figure 4 starts off with solar irradiance illuminating an 88x19 (series by parallel) array of single junction silicon cells. A buck converter is used in order to lower the input voltage. After lowering the input voltage a charger is used in order to charge a 10x8 Li-ion battery pack. Sensors, current and voltage references are used to control the charging of the Li-ion battery. Virtual Test Bed does not provide a model for NiCd battery which LionSat will be using.

Furthermore, an over-current relay circuit is used to isolate the fault on the load side by sensing the load current when it exceeds the reference current. The starting current of the relay is 10A, and the relay time is one second. The charging current reference for the charger is 10A, while the voltage reference for the charger is 41V.

The sample satellite system does not include LionSat specifications. It is used to give an understanding of a satellite power system. As of July 22, 2003, the LionSat solar array sizing and such are still to be determined.

Figure 4. Sample Satellite Power System[5]

---
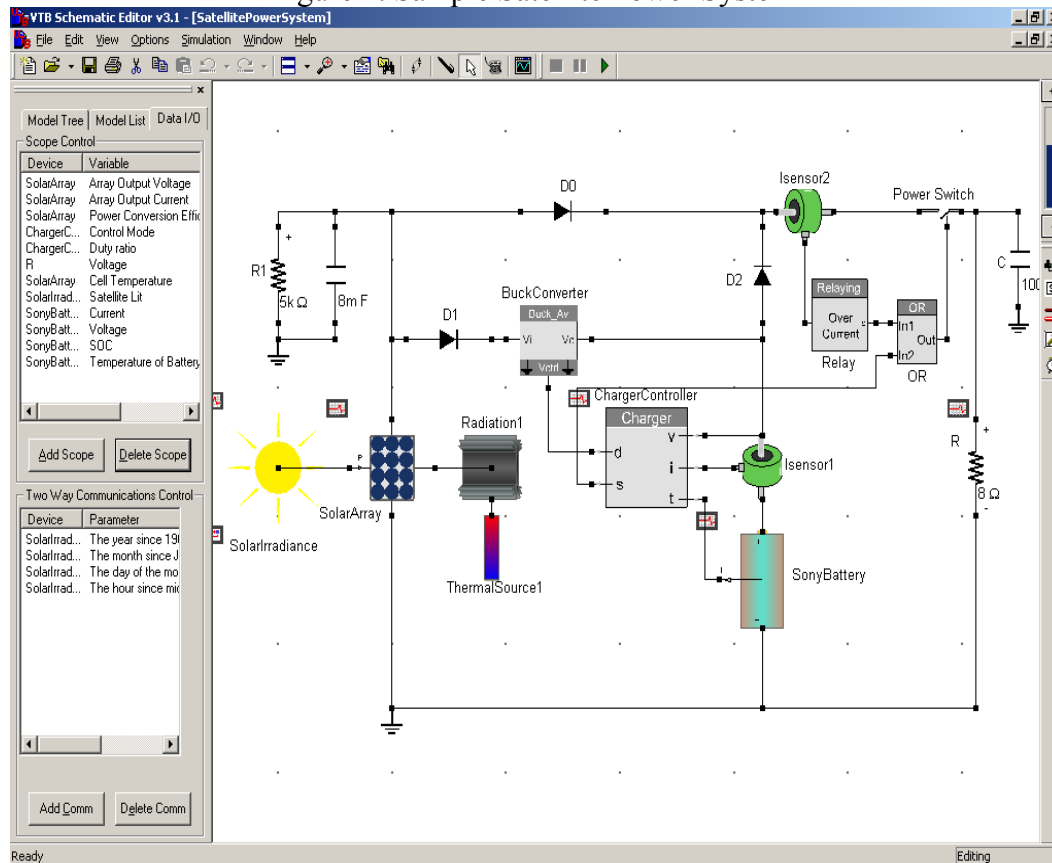
[5] The figure is the Satellite Power System given by VTB in the Sample System with a brief description. Specifications for LionSat are not yet determined as of July 22, 2003.

CONCLUSION

The paper described different methods for transferring, in the most efficient way, power from the solar cells to the battery system, and from the battery system to all loads of LionSat. Power sources and energy storage units that are preliminary choices for LionSat were presented and discussed. Issues such as DC-DC converter topologies, isolation, efficiency, and others are also presented with a brief description. The paper mentioned converters such as: buck (decreases voltage magnitude), boost (increases voltage magnitude), buck-boost (increases/decreases voltage magnitude), series connected boost converter (SCBC), etc.

It is important to note that a continuing effort is going on for the final LionSat power system.

ACKNOWLEDGEMENTS

REFERENCES

[1] H.J. Bergveld, W. S. Kruijt, and P.H.L. Notten, "Battery Management Systems Design by Modeling," *Philips Research,* **1** (25), 251-265, (2002).

[2] R.M. Button, "An Advanced Photovoltaic Array Regulator Module," *IECEC-96424: NASA Technical Memorandum 107304,* **1996 Record**, 1-6, (1996).

[3] A.K. Hyder, R.L. Wiley, G. Halpert, D.J. Flood, and S. Sabripour, "Power Management and Distribution," 353-411, *Spacecraft Power Technologies,* Space Technology-Volume 1, edited by N. Hanson, Imperial College Press, London, 2000.

[4] *VTB::Virtual Test Bed*. URL: http://vtb.ee.sc.edu [11 June 2003]

[5] *Power System*.
    URL: http://www.compulink.co.uk/~sjbradshaw/msc/power [18 June 2003]

SOFTWARE/HARDWARE DIAGNOSTICS FOR TESTING ROCKET PAYLOAD ELECTRONICS

Michael Ellis*
(Charles Croskey, J. Mitchell, Faculty Mentors)
Department of Electrical Engineering
Pennsylvania State University
University Park, PA 16802

*Undergraduate student of
Department of Electrical Engineering
Bucknell University
Lewisburg, PA 17837

ABSTRACT

Sub-orbital sounding rocket payloads are being developed for the investigation of various particulate-associated phenomena. Several probes are included for measurement of different electrical properties. Testing of the electronic circuits for these probes is necessary to ensure proper working order as well as for calibration purposes.

This project focuses on the design and development of a software program, using LabVIEW, to test the rocket payload instrumentation. The program will be used to control an Agilent 33120A Function Generator for input to the rocket payload instrumentation. It will also read and record from an Agilent 34970A Data Acquisition Unit that is attached to the instrumentation output. The merit of this project is that it removes the repetitiveness from the testing procedure and saves time as well. It will hopefully be flexible enough for use at a later date for instrumentation with several different specifications.

INTRODUCTION

Various particulate-associated phenomena (such as noctilucent clouds and polar mesosphere summer echo regions) have been witnessed in the mesosphere and lower thermosphere (65-95 km). This area is essentially inaccessible to both balloons and satellites, making the sub-orbital sounding rocket the ideal method

for investigation. By including several types of probes with the rocket payload, we can take measurements of different electrical properties of the atmosphere, such as the polar components of conductivity and their associated ion mobility and number density values. These measurements will hopefully lead to an explanation for the cause of the particulate-associated phenomena.

Such rockets have already been launched in regions of high latitude but these will be among the first to be launched in a region near the equator to investigate particulate-associated phenomena. The purpose of this investigation is to determine similarities and/or differences among the particulate-associated phenomena in the lower latitudinal regions and those already witnessed in higher latitudes.

Testing of the electronic circuits for these probes is necessary to ensure proper working order as well as for calibration purposes. Documentation of the various probes' calibrations will be necessary for accurate data analysis after the payload has been launched. Portability for this testing procedure is desired so that last-minute verifications of proper operation can be done on the payloads at the launch site. Due to the tedious nature of these tests, an automated procedure would be desirable. This would not only reduce the necessary time required to conduct them, but would also decrease the chance for human error that might effect the test results.

EXPERIMENTAL DESCRIPTION

In order to conduct the necessary tests on the payloads, it is necessary to generate a signal for input to the probes while, at the same time, measuring the output voltages. To do this, an Agilent 32120A Function Generator is used for input to the rocket payload instrumentation while an Agilent 34970A Data Acquisition Unit (DAQ) is used to measure voltage from the instrumentation outputs. In order for the tests to be automated, both units must be controlled by a single outside source simultaneously. After researching several options, LabVIEW was found to be the best resource for developing a program to control both Agilent units. Using LabVIEW and two sets of downloadable drivers (one for each unit), a program was written that allows a laptop computer to control the two Agilent units via a General Purpose Interface Bus (GPIB) connection. This permits the test procedure to be portable, thereby allowing it to be used on-site at the rocket launch.

In setting up the test, the function generator is connected to the input of the circuit board and the output channels of the board are connected to the DAQ, as seen in Figure 1. An Agilent 34902A 16-channel reed multiplexer plug-in module is inserted into the DAQ to switch between the output channels of the circuit board being tested. As the test is run, the laptop computer commands the function generator to output a certain voltage or frequency to the circuit board, and then commands the DAQ to read the resulting voltages at each of the output channels.

There are three different types of boards being tested, each with a different number of output channels. The Blunt Probes have just 4 DC output channels, the Langmuir Probes have 4 DC and 3 AC output channels, and the Nose-tip Langmuir Probes have 1 DC and 3 AC output channels. The architecture of the program must accommodate these three different output channel configurations as well as several other possible ones in the future.

Due to the nature of the tests, it is necessary to first conduct the DC sweep in order to attain the midpoint values of the output. These values will then be used during the AC sweep to bias the input voltage, so as to avoid any potential clipping. Because of this necessary input bias and the fact that the peak-to-peak voltage of the input AC signal is so small, it is difficult for a function generator to produce the required input signal. Most function generators can't produce an AC signal with a bias of several volts and a peak-to-peak voltage of only a few millivolts. Therefore, it is essential to have a DC bias source separate from the AC signal source for the AC sweep. The DC bias source will be controlled manually based on the midpoint values from the DC sweep while the AC signal source will be controlled by the test program. While this does remove some of the desired automation from the test, it is essential for accurate test results.
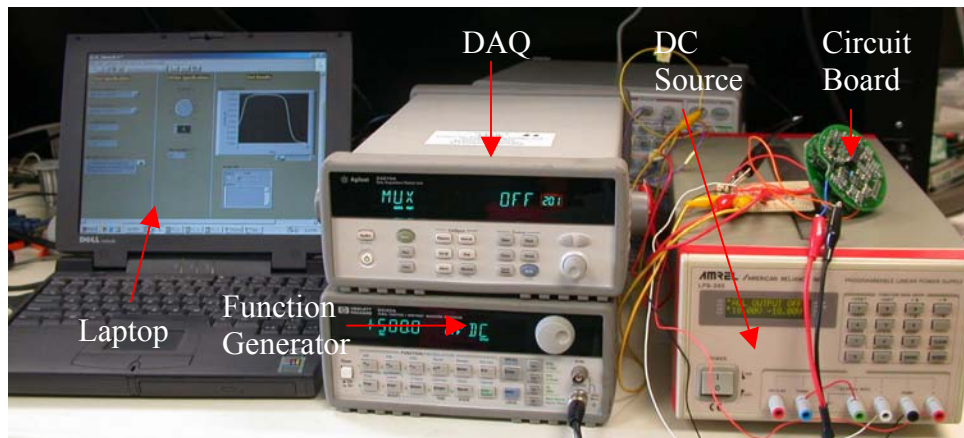

Figure 1: Test Equipment Setup

In conducting both sweeps, it is necessary to have a floating input voltage because the circuitry of the data board produces a $\pm2.5V$ bias voltage at the input. The 33120A Function Generator unit is ideal because it is capable of doing this.

PROGRAM FUNCTIONALITY

In designing the functionality for this program, there were several prerequisites that had to be met: 1) a simple user interface, 2) all necessary controls present and clearly labeled, 3) easy adjustment to different board specifications and 4) quick error fixing procedures. With all of these qualifications in mind, the AC and DC sweep programs were developed.

In order to design a simple user interface, all of the unnecessary controls had to be hidden, leaving only the ones that were essential to setting up and running the test. Then, the controls that were necessary had to be organized and labeled in a simplistic and logical manner to allow the user to quickly locate the necessary control. As seen in Figures 2 and 3, the control panel is set up to meet these requirements in a manner that is also visually appealing. The number of controls on the panels was minimized and the remaining controls were organized into three columns by function.

The left column contains controls for the test setup, such as the address locations of the Agilent units and the file path for the test results. In the DC sweep control panel, there are also controls for setting up the test parameters. The center column contains the controls for the setup of the DAQ. These controls allow the user to select the slot that the multiplexer plug-in module is in as well as the channel of the multiplexer that is scanning. In the case of the DC sweep, this is an indicator that shows the current channel being scanned. For the AC sweep the channel must be manually set for each scan, allowing the user to set the separate DC power supply to the appropriate value. The right column shows the results of the test. In the event that the program fails, this displays a description of the error to help the user debug the problem. There is also a graph on this column that displays real-time outputs for each of the channels being scanned. This allows the user to quickly discover any problems with the test by noting whether the outputs seem reasonable. This allows the user to quickly go back and redo the test without wasting time.
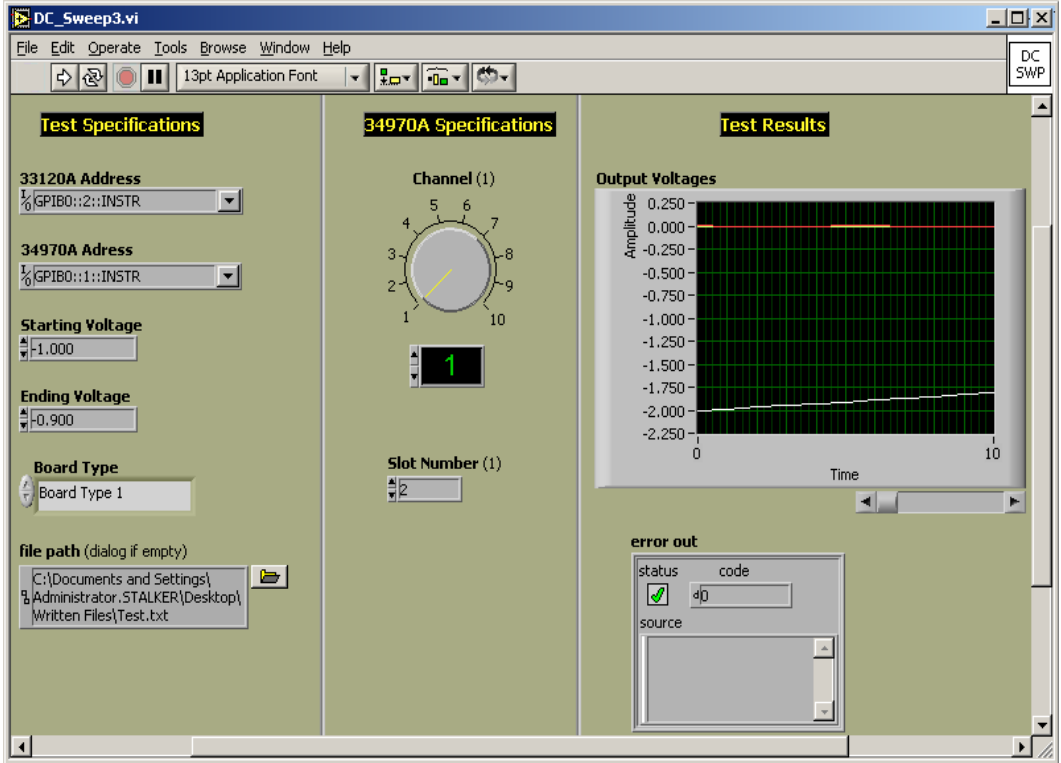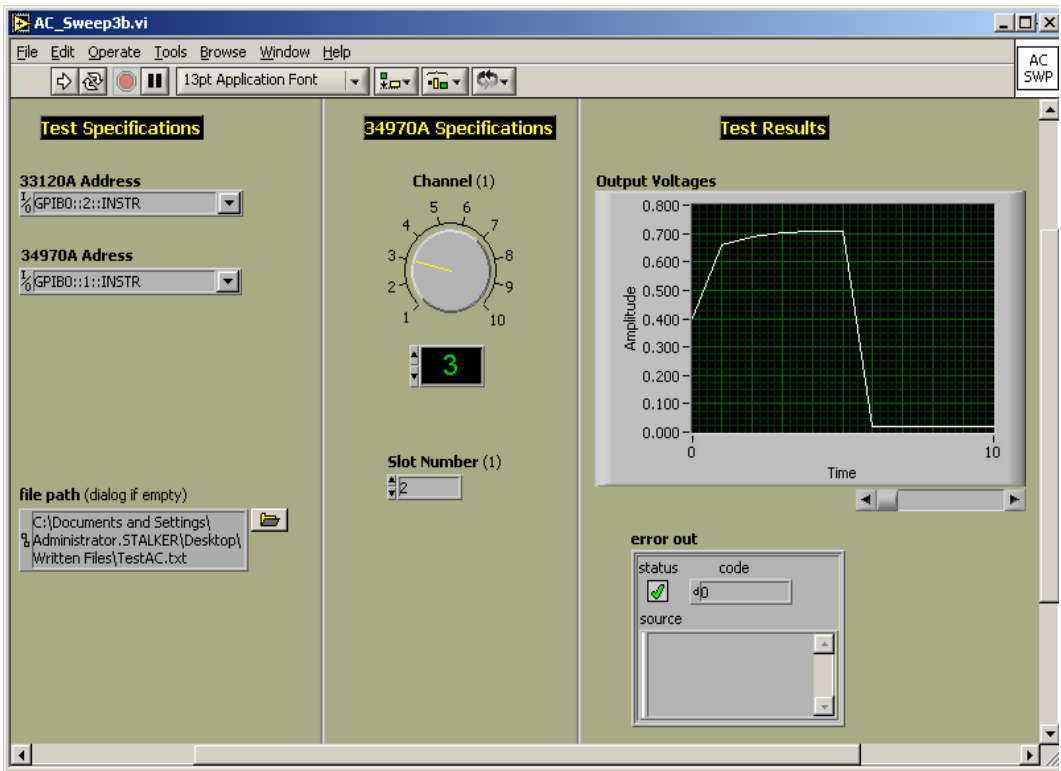
Figure 2: DC sweep control panel

Figure 3: AC sweep control panel

PROGRAM ARCHITECTURE

The primary function of both the DC and AC test programs is to sweep through a sequence of values and output them to the function generator while receiving and recording values from the DAQ. As seen in Figure 4, a FOR loop is the major function required in implementing these programs. The file output functions are the only part of the program not within the main loop.
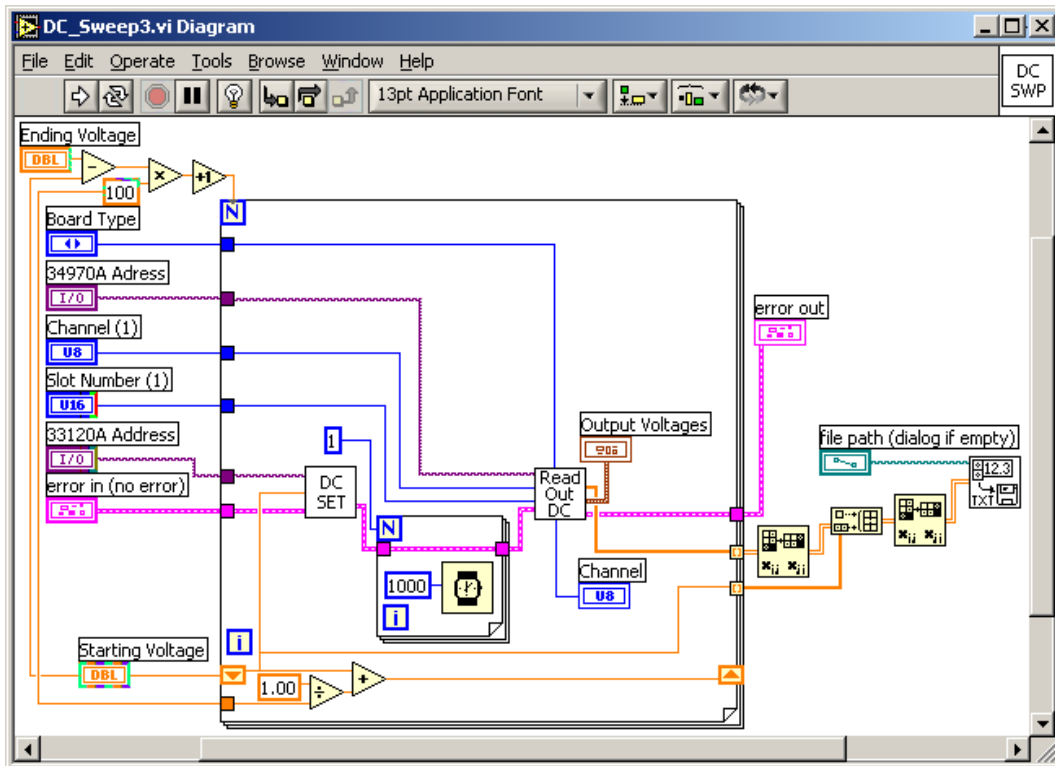

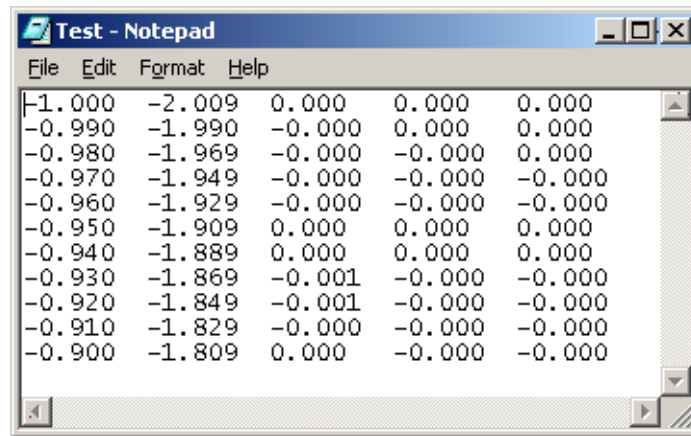Figure 4: Main schematic for DC sweep test program

DC Sweep Program

Within the main loop of the DC sweep program are two sub-VIs: one that sets the DC voltage and outputs it to the function generator and one that commands the DAQ to scan a certain channel and record the associated voltage. Between the two sub-VIs, a delay is implemented using a simple FOR loop and a VI that waits a set number of milliseconds. This delay is important because the circuit boards being tested need a small amount of time to stabilize after a voltage is applied to them. As seen in Figure 4, this delay is currently set at one second (1000 ms), although it can be changed as necessary.

The number of iterations for the main loop is set by subtracting the starting voltage value from the ending one and multiplying that by 100 before incrementing by 1. This current setting will give a resolution of 100 data points

for each voltage range scanned through. Altering the value currently set at 100 will change this resolution. Using a shift register, the DC value that is actually sent to the function generator to be outputted is integrated for each loop iteration according to the resolution that is set. The result is that the program begins by outputting the user-defined starting voltage and sweeps through a range of voltages according to the selected ending voltage and resolution. For each voltage that is set by the function generator, the DAQ scans all of the DC channels and records their associated voltages.

As the sweep is being conducted, the values acquired by the DAQ are stored in an array. Once the sweep is finished, these values are passed out of the FOR loop, combined with the DC input values, and outputted to an ASCII file as seen in Figure 5. This file is formatted so that any standard spreadsheet program can read it, allowing for the data to be analyzed at a later time. The leftmost column contains the DC input voltage values. The other columns contain the output voltage values for each of the DC output channels.

Figure 5: Example ASCII output file for DC sweep program

The *Set DC Value* sub-VI that is contained within the main FOR loop commands the function generator to output the DC voltage specified by the program. This sub-VI, as seen in Figure 6, contains VIs that are a part of the Agilent LabVIEW driver set available for download from the Agilent web page. Primarily, this sub-VI commands the function generator to output the DC signal according the parameters set within, including the DC voltage.
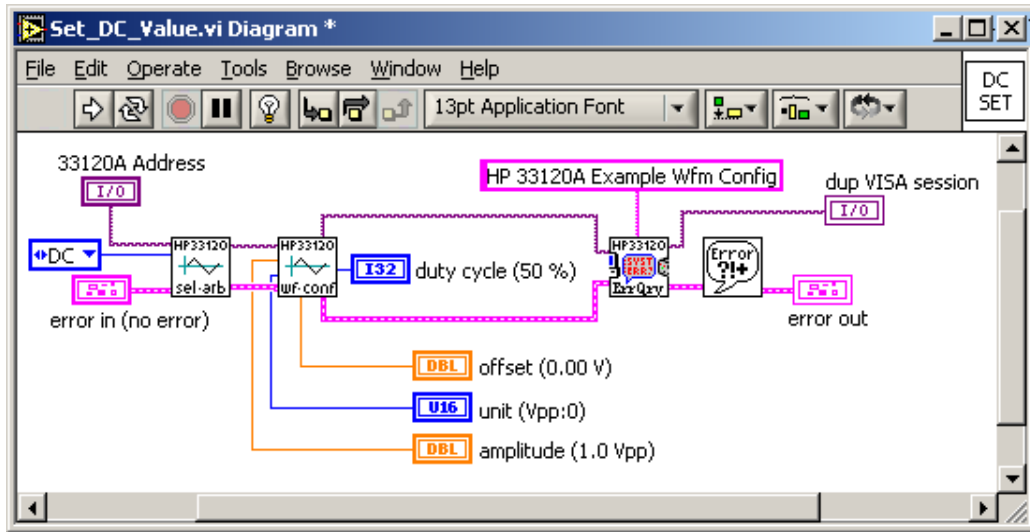
Figure 6: Schematic for *Set DC Value* sub-VI

The *Read Out DC Value* sub-VI found in the main FOR loop commands the DAQ to scan through each of the output channels of the circuit board and measure the voltages. As seen in Figure 7, the main body of this VI is a FOR loop within a case structure. The case structure is defined by the selection of which board type is being scanned. The only difference between the different cases is the number of DC output channels on the board, which defines the number of iteration for the FOR loop. Within the FOR loop, the channel is incremented by 1 for each iteration and the DAQ is commanded to scan that channel. Once each of the channels is scanned, the acquired values are passed out of the FOR loop and into both a graph and an array in order to be passed out of the sub-VI.
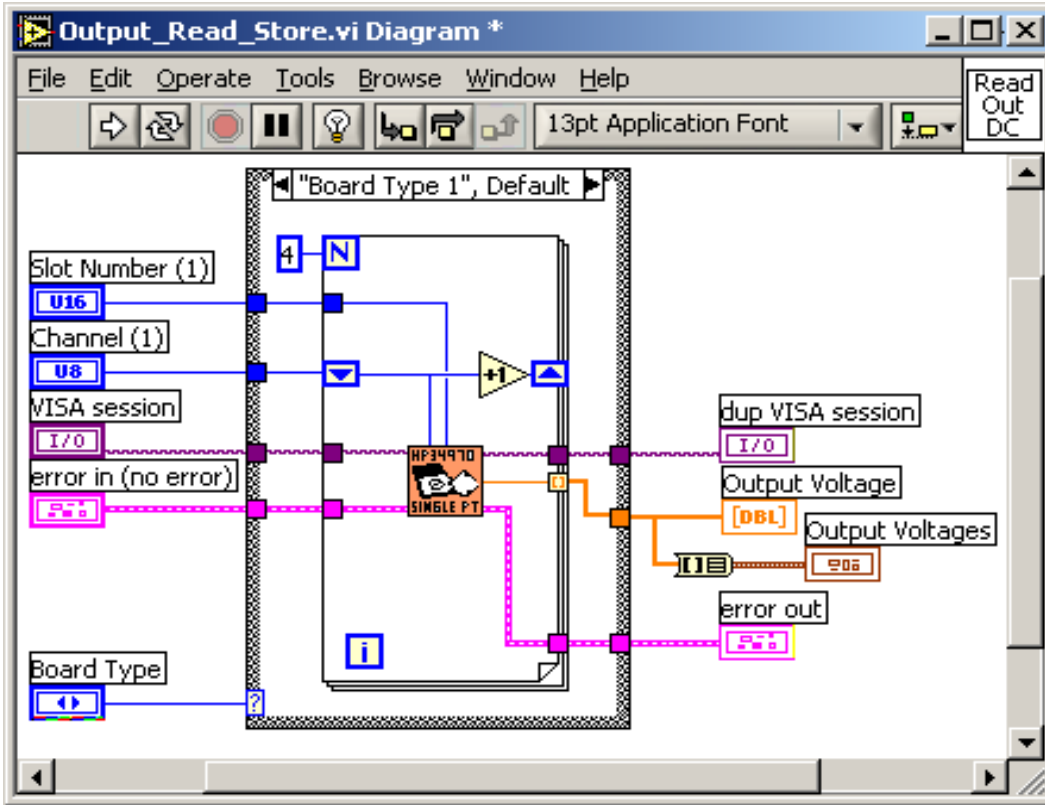
Figure 7: Schematic for *Read Out DC Value* sub-VI

AC Sweep Program

The structure of the AC sweep program is very similar to that of the DC sweep program. As seen in Figure 8, it contains two sub-VIs within the main FOR loop that act much the same as those in the DC sweep program. The primary difference in the structure of the two programs is way in which they generate the output file. Unlike the DC sweep program, this one uses a case structure in the implementation of the file output section. This is because of the manual control of this program that requires the user to scan each output channel individually. When the first channel is scanned, the case structure is set true and a file is created with the information for that channel. For each subsequent channel, the case structure is set false and that same file is amended with the new data. The resulting output file appears as it does in Figure 9. Note that the file is generated with a set number of columns filled with zeroes. For each channel scanned, this column is overwritten and saved, allowing channels to be rescanned several times and in any order.
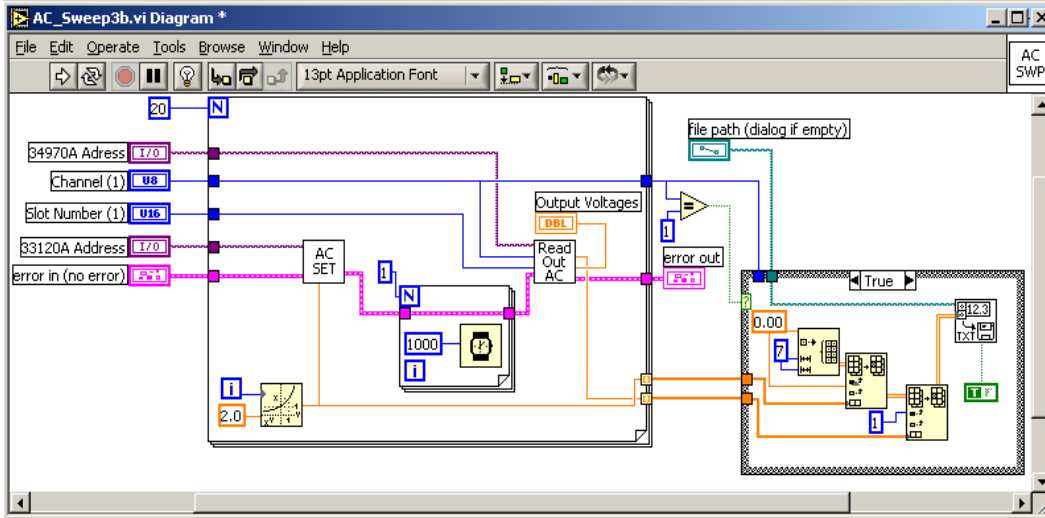
41

Figure 8: Main schematic for AC sweep program

Figure 9: Output ASCII file for AC sweep program

Another difference between the two programs is the way in which the parameters for the sweep are set. In the AC sweep program there is no way of picking the start and end frequencies as with the voltages in the DC sweep. This is because the frequency responses for the different boards are fairly similar, allowing the same frequency range to be used for all of the tests. An exponential sweep is used to account for the large frequency range from about 5 Hz to about 2 kHz.

As seen in Figure 10, the *Set AC Value* sub-VI used in the AC sweep is much the same as the *Set DC Value* sub-VI used in the DC sweep. The only difference between the two VIs is the preset parameters for the output signal (i.e. signal type, amplitude, offset, etc.). The *Read Out AC Value* sub-VI, on the other hand, is somewhat different than its DC counterpart. Because the user must manually select the channel being scanned, there is no need for a case structure to determine the number of channels being scanned. As seen in Figure 11, this VI is, therefore, much simpler than its DC counterpart. It only contains a sub-VI to command the DAQ to scan the appropriate channel and records the acquired values.
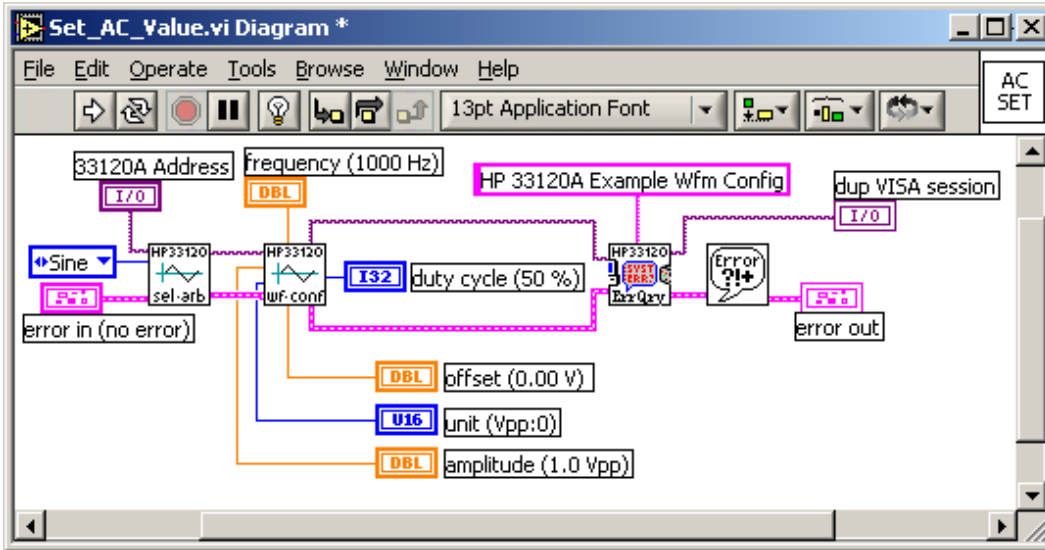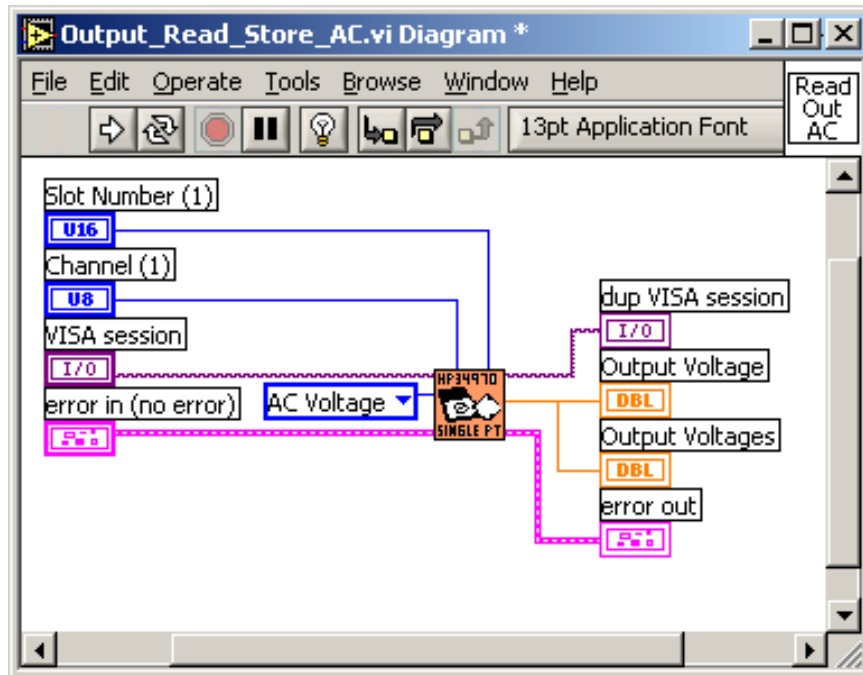
42

Figure 10: Schematic for *Set AC Value* sub-VI

Figure 11: Schematic for *Read Out AC Value* sub-VI

PROGRAM OPERATION

The circuit boards being tested vary slightly with respect to specifications, but they are all similar in function. All of the boards contain a differencing amplifier followed by a second-order Butterworth low-pass filter and an amplifier in sequence. Each of them, in effect, operates as a low pass filter and amplifier. The resulting outputs of the DC and AC sweeps can be seen in Figures 12 and 13, respectively. These figures are graphs of the data received from the testing of a

43

blunt probe in the lab. The values received in this test are as expected, therefore verifying that the test procedure is working as desired.
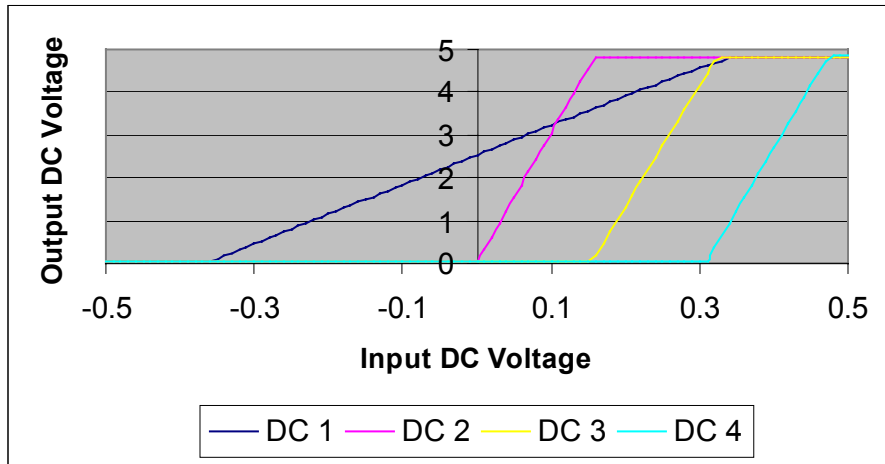

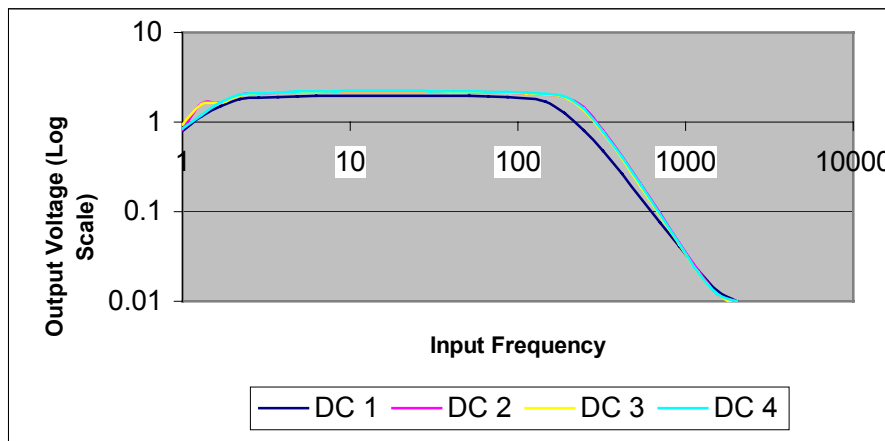Figure 12: Graphical outputs of DC sweep

Figure 13: Graphical outputs of AC sweep

ACKNOWLEDGEMENTS

INVESTIGATIONS INTO USING MATLAB FOR ACOUSTICAL ADAPTIVE FILTERING

Mark A. Colgan*
William K. Jenkins, Faculty Mentor
Dean J. Krusienski, Graduate Mentor
Department of Electrical Engineering
The Pennsylvania State University, University Park, PA 16802

*Undergraduate student of
Department of Electrical Engineering
Bucknell University
Lewisburg, PA 17837

ABSTRACT

This research provides an introduction into adaptive filtering algorithms, methods, and limitations when using Matlab and Simulink. LMS algorithms, system identification, single-channel equalization, and the filtered-x LMS algorithm were successfully constructed in Simulink and provided expected results. The process of understanding adaptive filtering, and the Simulink component of Matlab demonstrate the capability to construct a system to achieve crosstalk cancellation for experimentation of simulated 3-D audio environments.

INTRODUCTION

This paper describes background research performed to understand adaptive filtering and acoustical adaptive filtering using the Matlab programming environment. The methods presented outline the steps to understanding the implementation of multi-channel adaptive filtering for stereo sound reproduction. Specifically, this research intends to develop a system for experimentation in 3-D audio applications such as those described by Kirkeby et al. [1]. In such a system, stereo audio is processed by an array of filters so that the resulting waveforms at a listener's position closely match the original audio source. This processing effectively removes the crosstalk that results in the right channel sound signal being heard at a listener's left ear, and sound from the left channel being heard at a listener's right ear. Although several methods of achieving this effect are

known, the system devised by Nelson et al. [2] uses a least squares approach to tune the adaptive equalizers that is based upon the multiple error LMS algorithm published by Elliott et al. [3]. Similarly, the research presented here analyzes least square algorithms in an attempt to understand the fundamental operation of the system.

Whereas most published results cite using DSP boards, this study focused on using a PC and the Matlab software environment to design and implement the adaptive filtering processes. The crosstalk cancellation systems published all use similar speaker positioning with the listener approximately 1 to 2 meters from a pair of speakers. The speakers are placed parallel facing the listener with the separation of the speakers varying from 5 to 40 degrees as seen by the listener. As shown by Ward and Elko [4], the more closely spaced speakers (5 to 20 degrees as seen by the listener) achieve better sound reproduction than wider separation. In this research, upon the completion of the crosstalk canceller system, further speaker arrangements will be tested, including configurations where the speakers are not aimed in parallel directions. It is thought that such an arrangement could achieve the same effects as parallel-arranged speakers. These systems can also be scaled to multiple listeners at multiple locations. Nelson et al. [5] have demonstrated such a system using four speakers and 2 listening positions.

The initial objectives of this research included:

1) Construct and analyze adaptive filtering algorithms in standard configurations using Matlab.

2) Develop a test setup similar to that used by Nelson et al. [2] by using a PC with Matlab for the adaptive processing.

3) Compare various geometric speaker configurations and the resulting acoustical environments.

The work conducted as part of this research is intended to establish the basis for future audio projects as well as demonstrate the theory behind the filtering processes.

EXPERIMENTAL DESCRIPTION

In order to understand the intrinsic processes of the crosstalk canceller system, several adaptive filtering methods were first investigated. As an introduction into adaptive filtering and Matlab, the LMS algorithm provided in Hayes [6] was programmed and several simulations were conducted for different filter lengths, system arrangements, and convergence coefficients. A Gaussian random noise source was used as the input signal to the LMS algorithm. System identification and equalization were simulated for FIR and IIR plants. At this time it was discovered that the Simulink component of Matlab afforded simpler real-time processing of audio signals. The system identification and equalization configurations were also programmed in Simulink and comparable results obtained. Widrow and Stearns's [7] filtered-x LMS algorithm was also programmed in preparation for constructing the crosstalk cancellation system shown in figure 2. The filtered-x LMS algorithm shown in figure 1, uses two

LMS processes to identify the unknown plant and equalize a channel. This method ensures that the additive channel noise is not filtered, and thus provides a higher quality signal at the output of the system.

Several methods to construct a system to process the multiple error signals of the crosstalk canceller system (figure 2) were made. However, none provided sufficient results to continue with intended research into speaker geometries.
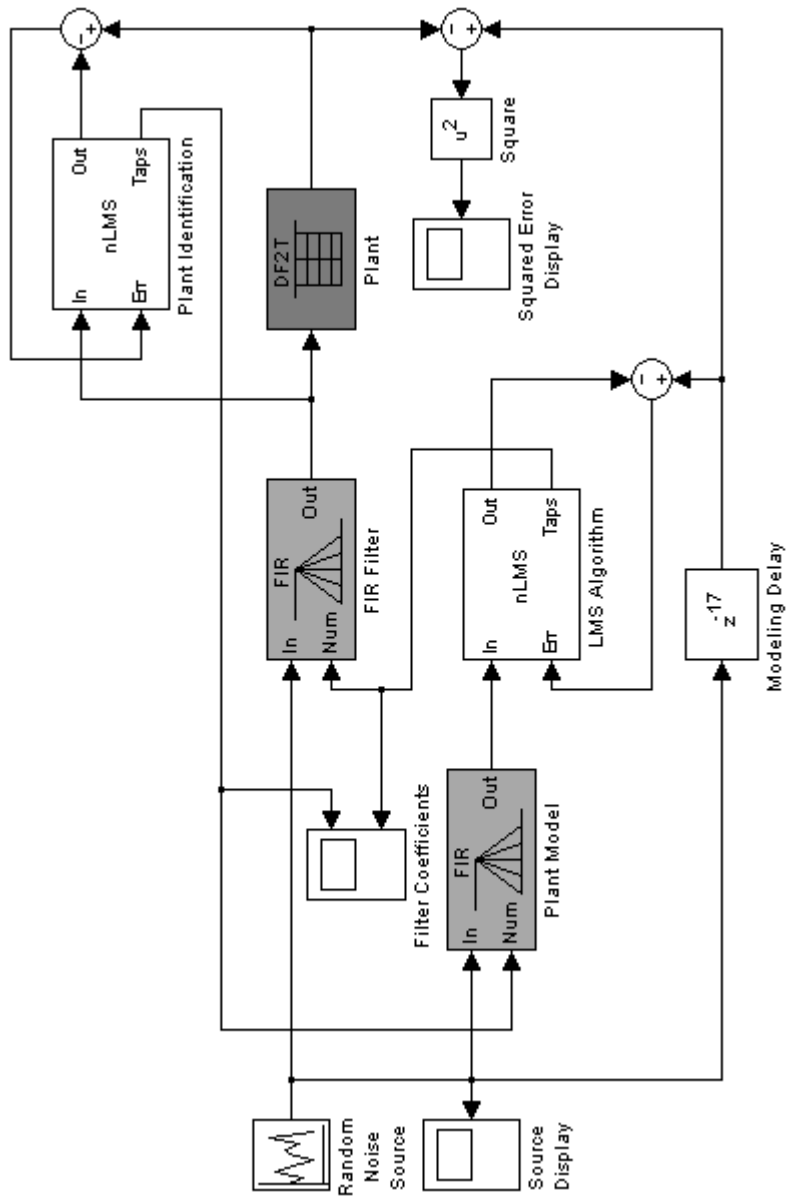

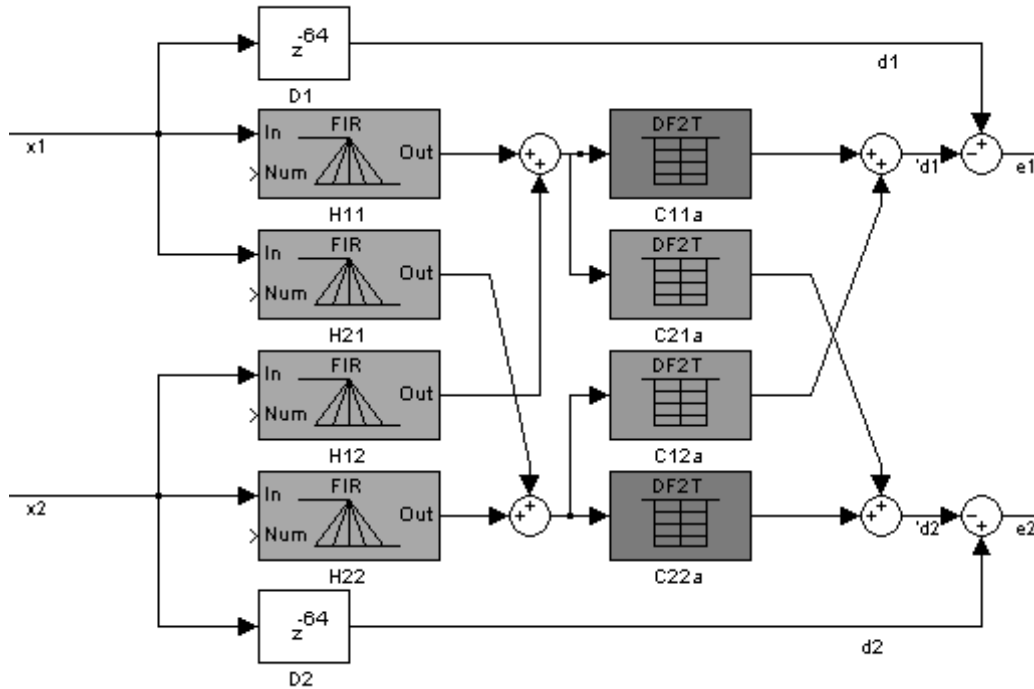Figure 1. Simulink schematic of filtered-x LMS algorithm.

Figure 2. Simulink schematic of adaptive filters (H), sample channels (C), and modeling delay (D). Inputs x1 and x2, desired outputs d1 and d2, actual outputs 'd1 and 'd2, error at outputs e1 and e2.

RESULTS

The results of the Matlab LMS algorithms provided in Haykin [3] are shown in figures 3-6. The coefficient training and minimization of squared error are shown for both system identification and equalization configurations.   Simulink programs for the system identification and equalization configurations demonstrated similar convergence plots. The filtered-x LMS algorithm of Widrow and Stearns [7] was successfully programmed in Simulink. Coefficient training and squared error minimization are shown in figures 7 and 8.

Several methods were attempted to calculate the coefficients of the crosstalk canceller, however a functional algorithm has not been reproduced in Simulink. The algorithms devised by Nelson et al. [2] created an unstable setup when used in Simulink. A method of using the single channel filtered-x LMS algorithms was constructed in Simulink and provided unpredictable results. It was found that occasionally one channel would converge, and both channels would converge if the cross-channel components were ignored or if only the cross-channel components were considered.

48

Figure 3. Filter coefficients of LMS algorithm in system identification mode of a known 4-tap FIR filter.

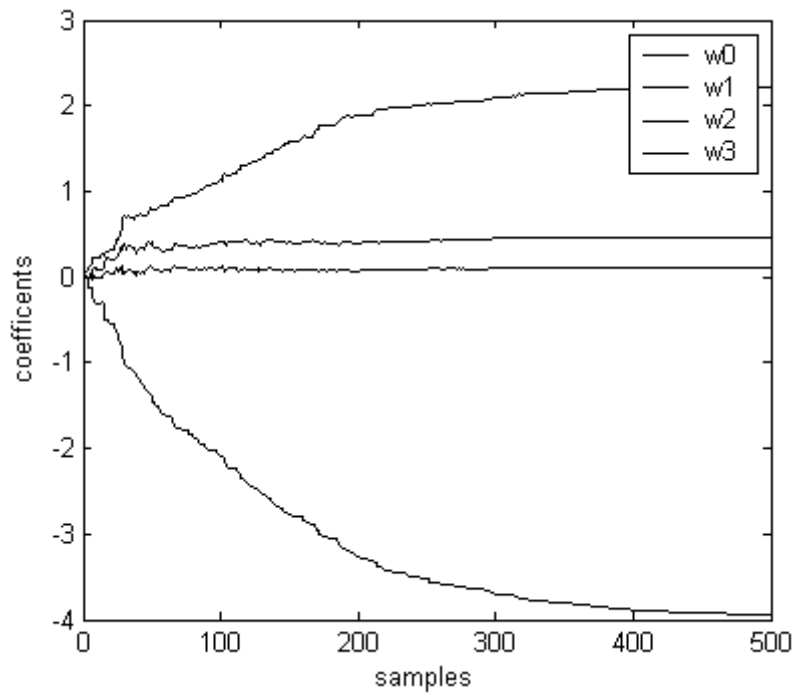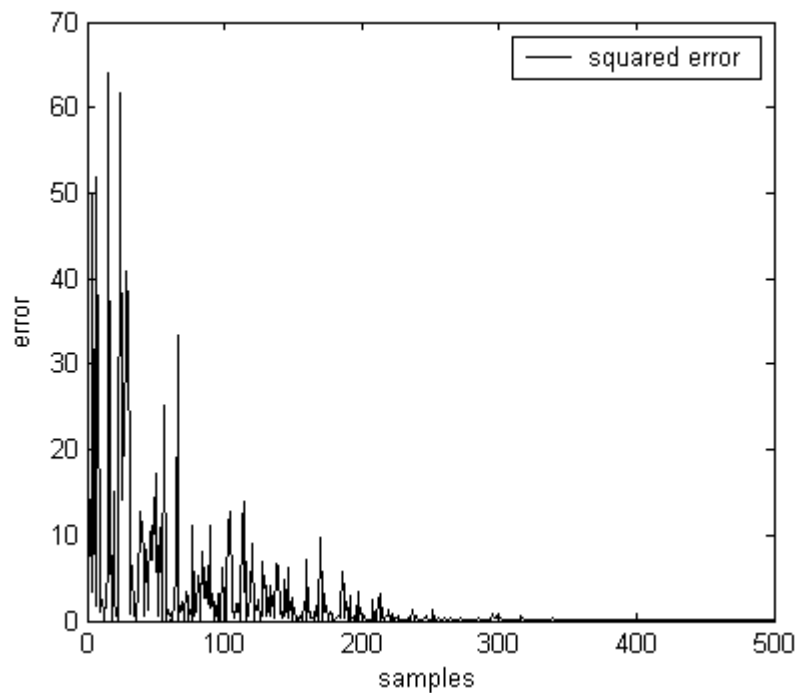Figure 4. Squared error of LMS algorithm in system identification mode of a known 4-tap FIR filter.
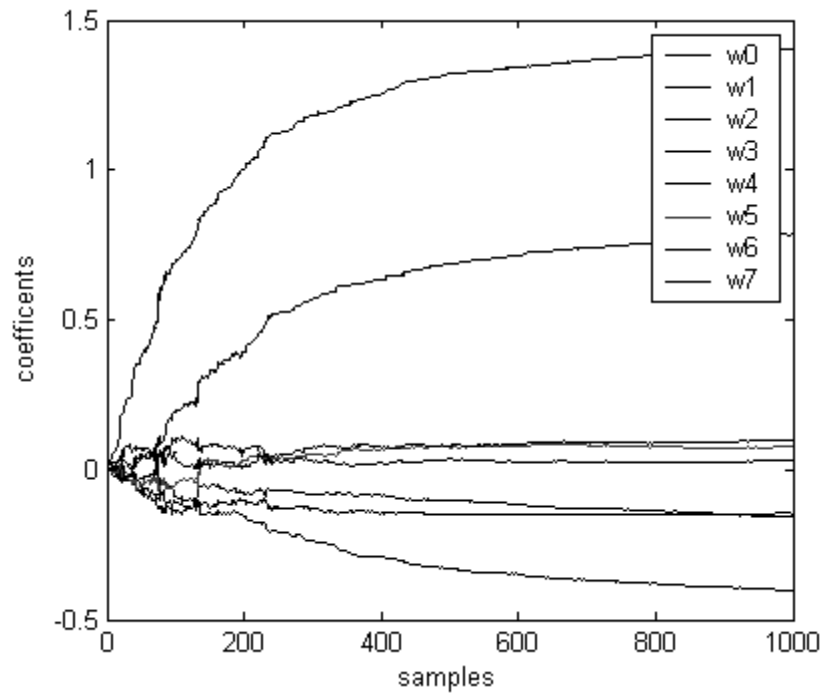
Figure 5. Filter coefficients of LMS algorithm in equalization mode of a known 4-tap FIR filter.
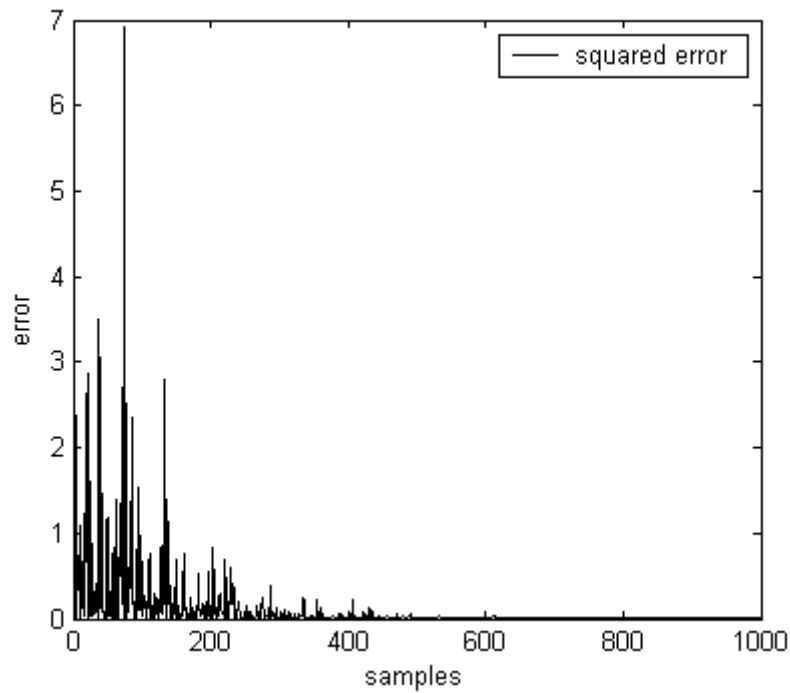
Figure 6. Squared error of LMS algorithm in equalization mode of a known 4-tap FIR filter.
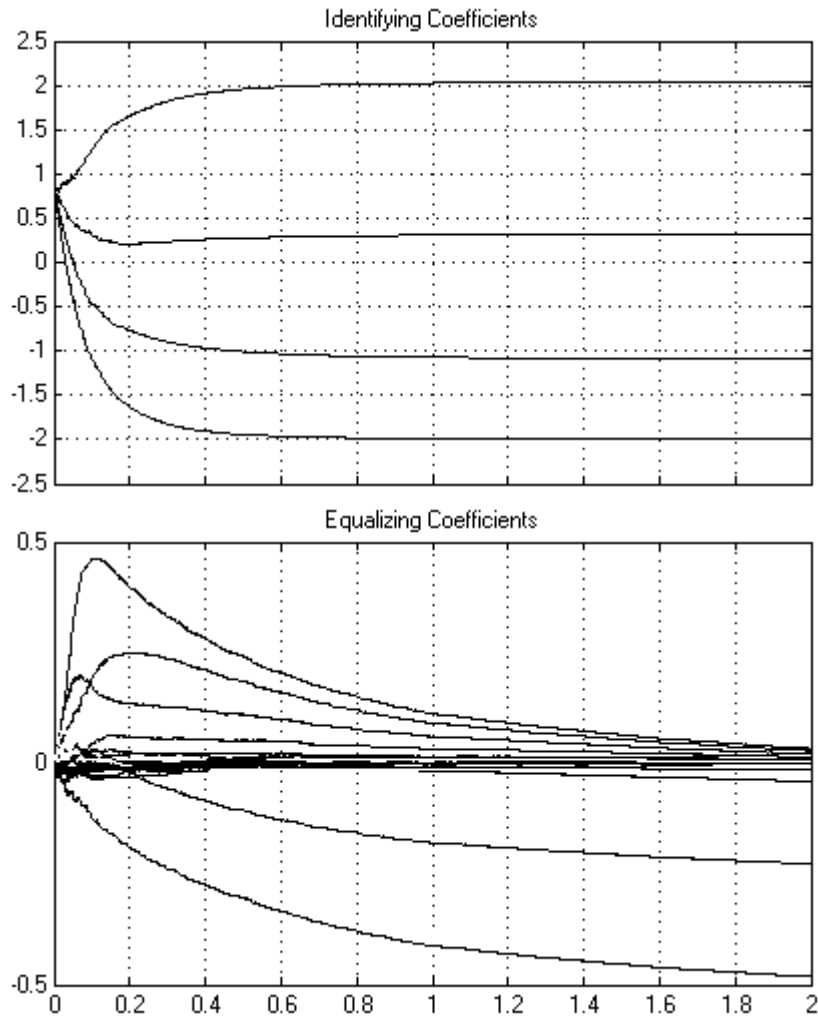
Figure 7. Coefficient values for LMS algorithms in filtered-x equalizer of a known 4-tap FIR filter.
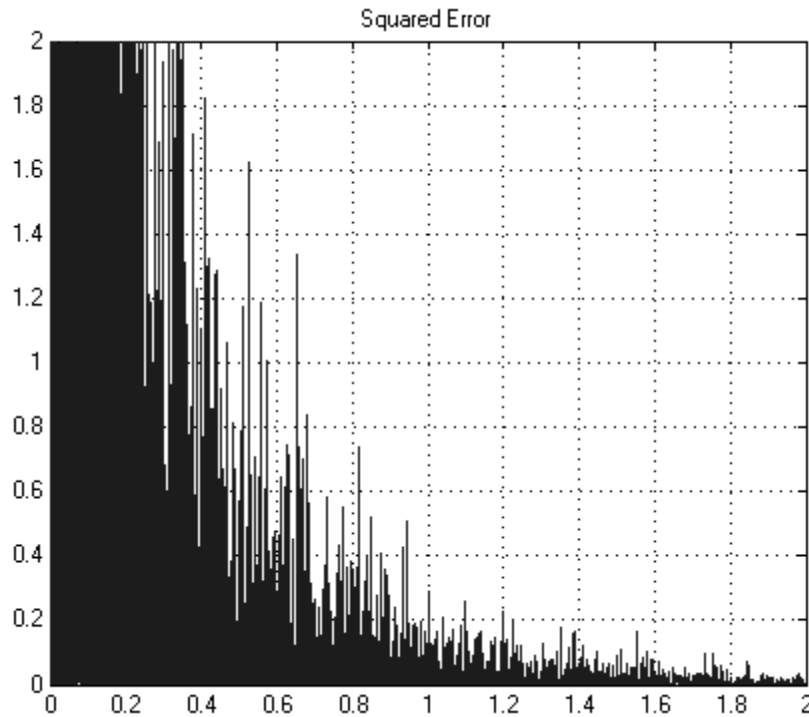
Figure 8. Squared error of filtered-x equalizer of a known 4-tap FIR filter.

DISCUSSION

This research provided an introduction into adaptive filtering algorithms, methods, and limitations when using Matlab and Simulink. LMS algorithms, system identification, single-channel equalization, and the filtered-x LMS algorithm were successfully constructed in Simulink and provided expected results. Although the intended research topics have not been realized, the background work conducted has established a basis for further efforts related to adaptive signal processing, Matlab, and Simulink. Additional efforts to achieve the desired crosstalk cancellation using Matlab and Simulink will be developed.

SUMMARY

Although the initial goal of this project was to conduct experiments using a crosstalk canceller system, the background knowledge necessary to understand and construct it required much more time than originally considered. Adaptive filtering methods using Matlab and Simulink were successful and suggest that the intended system is feasible. Further efforts will attempt to reach the original goals, even after the original timeline has expired.

ACKNOWLEDGEMENTS

REFERENCES

[1] O. Kirkeby, P. A, Nelson, and H. Hamada, "The Stereo Dipole – A Virtual Source Imaging System Using Two Closely Spaced Loudspeakers," *J. Audio Eng. Soc.*, vol. 46, pp 387-395, May 1998.

[2] P. A. Nelson, H. Hamada, and S. J. Elliott, "Adaptive Inverse Filters for Stereophonic Sound Reproduction," *IEEE Trans. Signal Process.*, vol. 40, pp. 1621-1632, July 1992.

[3] S. J. Elliott, I. M. Stothers, and P. A. Nelson, "A Multiple Error LMS Algorithm and Its Application to the Active Control of Sound and Vibration," *IEEE Trans. Acoustics, Speech, and Signal Process.*, vol. 35, pp. 1423-1434, October 1987.

[4] D. B. Ward and G. W. Elko, "Effect of Loudspeaker Position on the Robustness of Acoustic Crosstalk Cancellation," *IEEE Signal Processing Letters*, vol. 6, pp. 106-108, May 1999.

[5] P. A. Nelson, F. Ordunda-Bustamante, and H. Hamada, "Multichannel Signal Processing Techniques in the Reproduction of Sound," *J. Audio Eng. Soc.*, vol. 44, pp 973-989, November 1996.

[6] M. H. Hayes, *Statistical Digital Signal Processing and Modeling*. New York: John Wiley & Sons, Inc., 1996, ch. 9, appendix.

[7] B. Widrow and S. D. Stearns, *Adaptive Signal Processing*. Englewood Cliffs, NJ: Prentice Hall, 1985, ch 11.

EFFECTS OF VACUUM PRESSURE ON THE RESONANCE CHARACTERISTICS OF MEMS CANTILEVER STRUCTURES

Zachary Harmany*
(Dr. Srinivas A. Tadigadapa, Faculty Mentor)
Department of Electrical Engineering
Pennsylvania State University, University Park, PA 16802

*Undergraduate student of Physics (Electronics Option)
Pennsylvania State University
University Park, PA 16802

ABSTRACT

This report contains the results of experiments dealing with electro statically actuated MEMS (micro electromechanical systems) cantilever structures. A description of these MEMS cantilevers is presented, with an introduction to the squeeze-film damping theory. A description of the experimental setup used in order to find these resonant frequencies is needed to fully understand some of the background information and difficulties in studying these cantilever structures. The resonance characteristics will then be presented showing the effects of the vacuum pressure on the resonant frequency, and an explanation of the frequency shift observed using squeeze-film damping theory. This study hopes to show the counter-intuitive result that an increase in pressure actually yields an increase in the resonant frequency. These MEMS cantilevers should prove satisfactory for studying this phenomenon due to the small gap spacing in comparison to the length and width of the cantilever. In conclusion, pathways into future research will be presented in the areas dealing with MEMS cantilever structures.

INTRODUCTION

The expanding field of micromachining refers to the creation of any device with micrometer ($1x10^{-6}$ meters) dimensions. These devices are generally referred to as MEMS, for micro electromechanical systems. The cantilever devices studied in this report are ones created from a top-down approach, since they operate similarly to macroscopic cantilever systems. This top-down approach refers to the scaling down of manufacturing methods in order to make miniature smaller devices. This is in opposition to the bottom-up approach in

which devices are assembled from smaller components, generally at the molecular level. [1]

Since cantilever devices are thoroughly and often intuitively understood in the macro-scale, it is interesting to see what unusual effects predominate at the micro-scale. When shrinking the feature sizes on these MEMS devices, effects such as the strength-to-weight ratio become higher, allowing devices to be constructed with aspect ratios that would not be possible in the macro domain. It is impossible to imagine a five foot thick piece of metal the size of a football field suspended a foot above the grass, being held only at one end-zone. However, if these dimensions were scaled down by a factor of one million, such aspect ratios would be quite easy to manufacture. Also, surface tension and viscous forces become increasingly predominant at smaller dimensions. Many of us have seen various insects float effortlessly on water utilizing surface tension; where as we have never seen an elephant do the same. [1] These viscous forces present a challenge in observing the oscillation of the MEMS cantilevers. In order to observe this oscillatory behavior, we must use a vacuum pump to remove the majority of the air from the environment our samples will be in, although air damping is still significant at pressures of a few hundred mTorr.

We are interested in studying the behavior of these cantilever systems because they have quite a wide array of usages as sensors and actuators. They can be utilized to create highly sensitive force and mass sensors. In fact, these structures are utilized in atomic force microscopy (AFM) and scanning probe microscopy (SPM) which can probe extremely small features with a high resolution. These cantilevers can also be integrated into MEMS flow, pressure, and biochemical sensors. [2]

This report presents our experimental findings when studying the effect of vacuum pressure on the resonance characteristics of MEMS cantilevers. These cantilevers possess resonant frequencies that depend on geometric, elastic, and inertial parameters of the system, and can be correlated to theory existing concerning macroscopic cantilever systems. Since our cantilever samples have free-standing lengths and widths of 150μm and 100μm respectively (see figure 4) and a gap size of only 1μm, squeeze-film damping effects should be very noticeable. In the squeeze-film damping model, there exist both damping and spring factors that arise from the effects of the surrounding gas medium. The damping factors are related to the way in which energy is lost to the gas medium through thermal effects. The spring factor, however, occurs because the air under the cantilever is acting less like a dashpot, or damper, and more similarly to a piston that would exhibit resistance to compression. In special circumstances, this would cause an increase in the effective spring constant of the system which would outweigh the added damping effects and actually shift the resonant frequency up at increasing pressures (and therefore higher particle density under the structure). [3] Also, it should be noted that the quality factor of the cantilevers will also be affected by squeeze-film damping effects. It is our hope that the

results presented in this report can add further support and understanding to squeeze-film damping theory.

EXPERIMENTAL DESCRIPTION

1.Device Selection

Since the devices have already been fabricated by a graduate student, the first step in our experiment was to determine which devices were best suited for further testing. The problem with some of the cantilevers is that during fabrication, they must be released in order to form free-standing structures. Sometimes these structures are not released correctly and were permanently attached to the common electrode through the interaction of surface Van Der Waals forces in a state known as stiction. Surface profiles of these devices proved to be effective in determining which devices were in stiction. A Zygo NewView 100 white-light interferometric microscope was utilized in obtaining these surface profiles.
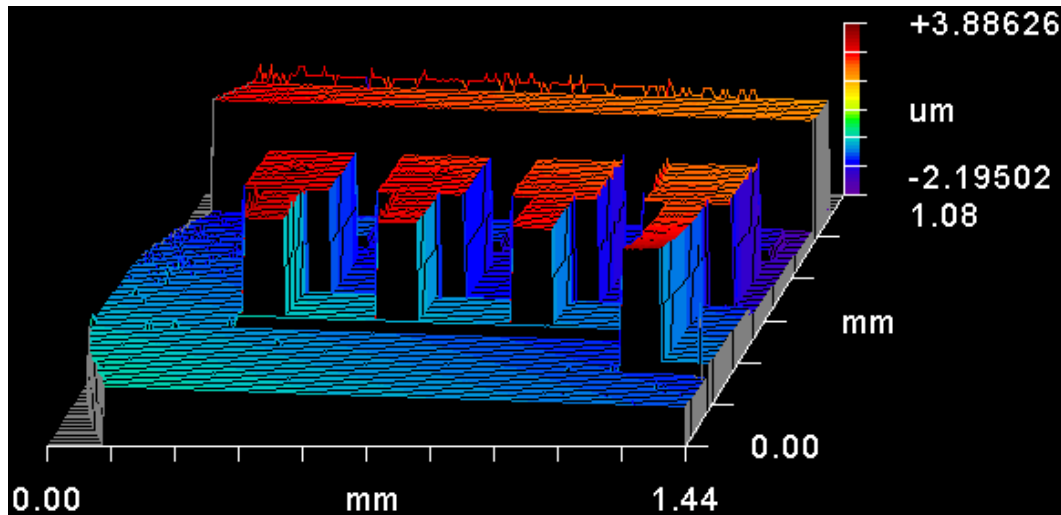

Figure 1: Three dimensional image of the cantilever structures.
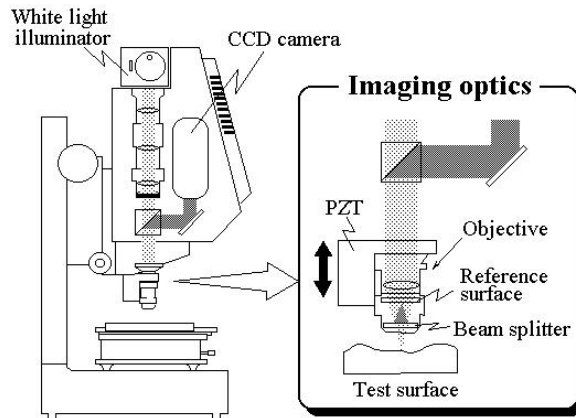
Figure 2: Diagram of the white light interferometric microscope.
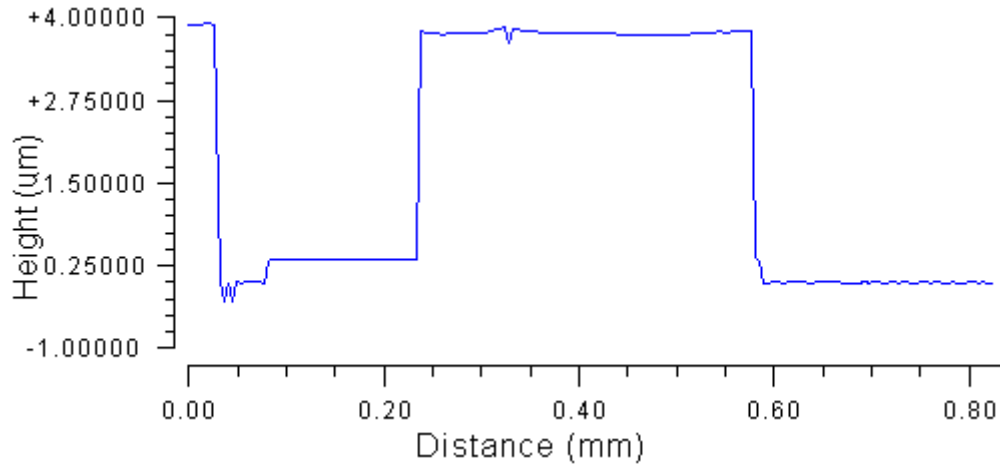
Figure 3: Example of a surface profile for a flat (non-stictioned) cantilever.

This imaging system, as seen in figure 2, operates by producing patters of interference fringes between a reference beam, and the beam that is reflected from the surface of the sample. These fringes arise from the alternating constructive and destructive interference that varies with the change in path length between the reference beam and the reflected beam. These patterns are then picked up by a charge-coupled device (CCD) camera which creates an image full of fringes where each fringe represents a plane that is equidistant from the objective. By moving the focal point vertically, a series of images are taken by the CCD camera and then analyzed by the software order to create a three dimensional image (figure 1). Sections of this image were extracted to obtain the surface profiles, an example of which is shown in figure 3. [4] This data shows which cantilevers are in stiction, which are roughly flat, and which are bent slightly upwards.

Figure 4: Optical picture of the first 4 cantilever structures.

2. Device Packaging

　　After examining all of our samples, four samples with flat or slightly bent up surface profiles were chosen for further testing.　In order to attach a measurement instrument to this device, they first must be packaged in a dual inline-pin (DIP) module.　TorrSeal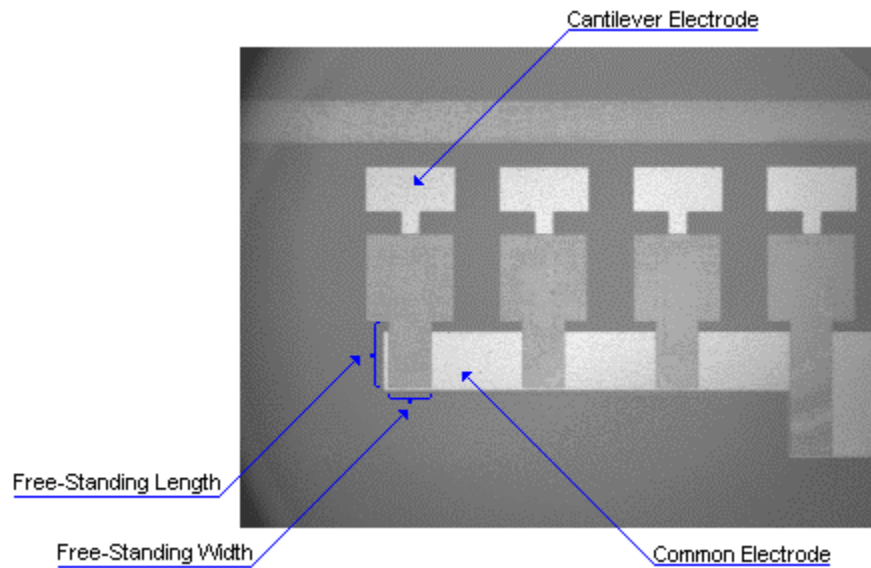, a high vacuum glue, was used to adhere the die to the package.　In order to expedite the drying of the glue, it was cured in an oven for 30 minutes at 60°C.　Afterwards a Kulicke & Soffa Model 4524 wire bonder allowed attachment of gold leads from the cantilever electrodes and common electrodes (as annotated in figure 4) to the package pins.

3. Measuring

　　Once these devices are packaged, their resonance characteristics can then be tested.　All of our tests must be conducted inside vacuum conditions since any atmospheric pressure dampens the cantilevers to such an extreme that no vibrations can be detected.　For instance, at approximately 1Torr, it is nearly impossible to discern the resonance frequencies on even our best devices.　Our vacuum chamber setup is comprised of the vacuum pump, an electronic pressure gauge, a bleeder valve for regulating the pressure, and the vacuum chamber itself. The first vacuum chamber that was utilized consisted of a large cylindrical chamber constructed from steel and aluminum.　This all-metal construction acted as a Faraday Cage to significantly reduce outside electrical interference when the measurements were made.　The top plate of our vacuum chamber has several BNC connections which allowed the attachment of an Agilent 4294A Precision Impedance Analyzer.　The impedance analyzer was used to measure series resistance and series capacitance (since the device is comprised of a flat common electrode and a floating cantilever, it acts as a parallel plate capacitor).　From the device response vs. frequency curves, we were able to discern the resonant frequency and the quality factor of the devices in the chamber.

Figure 5: Isometric view of the new vacuum chamber

　　In an additional experiment, we had the opportunity to use a Laser Doppler Vibrometer during a demonstration courtesy of Polytec PI, Inc., in order to make deflection and velocity measurements of our cantilevers (see figure 6). Unfortunately, a new vacuum chamber had to be designed to fit on the stage of the microscope, and have a glass lid which the laser could pass through (see Figure 5).
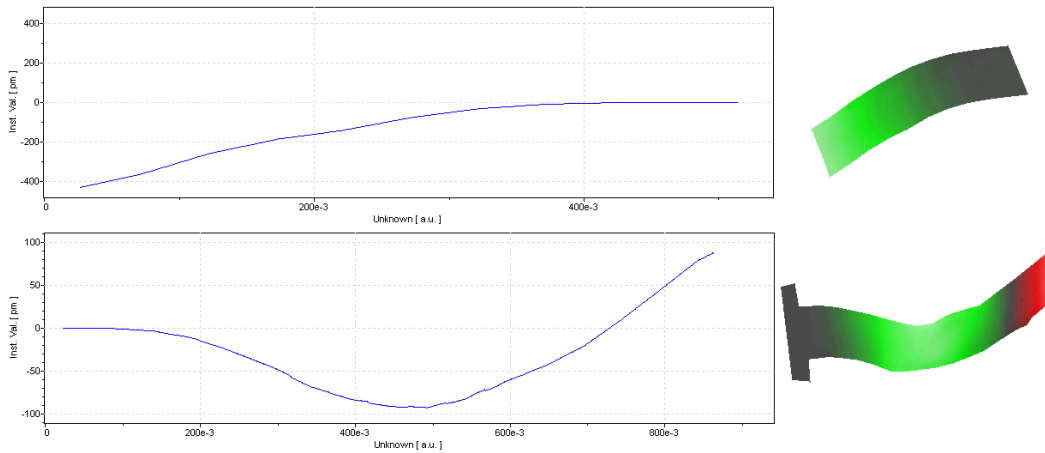
Figure 6: Displacement profile for a) first-mode oscillation of a 150x100um cantilever, b) second-mode oscillation of a 300x100um cantilever.

RESULTS

From Figure 7 and 8, we see the measurements of the resonant frequency as a function of the pressure inside the vacuum chamber. As these graphs clearly portray, the natural frequency of the cantilevers tends to increase with an increase in pressure.

Resonant Frequency vs. Vacuum Pressure for a 150x100um Cantilever

Linear Curve Fit:
y = 0.0005x + 74.194
R^2 = 0.9975
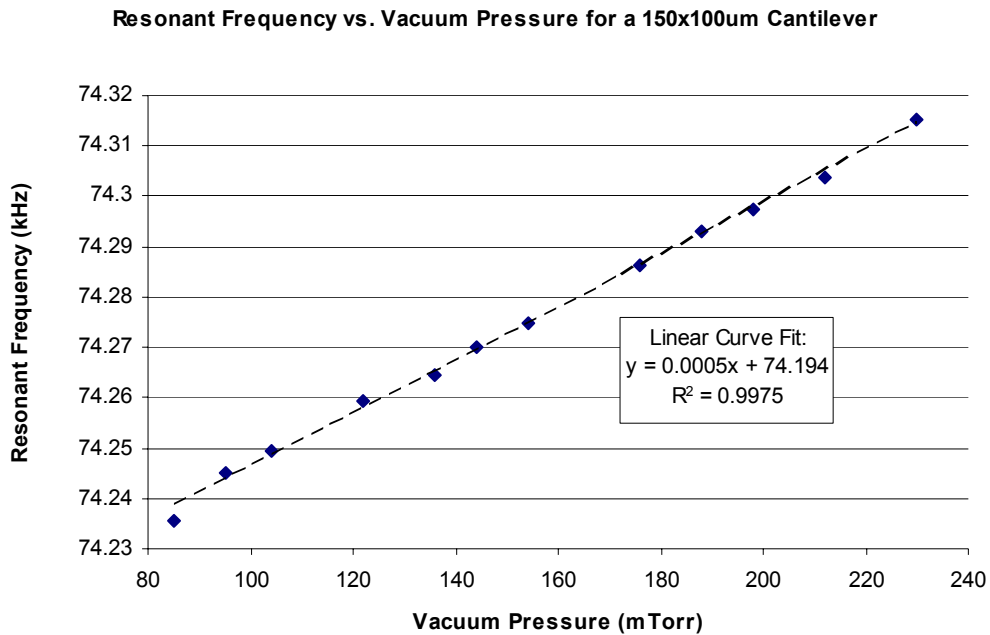
Figure 7: Frequency vs. pressure graph for a typical 150x100um cantilever

Resonant Frequency vs. Vacuum Pressure for a 300x200um Cantilever
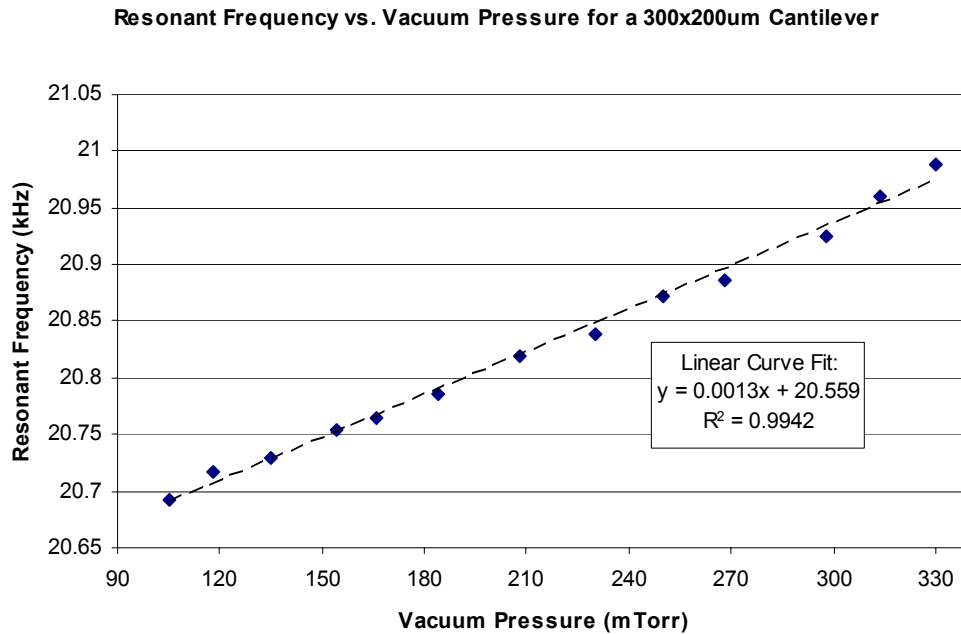
Figure 8: Frequency vs. pressure graph for a typical 300x200um cantilever

DISCUSSION
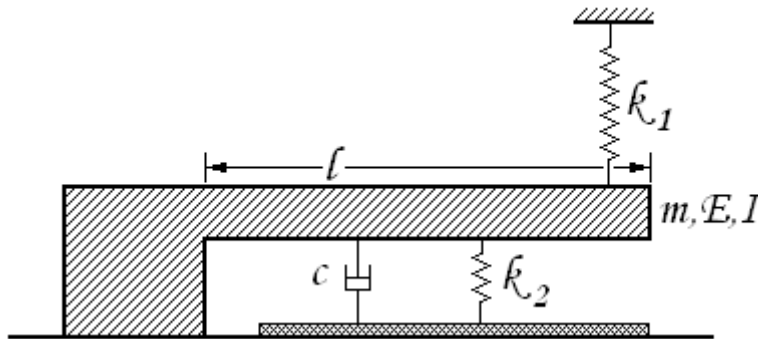
Figure 9: Simplified theoretical model for squeeze-film damping.

From figures 7 and 8 above, it is evident that there exists a measurable increase in the resonant frequency as the pressure of the air surrounding the cantilever is increased. The model shown in figure 9 is generally accepted as the model for a squeeze-film damping situation. In this model, l is the length of the cantilever, m is the mass of the cantilever, E is the Young's Modulus of the material (single crystal silicon), and I is the area moment of inertia about the neutral axis. [5] From those variables, we can determine some effective spring constant of the cantilever system that we will refer to as k_1. Modeling the air is slightly more complicated in that it has both elastic and damping components. The damping force arises due to frictional losses between the cantilever and the

gas particles. Since these cantilevers have such high length to gap and width to gap ratios, the air molecules do not have enough time to escape completely out from under the cantilever during a cycle. This causes the air underneath to become compressed, thus storing energy like a piston. One can easily imagine an analogy to a closed container with a straw. When blown into, the air inside becomes compressed, storing energy. As soon as the external pressure is removed, liquid squirts out of the cup, releasing the stored energy of the compressed air.

In assuming that the cantilever has clamped-free boundary conditions, we can use the following equation to calculate the natural frequency of our cantilever structure as a starting point in our model:

$$f_i = \frac{\lambda_i^2}{2\pi l^2}\sqrt{\frac{EI}{m/l}}$$
(1)

where λ is a dimensionless constant in order to determine the frequency of various modes. For the fundamental mode, $\lambda = 1.875$. [6] In order to arrive at an equation with known values, we can make the following substitutions:

$$I = \frac{wt^3}{12}$$
(2)

$$m = \rho V = \rho lwt$$
(3)

We then arrive at:

$$f_i = \frac{\lambda_i^2 t}{4\pi l^2}\sqrt{\frac{E}{3\rho}}$$
(4)

With the following data presented in figure 10, we can arrive at theoretical calculations for the resonant frequency, shown in figure 23.

Cantilever	Thickness, t	Length, l	Elasticity, E[7]	Density, ρ[7]
Type 1	3.17um	150um	172GPa	2333kg/m3
Type 2 & 3		300um		

Figure 10: Data table for resonant frequency calculations.

One may notice that the discrepancy in the frequency measurements between figures 7 and 8 above and figure 11 below. In order to explain the apparent doubling of the resonant frequencies, the way in which we are exciting our cantilevers must be examined. Anytime a voltage is applied to the cantilever, it is always attractive, irregardless to polarity. Since we are using a sinusoidal signal with no DC offset, each half-signal is attractive, therefore the electronic signal in our data actually represents half the mechanical resonance frequency, and therefore we must double our results in order to compare them to the theoretical calculations. [8]

As we have seen in figure 18 and 19, the vacuum pressure does play a role in determining the resonant frequency of our MEMS structures. However, in order to extract the k_2 and c values for our model, another experiment needs to be designed in which the gap height is varied between devices. This will allow the determination of the gap height at which the k_2 effects disappear, allowing a reference value to be established of the resonant frequency with only the predominant elastic effects of the cantilever itself.

Theoretical and Experimental Resonant Frequency vs. Length
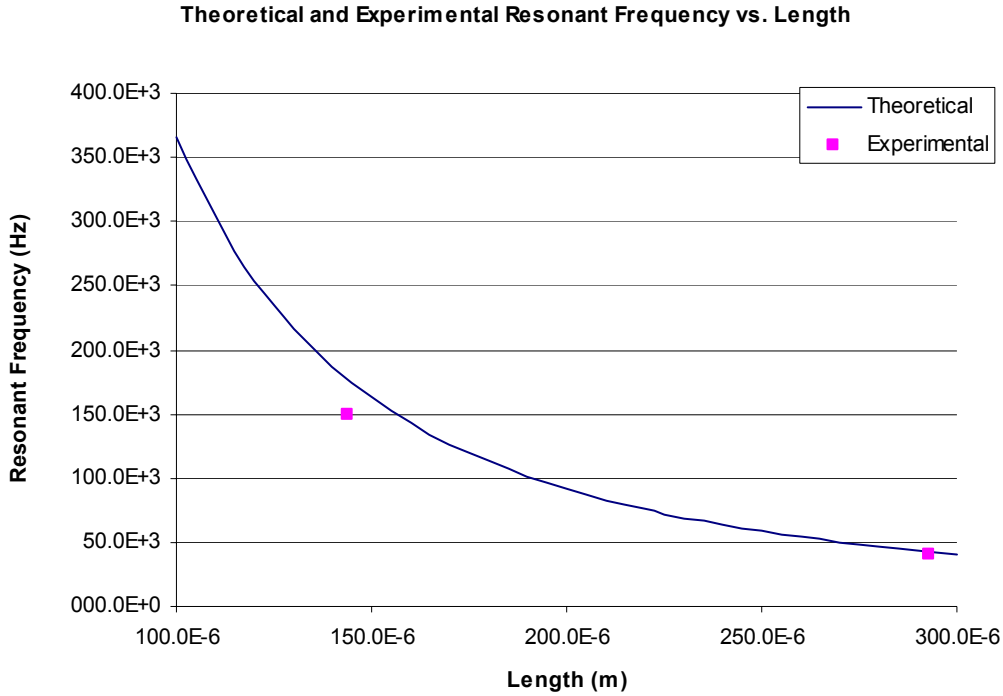
Figure 11: Experimental results compared with theoretical calculations for resonant frequency.

CONCLUSION

In conclusion, we found that the air-spring effects present in squeeze-film damping theory are observed to play an important role in the resonance characteristics of cantilever microstructures. Although further devices need to be fabricated in order to quantify this effect, such readily observable results prove that this effect is quite real and important to consider when fabricating and analyzing MEMS cantilevers. In the future, we hope to thoroughly analyze other devices that would allow us to construct a more complete theory behind the pressure dependant operation of these devices.

ACKNOWLEDGEMENTS

Biddle and his staff at the Earth and Mineral Sciences Machine Shop for machining our new vacuum chamber, to Paul Sunal, for fabricating the cantilever devices, and also to John Foley of Polytec PI, inc., for the demonstration of their Laser Doppler Vibrometer equipment.

REFERENCES
[1]Madou, Marc J. *Fundamentals of Microfabrication: The Science of Miniaturization, Second Edition.* Foreword pp 1-2, 536-542. CRC Press: Boca Raton, FL, 2002.
[2]Amit Gupta, John P Denton, Helen McNally, Rashid Bashar. "Novel Fabrication Method for Surface Micromachined Thin Single-Crystal Silicon Cantilever Beams." *Journal of Microelectromechanical Systems.* Vol. 12, No 2, April 2003. pp 185.
[3]Yao-Joe Yang, Marc-Alexis Gretillat, Stephen D. Senturia. "Effect of Air Damping on the Dynamics of Nonuniform Deformations of Microstructures. *1997 International Conference on Solid-State Sensors and Actuators.* Chicago, June16-19, 1997. pp 1094-1096.
[4]Zygo Corporation. *NewView 100 Operation Manual OMP-0348K.* pp.1-2 – 1-4. Middlefield, CT, 1996.
[5]David Herman, Michael Gaitan, and Don DeVoe. "MEMS Test Structures for Mechanical Characterization of VLSI Thin Films." *Proc. SEM Conference. Portland, Oregon. June 4-6, 2001.* pp 1-5.
[6]Robert D. Blevins. *Formulas for Natural Frequency and Mode Shape.* Krieger Publishing Company, Malabar, Florida, 1995. pp. 108
[7]Oliver Pierron. "EE 597F: MEMS Device Technology Spring 2003 Laboratory Report." pp. 3&13.
[8]Michael William Putty. *Polysilicon Resonant Microstructures.* Master of Science in Engineering Thesis. The University of Michigan, 1988.

PIEZOELECTRIC ULTRASONIC MICRO MOTOR OPTIMIZATION

Thomas J. Plummer*
(Advised by: B. Koc, K. Uchino, S. Cagatay, S. Dong)
International Center for Actuators and Transducers, Material Research Institute
The Pennsylvania State University, University Park, PA 16802, USA

*Undergraduate Student of Electrical Engineering with an Audio Emphasis
University of Miami
Coral Gables, Florida 33146

ABSTRACT

In understanding the gearless design of piezoelectric actuators, the uses of piezoelectric materials applied in ultrasonic micro-motors are investigated. The converse piezoelectric effect, in which an applied electric field on a piezoelectric ceramic causes a mechanical strain, gives the general means of operation for the motor. With this electrically induced mechanical strain of a piezoelectric ceramic, lead zirconate titanate (PZT), bonded on an elastic cylinder shaft (stator), at a precise resonance frequency of the applied AC current matched to that of the stator, a vibrating effect is produced. With idealized geometry of the stator an elliptical wobbling motion can be achieved. With a center axle rod or a rotor in contact with the stator surface, by means of contact friction we have a spinning effect. That is the basic idea of how an ultrasonic micro-motor works.

The main objective is to find the optimum stator structure. Experimental values of speed, efficiency, power, and torque will aid in the comparison. The output specifications should range as follows: (1) size= 1-15 mm, (2) speed= 100-1000 rpm, (3) torque= 1-100 mNm, which is 10-100 times higher than the electromagnetic micro motors, silicon MEMS or the previously reported micro ultrasonic motors. The plan is to achieve respectably high torque and efficiency with simplifying the stator structure and holding technique. Simplification with reducing the number of components, fabrication process and driving circuitry will provide a low cost ultra-sonic micro motor design.

INTRODUCTION

In various office equipment and communication devices, market research indicates that tiny motors smaller than one centimeter would be in large demand over the next ten years. In the mm-motor area, ultrasonic micro motors (USMM), whose efficiency is insensitive to size, is greatly favored over the conventional

electromagnetic motor (EMM). The USMM is more suitable for miniaturization for many reasons, including its compact size, 1/10 smaller in volume and weight while storing larger energy than the EMM. Magnetic shielding is not necessary, because the USMM generates no magnetic noise. The USMM also has no need for the complex gear system required for sufficient torque that is found with the EMM. The direct drive design offers high precision control and reliability that is needed for miniature applications. The USMM also possesses an added safety feature with the absence of gear backlash in off mode via the frictional lock with direct operation. With fewer components, reduced size with higher output, and cheaper production cost, it is apparent why USMM optimization is necessary. [1-3]
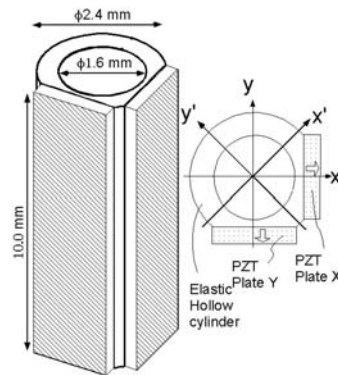

Figure 1: Basic stator structure with bending mode diagram

This study was performed to find the optimum geometry of the USMM stator with aiming at the elimination of parts by using the mechanical friction produced on the exterior of the stator when vibrating elliptically. Since the vibration amplitude generated by the piezoelectric element decreases with decrease in size of the motor, a 13.8mm long, 1.5mm thick square cylindrical stator is the first prototype. The stator is square in order to simplify the production process with a flat surface for the bonding of the piezoelectric plate. The two sides with the plates will be polished to be less thick than the other two sides for structural balance required to bring the resonating frequencies of the X and Y bending modes closer for greater elliptical motion. A second prototype will also be investigated of the same length and a 2.4mm diameter circular cylinder structure. PZT plates will be bonded to two polished flat sides at approximately 80 degrees. Reasoning behind the 80 degrees alignment of plates, are the stiffness in the X and Y directions are equal, so the cross sectional moment of inertias which make in result the X and Y bending mode frequencies to be equal as shown below (Fig. 2).
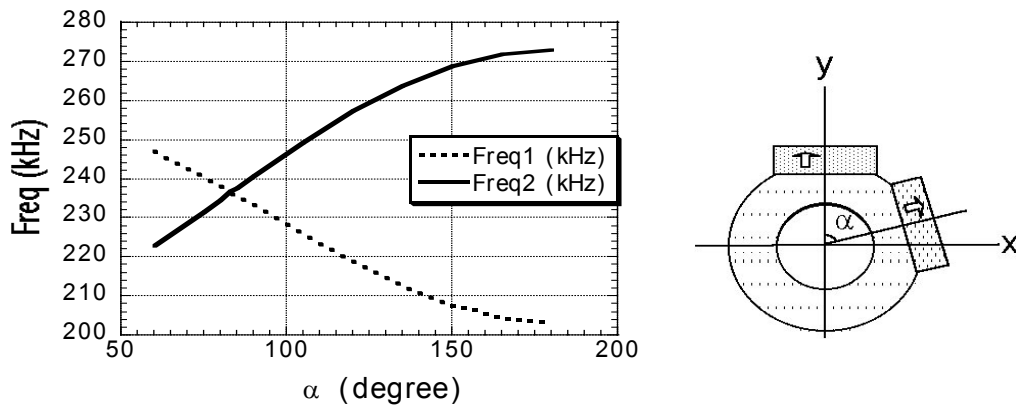
Figure 2: Changes of the two orthogonal bending mode frequencies as a function of plate orientation angle α [6]

   With this stator supported on one end the frictional interaction required for operation is on the exterior of the stator at the other end, where maximum displacement can be achieved. This is an advantage because the device being rotated is the actual rotor. For example, the stator is held with pre-stress at one end against a ball bearing at the other, when voltage is applied at the proper resonating frequency to the piezoelectric plate of the stator the bearing wheel will rotate. This leads to a reduction of amount of parts and a greater focus at the pre stress holding design of the stator. Within this discussion these USMM stator designs and their holding mechanisms will be described and simulated with output results clearly presented. [1-3]
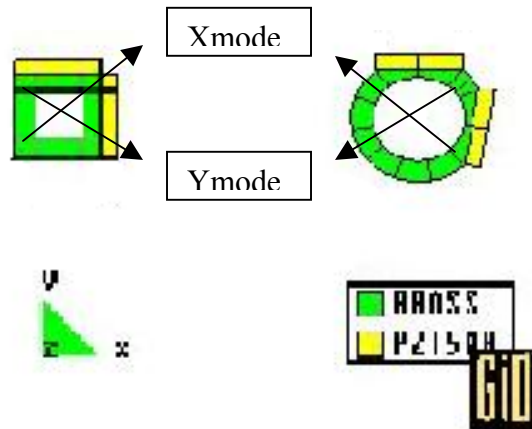

Figure 3: Prototype 1 is on the left, Prototype 2 is on the right with bending modes directed

66

EXPERIMENTAL SETUP

This experimentation took place during Summer 2003 at the International Center for Actuators and Transducers, Penn State University, State College, PA 16801

First, there must be a real test model fabricated. With aim for greater torque from max center displacement a 13.8mm length square (1.5mm x 1.5mm) brass cylinder and a 13.8mm, 2.4mm diameter circular brass cylinder were initially cut for their elastic properties. The two sides were ground with polishing techniques to have precisely flush surfaces for the PZT plates to be bonded on. PZT-5H, a soft piezoelectric ceramic was chosen for its medium-high mechanical quality factor and relatively high d_{33} constant, measured near $456X10^{-12}$ C/N for these. The PZT plates were cut to match the side of the square brass tube in dimension (13.8mm X 1.5mm), with thickness of 0.3mm and poling in the thickness direction. Two PZT plates were bonded with an epoxy at right angle to each other on the square stator and 80° on the circular stator, with corresponding poling directions, and then cured at 120 °C. It is important to have the poling direction corresponding in either inner or outer direction with respect to direction of applied AC electric field. The surface of the plate must be electroded to have proper voltage distribution. With applying an AC signal of 62 volts (rms) to one plate, various vibration modes could be excited at ultrasonic input frequencies above 20,000Hz. These resonant frequencies were calculated with ATILA finite element software [4].

Simulations using ATILA has multiple purposes. For example, using calculated bending mode frequencies and admittance magnitude graphs of the free stator to help find optimum frequency for desired operation. Seeing how surface constraints of different stator holding techniques affect the displacement magnitude and operating frequencies is very important in finding optimum performance. With ATILA, an accurate model can be designed with precise dimensions and material assignments, with thorough coefficients representing each. There are important preprocess steps for assigning surface conditions like potential voltage and displacement constraints. With respect to volumes the direction of polarization is assigned in organized directions for each PZT plate. When done with the design, one must assign a mesh to the design that breaks the entire product into smaller elements. These smaller elements are then processed with complex Finite Element Analysis within the program. The results are first viewed with a Modal Resantires analysis type that gives the calculated bending mode frequencies and effective coupling coefficients in the X and Y directions. From this information a frequency range is chosen with a close X and Y bending mode that is processed with the Harmonic analysis type of the ATILA program. An admittance graph is viewed that should show a few peeks; from this a frequency between the peeks is chosen to achieve both bending modes into elliptical motion. The visual representation can be viewed in motion with a total displacement scale having color- magnitude relations. Depending on the holding constraints the stator can achieve various magnitudes of displacement. It is

67

important to simulate in order to test various constraints and find optimum operating frequencies and holding conditions that are then utilized in fabrication and can be reflected upon in conclusion.

In retrieving characteristic values of max torque, speed, and efficiency the experimental setup was similar to that of the earlier 4mm USMM. In order to get any measurements a steel casing was designed for various holding positions of the USMM and frictionless rotation of a one mm diameter steel rod axle as the exterior rotor. After finding the optimum stator holding method, the next step was finding the torque using a transient characteristic method. Initially, an inertia mass disk made of brass was mounted on the end of the rotor with a calculated moment of inertia from:

$$I = M*r^2 \qquad\qquad (1)$$

A thin circular gauge also mounted on top of the inertia mass was evenly divided into 100 angular segments that was detected with an optical encoder (US Digital, HEDS-9100-S00). Here the signal was converted from frequency to a corresponding voltage via simple circuitry shown below. Because the output voltage of the converter was proportional to the input frequency of the rotating mass inertia, the speed (N) of the motor was obtained from a simple gain factor. With taking the derivative of the transient speed with respect to time the angular acceleration equation was determined. With this the transient torque could be calculated by multiplying the moment of inertia (1) with the angular acceleration.

$$T = a*I \qquad\qquad (2)$$

From this the mechanical output power with respect to time could be calculated by multiplying the output speed (N) with the output torque (2).

$$PMout = T * N \qquad\qquad (3)$$

Consumed electrical energy was found with using a 25ohm resistor in series after the motor. When measuring the (rms) voltage of the stator as the voltage of the system and using ohms law with the 25ohm resistor in series to find the input current, input electrical power could easily be calculated.

$$PEinrms = Vrms * I\,rms*\cos\theta \qquad\qquad (4)$$

The phase difference θ could easily be found by looking at the difference between the voltage and current with an oscilloscope. Finally, our USMM could be characterized by efficiency, simply by dividing Pmout (3) by PEin (4).

$$\eta = PMout/PEin \qquad\qquad (5)$$

With the previous calculated results one can compare and adjust each USMM for an optimum performance with various applications. [5]
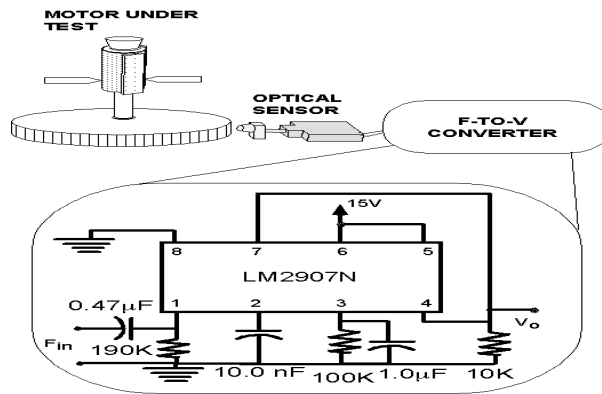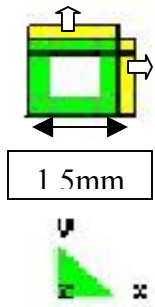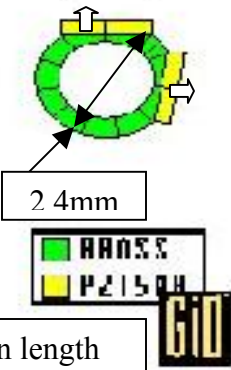
Figure 4: Motor Characteristics setup

Results

Prototype 1 Test No.1.1-1.4	Prototype 2 Test No. 2.1-2.4

1 5mm

2 4mm

Both stators are 13.8mm in length and soft PZT plates are .3mm thick.

Figure 5: ATILA results with diagrams and recorded measurements

ATILA Results By:
B. Koc and   18-
T. J. Plummer   Jul-03

.	Free Mode	Ends L. C.	One End L.C.	One End C.C.	Mode X(kHz)	Mode Y(kHz)	Mode S(kHz)	Max Dis.(um)
1.1	1	0	0	0	36.64	30.77	30.46	20(At Ends)
1.2	0	1	0	0	26.24	26.55	26.55	12(At Middle)
1.3	0	0	1	0	27.73	28.55	28.24	15(At End)
1.4	0	0	0	1	27.72	28.66	28.24	11 (At End)
2.1	1	0	0	0	38.75	38.95	38.84	90 (At Ends)
2.2	0	1	0	0	33.42	33.42	33.42	15 (At Middle)
2.3	0	0	1	0	34.95	35.26	35.15	56 (At End)
2.4	0	0	0	1	35.03	35.23	35.08	54 (At End)

Ends
C.C.=No
Motion
EndsL.C.=Ends loosely
clamped
Mode S.= Most circular
mode frequency
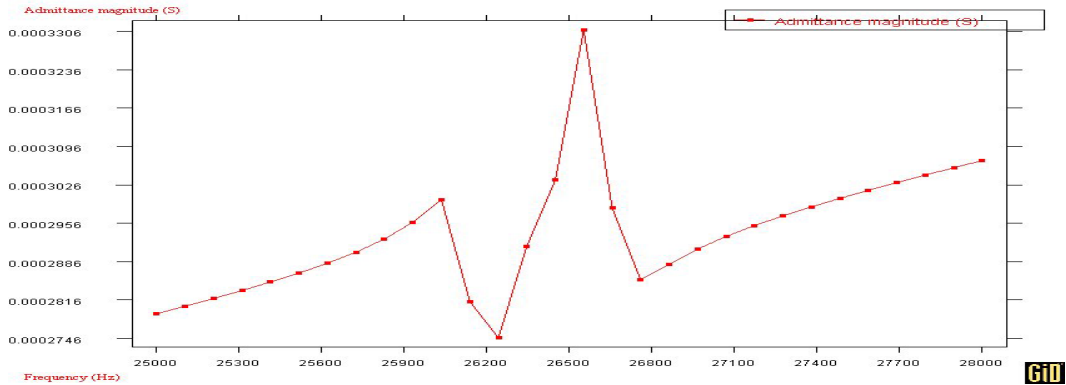
Figure 6: Prototype 1 admittance spectrum for both ends clamped

70
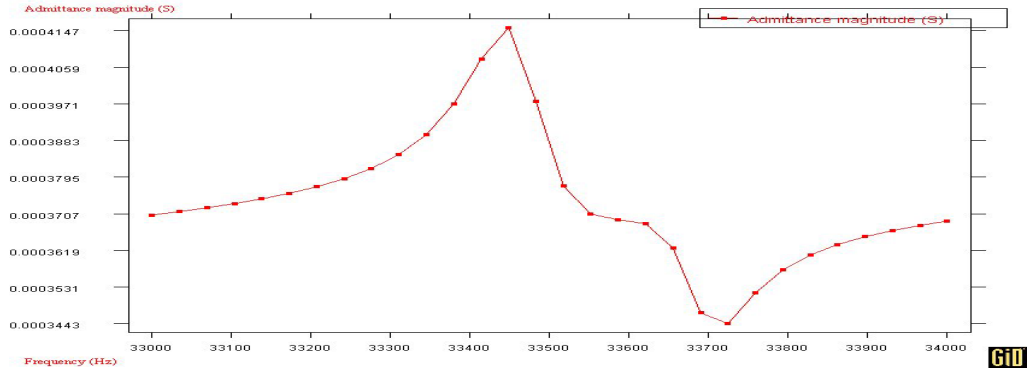
Figure 7: Prototype 2 admittance spectrum for both ends clamped

Figure 8: Prototype 1 and Prototype 2 left and right; both ends constrained

EXPERIMENTAL RESULTS

The circular prototype 2 with both ends clamped loosely and a small rubber band used in the middle for required pre-stress is described for its stability versus holding at one end. The results were taken under single source activation of one PZT plate, first in clockwise direction at 40.6kHz input and second in counter clockwise direction of rotation at 38.6kHz input.

71

Speed Vs. Time

$y = 0.4658x^3 - 6.1574x^2 + 29.259x - 0.1296$

Motor Characteristics (CW)

Figure 9: Experimental characteristic plots (1&2) of Prototype 2 in clockwise direction. In plot 1, speed found from frequency to voltage circuitry is used to find angular acceleration required for motor characteristics of plot 2.
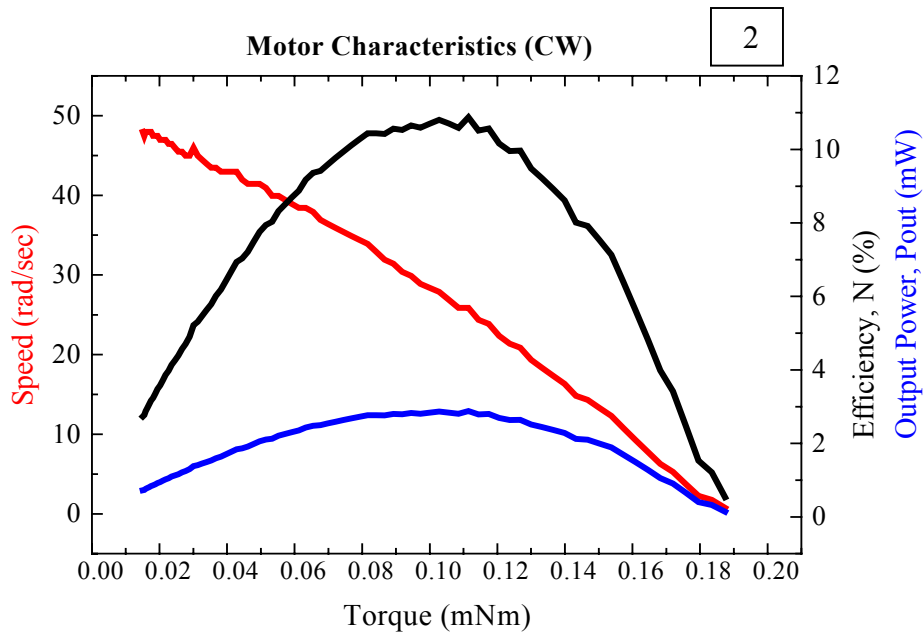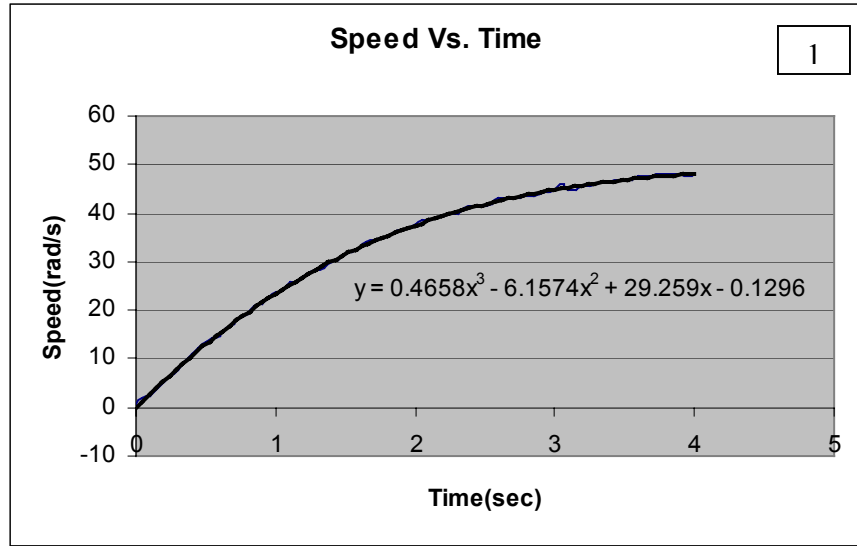
Speed Vs. Time

3

$y = 0.4658x^3 - 6.1574x^2 + 29.259x - 0.1296$

Speed(rad/s)

Time(sec)

Motor Characteristics (CCW)

Speed (rad/sec)

Efficiency, N (%)
Output Power, Pout (mW)

Torque (mNm)
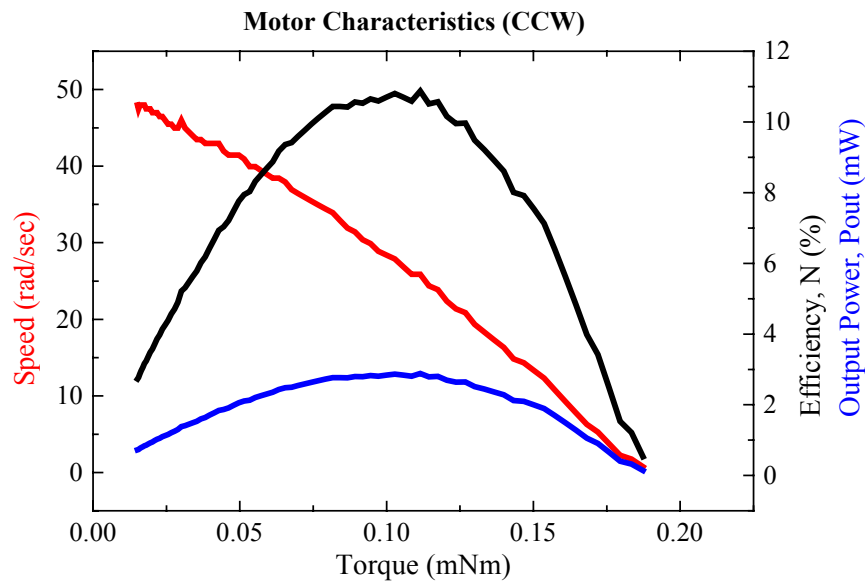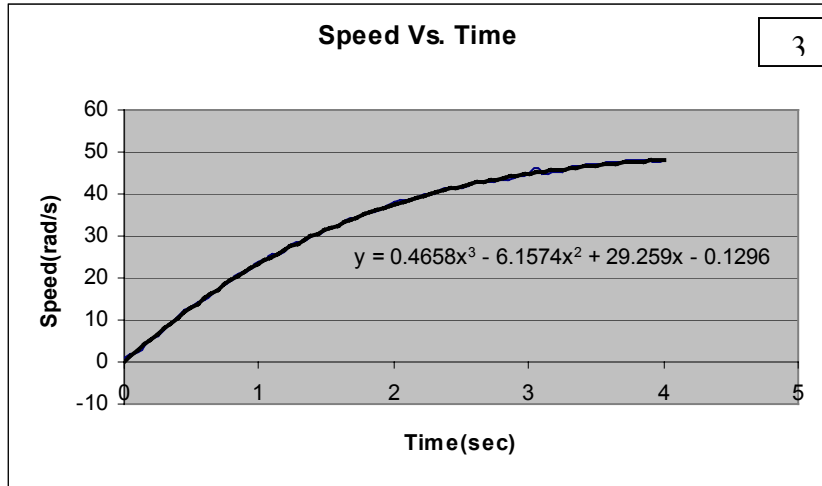
Figure 10: Similar experimental characteristic plots (3&4) of Prototype 2 in counter clockwise direction. In plot 3, speed found from frequency to voltage circuitry is used to find angular acceleration required for motor characteristics of plot 4.

DISCUSSION

With ATILA calculations maximum elliptical displacement of 90μm was seen with the circular Prototype 2 in free mode at 38.8kHz.   Since a stator cannot be operated in free position with no pre-stress, end constraints to both ends and one end were also simulated. It can be seen with the values in the table that holding the stator loosely by one end achieves the closest of 56μm circular displacement from center. From the ATILA table of values it was shown that prototype 2 was

more effective in terms of circular displacement required for exterior rotation. It can also be seen from the admittance spectra that followed for each prototype. The X and Y resonant peaks were almost overlapping with Prototype 2, while clearly separated with the square design. For elliptical motion a frequency must be applied between these two modes. Therefore greater displacement was achieved when the two frequency modes were the closest. From our ATILA results it was apparent that experimental values of the circular stator design was important for optimization.

Experimentally it was most beneficial for stability reasoning of the stator to hold at both ends loosely. In this way max performance at the center was successfully obtained with a rubber band for pre-stress against the exterior rotor. This circular design was activated with only one source applied to one plate. With clockwise rotation at 40.6kHz, maximum value of speed at 400 revolutions per minute, 0.19mNm for starting torque, 2.9mW of mechanical output power, and power efficiency of 10.7% were obtained. Counter Clockwise with the other plate activated produced similar results. This powerful motor was hard to stop once rotating and when the power was turned off the frictional pre-stress stopped rotation immediately.

CONCLUSION

With computer aided simulation one can test different stator designs and accurately choose an optimum structure. For exterior frictional rotation stator prototype #2, the circular design with 80° off set of plates was chosen for experimental description for its optimum ATILA simulation results. This exterior frictional design makes use of only two PZT plates, a brass cylinder grinded on two sides, an exterior rotor part of the actual device, and one alternating signal in the low ultrasonic frequency range. With regards to our optimized square structure, according to the simulation it produced less performance compared to the circular stator structure with 80° plate orientation, however from a fabrication point of view the square structure is less costly.

REFERENCES
[1] K. Uchino, "Ferroelectric Devices," chapters 1,3,4,7,11. Marcel Dekker, Inc. NY, NY 2000.
[2] K. Uchino, J. Giniewicz, " Micromechatronics," chapters 2,4,5,7,10. Marcel Dekker, Inc. NY, NY 2003.

[3] K. Uchino, "Introduction to Micromechatronics," Fifth International Conference on Intelligent Materials; Tutorial Courses," Penn State Materials Research Institute, State College, PA 2003.

[4] ATILA, 3D FEM software for piezoelectric & magnetostrictive structure, Magsoft (US), 1998.

[5] B. Koc, S. Cagatay, K. Uchino, "A Piezoelectric Motor Using Two Orthogonal Bending Modes of a Cylinder," IEEE Trans., Ultrason., Ferroelect., Freq. Contr. Vol 49, pp. 495-500, Apr. 2002

[6] B. Koc, S. Cagatay, K. Uchino, "Design Optimization And Miniaturization Of The Multi Mode Single Vibrator Type Piezoelectric Motor", Smart Actuators Symposium, State College, PA. April 2001

ELECTRICAL CHARACTERIZATION OF DOPED SILICON NANOWIRES GROWN IN ANODIZED ALUMINA MEMBRANES

Richard M. Bemben[1], K.K. Lew[2], Timothy E. Bogart[2], Sammy H. Wang[2], and Joan Redwing[2,3]

[1]The Bradley Department of Electrical and Computer Engineering
Virginia Polytechnic Institute and State University
Blacksburg, VA 24060

[2]Department of Materials Science and Engineering
[3]Department of Electrical Engineering
Pennsylvania State University, University Park, PA 16802

ABSTRACT

A method was developed to characterize the electrical properties of arrays of intentionally doped, p-type silicon (Si) nanowires . Nanoporous alumina membranes were used as a support structure for nanowire fabrication. Silver (Ag), cobalt (Co), and gold (Au), in that respective order, were deposited into the pores of anodized alumina membranes via electrodepostion. After these elements were deposited, silicon nanowires (SiNWs) were synthesized using the vapor-liquid-solid (VLS) growth method at 500°C using SiH_4 gas to supply the Si for the nanowires. During the VLS growth, the Co reacted with the SiNW to create cobalt silicide, which yielded an electrical contact at one end of the SiNWs. After the SiNWs grew out of the top of the membranes, an electrical contact was placed on top of the nanowires. Finally, current-voltage measurements were carried out in order to determine how doping level affected the electrical properties of the SiNWs.

INTRODUCTION

Recently, there has been increasing interest in one-dimensional nanostructures, such as nanowires, for several reasons. One reason is that nanostructures can efficiently transport electrons and holes, and therefore are considered ideal building blocks for the assembly of nanoscale electronic devices.[1] Another reason is that nanoscale electronics, using nanostructures as building blocks, could be assembled without complex and costly fabrication facilities, overcoming the fundamental and economic limitations of conventional lithography-based fabrication.[1,2] As the electronics industry races against Moore's Law to scale and miniaturize existing microelectonics[4], nanostructures could lead to a new, "bottom-up" paradigm for electronics manufacturing.[2]

There has been recent interest in the development of semiconductor nanowires, such as SiNWs, that may serve as building blocks in a "bottom-up" assembly approach. While there have been numerous reports on the synthesis of SiNWs, there have been relatively few studies of the electrical properties of these materials. This is due, in part, to difficulties handling the nanowires and making electrical contact. In this project, a new method was explored to characterize the resistivity of silicon nanowires. This method involved the growth of Si nanowires in nanoporous alumina templates. The templates act as a support structure for the Si nanowires which enables the fabrication of contacts on both ends of the wire.

It is well known that the resistivity of silicon decreases as the dopant density of either n-type or p-type dopant is increased.[6] This relationship can be seen in Figure 1 below, which displays data for boron-doped silicon and phosphorus-doped silicon. This inverse relationship is an important silicon semiconductor characteristic. Therefore, it is desirable to understand how a change in dopant density would alter the resistivity of a silicon nanowire.
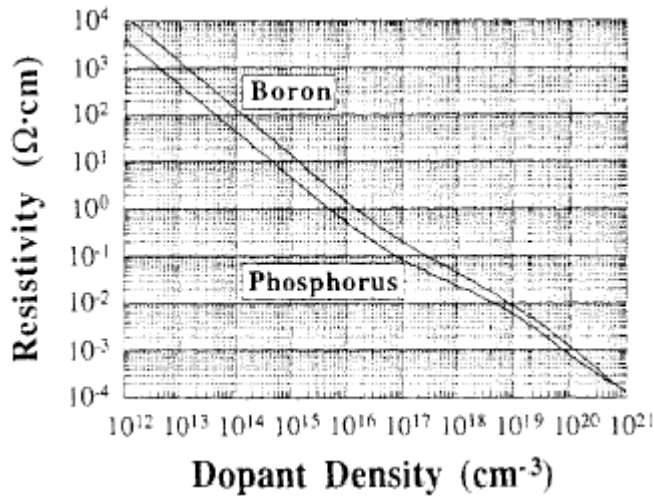

Figure 1 Doping density verses resistivity for p-type (boron-doped) and n-type (phosphorus-doped) silicon at 23°C.[6]

77

This report describes the method that was used to fabricate the SiNW arrays in alumina templates and preliminary results of a qualitative analysis of the electrical properties of these structures. The silicon nanowires were synthesized by the template-directed vapor-liquid-solid (VLS) growth technique described by Lew et al.[3] By applying indium as a top-side electrical contact to an array of intentionally doped silicon nanowires which are contained in the pores of anodic alumina membranes, current-voltage measurements were carried out in order to determine electrical resistance. By varying the dopant concentration in silicon nanowires a qualitative analysis of how the dopant concentration affects electrical resistance was obtained.

EXPERIMENTAL DESCRIPTION

Anodic alumina membranes, which are commercially available from Whatman Scientific, were used as templates in this study. These membranes had a nominal pore diameter of 200 nm and thickness of 60 μm.[3] Silver (Ag), cobalt (Co), and gold (Au), in that respective order, were deposited into the alumina membranes. The Ag and Au were deposited via current-controlled electrodeposition as described in Martin et al.[5] Co electrodeposition was preformed as described by Mohammad et al.[7] For this experiment, it was necessary to create a calibration curve for the electrodeposition of Co into the alumina membranes. This curve is included in the RESULTS AND DESCUSSION section of this report.

After Ag, Co, and Au were deposited, SEM (scanning electron microscopy) images of the membrane's top surface and cross-section were taken. The top surface was checked for chemical damage. The cross-section was taken to determine the amount of each element in the membrane's pores. Examples of a top surface and a cross-section can be seen in figure 2 and figure 3, respectively.
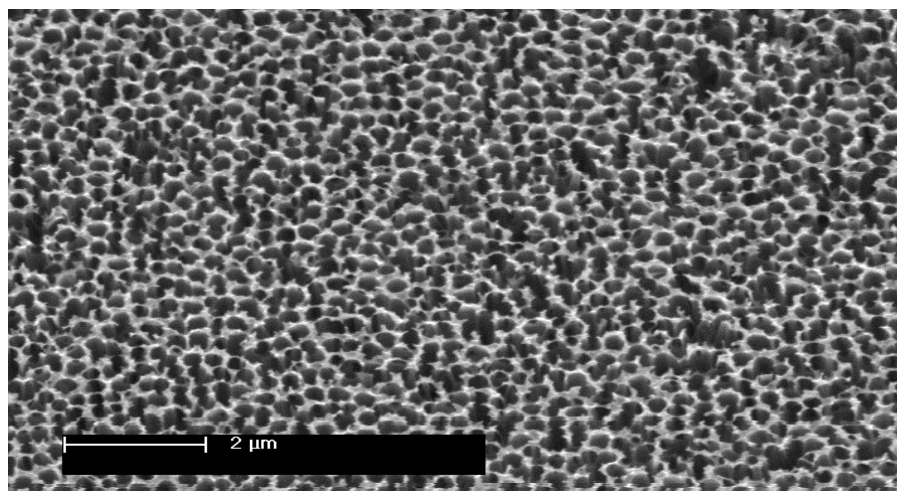

Figure 2 Top surface of membrane after deposition of Ag, Co, and Au
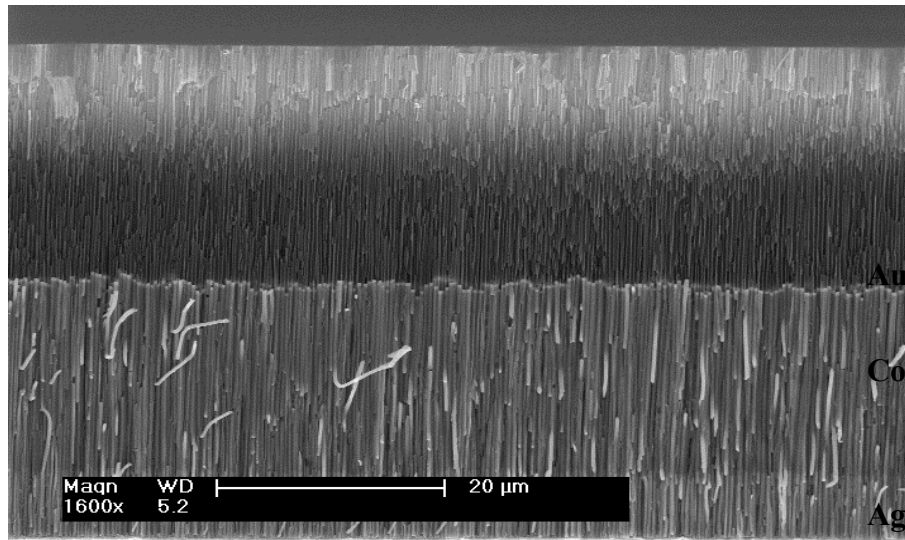
Figure 3 Cross-section of membrane after deposition of Ag, Co, and Au

Silicon nanowires (SiNWs) were grown out of the membranes via the vapor-liquid-solid (VLS) technique as described in Lew *et al.*[3] Figure 4, shown below, is the cross-section of a membrane with SiNWs.
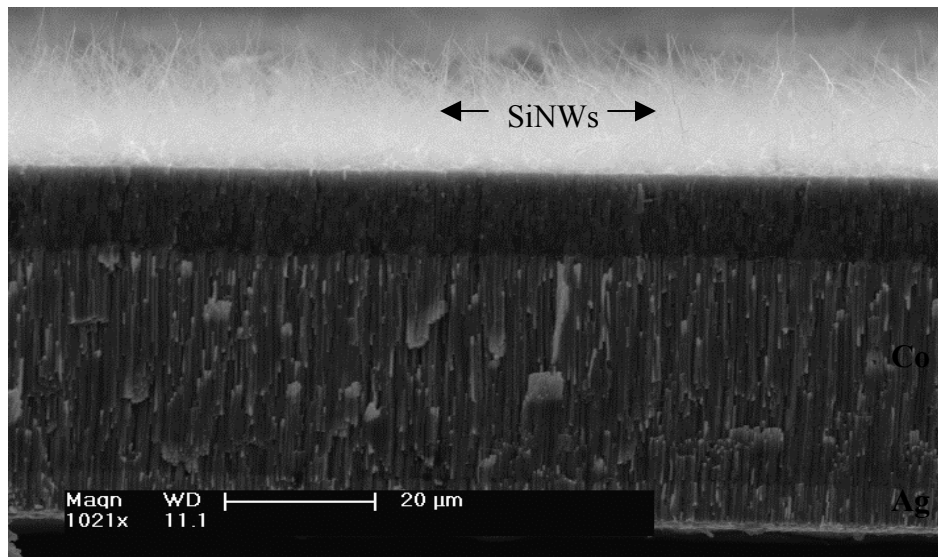
Figure 4 Cross-section of membrane with SiNWs

Following the nanowire growth, indium (In) was deposited on the top surface, the surface from which nanowires protrude. The indium was deposited by melting indium dots onto a glass slide being heated on a hot-plate. After the indium dots melted and changed phase from solid to liquid, the membrane's surface was dipped into the liquid indium and then allowed to dry and become solid again. After the top-side contact was dry, current-voltage measurements

were taken via the 2-point measurement technique using a Keithley 236 Source Measurement Unit.

RESULTS AND DISCUSSION

Electrodeposition of Cobalt

The cobalt calibration proved to be more difficult than expected, yielding two vastly different sets of data points. The first set of data points were taken between June 10, 2003 and July 18, 2003. During this period of time, the deposition of Ag, Co, and Au was compromised due to a faulty connection in the deposition apparatus. Therefore, this set of data points was deemed unreliable. They can be seen in table 1 and in figure 5. After the faulty connection was found and corrected, data collection restarted. The results of the cobalt calibration taken after July 18th did not yield a straight line as expected. Rather, it appears that there is about 20 microns of cobalt in the membranes from 20 to 40 minutes. Between 40 and 50 minutes there is an increase in the cobalt deposited in the membrane. These results were derived from the data in table 1 and can be seen in figure 6. It should be noted that although the first set of data was deemed unreliable, the results were linear as was expected, where the second set of data points was not linear.

June 10th - July 18th		After July 18th	
Time (minutes)	Thickness (microns)	Time (minutes)	Thickness (microns)
10	6.572	20	16.5
20	15.94	20	20.62
25	24.89	30	20.64
35	31.45	40	20.78
40	37.6	40	18.5
		40	21.2
		50	31.92

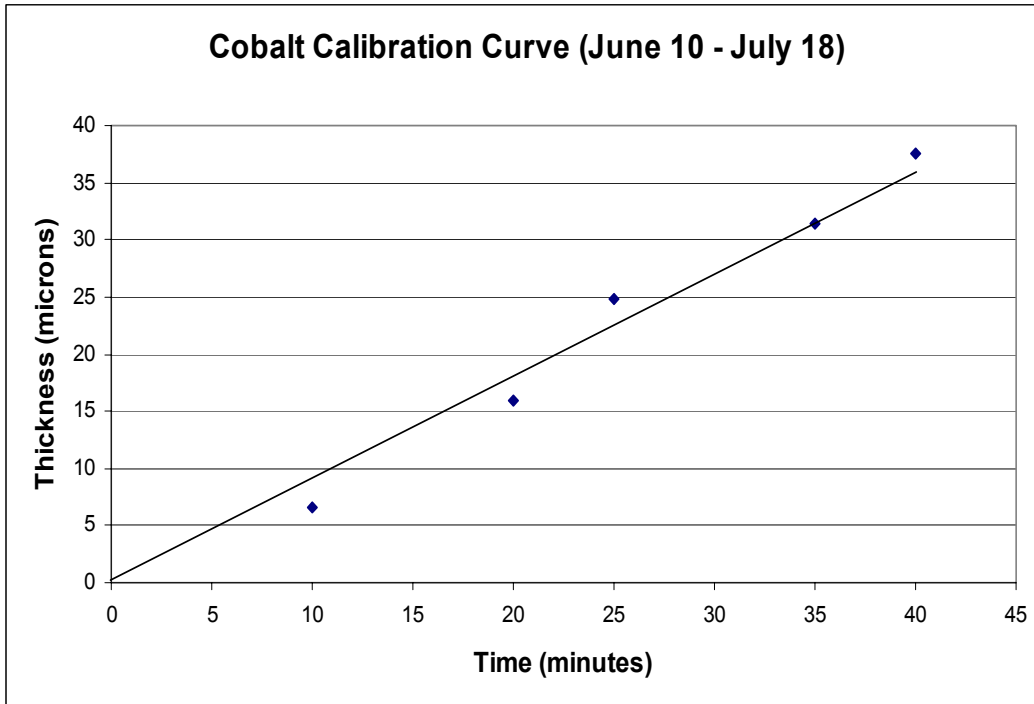**Table 1** Cobalt calibration table

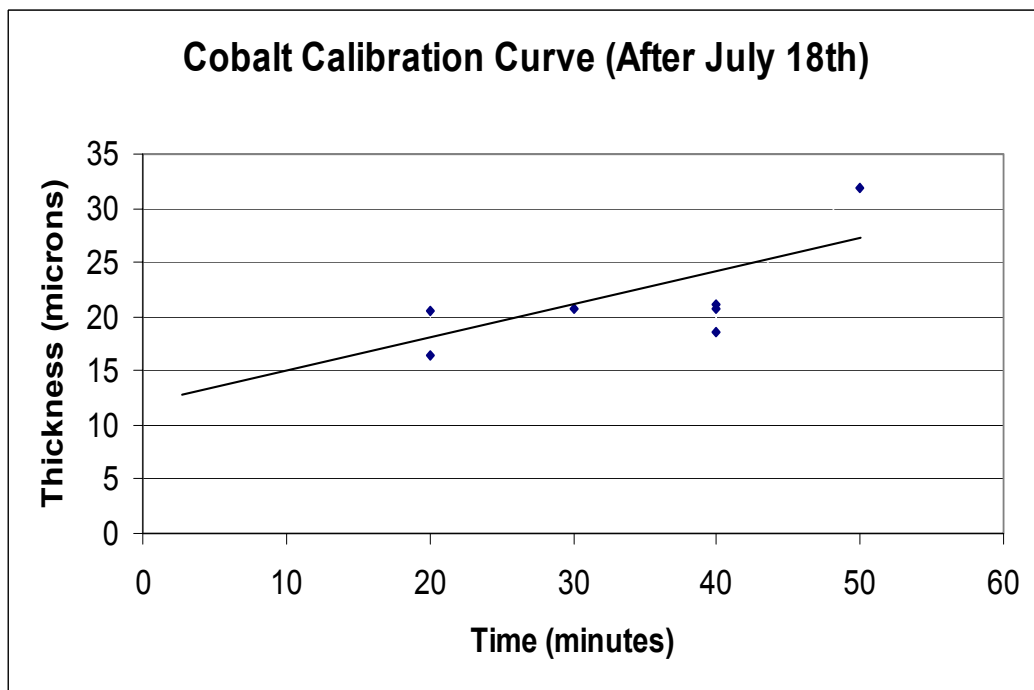**Figure 5** Cobalt calibration curve from June 10th to July 18th

Figure 6 Cobalt calibration curve after July 18th

Electrical Characteristics of SiNWs

As previously stated, it is well known that the resistivity of silicon decreases as the dopant density of either n-type or p-type dopant is increased.[6] Due to time limitations and complications with doped SiNW growth, only three samples were characterized thus far. The first sample was undoped SiNWs (labeled "undoped"). The second sample had a segment of the nanowire near the cobalt end that was doped with boron (p-type) and the rest of the wire was undoped (labeled "P+ undoped"). The third sample's SiNWs were lightly doped with boron and had an even dopant distribution their entire length (labeled "P+ lightly doped"). The SiNWs in all of these samples were grown out of the top surface of the membrane and indium was applied as the top-side electrical contact. Current/voltage measurements were preformed on these samples and yielded the results shown in figure 7.
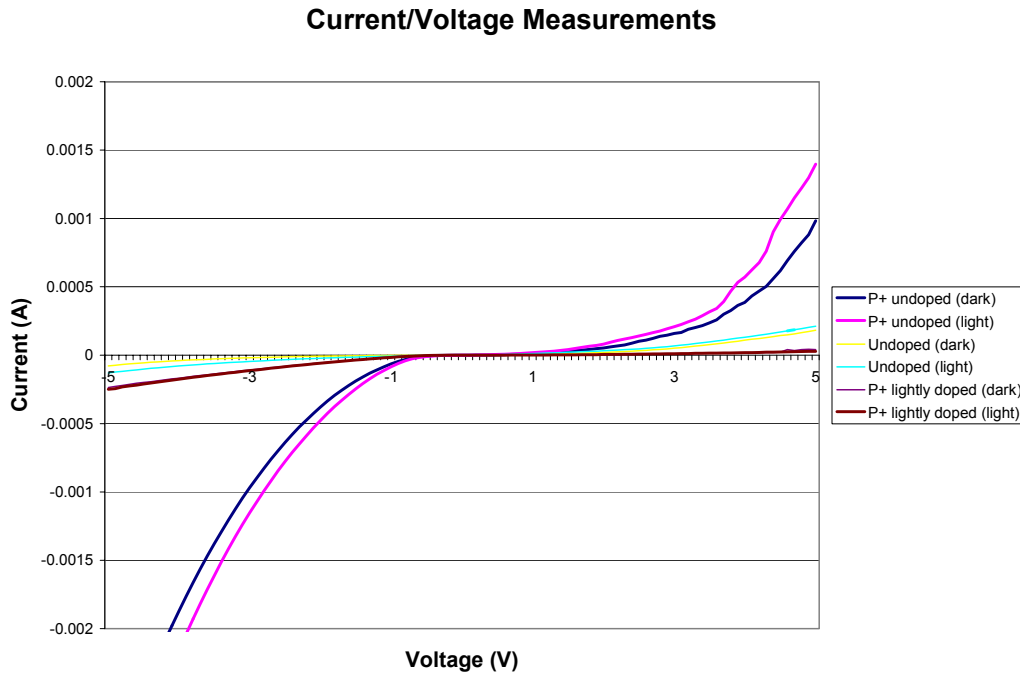
Figure 7 Current/Voltage characteristic for SiNWs

As seen in figure 7, the undoped SiNWs are more resistive than the P+ undoped SiNWs. This result was expected. On the other hand, the P+ lightly doped sample yielded the highest resistivity, when it should have yielded the lowest resistivity. There are several reasons why this could have happened.

The first possibility deals with the indium top-side contact. The problem can occur when the membrane is dipped into the heated indium. If the indium coated the top and wrapped around the edge to the bottom of the membrane (where the Ag is), then during the 2-point measurement the current will not go

through the SiNWs. Rather, it will flow from the indium on the top surface, over the edge and to the indium and silver on the bottom of the membrane, bypassing the nanowires and yielding undesired results.

Bowing of the membranes is another possible cause for the unexpected results of figure 7. Due to the differences in the thermal expansion coefficients of the different materials deposited in the membranes, bowing occurred after the SiNW growth. The bowing compromised the measurements because the samples could not rest flat against the metal stage during the 2-point measurements.

CONCLUSIONS

Although no solid conclusions can be drawn, several preliminary findings should be noted. First, differences in electrical characters were displayed from the 2-point measurements. This suggests that refining the methods described above could lead to more accurate findings. Minimizing bowing of the membranes as well as determining a more precise method for creating a top-side contact would be beneficial. Possibilities for the top-side contact include melting the desired contact in a furnace, sputtering the contact on the surface, or possibly removing the protruding portions of the SiNWs and then electroplating the contact onto the surface.

ACKNOWLEDGMENT

REFERENCES
[1]Y. Huang, X. Duan, Q. Wei, and C. M. Lieber, "Directed Assembly of One-Dimensional Nanostructures into Functional Networks," *Science*, **291** 630 (2001).
[2]Y. Cui and C. M. Lieber, "Functional Nanoscale Electronic Devices Assembled Using Silicon Nanowire Building Blocks," *Science*, **291** 851 (2001).
[3]K. K. Lew, C. Reuther, A. H. Carim, and J. M. Redwing, "Template-directed vapor-liquid-solid growth of silicon nanowires," *Journal of Vacuum Science*, **20** (1) 389-392 (2002).
[4]M. Lundstrom, "Moore's Law Forever?" *Science*, **299** 211 (2003).
[5]B. R. Martin, D. J. Dermody, B. D. Reiss, M. Fang, L. A. Lyon, M. J. Natan, and T. E. Mallouk, Adv. Mater. **11** 1021 (1999).
[6]D. K. Schroder, "Resistivity as a Function of Doping Density"; pp. 46-47 in *Semiconductor Material Device Characterization*, 2nd ed. John Wiley & Sons, Inc., New York, 1998.
[7]A. M. Mohammad, S. Dey, K. K. Lew, J. M. Redwing, and S. E. Mohney, "Novel method to fabricate cobalt silicide nanowire contacts to silicon nanowires," Accepted for publication in the Journal of the Electrochemical Society.

FERROELECTRIC AND MICROSCOPIC PROPERTIES OF PZT SINGLE CRYSTAL THIN FILMS

V. Morales*
(Ruyan Guo, Faculty Mentor)
Department of Electrical Engineering and Materials Research Institute
Pennsylvania State University,
University Park, PA 16802

*Undergraduate Student of
The Department of Electrical Engineering
Pennsylvania State University,
University Park, PA 16802

ABSTRACT

This research explores the ferroelectric properties of the PZT single crystal thin films through various methods of experimentation. The ferroelectric properties that are of main concern include the polarization status, the relative dielectric constant (K), and the dielectric loss (D). The relative dielectric constant and the dielectric loss were measured with a cryogenic system, and the high temperature dielectric equipment available in the Material Research Institute. Currently the synthesis and application of PZT single crystal thin films is an interesting field that invites for extensive scientific exploration.

INTRODUCTION

Throughout the following pages the ferroelectric properties of monocrystalline Lead Zirconium Titanate thin films, (001) $PbZr_{.52}Ti_{.48}O_3$ (PZT) on a thin, epitaxial interlayer of $SrTiO_3$ on Si substrates with a blanket of Ti/Pt electrode on top and bottom will be discussed. Ferroelectric is a unique property that can be found in pyroelectric materials. This property implies that the direction of the spontaneous polarization can be changed by an applied electric field or mechanical stress [1]. The ferroelectric properties that are of main concern are the relative dielectric constant (K) and the dielectric loss (D). The relative dielectric constant, dielectric loss, and phase transition were measured utilizing a cryogenic system and the high temperature dielectric equipment available in the Material Research Institute (MRI). Further studies, such as

hysteresis loop measurements and x-rays, were performed on this film for a better understanding of the crystallographic structure condition of the sample.

Since the compositions of interest are very close to the morphotropic phase boundary (MPB), such study will provide a better understanding of the complex structural and compositional interrelationships in such MPB families. This study is also valuable for the device performance improvement and for exploration of new devices, utilizing the monocrystalline thin films.

METHODOLOGY

The PZT film samples used in this study were previously deposited by using the sol-gel method over molecular beam epitaxy (MBE) STO, where STO is an epitaxial interlayer of $SrTiO_3$ [2]. There were a total of four different types of PZT samples studied. Two out of the four samples contained Lanthanum, these were identified as L7 and L8, and the remaining two were pure PZT denoted as T7 and T8. Samples T7 and L7 had a thickness of .5μm, and the T8, L8 samples had a thickness of .2μm.

The dielectric properties were measured at low temperatures using an ALCATEL DRYTEL 31 pump, a HC-2 APD Cryogenic System, a HP 3478A Multimeter, a LAKESHORE 330 Autotuning Temperature Controller, and a HP 4284A LCR Meter shown in figures 1-4 respectively. The relative dielectric constant was calculated by using the equation below

$$K = \frac{C \cdot t}{\varepsilon_0 \cdot a},$$

where C stands for the material's capacitance (F), t represents its thickness (m), ε_o corresponds to the constant value of permittivity (F/m) in free space, and A stands for area (m^2). For the relative dielectric constant (K) measurements the expected data values are usually well above the hundreds at low temperatures. The expected value for the losses was below 1%.

The phase transition and hysteresis loop measurements were carried out in the Dielectric Characterization Laboratory located in the Materials Research Institute (MRI). The hysteresis loop measurements were done with the aid of a bipolar operational power supply/amplifier, and by submerging the samples in a Galden HT200 solution that protected the film from breaking at edges. These measurements were useful to identify optimum poling conditions. Thin film x-ray diffraction data was also taken to verify that the samples were monocrystalline and that the film has orientation parallel to <001> direction. The instrument used was a theta-theta goniometer manufactured by Scintag, Inc. The measurement was done in the grazing angle geometry settings, with power settings of 40mV/45kV; the scan was collected continuously at the rate of 2 deg/min.

Figure 1
ALCATEL DRYTEL 31 pump

Figure 3
HP 3478A Multimeter
LAKESHORE 330 Autotuning Temperature
Controller

Figure 2
HC-2 APD Cryogenic System

Figure 4
HP 4284A LCR Meter

RESULTS AND DISCUSSION

The dielectric properties of the PZT films were examined at 100Hz, 1kHz, 10kHz, 100kHz, and 1MHz with no bias field applied, and 30mV of oscillation level (less than 1kV/cm for the film). The data obtained from samples L7, L8, and T8 yielded a low relative permittivity (not exceeding the value of 13), however the loss was kept relatively low (Figures 5-8). One sample that did have a good result was a 6 x 6 mm^2 PZT film of thickness 0.5μm; its results are shown in Figure 7.
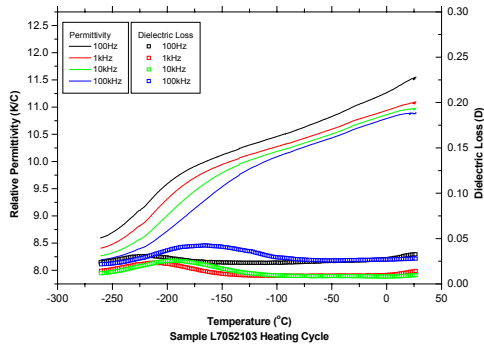
Figure 5
Dielectric property measurement run of
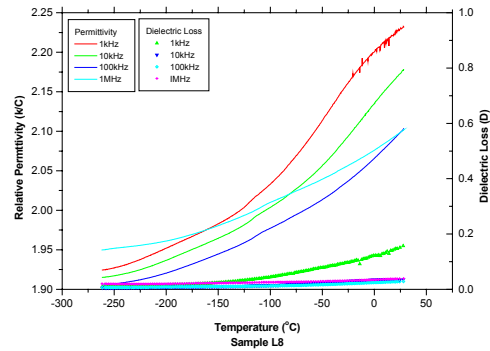Lanthanum sample, thickness .5μm.

Figure 6
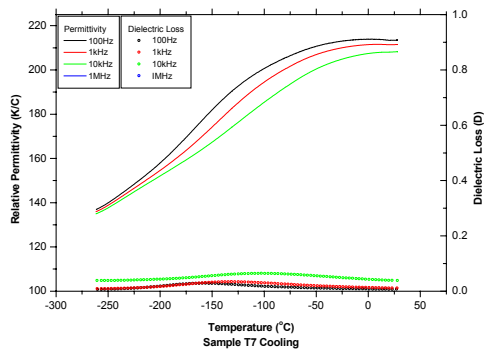Dielectric property measurement run of
Lanthanum sample, thickness .2μm.

Figure 7
Dielectric property measurement run of pure
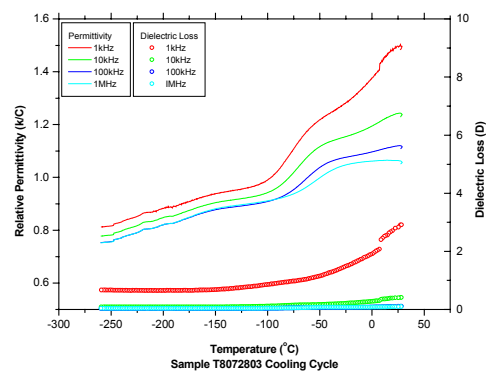PZT sample, thickness .5μm.

Figure 8
Dielectric property measurement run of pure
PZT sample, thickness .2μm.

Due to the unusual results acquired from the dielectric measurements lots of questions were raised. Were the samples poled? Were they crystallized properly? Is a segment of the large 6mm x 6mm square area damaged therefore corrupting the entire sample? In order to understand and answer these questions a phase transition study was done in the MRI Dielectric Characterization Laboratory. The dielectric constant of the PZT 52/48 films was measured as a function of temperature from 25°C to 450°C. The measurements taken were ramped at 2°C/min with an oscillation level of 30mV.

Figures 9 and 10 present the temperature dependence of the dielectric constant for samples L7 and T7, respectively, with frequencies 1kHz, 10kHz, 100kHz, and 1MHz. As was expected, all the films showed a dielectric anomaly due to the ferroelectric-paraelectric phase transition. The temperatures where the dielectric constant reached the maximum (T_m) were all around 420°C for these films. However, the dielectric constant peak at T_m was much lower in these films than bulk PZT ceramics.
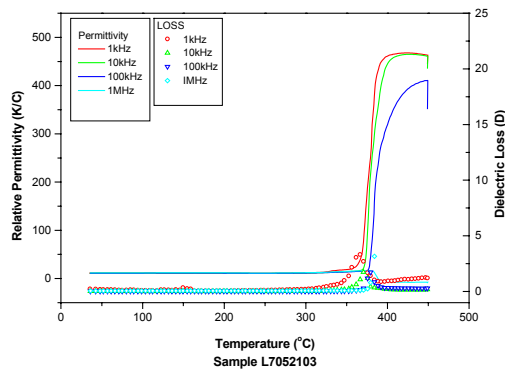
Figure 9

Temperature dependence of the dielectric constant, Lanthanum sample.
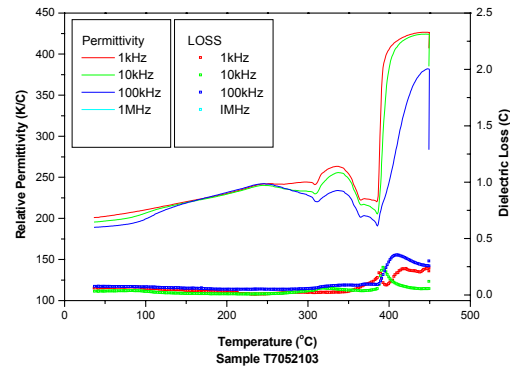

Figure 10

Temperature dependence of the dielectric constant, pure PZT sample.

Once all of the dielectric properties were studied, hysteresis loop measurements were taken. The measurements were done in the Dielectric Characterization Laboratory at the Materials Research Institute. The equipment used was the Automated Polarizing Measurement System; the data was taken with a period of .0998s, acquisition mode of one shot, and by incrementing the voltage every 5 volts.

The data collected from samples L7 and T8 are shown in Figures 11 and 12. A well-defined hysteresis loop was not possible to obtain but it can be observed that the formation could be noticed at 30 volts. These samples were particularly hard to measure demonstrating that reversing the direction of a monocrystalline sample is a tough task. It can be seen in Figure 11 that sample L7 has a cohersive field of approximately 7MV/m, and a charge of $56\mu C/cm^2$, and sample T8 has a field of approximately 36MV/m, and a charge of $50\mu C/cm^2$.

Figures 13 and 14 are a different case, sample L8 in Figure 13 was the closest to a hysteresis loop acquired, and it was possible by incrementing the voltage to 330 volts. The cohersive field (E_c) of this sample is approximately 109MV/m. In contrast, sample T7 has an E_c of 41.5MV/m, and the hysteresis loop was possible to study. The hysteresis loop was attained as the sample was driven near to its breakdown voltage, 30 volts (600kV/cm).

After completing all the hysteresis loop measurements and suspecting that the samples were effectively poled as grown, an x-ray diffraction analysis was done at MRI. Figure 15 is the graph showing the diffraction intensity as a function of diffraction angle (2ɵ). Comparing this data to Figure 16 [3] we were able to confirm that the film was oriented in the (100) plane. Figure 16 also demonstrates that a secondary effect to having a thin film, such as the one in the samples used in this study, is the absence of the diffraction peaks in a very thin film.

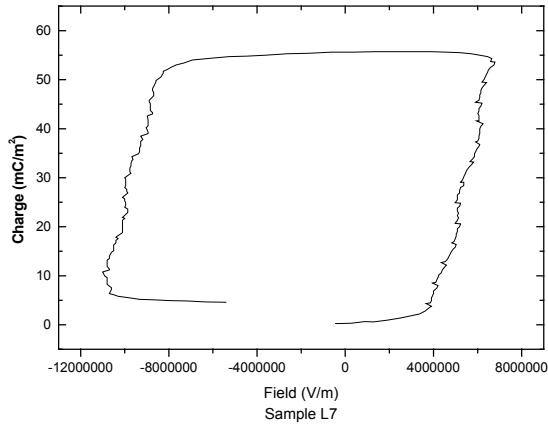**Figure 11**
Lanthanum sample, thickness .5μm,
hysteresis loop measurement.

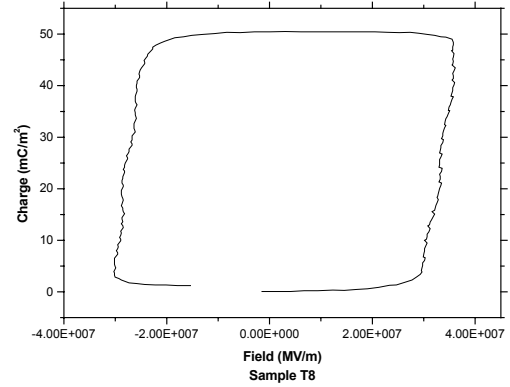**Figure 12**
Lanthanum sample, thickness .2μm,
hysteresis loop measurement.
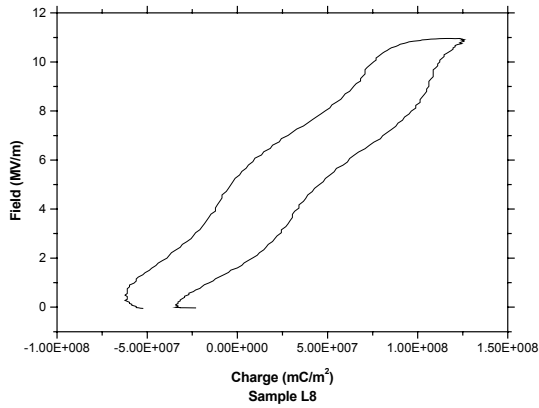
Figure 13
Pure PZT sample, thickness .2μm, hysteresis
loop measurement.
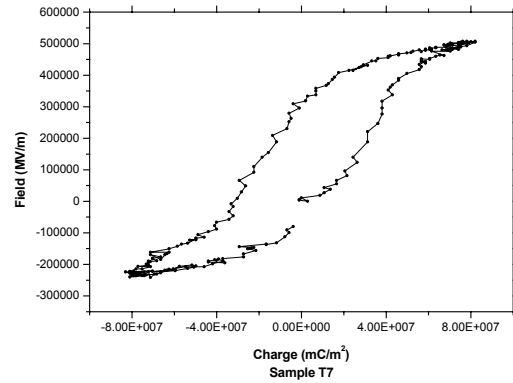
Figure 14
Pure PZT sample, thickness .5μm, hysteresis
loop measurement.
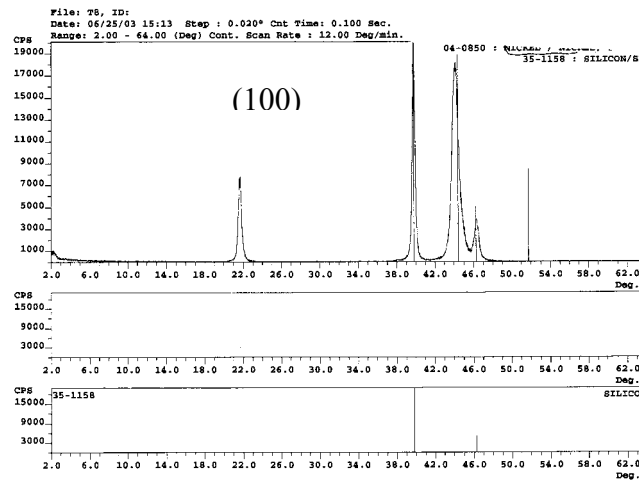
Figure 15
Powder run on sample T8 compared to silicon substrate x-ray diffraction.
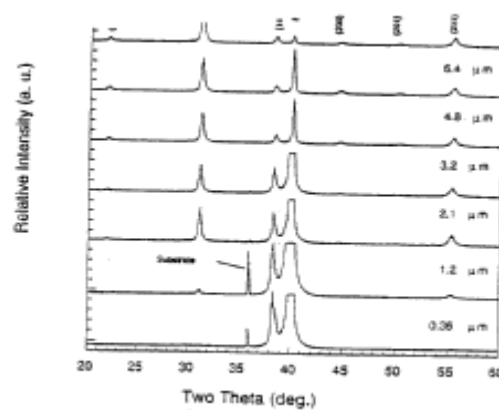
Figure 16
XRD patterns of PZT films deposited using acetyl acetone modified 2-mothoxyethanol solution and RTA process (Courtesy of W. Ren).

SUMMARY

Monocrystalline PZT thin films have been recently available, that demands characterization and understanding to explore their full potential. Results reported in this paper verified that pure PZT films (0.5μm thickness) synthesized over an epitaxy $SrTiO_3$ layer on a Si substrate indeed have (001) orientation. Such a thin film as grown is already self-poled and the switch of its polarization by electric field at room temperature is difficult (E_c~600kV/cm). Although the films doped with lanthanum were found of low permittivity, all films studied were verified to have a relatively low dielectric loss and high polarizability. Cryogenic

90

temperature dielectric properties also revealed that pure PZT thin film does have intrinsic permittivity approaching 130 at low temperature. All films showed dielectric relaxation behavior which needs to be studied further.

ACKNOWLEDGEMENTS

REFERENCES

1. A. J. Moulson and J. M. Herbert, *Electroceramics Materials Properties Applications,* Chapman and Hall, London (1997).
2. A. A. Talin *et al*., *Epitaxial PbZr$_{.52}$Ti$_{.48}$O$_3$ films on SrTiO$_3$/(001) Si substrates deposited by sol–gel method,* Appl. Phys. Lett. **81**, 1062 2002.
3. W. Ren and S. Troiler-McKinstry, unpublished work (1998).

LABVIEW-BASED INSTRUMENTATION FOR A MEMS BIOSENSOR FOR SENSITIVITY IMPROVEMENT

Bryan A. Martin*
(Srinivas Tadigadapa, Faculty Mentor)
Department of Electrical Engineering
Pennsylvania State University, University Park, PA 16802

*Undergraduate Student of:
Department of Electrical and Computer Engineering
Western Michigan University
Kalamazoo, MI 49006

ABSTRACT

The goal of the project was to implement MEMS microthermopiles as high performance biosensors. Lock-in detection techniques were utilized in order to improve the sensitivity of the device. My role in the implementation phase was to create software to control and further automate these processes. This was realized through the use of a programmable syringe pump, a lock-in amplifier, a function generator, and a basic PC with an IEEE 488.2 (GPIB) card. The function generator and the lock-in amplifier were used to produce a sinusoidal signal, which was then transmitted to the syringe pump. The syringe pump thereby moved the fluid being tested through the thermopile in a corresponding sinusoidal manner.

In order to accomplish this process, LabVIEW (Laboratory Virtual Instrumentation Engineering Workbench) was used. Once the software had been completed, it not only remotely controlled all necessary lab equipment from one centralized station, but it served to further automate the whole process in general. The goal of the new setup was to enhance the accuracy of the measurements by a factor of over 100. The software even automatically transposed and appended the readings taken to an existing spreadsheet data file to facilitate viewing and charting.

INTRODUCTION

The purpose of this experiment was to find a more precise way to calibrate MEMS microthermopiles, thereby making them high performance biosensors. Previously, they were tested and calibrated using a steady flow of water at a set temperature to heat the hot junction of the microthermopile. Since DC measurements need large bandwidths, the overall noise in such measurements is high and therefore limits the accuracy and precision of the measurements and calibration thereof.
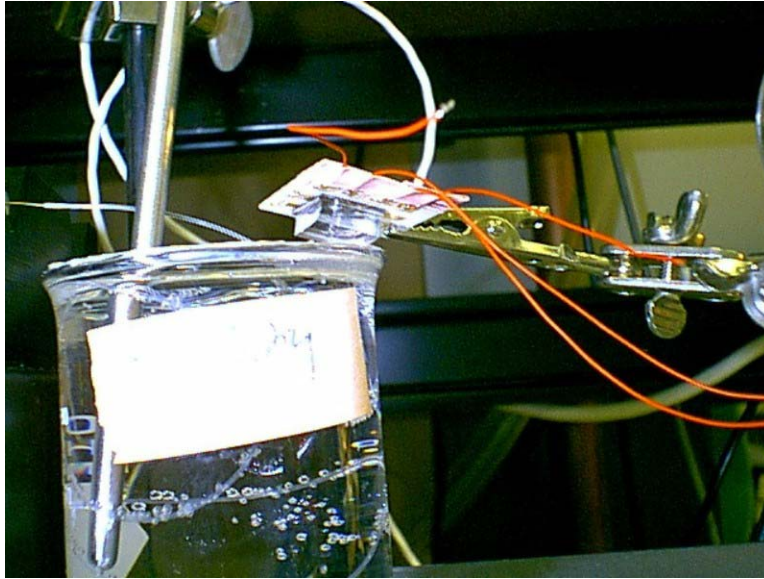
The microthermopile with fluidic membrane is positioned directly over the beaker of hot water. The hot plate underneath the beaker approaches temperatures as high as 150 ° C, hence the heat radiation interference.

It was realized, however, that there might be a way around this obstacle. The solution was to use a lock-in amplifier for precision voltage measurements. "[This] technique is known as phase-sensitive detection, … [which] singles out the component of the signal at a specific reference frequency and phase."[1] This technique is popularly used in optics and low signal electronic measurements at reference frequencies in the 10 Hz to 100 kHz frequency range. However, for microfluidic applications, the reference frequency and the signals needed to be considerably smaller, typically in the 5-10mHz range. Therefore, a lock-in amplifier capable of low-frequency measurements was used (specifically, a Stanford Research Systems SRS-830).

If a low frequency lock-in amplifier was used, and if the flow of water over the hot junction was varied in an AC style, the control signal for this flow and the output of the microthermopile would be adequate input to allow the lock-in amplifier to detect a clean, nearly noise-free signal.

EXPERIMENTAL DESCRIPTION

To even have a remote chance of success with this experiment, extensive automation was a must. Without it, there would have been no way to have all units outputting, reading, and commanding in synchronization with one another. To accomplish this level of control, Laboratory Virtual Instrumentation Engineering Workbench (LabVIEW) was used. LabVIEW is a versatile, powerful graphical programming language, which greatly simplified and facilitated the production of efficient, graphical user interface (GUI) style programs. The first step, obviously, was to learn to use this new software (a series of time consuming experiments in itself).

The first usable software produced was a program used to control a Keithley 2000 Multimeter via an IEEE 488.2 (GPIB) card. Although the software as originally built had many more features, most of them were deemed useless for our application, and were eliminated for the sake of efficiency. One of the greatest dilemmas of writing this program was the small size of the memory buffer within the Keithley 2000 itself. The buffer was only capable of storing 1024 readings at 6 ½ bytes a piece, and at two to four readings per second, this only allowed for about 4.25 to 8.5 minutes of data collection, whereas the experiment required fifteen to ninety minutes worth of data collection. This, of course, meant that the factory provided LabVIEW drivers could not be used effectively, thereby forcing the production of custom drivers capable of streaming large amounts of data.

The basic communication with a GPIB device is performed through ASCII character strings. Each device has its own GPIB communication address and command syntax. It was determined through extensive testing that the optimal process was to have the multimeter read seventy data points into its buffer, transmit this data to the PC, and repeat. Any more than seventy caused noticeable periodic time gaps between readings, and any less caused communication lag and wasted GPIB resources. However, the software did not improve the accuracy of the readings, as the noise in measurements was generated from the measurement setup itself and had not relation to automation. These DC measurements will be used as the control group, against which the new, cleaner data from the lock-in amplifier were compared.

Once the recording of the multimeter readings into the computer was successfully accomplished, it was time to move on to the experimental group. The first software made in this phase was for an EG&G 5207 Lock-In Amplifier. Once again, the available drivers were too slow, and they had to be custom made. Of course, the unit was rather old, and there was no manual accompanying it. After many long hours checking various manual vendor's inventories, a full copy was acquired through a parent company of EG&G out of Atlanta. Once the manual, including the syntax of all unit commands, was received, the programming of the unit could begin.

94

There were no buffer issues to be concerned with on the EG&G, and therefore single readings could be streamed from the unit without damaging performance. To describe the software design in a nutshell, once some preliminary configuration commands were sent to the EG&G, the reading-phase loop began. A command was sent to the EG&G telling it to take a "snapshot" of the current data. A small, intentional delay followed to prevent command overlap, and then an ASCII string of 10 bytes was read in from the device. These 10 bytes were then converted into an actual numerical data type, and multiplied by a coefficient read in during the configuration phase. This was the actual reduced noise output voltage of the unit, which was then appended to a temporary array, and the loop was repeated. Once the loop, and therefore the program, was stopped, the temporary array was saved into a previously specified text file, which could then be opened and analyzed with Microsoft Excel. However, in order for this unit to be useful, the input had to fluctuate synchronously with the reference signal.

The input of the lock-in amplifier was based on the output of the microthermopile. This output, however, was based on the temperature and, more importantly, the flow rate of the water being passed over it. In turn, this flow rate was controlled through the use of a Harvard Apparatus PhD 2000 Programmable Syringe Pump. In order for the output of the microthermopile to vary with the reference signal, the infusion rate of the syringe pump had to be frequently updated with the function generator's output. This is where the setup became complex.

In essence, the waveform generator had to "control" the syringe pump with its output. This became an involved task, as the function generator produced an analog signal, whereas the pump required commands in ACSII string format. The first step was to convert the analog signal to a digital one. After much contemplation, it was realized that a Keithley 2000 Multimeter could be used for this. The multimeter would read in the signal from the function generator, calculating the voltage. Using the multimeter's GPIB port, this datum could be transferred to the PC. The PC then used this voltage reading as a multiplier in conjunction with the user's supplied input (specifically, the minimum and maximum flow rates desired), to determine what the fluid flow rate should be. Once the flow rate was calculated, it was turned into an ASCII string, concatenated with the appropriate command syntax and a termination character, and sent to the syringe pump. However, this was easier said than done.

The PhD 2000 Syringe Pump was not equipped with a GPIB interface. It was only capable of receiving commands via an RS-232 (serial) connection. Therefore, a serial linking cable was purchased. The cable was attached to the unit, and the software was tested, but to no avail. The syringe pump did not respond to any commands. After some technical support, looking through several user manual appendixes, and a few cups of coffee, it was determined that the only way to communicate with the unit was to use an RJ-11 port (6x4 phone jack) on the backside of the pump. This posed as a problem, as there is nowhere to plug

the phone cord into the PC except the modem, and conveniently, the PC used was not equipped with one. Instead, a cable had to be custom fabricated.

The customized cable was actually a modified "straight-thru" phone cable. One end, for the pump, retained its original telephone connection plug. However, the other side of the wire bundle had to be cut, stripped, and soldered to a DB9 (serial) style connection using the specifications supplied with the manual. Once this custom cable was finished, the software was once again tested, and once again failed to function. As it turns out, the ma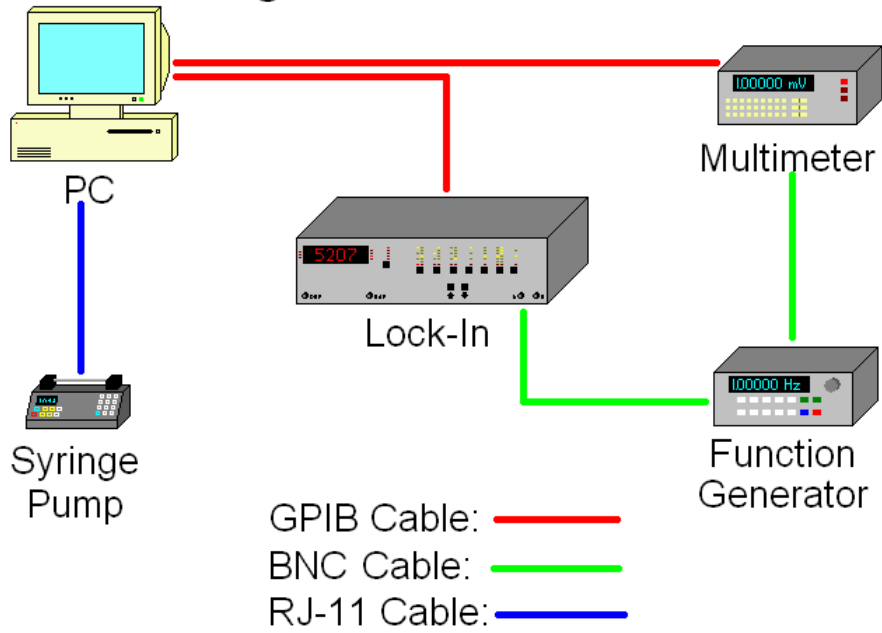nual had a misprint in the communication cable specifications appendix. This misprint led me to connect all wires completely backwards to the DB9 plug. However, once technical support was called again and this issue was remedied, the unit began taking orders beautifully from the PC. There was just one problem: RS-232 connections are quite sedate. This meant that the syringe pump could not accept commands, and therefore could not update the infusion rate, with a period of any less than 750 ms or without encountering command overlap and/or overheating. This speed issue meant that any frequency over 375 mHz would not work (and 375 mHz was even pushing it), as the infusion rate of the unit would simply become chaotic. Fortunately, this was not a limiting factor in the end, as the microfluid dynamics simply became unstable at frequencies over 100 mHz. This speed limitation, however, presented another major problem with our experimental concept.

As mentioned earlier, the lock-in amplifier uses a control, or reference signal, in conjunction with the actual input signal to filter out noise. Of course, these waveforms are almost DC signals as a result of their exceptionally low frequency. The dilemma came when it was discovered that the EG&G Lock-In Amplifier will not accept signals under 5 Hz (typically, these units are used at much higher frequencies, and this is not even an issue). This meant, of course, that all software made for the EG&G was now useless. Salvation, however, was right across the room. Sitting on a table was a Stanford Research Systems SRS-830 Lock-In-Amplifier. This lock-in amplifier was much more advanced than the EG&G, as it was capable of using frequencies down to 5 mHz, which is 1000 times slower than the EG&G. Once the owner of the unit was contacted, permission was granted to use the lock-in amplifier for an undetermined amount of time.

New software was then developed for use with the SRS-830. Of course, the syntax of the machine was totally different than that of the EG&G. However, in the end, not only did it allow us to use slower frequencies, it allowed for faster reading and data transfers, and it was even capable of giving us both the magnitude and the phase shift of the voltage input. In the end, the machines used were connected in the following format:
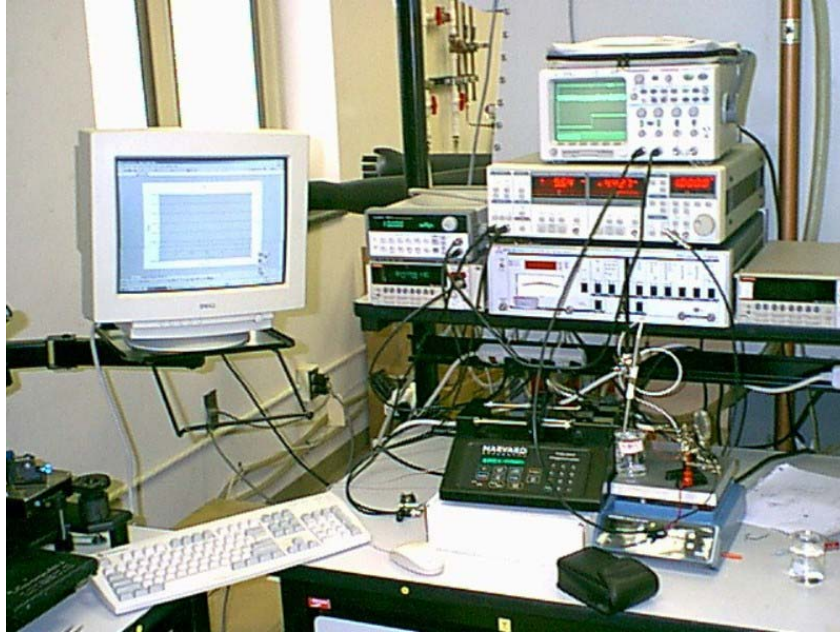
Experimental Device Configuration

Signal Connection Chart

PC

Multimeter

Lock-In

Syringe
Pump

Function
Generator

GPIB Cable: ——————
BNC Cable: ——————
RJ-11 Cable: ——————

Experimental Device Connection Chart

RESULTS

Multimeter Data
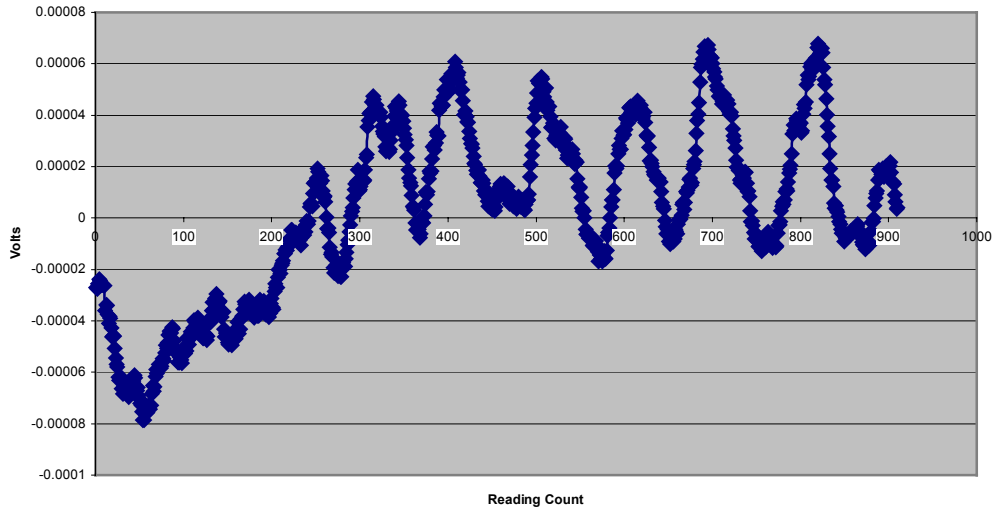
Graph #1
Source: Multimeter
Infusion Rate: 0.0-3.0 ml/hr, square wave input, 10 mHz @ 35% duty
Water Temperature: 60° C
Run time: 15 minutes @ 1 reading per second

Multimeter Data

Graph #2
Source: Multimeter

98

Infusion Rate: 0.0-3.0 ml/hr, square wave input, 10 mHz @ 35% duty
Water Temperature: 60° C
Run time: 15 minutes @ 1 reading per second

Lock-In Amplifier

Graph #3
Source: Lock-In Amplifier
Infusion Rate: 0.0-3.0 ml/hr, square wave input, 10 mHz
Water Temperature: 60° C
Run time: 60 minutes @ 2 readings per second

Lock-In Data

Graph #4

99

Source: Lock-In Amplifier
Infusion Rate: 0.0-2.5 ml/hr, square wave input, 10mHz
Water Temperature: 60° C
Run Time: 60 minutes @ 1 reading per second
Secondary Infusion: Room temperature water, 1.0 ml/hr steady

Lock-In Amplifier Data
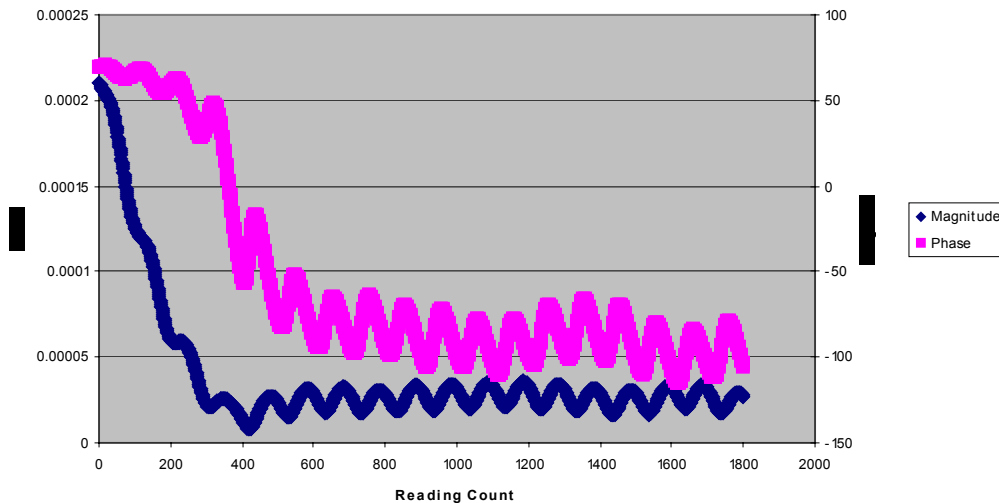
Graph #5
Source: Lock-In Amplifier
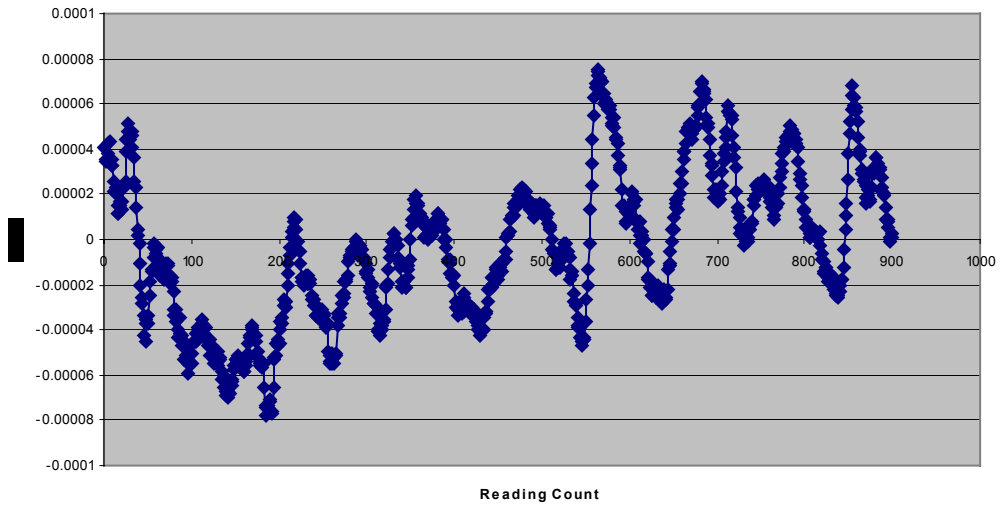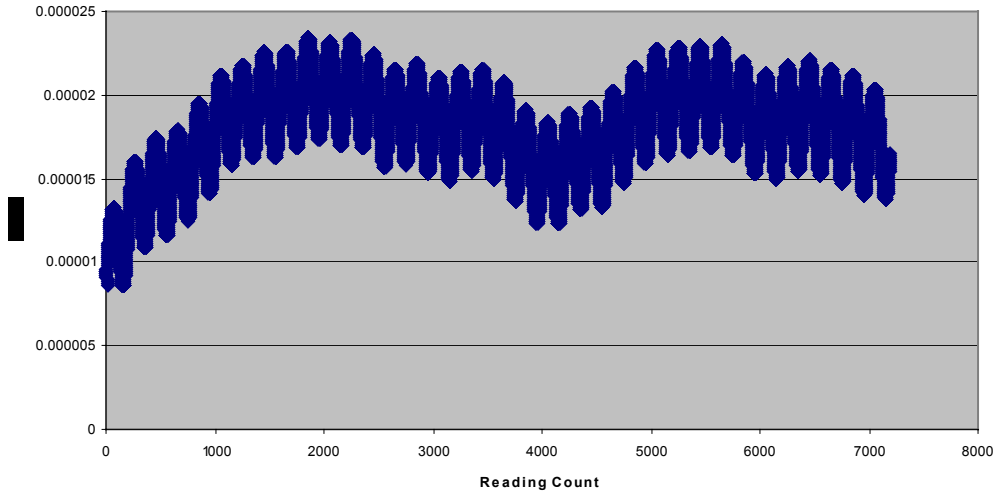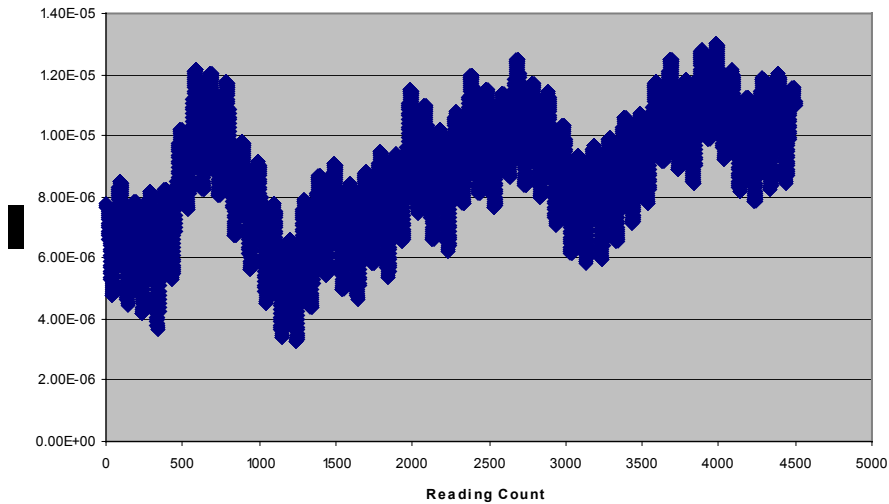*Infusion Rate: 0.0-3.0 ml/hr, square wave input, 10 mHz*
Water Temperature: 60 ° C
Run Time: 30 minutes @ 1 reading per second

DISCUSSION

- *Graph #1:* This is exactly what ideal data from the multimeter should look like. It is easy to see that every 100 readings, there is a full period consisting of a rising voltage and then a falling voltage. This is the sort of data that a lock-in amplifier could easily latch onto. However, this particular data test was unrepeatable.
- *Graph #2:* Although the simulation conditions were identical to those of Graph #1, the output data clearly was not. There is no significant periodic trend, and it is therefore useless to the lock-in amplifier.
- *Graph #3:* When the lock-in amplifier is used, ideal data will have a small sinusoidal fluctuation to it, but the overall trend will approach a horizontal asymptote and essentially become a straight line over time. This data just bounces around, and is therefore meaningless.

100

- *Graph #4:* As the experiments continued, it was hypothesized that if room temperature water was administered at a constant rate along with the pulsing hot water, the room temperature water might help cool the unit to a more consistent temperature between readings. This, in turn, would allow the output to stabilize quicker. However, when implemented, it had little effect on the data.
- *Graph #5:* Some of the latest data from the lock-in appeared to be more promising. Not only did the magnitude approach a steady predicted value, but the phase difference also did the same thing.

Much of the noise in the readings was produced by both radiations from the hot plate underneath the microthermopile and from the complex microfluidics of the situation, which will not be discussed in this paper. However, as one can see, by Graph #5 much of the noise encountered had vanished. This was accomplished through testing various combinations of lock-in amplifier modes of operation, i.e., adjusting the time constant, sensitivity, input style, etc. Also, the simple placement of the microthermopile in relation to the beaker of water, the syringe pump, and other devices has been altered and tested. It was through a large variety of small alterations in the experiment that the data slowly improved, and hopefully this trend can continue.

CONCLUSION

The original objective of this experiment, in a nutshell, was to use a lock-in amplifier in combination with any other equipment deemed necessary in order to acquire significantly more accurate voltage readings from a microthermopile. These readings, in turn, would be used to improve the calibration of these biosensors.

While these lofty goals may not have been met in full, much progress was made along the path to experimental success. Accurate, reliable, and user-friendly software was created to govern and record the actions and measurements of many pieces of lab equipment. I only wish I had more then nine weeks at PSU to further improve upon my software and to assist in more development and experimentation. I have greatly enjoyed my time with the NSF EE REU program here at PSU, but most importantly, I feel I learned a great deal. I learned not only about software development and MEMS, but also about life as a graduate student and researcher. I would enjoy nothing more than being able to continue working under the program in order not only to see this experiment through to the end, but also to develop more software for other future experiments.

Although the generated data are still not perfect, as the experiment moves along and further refinements are made to the experimental setup, the data will continue to improve in accuracy. The experiment is far from done; I would like to emphasize that this experiment is a work in progress. There are still countless combinations of infusion rates, temperatures, time constants, sensitivities, pulse styles, and many other variables to be tested. I truly believe that with further refinement of equipment configurations, this experimental concept will lead to

improvements in the field of testing and calibrating MEMS biosensors and microfluidic devices.

ACKNOWLEDGEMENTS

REFERENCE

[1]Stanford Research Systems, "SR830 Basics", 3-1, <u>Model SR830 DSP Lock-In Amplifier</u>, Revision 2.0, SRS Inc, Sunnyvale, CA, 1993.

CONTINUOUS-WAVE QUADRUPOLE RESONANCE SPECTROMETER

Bonnie R. Hammond*
(Jeff L. Schiano, Faculty Mentor)
Department of Electrical Engineering
Pennsylvania State University, University Park, PA 16802

*Undergraduate student of
Department of Engineering
Cedarville University
Cedarville, OH 45314

ABSTRACT
    Nuclear quadrupole resonance (QR) spectroscopy can detect explosives, biological warfare agents, and narcotics within sealed non-metallic containers. Commercial QR detection systems detect contraband by applying a series of radio frequency magnetic field pulses and detecting the material's response between the pulses. In contrast, continuous-wave spectroscopy excites the target material over a range of frequencies and reveals the frequency response of the sample. Developed in the 1950's, CW spectroscopy was replaced in favor of pulsed methods that provide a greater flexibility in spectroscopy experiments. Recently, CW has become attractive again because it uses much less power and is useful for identifying resonant frequencies in materials not previously studied using QR.
    The goal of this research was to analyze the operation of the lock-in detection system used in CW spectrometers. CW spectrometers use a lock-in amplifier to extract an NQR signal that has a signal-to-noise ratio of less than 60dB. Study of the Lorentzian lineshape describing the frequency response of the material provides information necessary to determine if received signals are NQR transitions or simply noise. The operation of a lock-in detector was also demonstrated using Simulink.

INTRODUCTION

There is an increased interest in preventing terrorist attacks involving explosives and biological weapons. Currently, luggage that is checked on airplanes is sent through X-ray machines and dusted for traces of explosives. However, metal detectors and X-rays cannot detect plastic explosives. Furthermore, dusting containers for explosives and biological spores only reveals whether there is residue on the outside; it cannot detect whether these materials are sealed within the container. Clearly, there is a need for a device that can detect concealed contraband materials.

Continuous-wave spectroscopy may provide a way to detect contraband such as explosives by revealing the presence of a quadrupole resonance. Quadrupole resonance detection systems use the electrical properties of nitrogen-14 nuclei to detect materials[1]. Because of the electrostatic interaction between the electric quadrupole moment of the nucleus and the electric field gradient of the surrounding electronic charges, the nucleus has preferred orientations. An external RF magnetic field with a frequency corresponding to the energy difference between two preferred orientations will cause the nucleus to rotate. A CW spectrometer reveals the absorption of energy by the nitrogen-14 nuclei as a function of frequency.

The objective of this project was to simulate the operation of a continuous-wave quadrupole resonance spectrometer using Simulink in Matlab. This was done to aid the design of an experimental system used for studying the applications of quadrupole resonance to explosives and biological weapon detection.

This work was in part motivated by results obtained from a prototype CW spectrometer[2]. The results show that there were parasitic signals that could be confused with a QR response. Mathematical analysis was used to identify more precisely the size, shape and location of the resonances.

THE LORENTZIAN LINESHAPE

The absorption of energy by the nitrogen-14 nuclei is described by the Lorentzian lineshape[3]

$$L(\omega) = \frac{T_2^*}{\pi(1 + (T_2^*(\omega - \omega_0))^2)} .$$

(1)

The Lorentzian lineshape is centered on the resonant frequency ω_0 and its width is determined by the parameter T_2^*. This function has been normalized to have unity area, as the area under the curve represents the number of nuclei that are in the sample. The maximum value of $L(\omega)$ is $\frac{T_2^*}{\pi}$. Another important parameter of the Lorentzian lineshape is the Full Width Half Maximum, or FWHM. This

measurement is the width of the curve at a height of half the maximum. Half the maximum is $\dfrac{T_2^*}{2\pi}$, and this value is obtained at $\omega - \omega_0 = \pm\dfrac{1}{T_2^*}$, so that

$$\text{FWHM} = \frac{2}{T_2^*}. \tag{2}$$

The Lorentzian equation can be normalized to eliminate T_2^* and ω_0, which are dependent on the material of interest, for example, explosives or biological weapons. The normalized Lorentzian is defined by

$$\overline{L}(\Delta\omega) = \frac{\pi}{T_2^*} L\!\left(\frac{\omega + \omega_0}{T_2^*}\right) = \frac{1}{1 + (\Delta\omega)^2}, \tag{3}$$

where $\Delta\omega = \dfrac{\omega + \omega_0}{T_2^*}$. This is the Lorentzian which has been plotted in Figure 1, where $\overline{L}(\Delta\omega)$ is centered at 0 on the $\Delta\omega$ axis and the FWHM $= 2$.
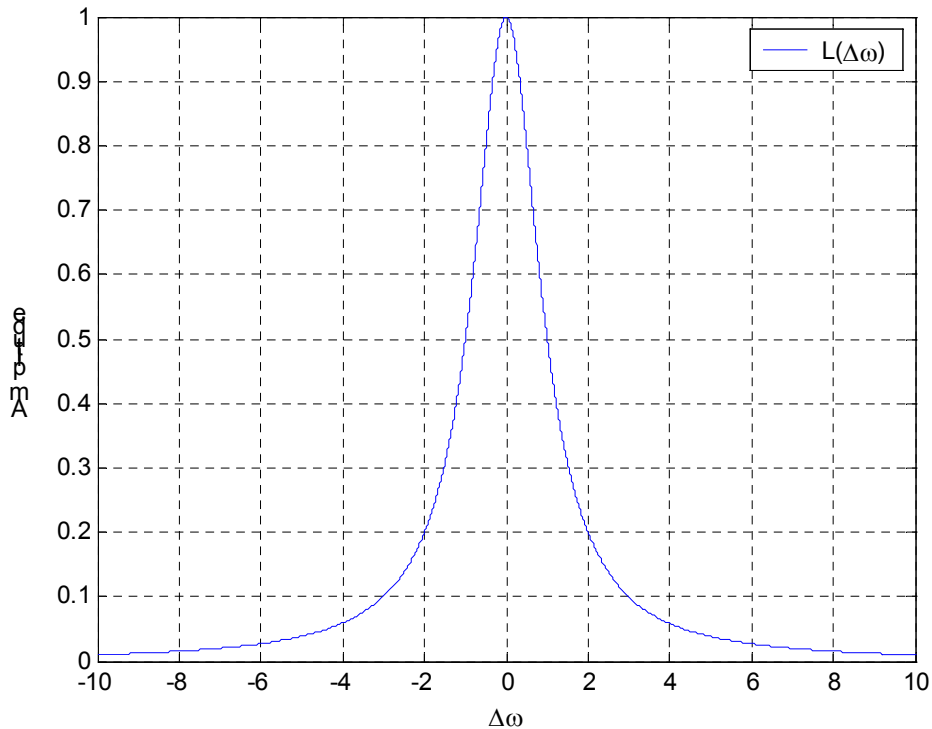
Figure 1: The Lorentzian lineshape.

CW spectrometers employing lock-in detection can reveal either the first or second derivative of the Lorentzian lineshape. Characterization of the shape of the first and second derivatives of the Lorentzian lineshape is important, as it provides information for distinguishing signal from noise in the CW spectrometer output. The first derivative is given by

$$\overline{L}'(\Delta\omega) = \frac{\Delta\omega}{(1+(\Delta\omega)^2)^2} \,, \tag{4}$$

and is shown in Figure 2.
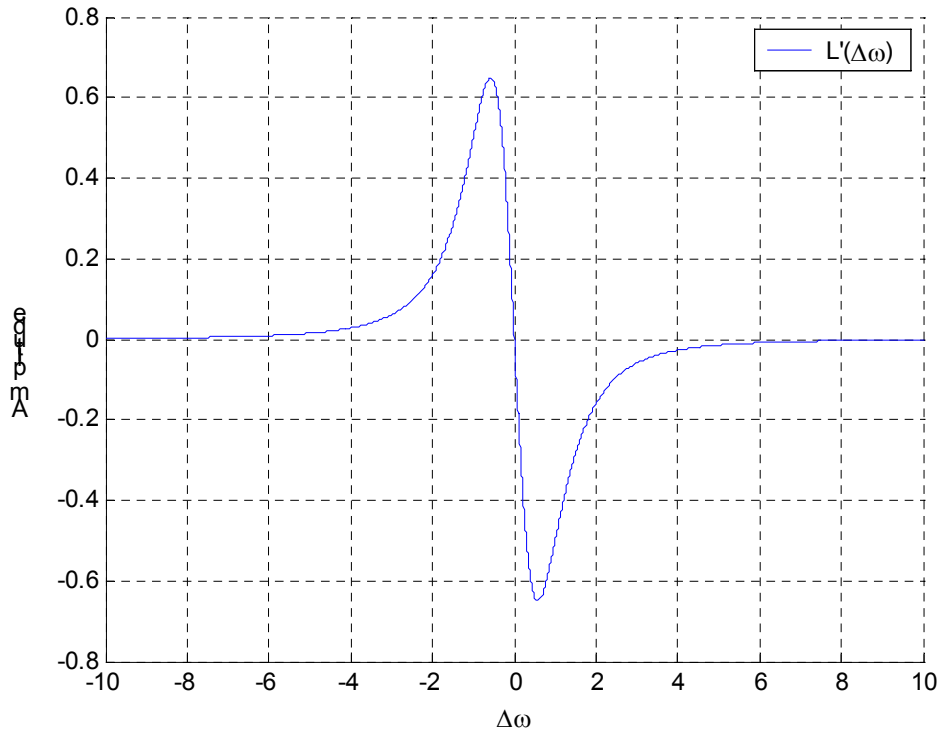
Figure 2: First derivative of the Lorentzian lineshape.

The second derivative of the normalized Lorentzian lineshape is given by

$$\overline{L}''(\Delta\omega) = \frac{\Delta\omega^4 + 4\Delta\omega^2 - 2}{(1+(\Delta\omega)^2)^4} \,, \tag{5}$$

and is shown in Figure 3.

106
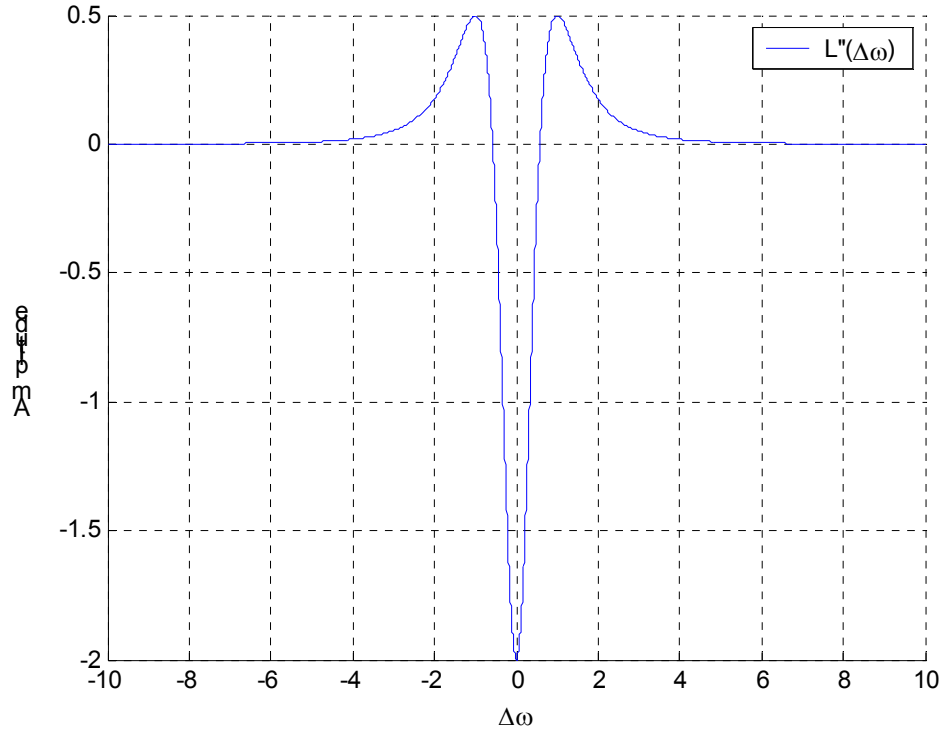
Figure 3: Second derivative of the Lorentzian lineshape.

The third derivative is also of interest as it is needed to find the maxima of $\overline{L}''(\Delta\omega)$, and is given by

$$\overline{L}'''(\Delta\omega) = \frac{-24\omega(\omega^2 - 1)}{(1 + \omega^2)^4}. \tag{6}$$

Using the second derivative, $\overline{L}''(\Delta\omega)$, it can be shown that the maxima of the first derivative are located at

$$\arg\max \left| \overline{L}'(\Delta\omega) \right| = \pm\frac{1}{\sqrt{3}}, \tag{7}$$

and $\overline{L}'(\Delta\omega = \pm\frac{1}{\sqrt{3}}) = \mp\frac{9}{8\sqrt{3}}$. The peak-to-peak value of $\overline{L}'(\Delta\omega)$ is

$$A_1 = 1.299. \tag{8}$$

107

Another important characteristic of the first derivative is $\Delta\omega_1$, which is the distance on the $\Delta\omega$ axis from the function's maximum to its minimum,

$$\Delta\omega_1 = 2/\sqrt{3} = 1.1547. \tag{9}$$

Using the third derivative, it can be shown that the points at which $\overline{L}''(\Delta\omega)$ has a local maximum or minimum are located at

$$\arg\max\left|\overline{L}''(\Delta\omega)\right| = 0, \pm 1. \tag{10}$$

The corresponding maxima satisfy $\overline{L}''(\Delta\omega = \pm 1) = 0.5$ and $\overline{L}''(\Delta\omega = 0) = -2$, so the peak-to-peak amplitude of the second derivative is

$$A_2 = 2.5. \tag{11}$$

The horizontal distance between the two local maximums in the second derivative is

$$\Delta\omega_2 = 2. \tag{12}$$

LOCK-IN DETECTOR

This section shows why lock-in detection reveals the first derivative of the Lorentzian line shape in a CW spectroscopy experiment[4]. Figure 4 shows the key components of a CW spectrometer and lock-in detector. The inductor L contains the target material. The inductor L and capacitor C form a tank circuit that determines frequency of oscillation. The voltage follower has a high impedance input that electrically isolates the limiter from the tuned circuit. The limiter feeds back a fixed signal level to sustain an oscillation. When a material with a quadrupole resonance is placed within the inductor, the level oscillation decreases as the frequency of the oscillator is varied through the quadrupole resonance.
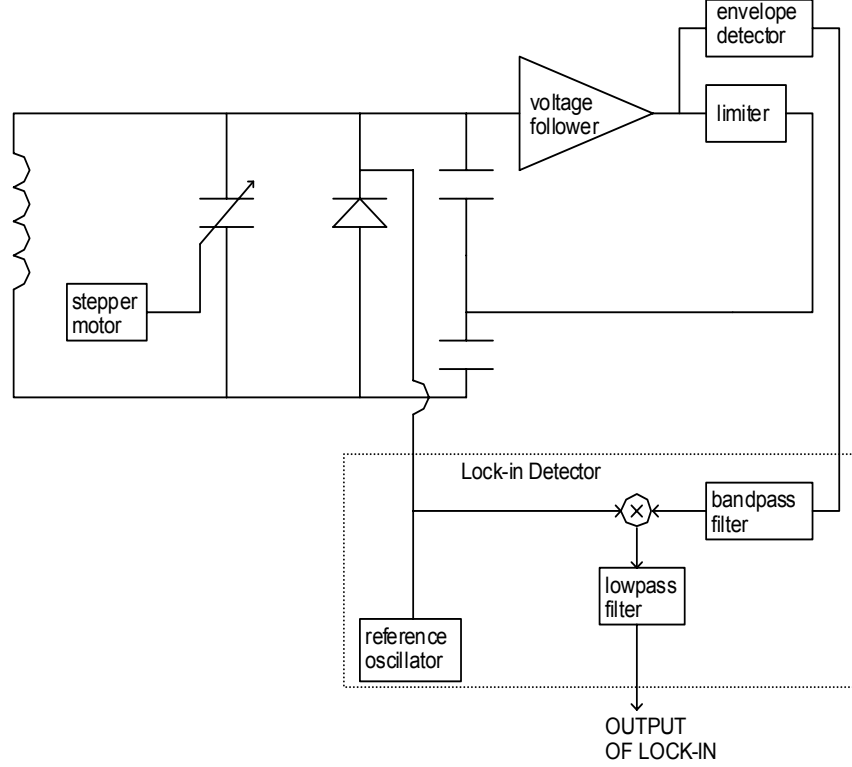
Figure 4: CW Spectrometer and Lock-in Detector.

The input to the envelope detector is $[A_0 - \alpha L(\omega(t))]\cos[(\omega(t))t]$, where $\omega(t)$ is the frequency of the oscillator, A_0 is the amplitude of oscillation in absence of a quadrupole resonance, and $L(\cdot)$ describes the absorption of energy by the nuclei. The envelope detector retains the first factor, resulting in an output of $[A_0 - \alpha L(\omega(t))]$. When $\omega(t)$ approaches the QR transition, the nuclei absorb energy and the level of oscillation decreases. Because

$$A_0 \gg \max[\alpha L(\omega(t))] ,\qquad(13)$$

and since the goal is to detect the presence of the term $\alpha L(\omega(t))$, the SNR is low. The reference oscillator produces a signal that dithers the frequency of the CW oscillator. The reference oscillator signal is multiplied by the filtered envelope signal and then low-pass filtered, removing all but the DC component. The output of the lock-in detector when the CW oscillator is tuned to ω_0 is

$$-\alpha \left.\frac{dL}{d\omega}\right|_{\omega_0} \frac{1}{2}\omega_m ,\qquad(14)$$

109

where ω_m is the variation in frequency of the CW oscillator produced by the reference oscillator. By using a stepper motor to vary C, we can change ω_0 and obtain a plot of $\dfrac{dL}{d\omega}$ as a function of ω_0.

SIMULATION RESULTS

The Simulink model, shown in Figure 5, simulates the operation of the CW spectrometer. The first sine wave source represents the reference oscillator in the lock-in detector that dithers the frequency of the CW spectrometer. The second sine wave source is identical to the first when it is desired to obtain the first derivative of the Lorentzian lineshape at the lock-in detector output. By doubling the frequency of the second source, it is possible to obtain the second derivative of the Lorentzian lineshape. The ramp represents the slow sweep of the CW frequency across a large range. The Lorentzian lineshape is modeled by a function in Simulink. The right side of the model represents the lock-in detector. Multiplying the signal by the reference sine wave and passing it through a Butterworth filter produces the output of the lock-in detector.
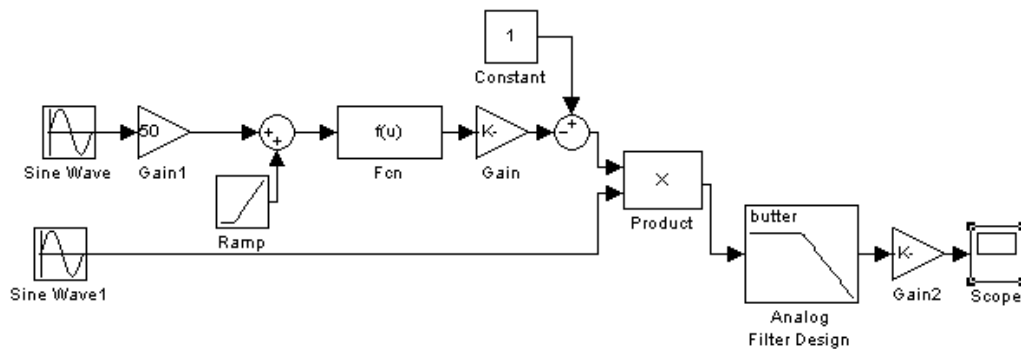
Figure 5: Simulink model of continuous wave spectroscopy.

Figure 6 shows the results from a Simulink simulation using the block diagram in Figure 5. The output of the lock-in detector is shown in Figure 6, and as expected, has the shape of $-dL/d\omega$. For convenience, the output of the lock-in detector is shown as a function of time, rather than as a function of frequency of the CW oscillator.

SUMMARY

The Simulink simulation of the CW spectrometer matched the results predicted from theory. Given a model of the CW spectrometer that can be simulated in Matlab, it is now possible to study and predict the behavior of CW detection experiments. The next step is to include noise into the simulation and observe the results. A careful study of the simulation results may lead to techniques for eliminating spurious signals in the prototype CW spectrometer.
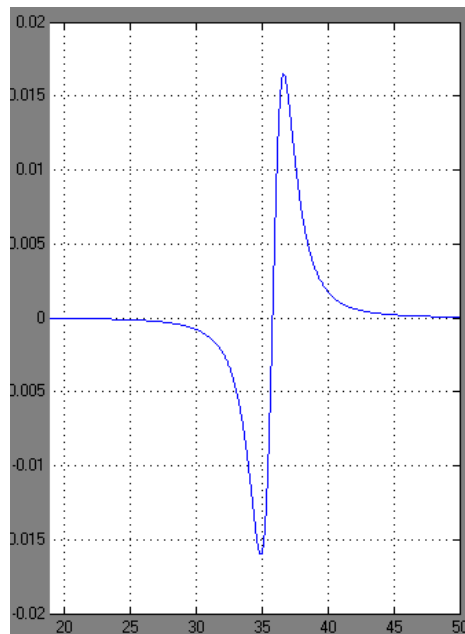
Figure 6: Results from Simulink simulation.

ACKNOWLEDGEMENTS

REFERENCES
[1]Garroway, A.N., M.L Buess, J.B. Miller, B.H. Suits, A.D. Hibbs, G.A. Barrall,   R. Matthews, L.J. Burnett. "Remote Sensing by Nuclear Quadrupole   Resonance". IEEE Transactions on Geoscience and Remote Sensing,   39:1108-1118, 2001.

[2]Hilferty, C. L. *Design and Analysis of a Continuous Wave Quadrupole Resonance Spectrometer*. Thesis, Pennsylvania State University, 2003.

[3]Smith, J.A.S. "Nuclear Quadrupole Resonance Spectroscopy: General principles". *Journal of Chemical Education*, 48:39-49, 1971.

[4]Meade, M. L. *Lock-in Amplifiers: Principles and Applications*. Peter Peregrinus Ltd., London, 1983.

SUMMARY OF PROJECTS WORKED ON IN DR. KHOO'S NONLINEAR OPTICS LABORATORY

Dean M. Kissinger*
(I.C. Khoo, Faculty Mentor)
Department of Electrical Engineering
Pennsylvania State University, University Park, PA 16802

*Undergraduate student of
Department of Electrical Engineering
Pennsylvania State University
University Park, PA 16802

ABSTRACT

The past two months I have been working on various projects in Dr. Khoo's nonlinear optics laboratory at the Pennsylvania State University. The main focus of my research was a project involving the photorefractivity of carbon nanotube doped nematic liquid crystal. As of now, I have not begun collecting data related to this project. I am a student at Penn State and will be continuing my research with Dr. Khoo's laboratory through the fall 2003 semester. While waiting for nanotube samples to be prepared by a physics research group, I began working on other projects for Dr. Khoo. One project I began working on was incoherent to coherent optical conversion using a white light source and argon laser. The second and most recent, additional project deals with polymer dispersed liquid crystal (PDLC). In the following summary, I will briefly describe the projects that I have been involved with, and the work that I have done.

INVESTIGATION OF THE PHOTOREFRACTIVITY OF CARBON NANOTUBE DOPED NEMATIC LIQUID CRYSTAL

INTRODUCTION

Nanotechnology is currently one of the most heavily researched areas of physics, chemistry, and engineering. Carbon nanotubes, in particular, are being intensely studied because of their outstanding physical an electrical properties. Their strength, conductivity, flexibility, and novel electrical characteristics make carbon nanotubes an ideal liquid crystal dopant [1]. Nematic liquid crystals are known to possess very large optical nonlinearities due to the reorientation of the director axis by an optical field [2]. Doping the liquid crystals with absorbing

dyes has been shown to greatly enhance the director axis reorientation [3]. Liquid Crystal doped with C_{60} (fullerene) also shows an enhancement of the director axis reorientation. The large birefringence of nematic liquid crystals makes them a great material for many photonic applications. Carbon nanotubes are one of the best dopants for increasing the photorefractive efficiency of liquid crystals.

Previous studies by Lee *et al.* have achieved an index-change coefficient n_2 of $\sim 10^{-1}$ cm^2/W [4]. Recently we attempted to observe this large photorefractive efficiency. Our results showed the increase in photorefractive efficiency by the addition of carbon nanotubes to the liquid crystal. The results, however, were not very consistent from sample to sample. With the results that we have previously obtained, we could not determine the actual increase in photorefractive efficiency caused by the carbon nanotubes. We postulate that the inconsistency in our results is due to inconsistencies in preparation of the samples. Another possibility is that the carbon nanotubes used in previous studies may have been bundled, causing problems with the alignment of the liquid crystals.

In this study, we will create a liquid crystal solution containing dissolved unbundled carbon nanotubes. We believe the single nanotubes will eliminate inconsistencies due to the structures of the nanotube bundles interfering with the alignment of the liquid crystals. The single nanotubes may also dissolve better than the bundles. Harte reported that liquid crystals supersaturated with carbon nanotubes required three times the field to induce the same director axis reorientation as liquid crystals without carbon nanotubes. This suggests that there is some sort of reaction between the nanotubes and liquid crystals if the nanotubes are not properly dissolved [5]. We will attempt to investigate the orientation of the liquid crystals in the samples before and after reorientation.

EXPERIMENTAL SETUP

The samples used will be E7 liquid crystal (a mixture of four nematic liquid crystals) doped with approximately 10^{-6} grams of carbon nanotubes per gram of liquid crystal. The liquid crystal will be homeotropically aligned (director axis is in the *z*-direction) between transparent (ITO coated) electrode windows. Samples will range in thickness from $10 \sim 50$ μm. A linearly polarized, 5145-angstrom continuous wave Argon-ion laser will provide two writing beams to the sample. The interference pattern of the two beams will create an intensity grating in the sample at an angle off the director axis. A linearly polarized He-Ne laser will be used to read the diffraction grating formed in the sample.

DISCUSSION

The above sections are introduction and experimental sections of the paper I will be writing through this fall about my investigation of the photorefractivity of carbon nanotube doped nematic liquid crystal. So far, I have been studying previous work pertaining to the physical properties of carbon nanotubes. Their unique mechanical and electrical properties can greatly enhance the

photorefractive efficiency of dye doped nematic liquid crystal. Previous studies in Dr. Khoo's laboratory have shown that the change in refractive index is greater with the presence of carbon nanotubes. Our theory is that the nanotubes affect the elastic constant of the liquid crystal solution, thus making it more photorefractive. We hope to validate this theory in the current study. I also believe that the concentration of nanotubes in the liquid crystal solution can affect the photorefractivity. I believe a liquid crystal solution which is supersaturated with carbon nanotubes will actually be less photorefractive than an undoped sample. In the current study, I plan to validate this theory by using samples with different concentrations of carbon nanotubes.

INCOHERENT TO COHERENT OPTICAL CONVERSION USING NEMATIC LIQUID CRYSTAL

INTRODUCTION

Incoherent to coherent optical conversion is very useful in the field of optical storage. The ability to optically induce and erase a stable birefringence in dye doped nematic liquid crystal makes for a useful optical storage material. Usually incoherent to coherent optical conversion is achieved by using a conventional spatial light modulator. The conversion can also be achieved by a holographic method. An image would be formed by the interference of two coherent plane waves, and then locally erased by incoherent light. Our method was to use incoherent light to erase the polarization and reproduce a negative coherent recreation of the incoherent image.

EXPERIMENTAL SETUP

We attempted to use several different nematic liquid samples for this experiment. I was taught how to prepare homeotropic, planar and twisted nematic liquid crystal samples. The samples I made were planar 5CB + methyl red dye doped NLC, E7 + C_{60} NLC, and E7 + CNT NLC solutions. The samples I made were 50 microns thick. I also learned to check the alignment of the samples by placing them between two crossed polarizers and observing how much light passed through. A good sample will allow no light to pass when the polarizers are crossed, and total transmission when the polarizers are aligned. Of seven samples that I prepared, four were prepared very well. It takes some practice before consistent samples can be easily prepared.

Our incoherent light source was a white light Hg lamp. We passed the light through a linear polarizer which was vertically aligned. The linear polarized light was then expanded and focused on our image plate, a set of horizontal bars. After the image, the light was focused into a small (~1 mm diameter) spot on the liquid crystal sample. The liquid crystal sample was aligned 45 degrees off vertical to enhance the reorientation of the director axis of the liquid crystal. Finally, the light passed through a linear polarizer aligned horizontally before reaching an intensity sensor. An argon laser was focused onto the image plane

and focused onto the same spot of the liquid crystal sample as the incoherent light was. A vertically polarized He-Ne laser was focused onto the sample at the spot of the incoherent light and argon laser to read the image formed in the sample.

The sample was exposed to the incoherent light and the argon laser simultaneously. This allows for the simultaneous formation and erasure of the polarization anisotropy in the sample.

DISCUSSION

In this experiment, we were supposed to observe an image formed by the He-Ne laser passing through the sample at the point where the incoherent and coherent light were simultaneously forming and erasing the polarization. After using several samples, we observed no image at the sensor. We also attempted to observe a change in intensity of the He-Ne laser at the sensor when the argon laser was blocked from focusing on the sample. The He-Ne laser was supposed to be more intense at the sensor when both the Hg lamp and argon laser were focused on the sample. We observed no change in intensity of the He-Ne laser.

We went through several steps to troubleshoot our experimental setup. First, we checked the polarization of the two lasers and the incoherent source. The beams were all correctly polarized, and focused at the same point. Next, we tried focusing the Hg lamp and argon laser on a larger image. Our reasoning was that there would be a larger area of polarization change in the sample. We again attempted to use several different samples and observed no image or change in intensity of the He-Ne laser. At that point, we began to wonder if our incoherent light source was intense enough to have any affect on the sample. After measuring the intensity of the incoherent Hg lamp at the sample, we determined that it was intense enough to have an effect on the liquid crystal sample.

Currently, we are evaluation our experimental set up and sample preparation. We are thinking of reasons why the experiment yielded no results. One theory is that we have to project an image of a sinusoidal grating on the sample in order to have simultaneous formation and erasure. Another possibility is the orientation of the sample, and the angle between the incoherent light/argon laser and the He-Ne laser.

POLYMER DISPERSED LIQUID CRYSTAL

The newest project I've been working on is the investigation of polymer dispersed liquid crystals. A liquid crystal solution is cured in optical glue using ultraviolet light. The liquid crystal droplets are arranged in a regular crystalline pattern in the cured polymer. Within the past few days we have been able to arrange the liquid crystal droplets in a crystalline structure in a 50 micron thick liquid crystal sample. The presence of the three dimensional structure was identified by the change in color on the surface of the liquid crystal sample. The sample reflected multiple colors when rotated in front of a light source.

The structure was formed using a two wave mixing process. In the near future we are going to construct a four wave mixing experimental setup to

produce crystal structures in PDLC. We are also interested in producing crystal structures in thicker (~100 micron) liquid crystal samples.

ACKNOWLEDGEMENTS

REFERENCES
1. R. Saito, G. Dresselhaus and M. S. Dresselhaus, *Physical Properties of Carbon   Nanotubes* (Imperial College Press, London 1998).
2. I. C. Khoo *Liquid Crystals: Physical Properties and Nonlinear Optical Phenomena.* New York, NY: Wiley Interscience, 1994.
3. I. C. Khoo, H. Li, and Y. Liang, "Optically induced extraordinarily large negative orientational nonlinearity in dye-doped liquid crystal," *IEEE J. Quant. Electronics,* vol. 29, pp. 1444-1447, 1993.
4. W. Lee and C. S. Chiu, "Observation of self-diffraction by gratings in nematic liquid crystals doped with carbon nanotubes," Opt. Lett. 26, 521-523 (2001).
5. A. Harte, "Liquid crystals allow large-scale alignment of carbon nanotubes," *Cal Tech CURJ,* pp. 44-49, Nov. 2001.

AC MODULATION OF STIMULATED ORIENTATIONAL SCATTERING IN NEMATIC LIQUID CRYSTALS
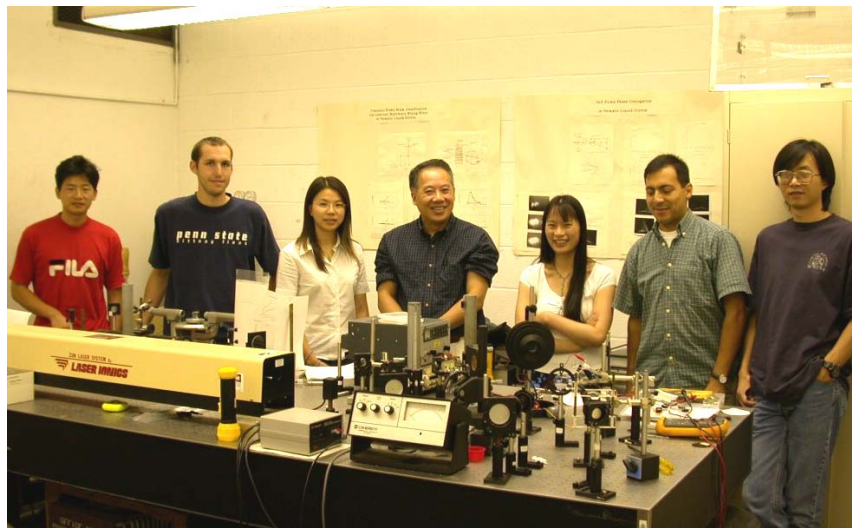
Xiao-Shan Tao[*]
(I.C. Khoo, Faculty Mentor)
Department of Electrical Engineering
Pennsylvania State University, University Park, PA 16802

[*]Undergraduate student of
Department of Computer and Electrical Engineering
Cornell University, Ithaca, NY 14850

ABSTRACT

   Laser induced dynamic grating and optical wave mixings in nonlinear optical media have been studied under various contexts, among which Stimulated Orientational Scattering (SOS) is a new research topic. SOS is a process that a weak scattered noise grows into a strong signal via the interaction between the coherent laser beams and nematic liquid crystal director. Some detailed theoretical analysis for steady state SOS effect has been studied in the past years. Active research is still carried on to both steady-state and dynamic analysis on the SOS effect of the liquid crystal materials.

In this report, I will present both experimental results and preliminary explanation on how AC modulating field affects the interaction between laser beams and nematic liquid crystal director. Specifically, frequency and magnitude modulation effects will be discussed in detail.

INTRODUCTION

Liquid crystals (LC) have long been recognized as nonlinear optical materials because of their particular physical properties, namely, their large dielectric anisotropy and broadband birefringence.[1] A linearly-polarized laser impinging on a LC sample will induce a rearrangement of the molecules; and thus changes its director axis[1], i.e., as shown in Figure 1. Among various LCs, nematic liquid crystal (NLC) is the only LC that used in SOS experiments due to its unique molecular structure[2] and large nonlinearity, which allows the reorientation of the director axis and requires a low power laser.
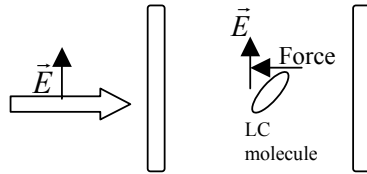

Figure 1. The director axis is changed under the torque induced by electric field

SOS is a two-beam coupling effect describing the interaction between the transmitted pump and generated signal beams induces a dynamic grating in NLC sample, through which the energy transfer from the input beam to the scattered beam takes place. In other word, under appropriate condition, a laser beam incident on NLC would result in diminish of the transmitted e-wave and the amplification of generated o-wave.[3] Theoretically, if we employ thick sample and long enough interaction length, we can achieve complete polarization conversion. The basic idea of SOS is shown in Figure 2.
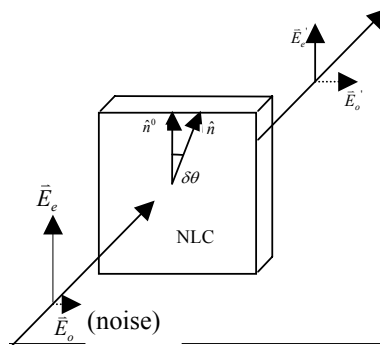
Figure 2. Basic theory of SOS

---

[1] LC molecules are aligned in a general direction defined by a unit vector $\hat{n}$, so is called "director axis."
[2] Detail information of NLC molecular structure is referred to Chapter 3 of Reference [1].
[3] E-wave: extraordinary wave, which the direction of electric field is parallel to the optical axis;
  O-wave: ordinary wave, the direction of electric field is perpendicular to the optical axis.

SOS is a new topic in optics; it has many potential applications. For example, it can be used as broadband polarization converter, because the energy is transferred from one polarization to the other. AC filed modulation can enhance the threshold; and thus, triggers the SOS effects at lower input power. It is also a good object for chaotic analysis because of the abundant dynamic behaviors of NLC materials under intense optical waves.

Base on the previous work on SOS, we discovered that the generated signal would be modified with an AC field applied on the sample. In the rest of this report, I will present the experimental results of AC field modulation of SOS on NLC. In other words, relevant parameters and various relationships involve will be examined, such as the frequency as an input parameter and the input and output relationship.

EXPERIMENTAL DESCRIPTION

There are two parts involved in preparing the SOS experiment, namely, sample preparation and equipment setup.

1. NLC Samples Preparation

Our sample is made up of four components: two pieces of optical glasses, one plastic spacer (250μm thick), two pieces of 0.4x5cm foil, and pure liquid crystal E7 (from EM Chemicals). The followings are the key steps of making an NLC sample for AC field effects in SOS:

i.   Clean the optical glasses, plastic spacer, and the foil with ethyl alcohol;

ii.   Wrap the two sides of the plastic frame with foil such that the distance between the foil is ~4mm as shown below;
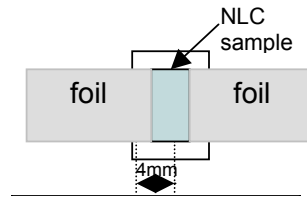

Figure 3. Cross section of NLC sample

iii.   Carefully put 3~4 drops of E-7 sample inside the plastic frame;

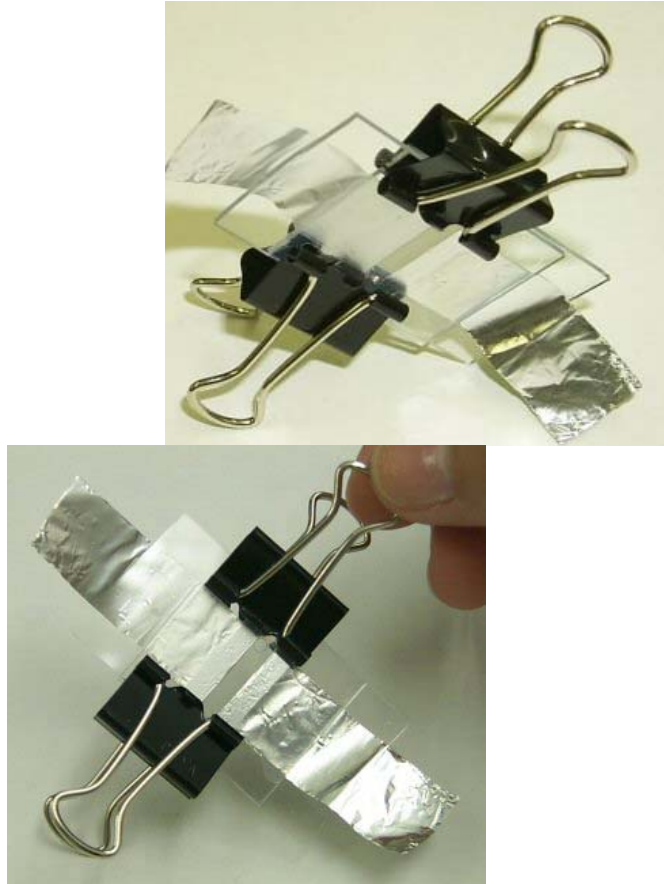iv.   Clip the two sides of the glasses so that the sample looks as in Figure 4.

Figure 4. NLC samples in "AC field effect on SOS" experiment

2. Experimental Setup

In order to observe the input-output relationship of the SOS effect, we require optical equipments which can continually change the wave intensity and the polarization direction which include argon laser, linear polarizer, beam-splitter, focus lenses, and detectors (which are connected to an oscilloscope for observing the output). The Argon laser irradiates a beam on an analyzer-polarizer to ensure the appropriate beam intensity and polarization. The tight focus lens (focal length 10mm) converge the beam on the NLC sample. The second lens is used to collimate the output beam. After the lens 2, the e- and o- waves are separated by the polarizing beam splitter (PBS) and goes to respective detectors. Each experiment was setup distinctively for examining different effects of the AC field on sample. The general setup is shown in Figure 5.
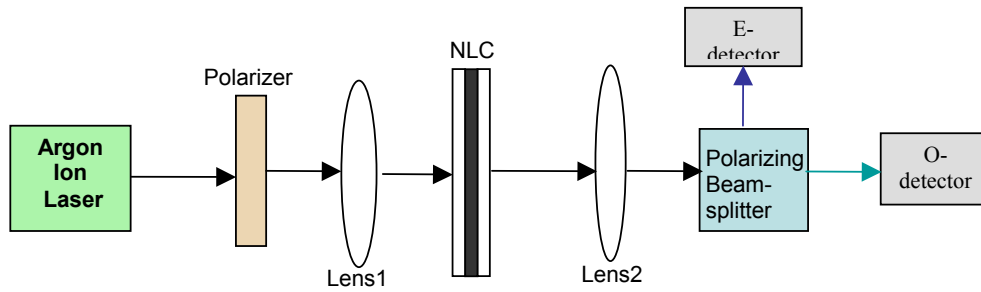
Figure 5. General SOS experiment setup

a. Frequency Modulation

In this experiment, we examined how the frequency modulation in input would affect the output. Thus, we would only measure the change of e-wave because o-wave simply has the inverse relationship. In that case, o-wave detector could be replaced by an absorber. Throughout the experiment, input intensity and the AC field remained constant. E-wave detector would be connected to the oscilloscope and the average values of the e-wave output would be recorded.

b. AC Field Modulation

Due to the fact that long exposure of the sample under the heat produced by the laser would destroy the molecular structure sample, a screen was used to block the laser from the sample between every datum recorded.

In this part, both e- and o-wave detectors were used for measuring the outputs. Since we need to examine the relationship between input and output, we would require another detector to detect the power of the input after the first polarizer. However, inserting a detector between two components would block the beam. As a result, we used an optical glass as partial reflector to achieve this, as shown in Figure 6.
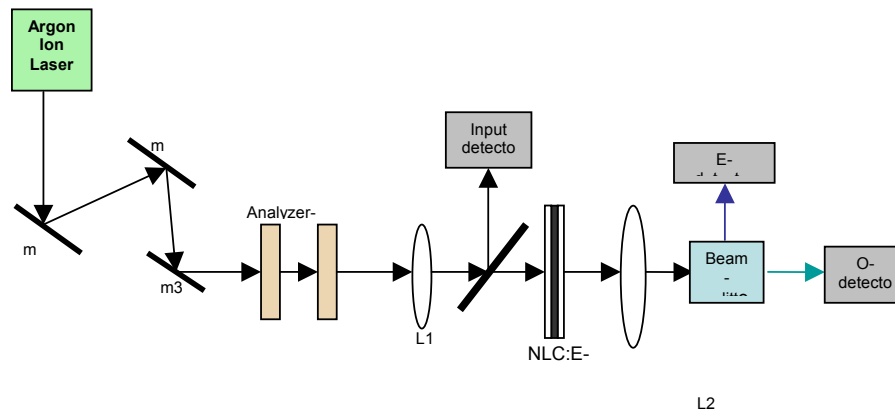
Laser: CW Argon Ion laser, wavelength 0.532µm;

121

NLC: Planar[4], 250μm, viscosity coefficient 0.07 poise, bending elastic constant 3.0×10^{-12} N, refractive indices $\hat{n}_e \sim 1.75$ and $\hat{n}_o \sim 1.54$;

L1,2: Focusing Lens, diameter ~ 30 mm;

Figure 6. Setup for examining the output interference[5]

RESULTS

1. Frequency modulation

Starting from frequency ~ 5Hz, twenty pieces of data with incremental size of 5Hz were collected. The five figures shown below are several Fourier Transform (FT) of the outputs. In this part, only e-wave (the signal) was detected. Figure 7a is the FT of which there was no AC field applied. Figure 7b and 7c are two typical FT's when inputs were below threshold; while Figure 7d and 7e are FT's of which inputs were above threshold.
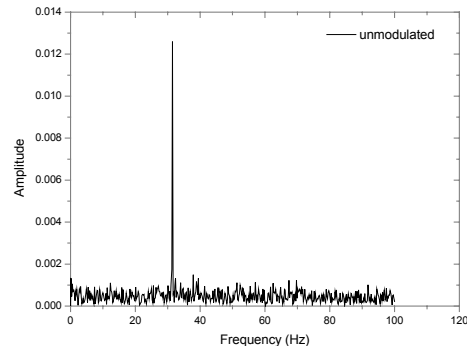
Figure 7a E-Output without applying AC field

---

[4] Planar: NLC molecules align parallel to the optical cell
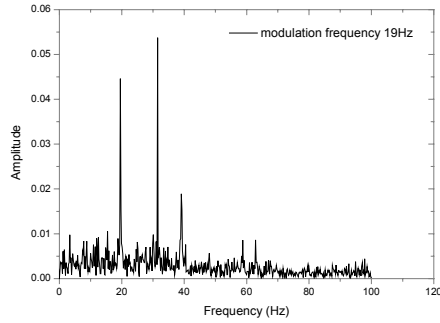
Figure 7b FT at Modulated Freq = 19Hz
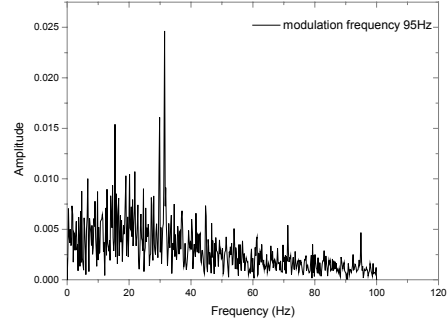
Figure 7c FT at Modulated Freq = 95Hz
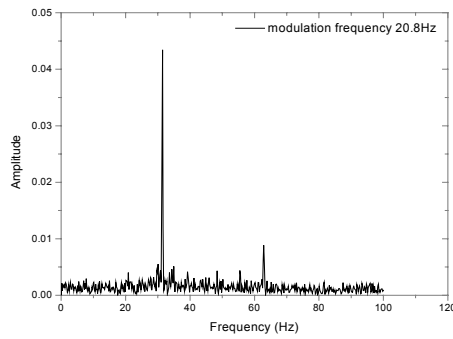
Figure 7d FT at Modulated Freq = 20.8Hz
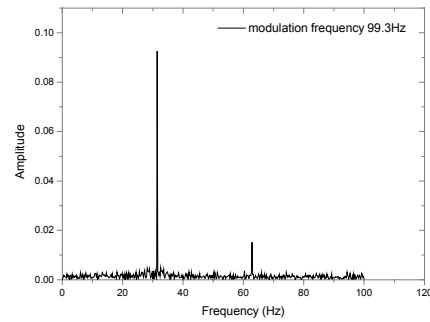
Figure 7e FT at Modulated Freq = 99.3Hz

2. Input vs. Output with AC Field Modulation

With parameters AC field voltage=120V, gap distance of foil=3mm, we had AC field strength = 4×10^4 V/m. Applying AC field to the two setups shown in Figure 8a and b, the following results were obtained:
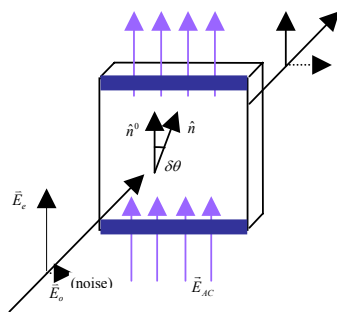
Figure 8b. Case II: $\vec{E}_{AC} \perp \vec{E}_e$
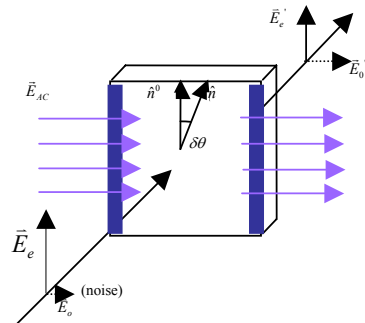
Figure 8a. Case I: $\vec{E}_{AC} // \vec{E}_e$

I. AC modulation field is parallel to input laser polarization

Figure 9a and 9b are the theoretical and experimental results showing the relationship between input and two output beams when AC field is applied parallel to the input laser polarization (Figure 8a).
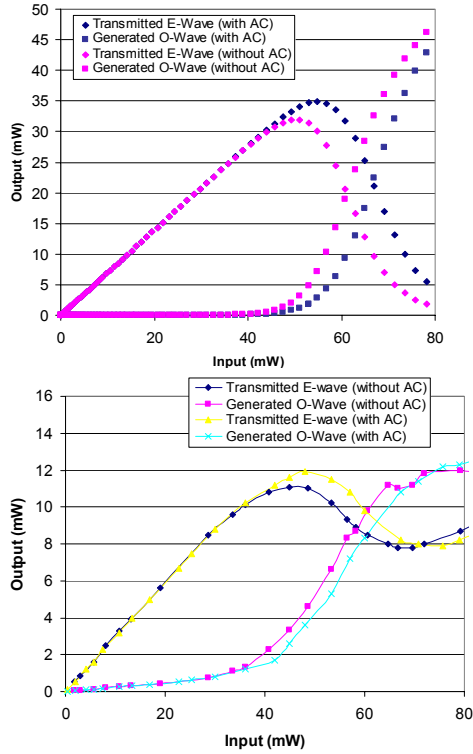
Figure 9a. Theoretical outputs of AC AC modulation effect

Figure 9b. Experimental results of the modulation effect

II. AC modulation field is perpendicular to input laser polarization

Figure 10a and 10b are the theoretical and experimental results when the AC modulation is applied perpendicularly to the input polarization (Figure 8b).

124
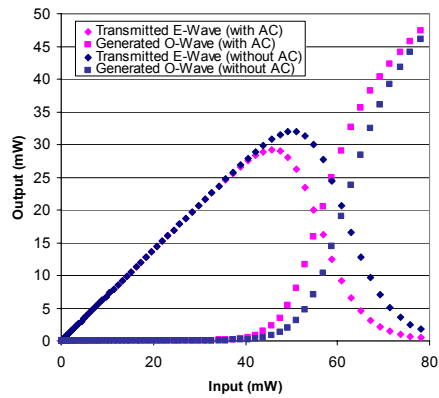
Figure 10a. Theoretical results   Figure 10b. Experimental outputs
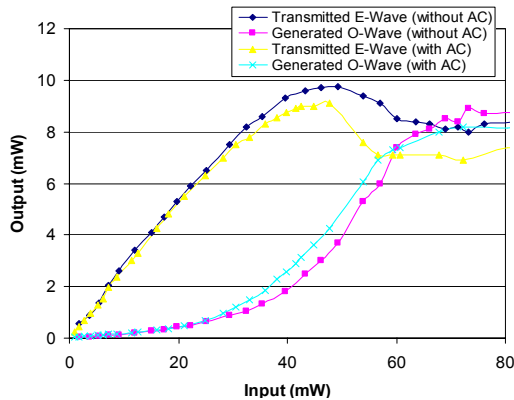
DISCUSSIONS

Using the setup shown in Figure 6 and the given parameters, Figure 7a indicates the system had a resonant frequency at ~30Hz. Input laser intensity was unchanged throughout this experiment. With the appliance of the modulation field, a similar spectrum pattern was observed with the variation of the modulation frequencies. Specifically, the generated output beam oscillates mostly around 30Hz, which is the dominant oscillating frequency of the NLC director. Further research on this experiment is still carrying on.

Previous works[6] indicated that below threshold, both the transmitted e- and o-wave are "linearly dependent on the input power;" while above the threshold, o-wave "grows exponentially" and "eventually surpasses the power of the transmitted e-wave."[3] In this experiment, we examined the AC modulation effects on SOS. In other word, AC field would affect the NLC director reorientation and enhance or hamper the SOS effect depending on the direction of the AC field applied. All experiment results agreed well with the theoretical works. As shown in Figure 9a and 9b, when AC modulation field is applied parallel to input laser polarization, the field weakens the scattering. In other word, the input value where two output beams intersect (so called

---

[6] Threshold ≈ 60mW in our experiment, where sample thickness is 250μm and laser wavelength is 0.532μm.

"threshold") would increase, which means higher input power is required. In contrast, perpendicularly applying AC field would enhance the SOS effect, i.e., reduce the threshold.

CONCLUSION

I have presented the experimental results of AC modulation on SOS effects.[7] Experimental results of frequency modulation effects agree well with the previous theoretical works. The generated output beam of our system oscillates primarily around 30Hz.

Furthermore, anterior simulation anticipated AC modulation would have influence in SOS. Our experiments have proved that AC field modulation could either enhance or weaken the SOS effect, depending on the relative direction of the beam polarization, NLC director, and the electric field. That is, perpendicularly applying AC field would lower the threshold, and vice versa.

ACKNOWLEDGEMENT

REFERENCES

1. I.C. Khoo. *Liquid Crystals: Physical Properties and Nonlinear Optical Phenomena.* John Wiley & Sons, Inc. New York, NY 1995
2. I.C. Khoo, Yu Liang, and H. Li. "Observation of stimulated orientational scattering and cross-polarized self-starting phase conjugation in a nematic liquid-crystal film," *Optical Letters*, Volume 20 No. 2, January 1995
3. I.C. Khoo and Y. Liang "Stimulated orientational and thermal scatterings and self-starting optical phase conjugation with nematic liquid crystals," *Physical review E*, Volume 62 No. 5, November 2000
4. I.C. Khoo and J. Ding. "All-optical cw laser polarization conversion at 1.55μm by two-beam coupling in nematic liquid crystal films," *Applied Physics Letter*, Volume 81 No. 14, September 2002
5. J. Ding. Master thesis, (2003), Penn. State University, Electrical engineering Department
6. J. Ding. MS Presentation "*Stimulated Orientational Scattering in the Nematic Liquid Crystals,*" 2002.

---

[7] Theoretical deviations of SOS are referred to References [5] and [6].

ELECTROMECHANICAL PROPERTIES OF PIEZO-ELECTRIC THIN FILMS BY OPTICAL INTERFEROMETRY

Amanda Skrabut*
Johm Y. Fu (Graduate Assistant) and Dr. Ruyan Guo (Faculty Mentor)
Department of Electrical Engineering
The Pennsylvania State University
University Park, PA 16802

*Undergraduate Student of the Department of Electrical Engineering at The Pennsylvania State University

ABSTRACT

This research project focus on precision determination of electric field induced strain in a thin film sample due to piezoelectric effect. When dimension change of a sample results in development of an electric field it is known as piezoelectric effect; or conversely an applied electric field to a sample resulting in a change in the sample dimension is known as converse piezoelectric effect. It remains as a challenge to directly measure the displacement of a thin film sample as the displacement is typically in the order of sub nanometer for films of a few hundred-nanometer thick. The optical interference technique that utilizes amplitude modulation and phase-lock will be used to measure the low level displacement. Such measurements are important for electromechanical transduction and sensor application.

In this project, a single beam optical interferometer will be constructed to study $Pb(Zr,Ti)O_3$ (PZT) thin films. It will then be of particular interest to compare the effects of the polycrystalline thin films with single crystal thin films. The single crystal thin films have only been recently available by MBE technique.

INTRODUCTION

When a mechanical stress is applied to a non-conducting substance, a voltage is produced between the two surfaces. This phenomenon known as the piezoelectric effect occurs in certain crystals, quartz and Rochelle salt and ceramic materials. This property can also have a converse effect; a voltage difference can be applied over the surfaces resulting in a distortion of the material.

The piezoelectric effect is an important area of study because it is used in many significant products today such as transducers, phonograph cartridges, microphones and strain gauges. In these products, a mechanical input is used resulting in a voltage. The converse effect can also be observed in products such as earphones and ultrasonic radiators where a voltage is used to produce a mechanical output.

When dealing with the converse effect, there are numerous methods with differing advantages to measure the strain of the material. One quick and easy solution is to use mechanical devices. However, with the need of high precision in these products this poses a problem. In this experiment the laser interferometer technique is being used which can increase the accuracy of strain measurements from an order of about 1µm for mechanical devices to about 10^{-3}Å.

In this experiment, the piezoelectric coefficient will be determined for a PZT ceramic, an unpolarized PZT thin film crystal and a polarized PZT crystal thin film under different driving frequencies. Although the PZT ceramic piezoelectric coefficients have been found before, the coefficients of the PZT crystal thin film have not been found since it was fabricated in Motorola in 2002. The results obtained show that the piezoelectric coefficients of the d33 are different from the crystal thin film and to the best of our knowledge are the first time that they are measure.

OPTICAL INTERFEROMETER MEASUREMENT

The laser interferometer technique uses the resulting intensity of a monochromatic beam of light that has interfered with a reference beam to measure the strain. For a laser with wavelength λ, the interference light intensity at a detection point is[1,2,3]

$$I = I_P + I_R + 2\sqrt{I_P I_R}\cos\left\{\frac{2\pi}{\lambda}(2\Delta l)\right\},$$

128

where I_p and I_r are the light intensities of the probing beam and the reference beam, and Δl is the length difference of these two beams. The maximum and minimum intensity values occur when $\cos\left\{\dfrac{2\pi}{\lambda}(2\Delta l)\right\} = 1$ and $\cos\left\{\dfrac{2\pi}{\lambda}(2\Delta l)\right\} = -1$, respectively and are given by

$$I_{MAX} = I_P + I_R + 2\sqrt{I_P I_R},$$
$$I_{MIN} = I_P + I_R - 2\sqrt{I_P I_R}.$$

A difference between the two beams, Δl, results in interference in the beams of light which can either add constructively or destructively, changing the intensity of the light. Since these changes in light correspond to such small displacements, intensity measurements should be taken at $\Pi/2$ points of the sinusoid which correspond to a path length difference of $(2n+1)\lambda/8$. At these points, shown in Figure 1, the light intensity change is maximized since the derivative is at its maximum and increases the sensitivity of the system. To further
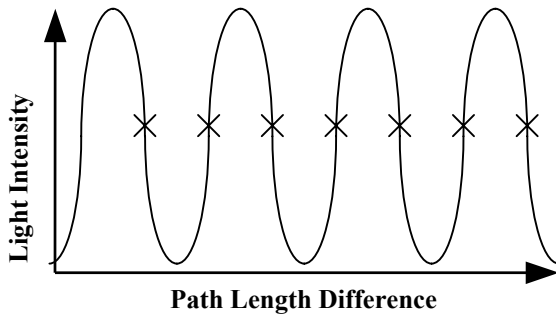
Figure 1: $\Pi/2$ points

improve the sensitivity of this system, a lock-in amplifier is used to reject noise of mechanical vibration and air turbulence. Near these $\Pi/2$ points the displacement can be written as

$$\Delta l = l_{AC} + (2n+1)\frac{\lambda}{8},$$

and the intensity can now be expressed as

$$I = \frac{1}{2}(I_{MAX} + I_{MIN}) \pm \frac{1}{2}(I_{MAX} - I_{MIN})\sin\left[\frac{2\pi}{\lambda}(2l_{AC})\right],$$

When I_{AC} is small,

$$\sin\left[\frac{2\pi}{\lambda}(2l_{AC})\right] \approx \frac{2\pi}{\lambda}(2l_{AC})$$

and the intensity can be written as

$$I = \frac{1}{2}(I_{MAX} + I_{MIN}) \pm \frac{1}{2}(I_{MAX} - I_{MIN}) \left[\frac{2\pi}{\lambda}(2l_{AC}) \right] \text{ or}$$

$$I = I_P + I_R + 2\sqrt{I_P I_R} \cos\left\{ \frac{2\pi}{\lambda}(2\Delta l) \right\}. \qquad (1)$$

The AC signal can be further simplified by just using the positive sign in front. Since the $\pm$ is only dependant on whether n is even or odd, and when this signal is sent through the Lock-in amplifier only the AC component is detected the sign is not a problem if the maximum value is only considered. To find the so-called $\pi/2$ points, we use scanning reference beam method. The principle of this method is as follows: the optical path length of the reference beam is controlled by that piezoelectric driven mirror, to change periodically for more than one wavelength distance. As a result, the interference intensity is modulated by phase shifts in both the reference and the probing beams. Where $\Delta l = l_{AC} + l_{SCAN} + (2n+1)\frac{\lambda}{8}$. and l_{scan} is the length difference in reference beam caused by the scanning of the piezoelectric driven mirror. The intensity can now be simplified to

$$I = I_P + I_R + 2\sqrt{I_P I_R} \left\{ \cos\left[\frac{2\pi}{\lambda}(2l_{SCAN}) \right] + \left[\frac{2\pi}{\lambda}(2l_{AC}) \right] \sin\left[\frac{2\pi}{\lambda}(2l_{SCAN}) \right] \right\}$$

From the above equation, the maximal modulation position can always be reached at

$$\frac{2\pi}{\lambda}(2l_{SCAN}) = (2m + \frac{1}{2})\pi$$

Because, at this point, $l_{SCAN} = \frac{\lambda}{4}(2m + \frac{1}{2}) = \frac{\lambda}{8}(4m+1) = \frac{\lambda}{8}(2n+1)$.

For a sinusoidal displacement, $l_{AC} = l_0 \cos \omega t$, the optical signal is converted by a photo-detector to voltage signal. This voltage signal is detected by a Lock-in amplifier as V_{OUT} corresponding to the displacement $l_0/\sqrt{2}$. Therefore

$$l_0 = \frac{\lambda}{\pi\sqrt{2}} \frac{V_{OUT}}{V_{P-P}}$$

where V_{P-P} is the peak-to-peak value of the interference signal, which correspond to the change in the interference signal ($I_{MAX} - I_{MIN}$).

130

For piezoelectric coefficient d_{33}, we have formula,

$$\frac{\Delta l}{l} = d_{33} E \qquad\qquad (2)$$

and when Δl is substituted with l_0, E with $\dfrac{V_{Lock-in} \sqrt{2}}{l}$ in Eq. (2), we get

$$d_{33} = \frac{1}{V_{Lock-in}} \frac{\lambda}{2\pi} \frac{V_{OUT}}{V_{P-P}} = \frac{l_0}{V_{Lock-in} \sqrt{2}}$$

EXPERIMENTAL SETUP

The setup for the experiment is shown below in figure 2. A 630Å laser is reflected off a mirror and then passed through an apparatus that blocks the edges of the laser beam. This step ensures that the intensity of the laser is uniform. The laser then continues on and is passed through a beam splitter which, as the name says, splits the beam into two beams of equal intensities. One beam is passed through the splitter onto the sample and the other is reflected to the piezoelectric mirror where both lasers travel paths of equal length. The beams are then recombined again at the beam splitter and the intensity is gathered at the photo-detector. Since these values are obtained from interference of a laser, they are very sensitive and need to be taken in a quite area free of air turbulence. The values taken in this experiment were taken from midnight to about six in the morning to avoid disruption.

To avoid further error in the experiment, it is very important to pay particular attention the placements of these apparatuses. The purpose of the first mirror's location is to protect the stabilization of the laser and needs to be placed before the beam splitter. The mirror redirects the laser path so that when reflections occur off the beam splitter, sample and piezoelectric mirror, it does not reflect back to the laser and interfere with laser intensity, but to the mirror instead. The locations of the piezoelectric mirror and the sample are also of importance. They need to be located as close to the beam splitter as possible so that the true beam is reflected back and
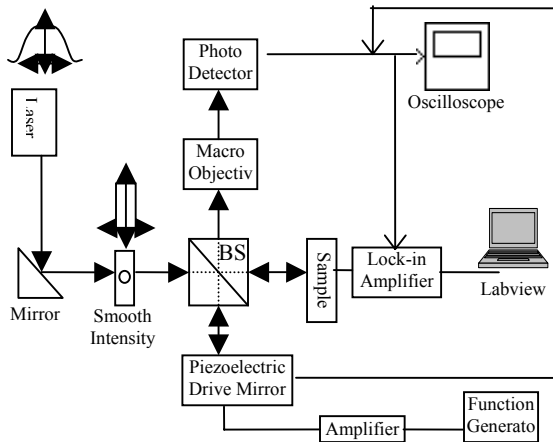

Figure 2: Experimental Setup

131

not a beam of different intensity. It is also important to make sure that these objects are oriented so that they pass the laser parallel to the table surface you are working on so that the laser is reflected properly and with the right intensities. If everything is set up correctly, the laser should reflect off the piezoelectric driven mirror and sample and be recombined at the beam splitter with the same phase and intensity as the original beam.

After the initial setup is complete, a varying voltage is applied to the piezoelectric mirror. This drives the mirror to slowly oscillate in the direction of the mirror changing periodically. This oscillation should occur for more than one wavelength distance as shown in figure 3 and creates a constant change in the path lengths of the two beams. The path length difference being controlled by the piezoelectric driven mirror, results in constructive and destructive interference of intensities when the beams unite at the beam splitter.

Once these beams are combined at the beam splitter, the laser travels though a macro objective, which enlarges the spectra. This light then is shined onto the photo-detector where the optical signal is converted to a voltage signal. This voltage signal is detected by a Lock-in amplifier as V_{OUT} which is an rms value of the detected intensity signal. The lock-in amplifier is used to obtain these values because it helps reduce the noise that may occur otherwise.

To obtain these voltage readings, a data acquisition device is connected to the output of the lock-in and then to a laptop where a program called LabView is used. A schematic of the program created by Youwei Fu that was used is included in appendix A. A. Once the data is obtained from labview, the average value of the maximum peaks is calculated from a program created in MATLAB included in Appendix B. A maximum and minimum value was set for each set of data to avoid including the second maxima points caused by the displacement direction in the average.

Figure 3: The displacement inflection point occurs at a point besides the maximum and minimum creating a second maximum peak
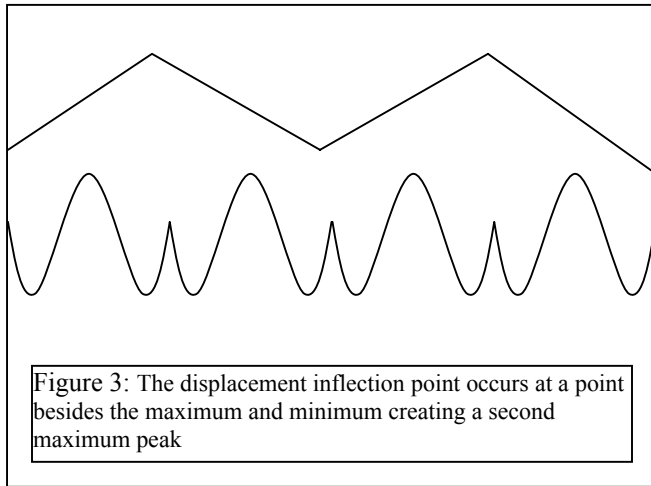
RESULTS

The PZT ceramic thin film had measurements taken at a driving voltage of 1V. As the Figures 4 and 5 illustrate, the ceramic has piezoelectric coefficients and displacements that decrease as the frequency increases most of the time. There are cases however at frequencies, such as 110 Hz, where the coefficient or displacement increases instead of decreasing resulting in a spike in the graph. Both the non-polarized crystal sample and the polarized crystal sample in figures 8 and 11 seem to have a much smoother graph that is constantly decreasing. This is because the PZT crystals are much denser and therefore would have a more uniform structure. When the polarized crystal thin film piezoelectric coefficients are compared to the ones from the ceramic thin film in figure 7, it seen that the ceramic thin film has higher piezoelectric coefficients for the frequencies shown. The ceramic thin film however, was expected to have lower coefficients than the crystal at lower frequencies, but the instrumentation did not allow for these low frequencies to be tested. When the ceramic thin film was tested a 1Hz, an accurate reading could not be read and the testing had to start from 5Hz making the lower frequencies incomparable.

Figure 4. Relationship between the driving frequency and the displacement.

Figure 5. Relationship between the driving frequency and the piezoelectric coefficients.

Figure 6. Relationship between the driving frequency and the displacements.

Figure 7. Relationship between the driving frequency and the piezoelectric coefficients.

The next testing that was done was on a crystal thin film that was previously polarized. This sample was tested with a driving voltage of 5V. The same voltage could not be used as was on the ceramic sample because the data unreadable.   The interferometry method that was used has a maximum measurement of about 130Å. The 1V applied to this sample probably caused the displacement of the sample to be out of this range and a higher voltage was needed.

Figure 8. Relationship between the driving frequency and the displacements.

135
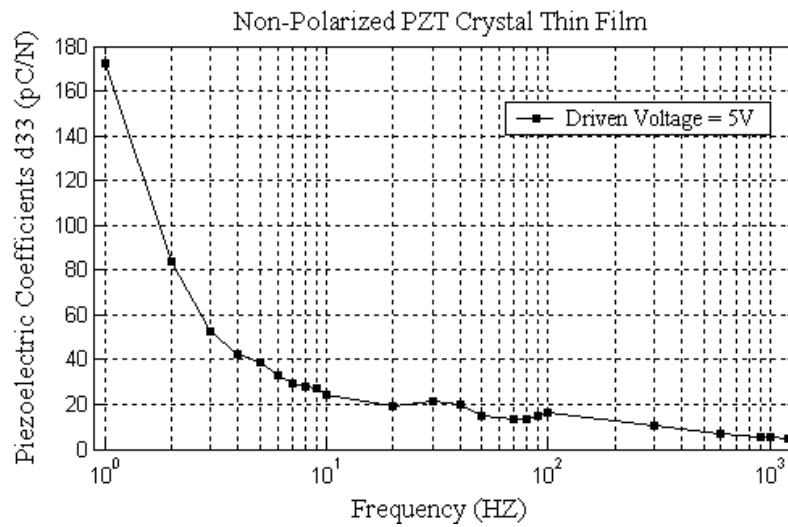
Figure 9. Relationship between the driving frequency and the piezoelectric coefficients.

The last sample to be tested was the polarized thin film crystal. For reasons stated earlier the driving voltage used for this sample was 2V. As shown in figures 10 and 11 the, this sample has had the smoothest results yet. The displacement and piezoelectric coefficients are at a constant decrease as the frequency is increased to around 10Hz. After 10Hz the sample approximately has the same piezoelectric coefficient and displacement. When the polarized sample is compared to the non-polarized sample in figures 12 and 13 it seems that the polarized sample has a much higher piezoelectric coefficient and displacement.
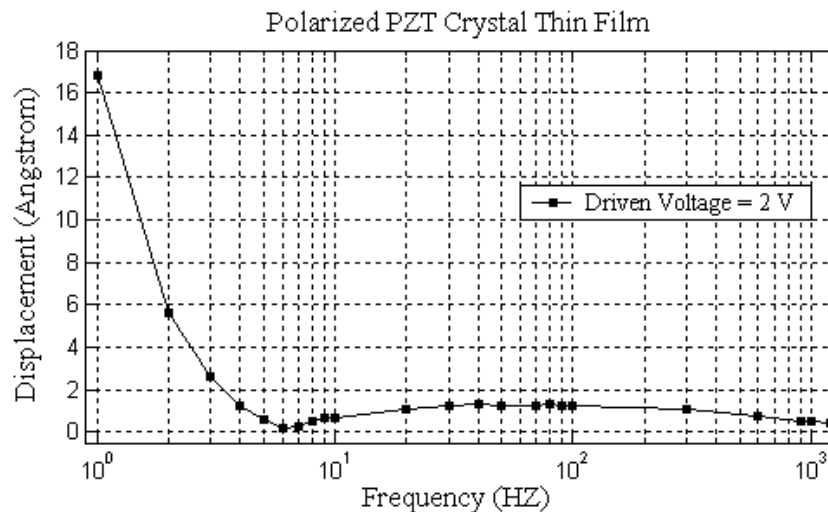
Figure 10. Relationship between the driving frequency and the displacements.

136
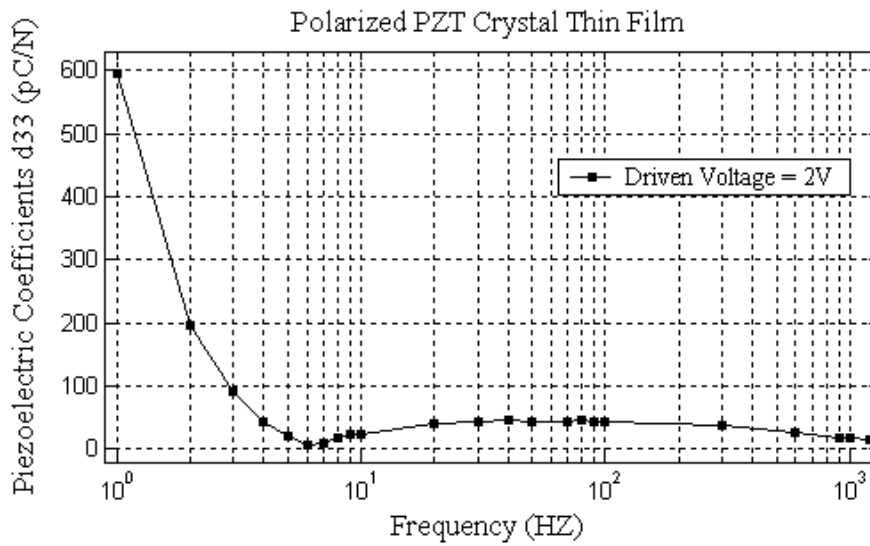
Figure 11. Relationship between the driving frequency and the piezoelectric coefficients.
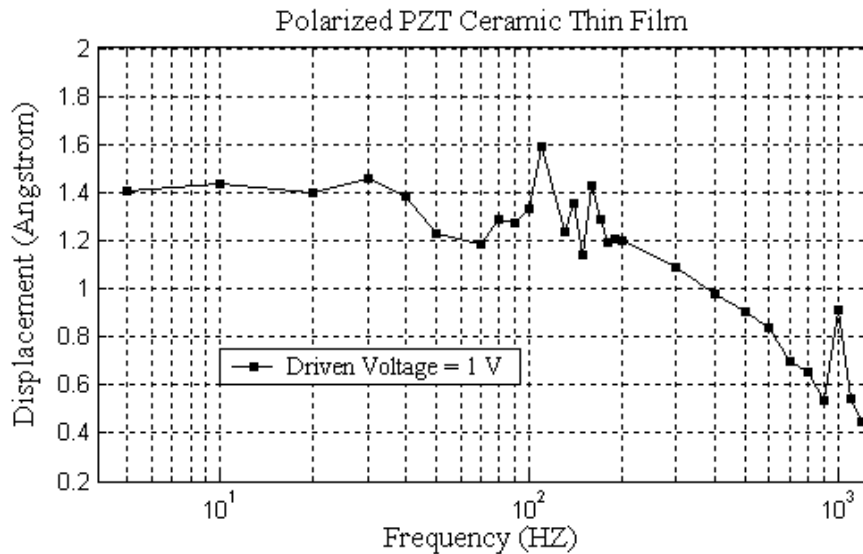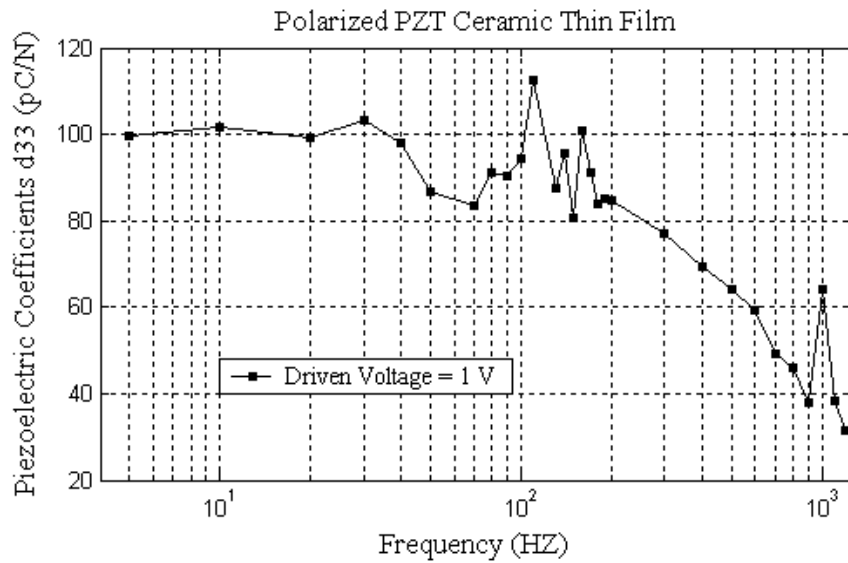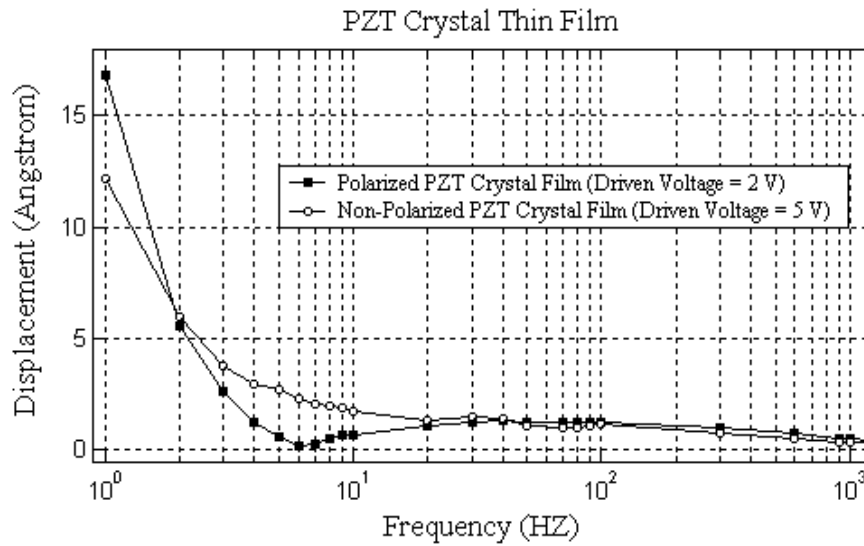

Figure 12. Relationship between the driving frequency and the displacements.

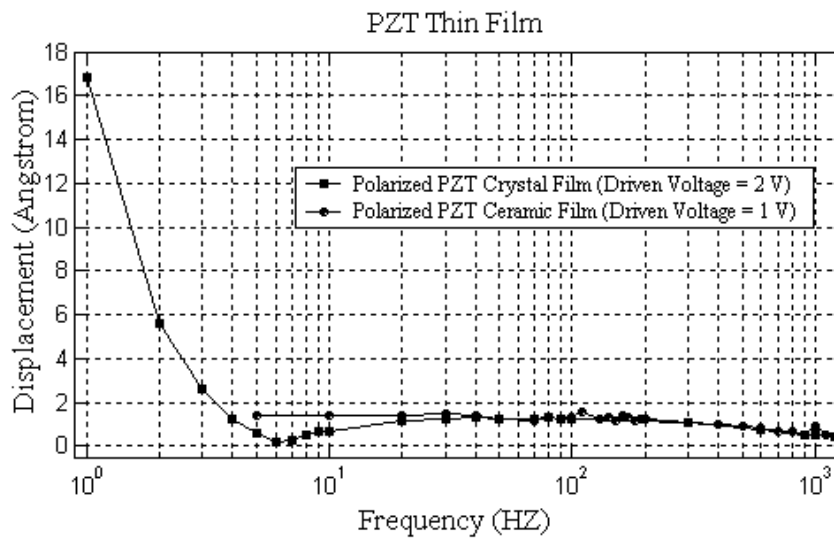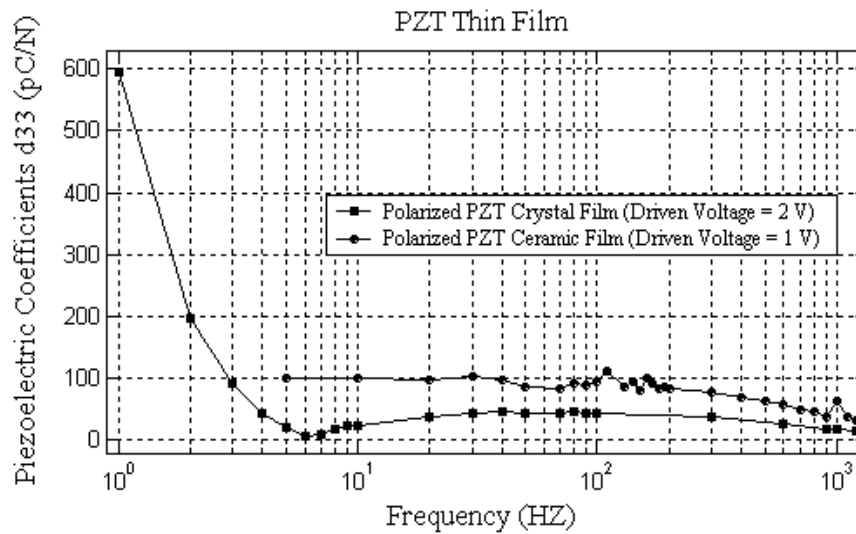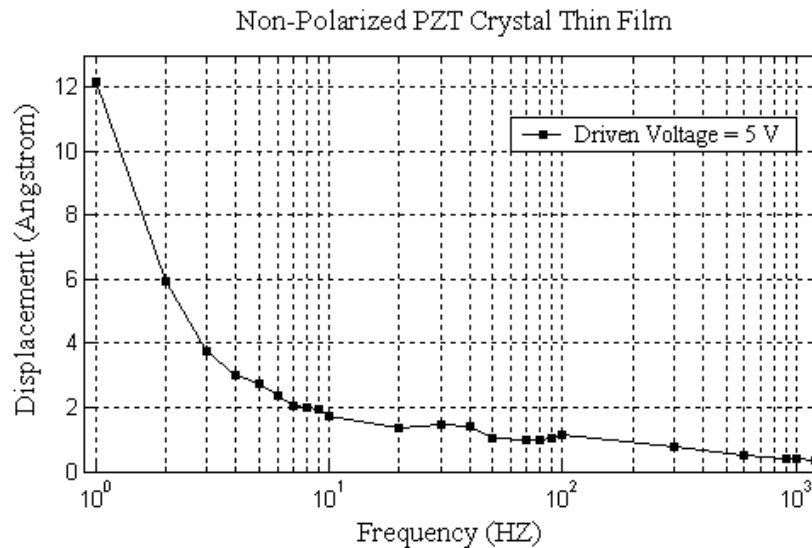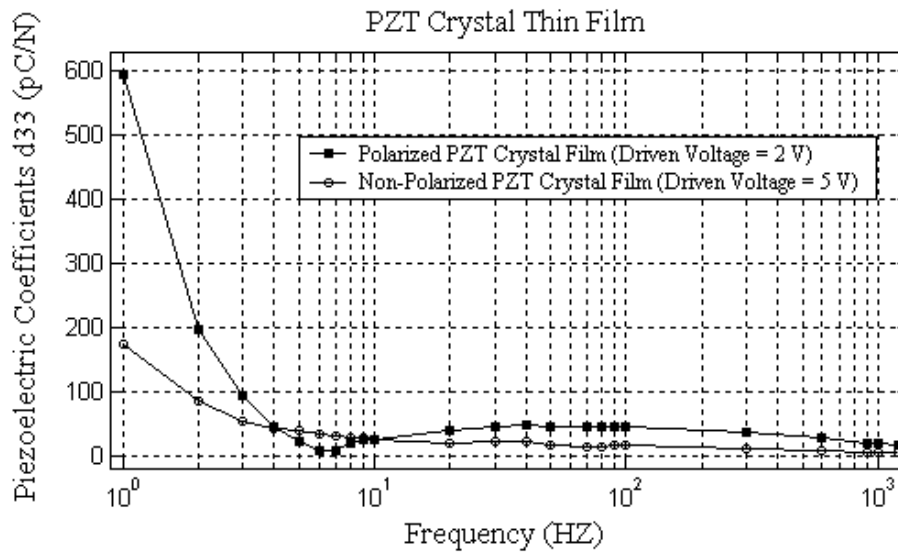Figure 13. Relationship between the driving frequency and the piezoelectric coefficents.

CONCLUSIONS

In summary, we have demonstrated the relationship between the external driving frequencies and both the polarized and non-polarized monocrystalline PZT films. Our experimental results show that both the monocrystalline films have a more uniform response to external voltage when compare to the common polarized PZT ceramic film. We have also measured for the first time the piezoelectric coefficients of the monocrystalline PZT film before and after it was polarized. We found that the film has a better response than the polarized thick PZT ceramic film even before it was polarized. Thus, we believe that it is naturally partially polarized from the way it was fabricated.

In our experiments, we observed that the polarized monocrystalline PZT film has a stronger piezoelectric effect when the external driving frequency is low. The effect drops dramatically when the external driving frequency goes high. However, at the high driving frequencies all three films have almost the same piezoelectric coefficients. This means that the responses of the films to the external driving signal saturate almost at the same level.

Finally, we demonstrated that our optical interferometry system is capable of measuring the piezoelectric coefficients of the monocrystalline PZT films at a very high accuracy level under small displacements.

138

ACKNOWLEDGEMENTS

REFERENCES

[1] W.Y. Pan and S.J. Jang, Rev. Sci. Instrum. **61**, 2109 (1990).
[2] Q.M. Zhang, W.Y. Pan and L.E. Cross, J. Appl. Phys. **63**, 2492 (1998).
[3] W.Y. Pan and L.E. Cross, Rev. Sci. Instrum. **60**, 2701 (1989).
[4] Yu Lu, PhD. Dissertation, The Pennsylvania State University (2001).

Appendix A: MATLAB code

```
%%%%%%%%%%%%%%%%%%%%%%%%%%%%%%%%%%%%%%%%%%%%%%%%%%%%%%%%%%%%%%%%%%%%
%      Load Samples and Get Number of Samples to be Examined      %
%%%%%%%%%%%%%%%%%%%%%%%%%%%%%%%%%%%%%%%%%%%%%%%%%%%%%%%%%%%%%%%%%%%%

N=input('Please enter the number of sample points.')
A=load('PZT-V5v-F50HZ-VPP224mv.dat');

%%%%%%%%%%%%%%%%%%%%%%%%%%%%%%%%%%%%%%%%%%%%%%%%%%%%%%%%%%%%%%%%%%%%
%                     Initializing Variables                     %
%%%%%%%%%%%%%%%%%%%%%%%%%%%%%%%%%%%%%%%%%%%%%%%%%%%%%%%%%%%%%%%%%%%%

R=input('Enter the number of points: 5, 10, 20 or 30, to be
examined before and after each point:');

N1=R+1;
N2=N-R;
i=0;
j=0;
Average=0;

%%%%%%%%%%%%%%%%%%%%%%%%%%%%%%%%%%%%%%%%%%%%%%%%%%%%%%%%%%%%%%%%%%%%
%                      Finding the Maximums                      %
%%%%%%%%%%%%%%%%%%%%%%%%%%%%%%%%%%%%%%%%%%%%%%%%%%%%%%%%%%%%%%%%%%%%

for n=N1:N2
    smax=-1000000;
    for m=1:R
        if (smax<A(n-m))
            smax=A(n-m);
        else
```

```
        end
        if (smax<A(n))
            smax=A(n);
        else
        end
        if (smax<A(n+m))
            smax=A(n+m);
        else
        end
    end
    if (smax==A(n))
        i=i+1;
        B(i)=A(n);
    else
    end
end

%%%%%%%%%%%%%%%%%%%%%%%%%%%%%%%%%%%%%%%%%%%%%%%%%%%%%%%%%%%%%%%%%%
%                         SETTING LIMITS                        %
%%%%%%%%%%%%%%%%%%%%%%%%%%%%%%%%%%%%%%%%%%%%%%%%%%%%%%%%%%%%%%%%%%

Top=1.4;
Bot=1.2;
for n=1:i
    C(n)=0;
end

for n=1:i
    if (B(n)<Top & B(n)>Bot)
        j=j+1;
        C(j)=B(n);
    else
    end
end

%%%%%%%%%%%%%%%%%%%%%%%%%%%%%%%%%%%%%%%%%%%%%%%%%%%%%%%%%%%%%%%%%%
%                       Finding the Average                     %
%%%%%%%%%%%%%%%%%%%%%%%%%%%%%%%%%%%%%%%%%%%%%%%%%%%%%%%%%%%%%%%%%%

for n=1:j
    Average=Average+C(n);
end
plot(C,'k*')
j
Average=Average/j
```

Appendix B:
Labview Schematic
Graphics
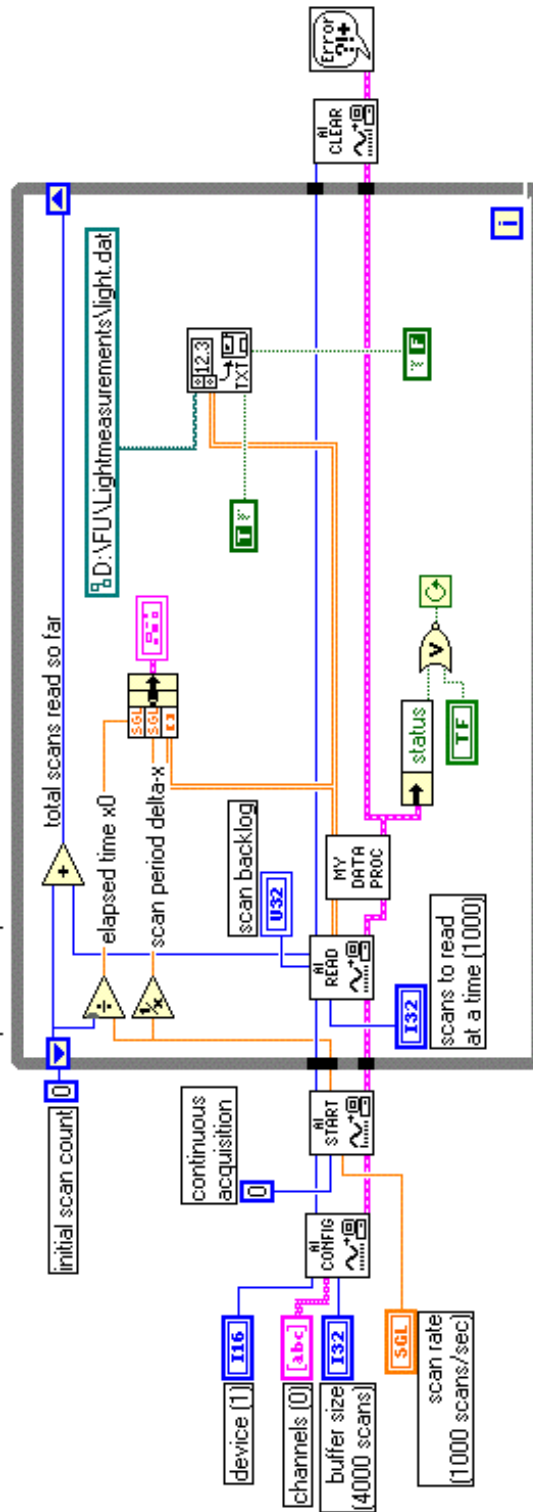
TRUE COLOR OF STREAMERS

Mark Lininger*
(Dr. Victor P. Pasko, Faculty Mentor)
Department of Electrical Engineering
Pennsylvania State University, University Park, PA 16802

*Undergraduate student of
Pennsylvania State University
University Park, PA 16802

ABSTRACT

Sprites are generated by a quasi-electrostatic field pulse that travels upward toward the ionosphere created usually by a positive cloud-to-ground stroke of lightning. This discharge of lightning will remove the positive charge allowing the quasi-electrostatic field to appear above the cloud line at all altitudes. As a result ambient electrons are accelerated, exciting the atmosphere. The breakdown electric field is proportional to the air density and decreases much faster than the electric field generated by the cloud. The sprite phenomenon is produced when the electric field from the cloud crosses this breakdown field. The streamer region of the sprite is composed of millions of narrow channeled gaseous discharges. A streamer can produce from an avalanche initiated by a single electron. By analyzing the optical emission bands, the true color of a streamer may be found. The optical emissions considered are the first and second positive bands of N_2, meinel N_2^+, first negative band of N_2^+, and the first negative O_2^+. The color will change depending on the altitude and distance at which the streamer is observed. This results because the atmosphere will absorb some of the color.

INTRODUCTION

Sprites are natural phenomena that occur in the upper levels of the atmosphere during lightning storms. They result from a quasi-electrostatic field produced from a large discharge in the cloud below. Reports of sprites date back to 1886, but the first recorded sprite was not until 1989 at the University of Minnesota. Researcher's were testing a low light camera and hoping to record

northern stars, but when the video was reviewed they saw what is known today as sprites [1]. Sprites typically occur at lower ionosphere altitudes ranging from 50 to 90km, and have a diameter that can extend almost 100km [2]. They usually appear in clusters and only last for several milliseconds. Sprites are dim making them hard to see with the naked eye. Only someone with dark-adapted eyes will be able to see this phenomenon. A sprites image has only been captured at night, typically with highly sensitive monochromatic cameras. Their glow is predominantly red in color but gradually changes to blue as it decreases in altitude. The brightest region lies in the altitude range 65-75 km. Blue tendril-like filamentary structures often extend downward to as low as 40 km. The color signifies that nitrogen is the most abundant gas in the upper atmosphere [3]. Sprites are divided into two altitude regions. The upper portion of the sprite is called the diffuse region, and the lower portion is called the streamer region. The transition between the two regions occurs approximately between 72 and 80km [2]. The streamer region is made up of millions of narrow channeled streamers that have a lifetime of only a few milliseconds. They can reach speeds up to one-tenth the speed of light. Streamers are caused by a build-up of quasi-electrostatic charge in the atmosphere. The quasi-electrostatic field can cause the air to ionize where the field is greater than the breakdown field. The transverse size of the streamer has an observed range from 50 to 200m. Since nitrogen is the dominant gas in the upper atmosphere the first positive, second positive, meinel and first negative N_2 optical emission bands will produce the majority of the color found in streamers. The first negative O_2^+ will also be taken into account for this experiment. The data found from these optical emissions will be explored and simulations will be done to produce true color images of a streamer. The effects of sprites on the environment are still unclear. They need to be studied so more may be learned about the upper levels of the atmosphere and the possible impact sprites may have.

EXPERIMENTAL DESCRIPTION

The intensities of each optical emission used in this experiment were calculated using the following equation [3]:

$$I_k = 10^{-6} \int_L A_k n_k dl \qquad (1)$$

The integral is taken with respect to L, representing the horizontal line of site. A_k represents the radiation transition rate in state k. The n_k is the number density of excited particles also in state k. To find n_k the following equation was used:

$$\frac{\partial n_k}{\partial t} = -\frac{n_k}{\tau_k} + \sum_m n_m A_m + v_k N_e \qquad (2)$$

143

Where τ_k is the total lifetime of state k, and the sum over the terms $n_m A_m$ represents the increasing in n_k resulting from cascading from higher-energy states. v_k is the excitation coefficient and N_e is the electron number density. The negative sign in front of the equation signifies the decreasing density of excited particles. With these equations the intensities for the following optical emissions were found: 1st positive N_2, 2nd positive N_2, 1st negative N_2^+, 1st negative O_2^+, and meinel N_2^+.

To find the true color of a streamer the corresponding wavelengths for each intensity must be found. From Aurora the partial intensities, total intensity, and corresponding wavelength were present for each optical emission [4]. The ratio of partial intensity to total intensity was calculated and multiplied by the intensities used in this experiment. This correlates aurora's data with the data used in this experiment and gives the corresponding wavelengths. These wavelengths were than passed through a filter that takes into account the device the data was measured. The filter is a color TV response corrected for atmospheric scattering and transmission through the aircraft window, shown in figure I.
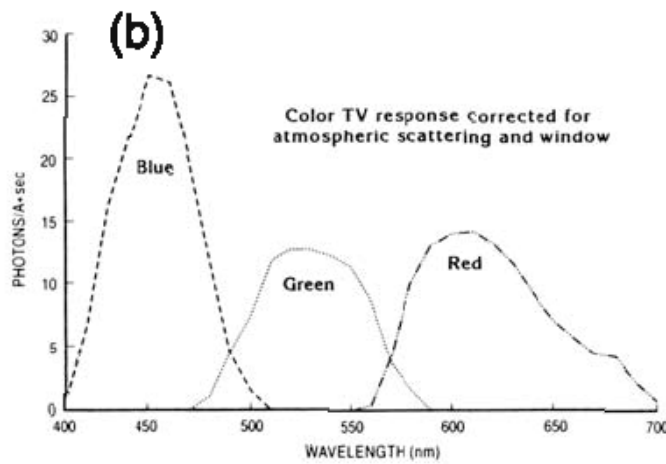
Figure I: Color TV response corrected for atmospheric scattering and transmission through aircraft window [5].

144
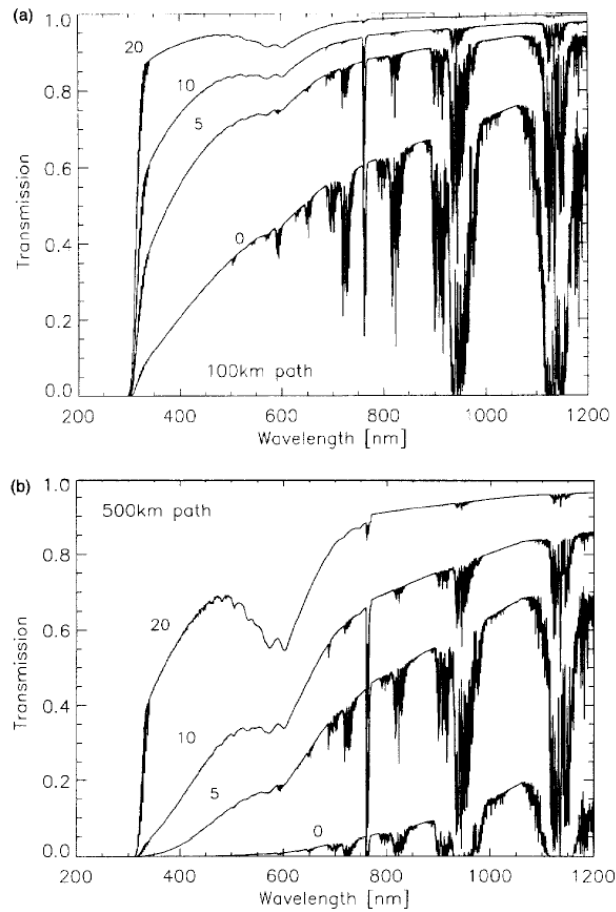
Figure II: Atmospheric attenuation between 65km and observation altitudes of 0, 5, 10, and 20km along (a) 100km and (b) 500km path lengths [6].

Figure II is an atmospheric filter used to find the color at different altitudes and different distances from the steamer. Figure II (a) shows the atmospheric attenuation of a sprite at 65km from altitudes of 0, 5, 10, and 20km at 100km lateral distance. Figure II (b) shows the atmospheric attenuation at the same altitudes but a path length of 500km instead of 100km. These filters represent observation altitudes from the ground, mountain, airplane, and balloon. These atmospheric filters show that the shorter wavelengths in the visible range are absorbed more by the atmosphere than longer wavelengths in the visible range.

RESULTS

In figure III a true color image of a streamer can be seen at 4 different time intervals. The images show the streamers true geometry. At 0m the actual altitude is 70km. The streamer will reach a total length of about 210m. The initial starting

145

point of the streamer is at the center point of the plot. It expands out in the upward and downward directions away from the center point. This is referred to as a double-headed streamer. The positive head is going downward and the negative head is moving upward. The negative head has a larger electric field than does the positive head. Figure IV shows the color of a streamer at 65km and a path length of 100km observed at 4 different altitudes. Figure V also shows the color of a streamer at 65km but has a path length of 500km observed from the same 4 altitudes. Both figures IV and V show true geometry of the streamer. Figure III (d) uses the same time interval as the plots in both figures IV and V, so a comparison can be made.

Figure III: True color of streamer at 70km at 4 different time intervals.

Figure IV: Shows the true color of a streamer at path length of 100km and observation altitudes of (a) 0km, (b) 5km, (c) 10km, and (d) 20km.

Figure V: Shows the true color at a path length of 500km and observation altitudes of (a) 0km, (b) 5km, (c) 10km, and (d) 20km.

DISCUSSION

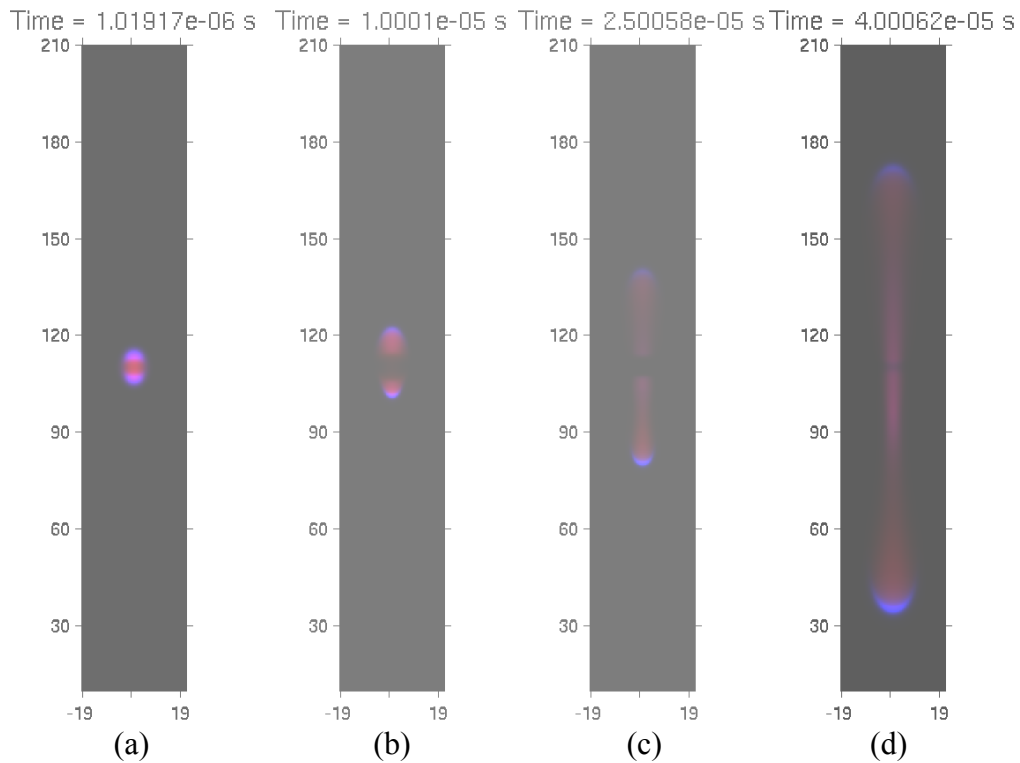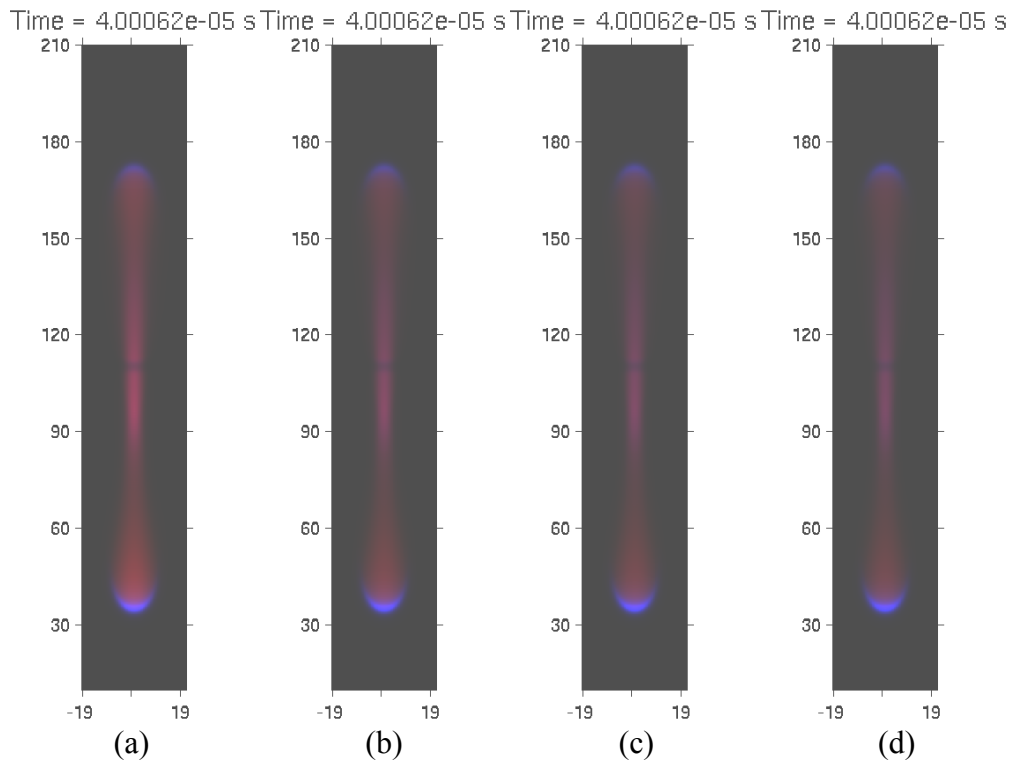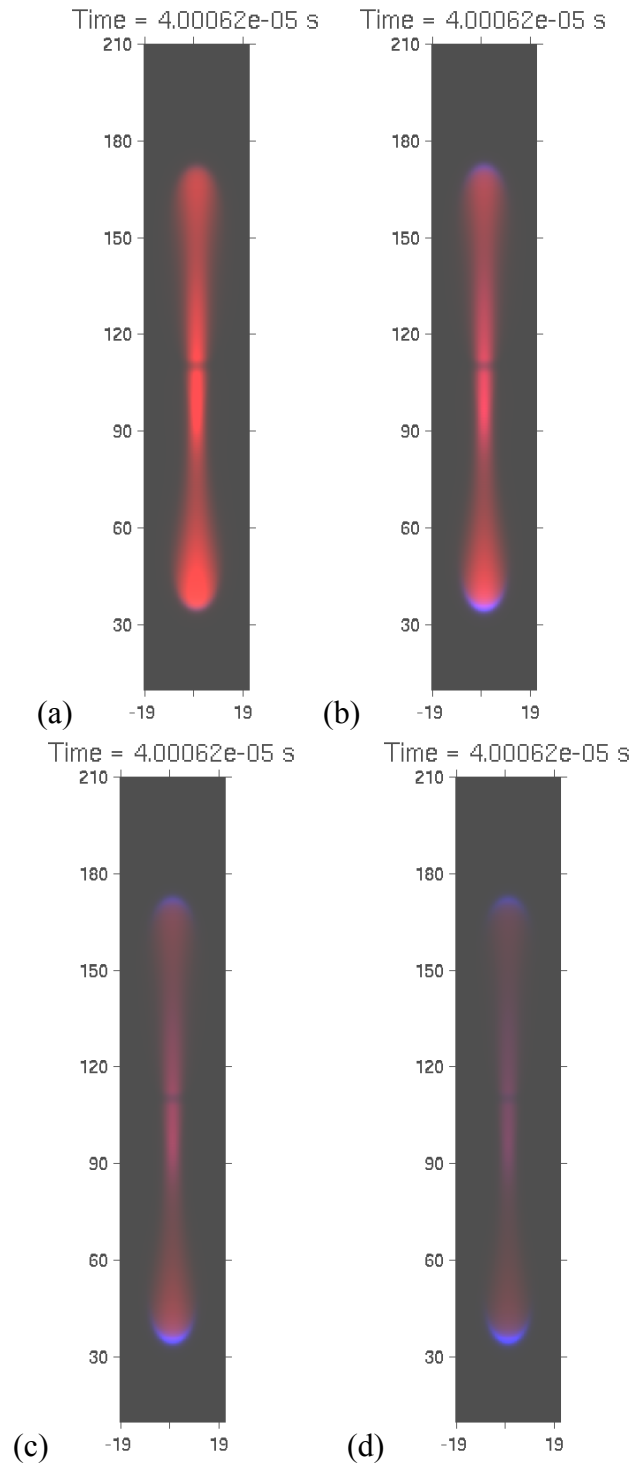From figure III it can be seen that the simulated streamer is blue on the tips of both the negative and positive streamer heads. The negative tip has a deeper blue because the negative streamer is more intense than the positive streamer. The body of the streamer is red and there is a small amount of purple in the transitions from red to blue. This result is partially a surprise, because initially it was thought to be more reddish. The first positive N_2 makes up the majority of the atmosphere at 70km and produces a red color [7]. However, this is justifiable because the second positive N_2 is the most intense optical emission and produces a blue color. The first negative N_2^+ also produces a bluish color but is not near as intense as the second positive N_2 [7]. The first negative O_2^+, and meinel N_2^+ do not have much effect on the color of the streamer because their intensities are a few orders of magnitude smaller than the first positive N_2, second positive N_2, and first negative N_2^+. The intensity curves of the first positive N_2 shows the most intense region is the middle and decreases slightly as it gets closer to the tips. The second positive N_2 is most intense at the tips of the streamer and is much less intense in the body of the streamer. The first negative N_2^+ has a similar curve as that of the second positive N_2, but again not nearly as intense.

Figures IV shows the streamer at a single point in time at different altitudes and different path lengths. From these results it can be seen that the color changes more drastically as the observer is farther away and at lower altitudes. The color becomes more reddish and less bluish as the observer moves farther away and closer to ground level. From the atmospheric attenuation plots in figure II it becomes clear why this occurs. Shorter wavelengths tend to be absorbed more by the atmosphere than longer wavelengths, in the visible spectrum, and more light is transmitted through the atmosphere as altitude increases. At ground level and a path length of 500km none of the blue light makes it through the atmosphere and the image becomes all red.

CONCLUSION

The results show that the true color of a streamer has more blue than anticipated but is still mostly red in color. The color changed as the observer changed altitude and the lateral distance away from the streamer because of the absorption from molecules in the atmosphere. The atmospheric attenuation could have been more accurate if the altitude of the sprite used to produce figure II was the same altitude as the sprite used in this simulation. A true color image of a streamer can tell researcher more about the gases in the upper atmosphere.

149

REFERENCES
1. W. A. Lyons, "The hundred-year hunt for the red sprite," WRC NBC Washington   Weather Almanac, (2003).
2. V.P. Pasko, and H.C. Stenbaek-Nielsen, "Diffuse and streamer regions of sprites," Geophysical Research Letters, vol. 29, Number 10, (2002).
3. V.P. Pasco, U.S. Inan, and T.F. Bell, "Sprites Produced by quasi-electrostatic heating and ionization in the lower ionosphere," *Journal of Geophysical Research*, vol. 102, pp. 4529-4561, (1997).
4. Wescott, E. M., D. D. Sentman, M. J. Heavner, D. L. Hampton, and O. H. Vaughan Jr., "Blue jets: Their relationship to lightning and very large hail fall, and their physical mechanisms for their production," J. Atmos. Sol. Terr. Phys., vol. 66, pp. 713-724, (1998).
5. A. V. Jones, "Aurora," Geophysics and Astrophysics Monographs, pp. 81-139, vol. 9, B. M. McCormac, (1974).
6. J.S. Morrill, E. J. Bucsela, V. P. Pasko, S. L. Berg, M. J. Heavner, D. R. Moudry, W. M. Benesch, E. M. Wescott, D. D. Sentman, "Time resolved N_2 triplet state vebrational populations and emissions associated with red sprites," Journal of Atmospheric and Solar-Terrestrial Physics, Vol. 60, pp. 811-829, (1998).
7. V. P. Pasko, U. S. Inan, and T. F. Bell, "Spatial structure of Sprites," Geophysical Research Letters, vol. 25, pp. 2123-2126, (1998).

SPECTRAL ANALYSIS METHODS IN THE STUDY OF GRAVITY WAVE BREAKING

Adeel Haroon*
(Jonathan B. Snively and Victor P. Pasko, Faculty Mentors)
Department of Electrical Engineering
Pennsylvania State University, University Park, PA 16802

*Undergraduate student of
Pennsylvania State University
University Park, PA 16802

ABSTRACT
        Gravity waves are traveling mechanical waves of low frequency and large wavelengths, resulting from disturbances of the balance between buoyancy and gravity forces. Gravity wave breaking occurs when the sum of the perturbation and wind velocities approaches the phase velocity of the wave. The breakdown of low frequency gravity waves is known to excite higher frequency harmonics of the source wave; however, in the presence of winds, these secondary waves may also be unstable. As gravity waves break some of their energy is transferred to wind flow, which further increases the likelihood that secondary waves will break. In order to study the properties of breaking gravity waves, it is necessary to visualize the propagation of individual secondary wave modes separately from the primary wave. Given a two dimensional spatial Fourier spectrum, a range of wave numbers may be chosen from which two-dimensional bandpass filters may be applied. The effect of wind on wave breaking and its ability to generate coherently propagating, smaller scale waves can then be explored.

INTRODUCTION
        On very large scales, the atmosphere acts much like an incompressible fluid. An important component of stably stratified fluids, such as the atmosphere, is the buoyancy restoring force.[1] When a parcel is displaced in a statically stable atmosphere, it will oscillate at the Brunt-Väisälä frequency and thus excite propagating gravity waves.[2] In order for a wave to be classified as a gravity wave, its frequency must be lower than the Brunt-Väisälä frequency but high enough not

to be considered a planetary wave or Rossby wave.[3] The Brunt-Väisälä frequency is defined as:

$$N^2 = -\frac{g}{\rho_o}\frac{\partial \rho_o}{\partial z}$$

(1)

where N is the Brunt-Väisälä frequency, g is the acceleration due to gravity, and ρ_o is density. Gravity waves grow exponentially with height due to conservation of energy. Since energy is dependent on the relation $\rho_o v^2$, the velocity must increase as density decreases with height. Since gravity waves propagate upwards, waves generated in the troposphere will travel upwards to the mesosphere and affect motions in the upper atmosphere. [3]

Realistically, the atmosphere is compressible. However, when dealing with gravity waves, the atmosphere can be considered incompressible. This simplification is applied because it filters out high frequency acoustic wave solutions from the wave equation and leaves gravity wave solutions, which are below the Brunt-Väisälä frequency. [3] Even though this simplification may seem like it does not represent a realistic atmosphere, it has been found to adequately describe gravity wave motion observed in the real atmosphere. [4] Therefore, using the Euler equations that define wave motion in an isothermal atmosphere, the wave equation for gravity wave motion can be determined. Conservation of energy states that the wave's kinetic energy with height remains constant. We can solve for a normalized vertical perturbating velocity, W_z:

$$W_z = \left(\frac{\rho_o}{\rho_s}\right)^{1/2} V_z$$

(2)

where V_z is the vertical perturbation velocity, ρ_o is the density at the altitude of the wave, and ρ_s is the density of the source. Applying the substitution for the Brunt-Väisälä frequency from (1), the gravity wave equation becomes:

$$\frac{\partial^2 W_z}{\partial z^2} + \left[\left(\frac{k_x^2}{(\omega - Uk_x)^2}\right)(N^2 - (\omega - Uk_x)^2)\right]W_z = 0$$

(3)

where k_x is the horizontal wavenumber, ω is the frequency, and U is the wind component. The coefficient of W_z is set equal to k_z^2, where k_z is the vertical wavenumber. Then solving for the frequency, the dispersion relation is:

$$\omega = Uk_x \pm N\left[\frac{k_x^2}{k_x^2 + k_z^2}\right]^{1/2}$$

(4)

From this relation, important properties of gravity wave motion can be determined specifically, the group velocity and phase velocity in both horizontal and vertical direction. For this study, the horizontal wave velocity is very significant, since wavebreaking will occur when the sum of the perturbation and wind velocities must approach this term. This phase velocity is:

$$V_{px} = \frac{\omega}{kx} = U \pm N[\frac{1}{kx^2 + kz^2}]^{1/2}$$

(5)

Gravity waves are described as vertically transverse in that they are dominated by motions normal to the direction of propagation. A packet of waves travels at the group velocity. [3] This group velocity is perpendicular to the phase velocity of the individual phase fronts. Vertical phase and group velocities are in opposite directions; however horizontal wave phase and group velocities are in the same direction.[4] Since gravity waves travel rather slowly, horizontal phase and group velocities are always less than the speed of sound. The direction of energy propagation is the same as the group velocity but perpendicular to the direction of phase propagation.[5] See Figure 1 for illustration.
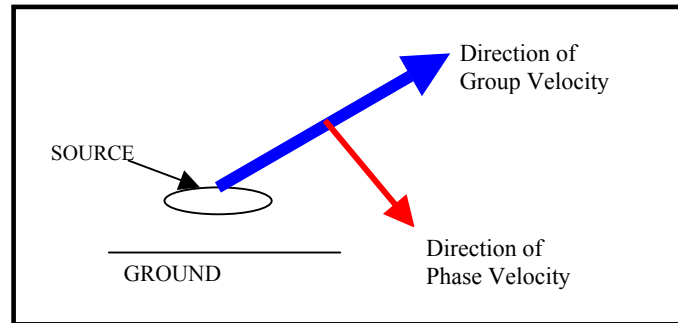
Figure 1. Illustration of gravity wave motion.

Isolated thunderstorms, which are located in the troposphere, have been identified as the common source for gravity waves.[5] The process of convection inside a thunderstorm produces the oscillation needed to cause gravity waves. In the early stage of a thunderstorm, updrafts cause instability in the lower atmosphere. During the storm, the updrafts become more intense. When unstable air reaches an equilibrium height, which is around the cloud tops, the parcel will oscillate.[6] The period of this oscillation is approximately equal to the local Brunt period.[6] These convective oscillations generate vertically propagating gravity waves.[5] As the gravity wave propagates vertically, it will experience thermal refraction; near the source, the group velocity will be very low and directed horizontal, but with increasing altitude, the Brunt frequency is higher and the wave will propagate vertically.[6] Taylor and Hapgood (1988) observed a gravity wave, which was likely generated by a thunderstorm, with a wavelength $\lambda = 6.5 \pm 1.5$ km, a phase velocity $v = 5 \pm 2$ m s-1, and a period $\tau = 21 \pm 1$ min. Typically

153

gravity waves have periods greater than five minutes and wavelengths spanning tens of kilometers while keeping the frequency lower than the Brunt-Väisälä frequency. The vertical wavelengths are relatively smaller than the horizontal wavelengths. While vertical wavelengths generally range from 1 – 30 kilometers, horizontal wavelengths range from 10 – 1000s kilometers.[1]

Another phenomenon that occurs with gravity waves is wavebreaking. This occurs when the sum of the horizontal perturbation and wind velocities approaches the phase velocity of the gravity wave. When wavebreaking occurs, the primary wave excites higher frequency harmonics called secondary waves. Breaking also accelerates the wind flow, which may cause the secondary waves to break. Secondary waves are weaker in magnitude than the primary waves. Along with a higher frequency than the primary waves, the secondary waves also have longer vertical wavelengths.[7] The secondary waves' vertical wavenumbers are thus approximately half that of the primary wave.[8] The secondary waves have approximately twice the horizontal wavenumber and frequency of the source. Franke and Robinson (1998) determined that primary waves of lower frequency generated secondary gravity waves, which have a frequency higher than the primary wave but still below the buoyancy frequency. However; the secondary waves produced by a high frequency primary wave are often in the form of acoustic waves. Also, unlike the primary waves, the secondary waves propagate vertically both downward and upward.[8] As a result of wavebreaking, energy is removed from the primary wave by the reduction of its amplitude, which is then transferred to the secondary waves and to wind flow.[7]

In a windless isothermal atmosphere, primary wave will break when the perturbation velocity approaches the phase velocity of the wave. However, waves also break when the sum of the perturbation velocity and wind velocity approaches the phase velocity. Wind is a very important variable in the production of the smaller scale secondary gravity waves. When gravity waves break in the presence of wind, the secondary waves are also less stable and more susceptible to breaking. For example, a very weak gravity wave breaking at a wind induced critical layer will be completely absorbed and produce no coherently propagating secondary waves.[4]

EXPERIMENTAL DESCRIPTION

Simulation results from the numerical model used in Snively (2003)[9] based on the CLAWPACK software package developed by Randall LeVeque (2002), are considered as test cases.[10] The first illustrates a wavebreaking in a realistic atmosphere with no wind. In this case, a wave is generated whose parameters are frequency, period $\tau = 9.52$ in and horizontal wavenumber $k_x = 0.00011$ 1/m, which breaks to generate secondary waves with $\omega = 0.022$ rad/sec and $k_x = 0.00022$ 1/m. The second case considers a wave breaking in a periodic atmosphere with a horizontal wind generated by breaking. In this case, the primary wave's frequency is $\omega = N / (2 \sqrt{2})$; therefore, the secondary waves should break at $\omega = N / \sqrt{2}$. The results include images showing the field

154

quantities such as vertical perturbation velocity and horizontal perturbation velocity.

Filter Design

In order to observe the behavior and properties of the secondary waves, it is crucial to isolate them from the primary wave. Since secondary waves have a higher frequency and horizontal wavenumber, a filter can be applied to separate them from the primary wave. Two-dimensional highpass and bandpass filters are applied to the wave spectrum to isolate the higher frequency secondary waves. A two-dimensional low pass filter is applied to view the primary wave's propagation.
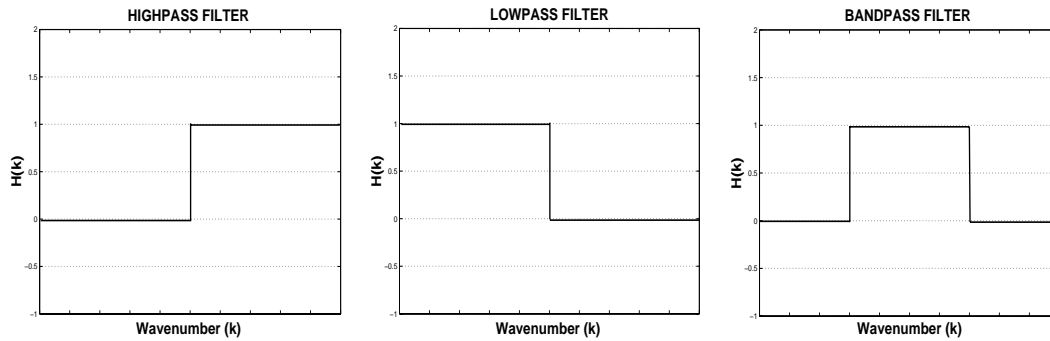
Figure 2. Plots of ideal Highpass, Lowpass, and Bandpass filters.

The highpass and lowpass filters were only applied in the x-direction to k_x, while the bandpass filter was applied for both horizontal and vertical wavenumbers, k_x and k_z. This filter is applied using a rectangular window. Although other windows, such as the Hamming window, are used more often when dealing with filters, a rectangular window suits this situation. The advantage of a rectangular window is that its transition region is narrowest at $4\pi/M$ while the Hamming window is twice that at $8\pi/M$, where M is the length of the window and fourier transform.[11] As a result, less undesired frequencies are passed through to the filtered image. Figure 2 shows for frequency responses for rectangular and hamming windows.
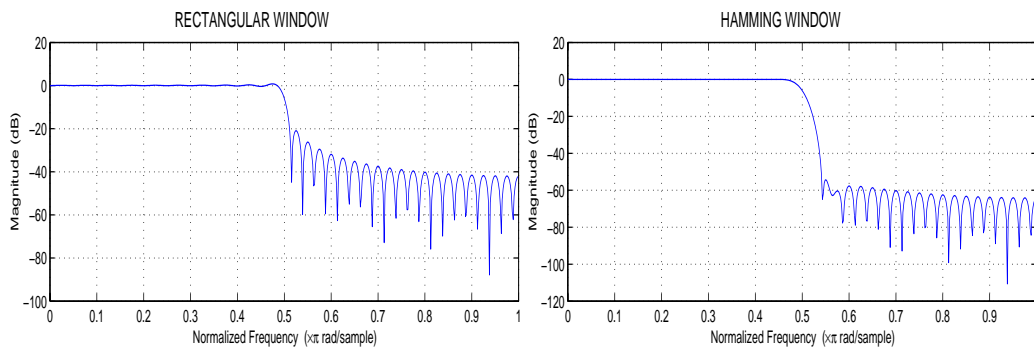
Figure 3. The frequency response of rectangular and hamming window. Notice the short transition period of the rectangular window compared to that of the Hamming window and the -20dB peak sidelobe of the rectangular window in this example.

The drawback to the rectangular window is it has a high peak sidelobe of approximately -13 dB. However, the ringing effects caused by high sidelobes are insignificant in this case. The peak sidelobe of -13 dB converts into an approximate factor of 1/20, which visually translates to a color representing a value very close to zero; therefore, it is indistinguishable from zero and causes no significant visual affect. After the filter is applied, the motion of the desired secondary waves can be viewed without the interference of the primary wave.

RESULTS
Test Case 1: Realistic Atmosphere with no wind
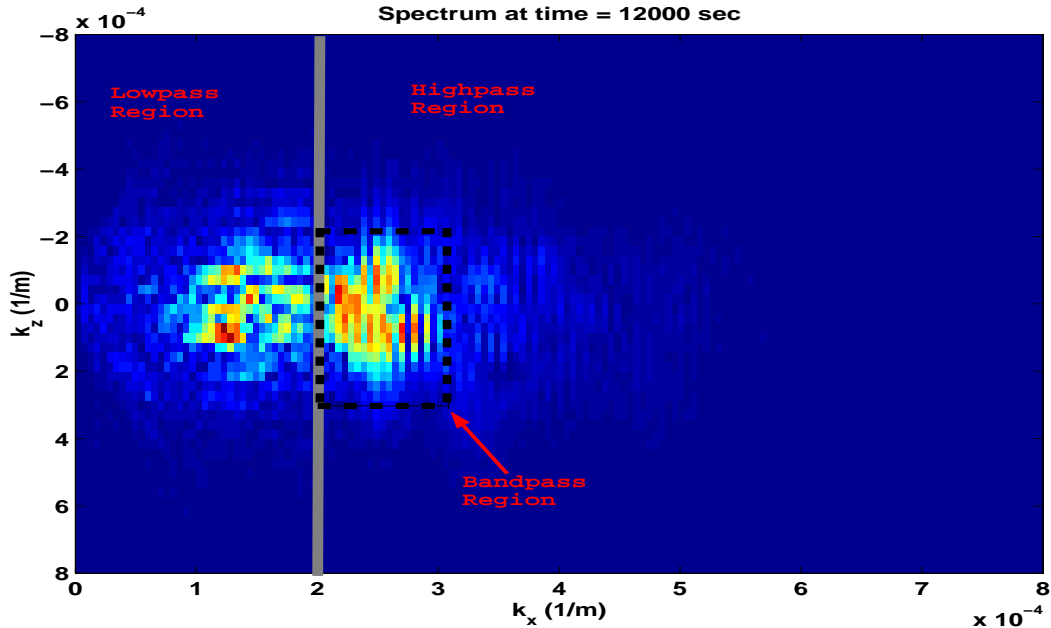
Figure 4. Spectrum of the wave at time = 12000 sec with the outlined regions for filtering labeled.
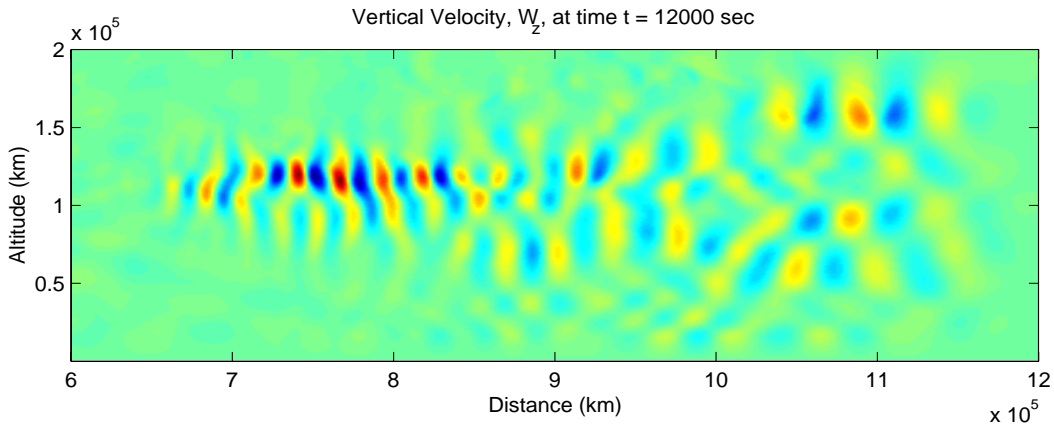
Figure 5. Vertical Velocity plot of whole system showing both primary and secondary waves propagating together.
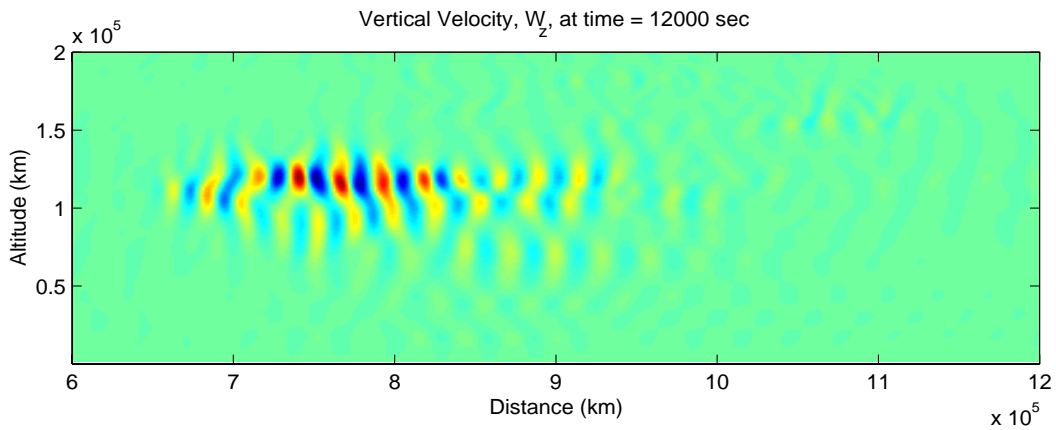
Figure 6. Vertical Velocity plot of highpass filtered region to isolate secondary waves showing that the secondary waves are trapped in lower thermosphere.
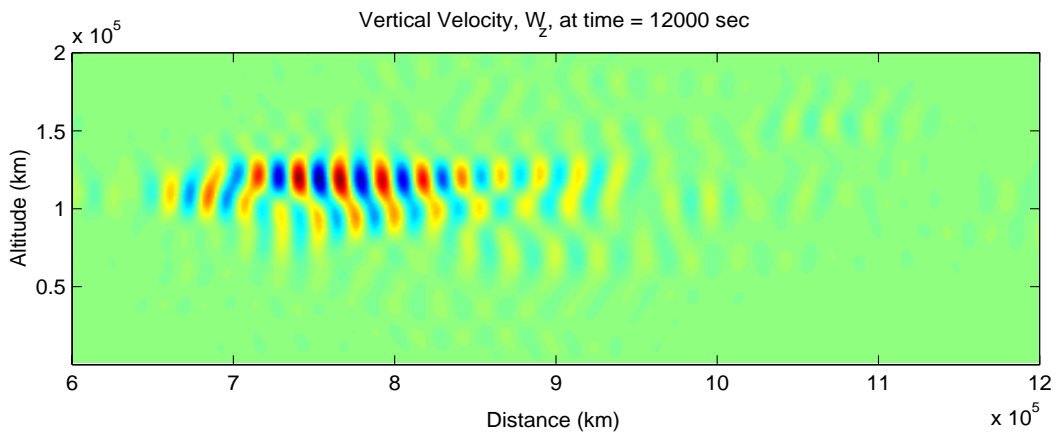
Figure 7. Vertical Velocity plot of bandpass filtered region to isolate secondary wave, which is very similar to that of the highpass filtered region in Figure 6, showing the magnitudes of the secondary waves are still quite strong.
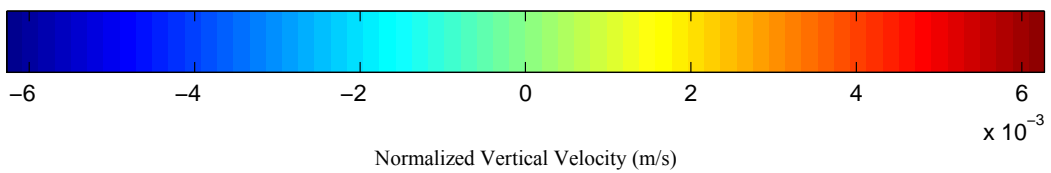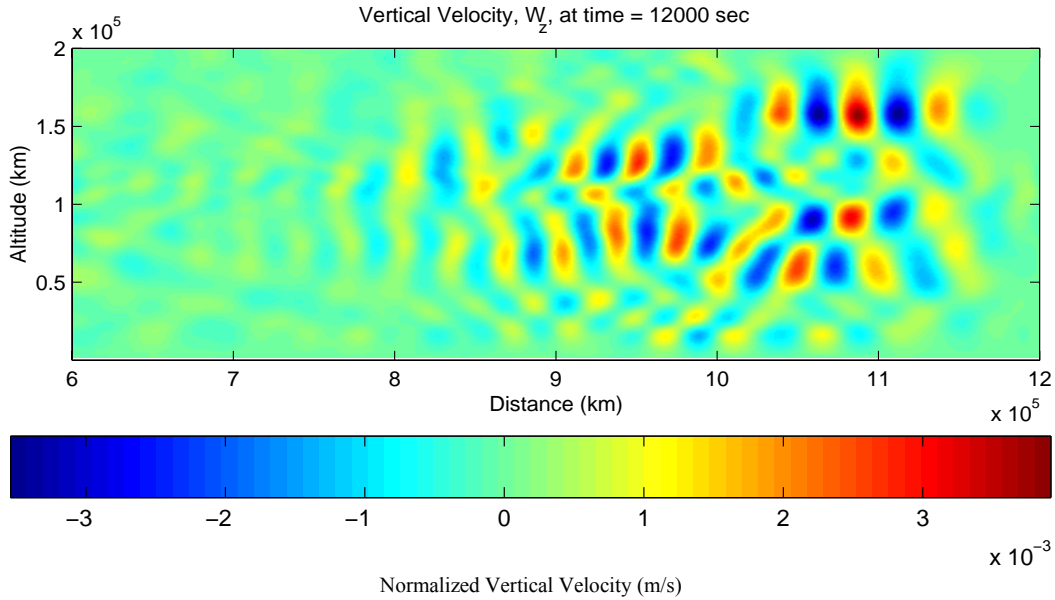
Figure 8. Vertical Velocity plot of lowpass filtered region to isolate primary waves showing that the early parts of the primary wave went without breaking; however, there was a loss of energy as can be seen from the decreased magnitude.

Second Test Case: Periodic Atmosphere
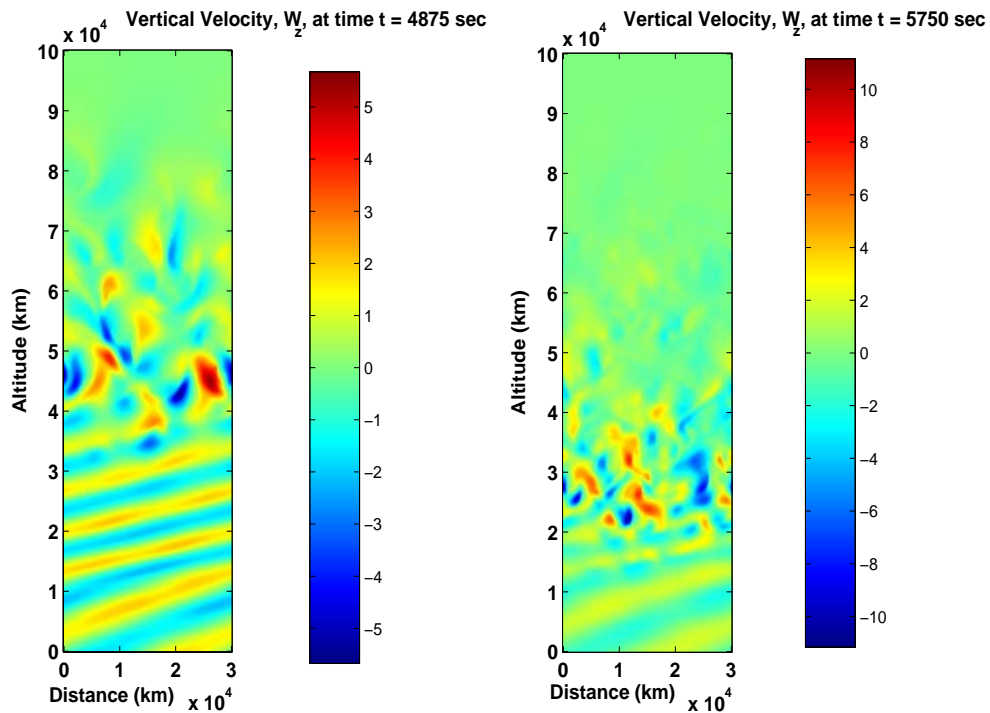
Figure 9. Vertical Velocity plots of the periodic simulation. Winds affect on the wave can be seen here where it first causes the wave to become unstable in the breaking region but then causes the whole system to become unstable.

158
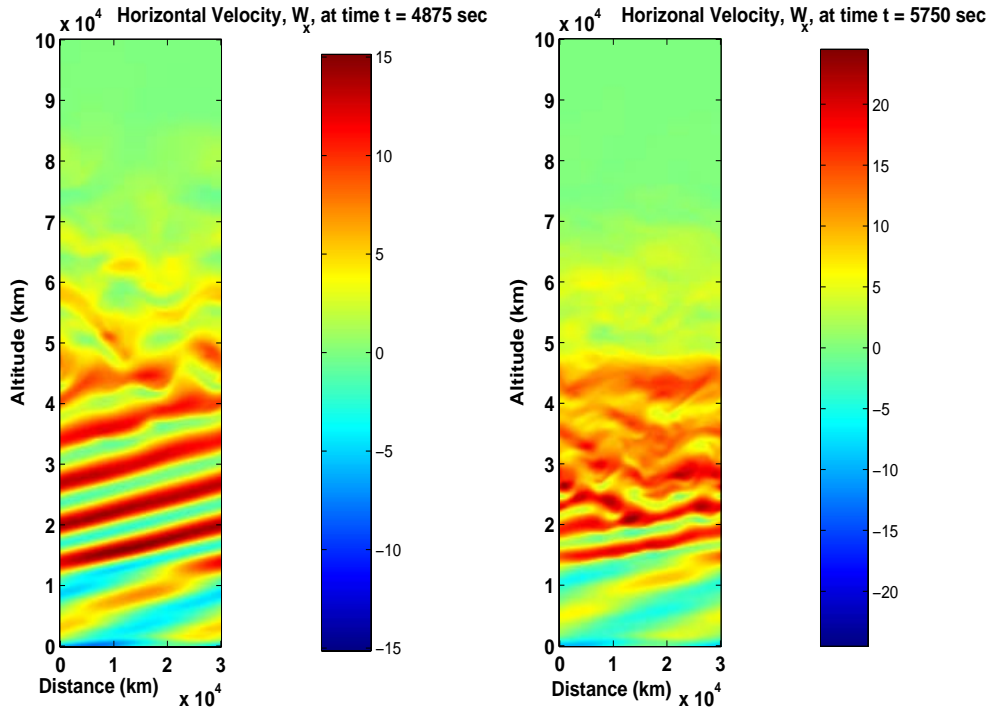
Figure 10. Plots of Horizontal Velocity of the periodic simulation. First plot shows how the wind first interacts with the wave to destabilize it and second plot shows how only a prevailing wind is left.
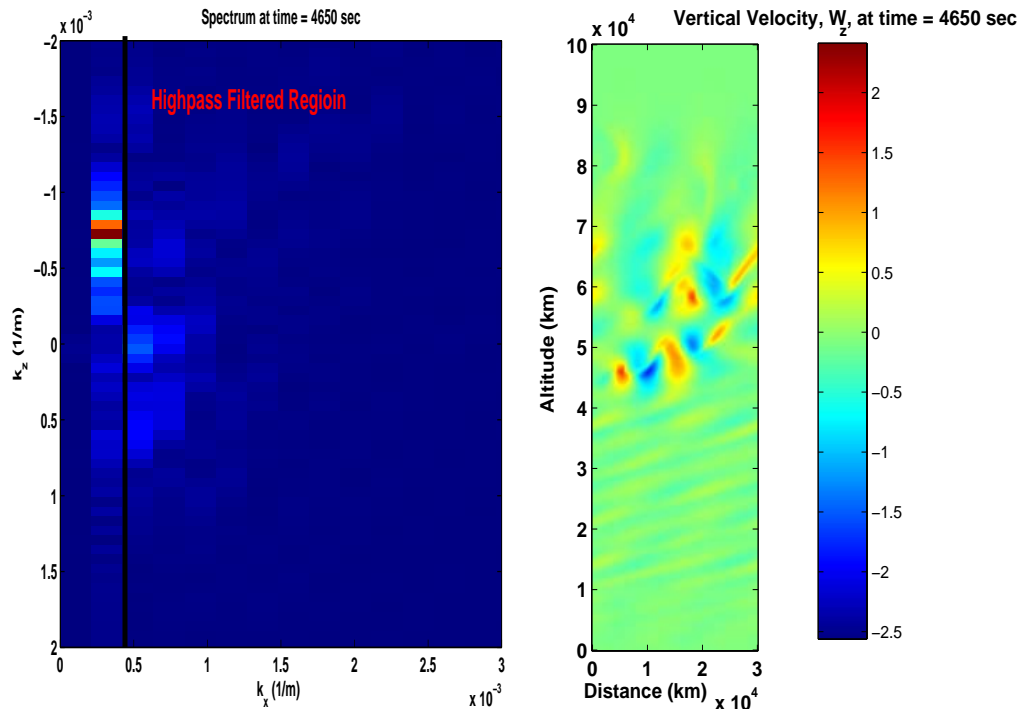
Figure 11. Spectrum of the wave with the highpass filtered region labeled. The wave, even at early time steps, does not form coherent secondary waves as can be seen by the filtered vertical velocity plot.

DISCUSSION

The first test case was a wave breaking in a realistic atmosphere with no wind. Figure 5 shows the spectrum of the wave and the regions of filtering are labeled. With the use of the highpass and bandpass filters in Figures 6 and 7, it can be seen that the wave breaks in region of altitude of 100 – 150 km. In accordance to law of conservation of energy, the magnitudes of the secondary waves follow that of the primary wave. The secondary waves are stable and continue propagating, trapped in the lower thermosphere. The propagation of the primary wave can now be clearly seen using the lowpass filter in Figure 8. The primary wave's magnitude, where secondary waves are present, is reduced after breaking because of the energy dissipated to the secondary waves.

The second test case dealt with a wave breaking in a periodic atmosphere. Although this periodic atmosphere is not realistic, wind's affect on wind can be seen. With the introduction of wind generated in breaking in the periodic simulation, the waves became highly unstable. The formation of secondary waves could not be seen, instead, the increasing wind caused turbulence. As wind grew with time due to the periodic nature of the simulation, the altitude of the wavebreaking region decreased. Figure 9 shows the vertical velocity plot of the wave in two time regions. The wave becomes unstable because of the affect of wind and its acceleration of the mean flow velocity. Finally, the wind becomes the dominant component as can be seen in the horizontal velocity plot of Figure 10. No coherent secondary wave structure could be seen. Figure 11 shows the spectrum with the highpass filtered region labeled; ideally this is where the secondary waves lie. However, the wind's destructive nature never lets any secondary waves to properly form as can be seen from the filtered image of the vertical velocity plot in Figure 11.

CONCLUSION

It was found that the rectangular window was sufficient for filtering the two-dimensional simulation results. Its narrow transition region was suitable, and its high peak sidelobe did not affect the filtered image significantly. The filtered results of the wave breaking were as expected. However, in the periodic simulation the wind had an immense effect on the wave. The wind flow becomes so intense that it completely annihilates the gravity wave and there is nothing left but an extremely strong horizontal wind. Therefore, no coherent secondary waves were generated.

ACKNOWLEDGEMENTS

REFERENCES

[1] Alexander, J. M., *Gravity Wave Sources and Propagation in the Middle Atmosphere*, Cedar Tutorial, 3-11, 2002.

[2] Taylor, L. L., "Mesospheric Heating Due to Intense Tropospheric Convection", *NASA Contractor Repor*t, 3131, 2-5, 1979.

[3] Gossard, E.E., and W.H. Hooke, *Waves in the Atmosphere*, Elsevier Scientific, 1975.

[4] Beer, T*., Atmospheric Waves*, John Wiley & Sons, 4 78-79, New York, 1974.

[5]Taylor, M.J. and M. A. Hapgood, "Identification of a Thunderstorm as a Source of Short Period Gravity Waves in the Upper Atmospheric Nightglow Emissions", *Planetary Space Science*, 36, 975-985,1988.

[6] Pierce A.D. and S.C. Coroniti, "A Mechanism for the Generation of Acoustic-Gravity Waves During Thunderstorm Formation", *Nature*, 5042, 1-2, 1966.

[7] Franke, P. M and W. A. Robinson, "Nonlinear Behavior in the Propagation of Atmospheric Gravity Waves", *Journal of the Atmospheric Sciences*, 56, 310-327, 1998.

[8] Zhou, X. L., J. R. Holton, and G. L. Mullendore, "Forcing of Secondary Waves by Breaking of Gravity Waves in the Mesosphere", *Journal of Geophysical Research*, 107, 1-7, 2002.

[9] Snively, J. B., *Tropospheric Forcing as a Source of Quasi-Monochromatic Short-Period Gravity Waves Observed in the Upper Mesosphere and Lower Thermosphere*, MS Thesis,30-36, 2003.

[10] LeVeque, R.J., *CLAWPACK Version 4.1 User's Guide*, http://www.amath.washinton.edu/`claw, 2002~.

[11] Proakis, J. G. and D. G. Manolakis, *Digital Signal Processing: Principles, Algorithm, and Applications*, Third Edition, Prentice Hall, 624-630, Upper Saddle River, NJ, 1996.

ACCURATE COMPUTATION OF SCHUMANN RESONANCES FROM
NARROWBAND FDTD ELECTROMAGNETIC FIELD DATA

Scott Kiefer
(Dr. Victor P. Pasko, Faculty Mentor)
Department of Electrical Engineering
Pennsylvania State University, University Park, PA 16802

Undergraduate student of
Pennsylvania State University
University Park, PA 16802

ABSTRACT
        In the earth's atmosphere, large electrical discharges such as lightning can
emit broadband waves of electromagnetic energy. Due to the resonant properties
of the earth-ionosphere waveguide, these waves can travel laterally and be
received around the world. There are various resonant modes in the earth-
ionosphere waveguide known as Schumann resonances. Accurate measurement
of these modes is important to atmospheric studies, including conductivity and
temperature profiles of the atmosphere. However, the amount of data needed to
find these modes with good resolution is often impractically large. Therefore, the
Lagrange method, the Cubic Spline method and the Cauchy method are used to
interpolate the narrowband data over a broadband range to get accurate
measurements of the Schumann frequencies.

INTRODUCTION
        Due to extremely high electron densities in the earth's ionosphere, it can
be considered very close to a perfect conductor. The high conductivity of the
earth's surface along with the conductivity of the earth's ionosphere form a
waveguide cavity with air acting as a very low conducting insulating medium
inside the cavity. While the conductivity of the earth-ionosphere cavity causes
high-frequency signals to be quickly attenuated, signals in the extremely low
frequency (ELF, 3-3000Hz) range can propagate numerous times around the earth
without any considerable attenuation.

This resonant property was originally proposed by W. O. Schumann in 1952, along with calculations for resonant frequencies within this waveguide cavity, called Schumann resonances (SR). If the earth and ionosphere were perfect conducting boundaries, the first three SR frequencies would occur at 10.6, 18.4 and 26.0 Hz, according to Tran and Polk[1]. However, the complex conductivity profile of the lower ionosphere causes the actual measurements to fall closer to 8, 14, and 20 Hz[2].

Due to the continuously changing features of the lower ionosphere and the inherent limitations of the current measuring techniques, it is difficult to generate an accurate model of the electron density profile of the whole region within the earth-ionosphere cavity. Differing amounts of solar radiation during the daytime and nighttime cause a diurnal shift in the electron density profile. Therefore, time of day and position with respect to the sun play significant roles in measurements across the globe. Nighttime ionospheric features also tend to be more pronounced due to the decrease in solar radiation and background noise, according to Cummer[3]. Ionosondes are capable of measuring electron densities at varying altitudes by sweeping through a range of frequencies between 500kHz and 25MHz, but they are only capable of collecting measurements down to the E-region (90km) of the ionosphere[4]. Because the D-region (<90km) simultaneously refracts and absorbs radio waves, lower frequency ionosonde measurements do not produce usable data below that region. ELF propagation, however, is most affected by the conductivity and electron density of the D-region[1], and so other techniques must be found to measure the states of this region. Because of the inability of current methods to make accurate measurements of the electron density profile, the Schumann resonances are being studied as a means of obtaining such data. With accurate SR data, electron densities in the lower ionosphere can be measured. Changes in the profile can also be examined and used for such purposes as meteorological predictions. Finally, this information can also be put to use to pinpoint the placement of individual lightning strikes, helping scientists analyze all types of atmospheric phenomena.

Using finite difference time-domain (FDTD) data and the fast fourier transform (FFT), a discrete collection of frequency points was able to be collected and analyzed for three different electron density profiles. However, in order to find accurate resolution of the SR frequency data for these profiles, the numbers of collected data points for each set would have to be impractically large. Therefore, different approximation methods were used to analyze the data around the Schumann frequencies and interpolate this data. Three different interpolation methods were used to analyze the data, and their individual results were compared against each other. The three methods used were the Lagrange, Cubic Spline and Cauchy approximation methods. These three methods, which will be explained in detail in the research description, were all separately applied to the three sets of FDTD data to collect the first SR frequency.

EXPERIMENTAL DESCRIPTION

The initial FDTD data received was in the form of discrete time domain data for the magnitude of the electromagnetic field along with a time reference. This data was easily converted to the frequency domain using the Fast Fourier Transform (FFT) function in MATLAB. This data was then used with each approximation method to find the first SR frequency.

1. Lagrange Method:

The Lagrange method is a general interpolation method that does not require evenly spaced intervals between the data points. It takes the form of a polynomial to the order of n where the maximum n is the number of data points given. The order of magnitude used is this paper is equal to the number of data points.

The method used in this paper follows the method laid out by Maron[5]. To begin, we assume that data is given in the form of

$$(x_0, y_0), \ldots, (x_n, y_n) \ where \ y_i = f(x_i) \tag{1}$$

We then construct a polynomial, p, with the condition

$$p_i(x_j) = \delta_{ij} = \begin{cases} 1 \ if \ j = i \\ 0 \ if \ j \neq i \end{cases} \tag{2}$$

The polynomial takes the form

$$p_i(x) = \frac{(x - x_0)(x - x_1)\cdots(x - x_{i-1})(x - x_{i+1})\cdots(x - x_n)}{(x_i - x_0)(x_i - x_1)\cdots(x_i - x_{i-1})(x_i - x_{i+1})\cdots(x_i - x_n)} \tag{3}$$

and the final approximation then takes the form

$$L_n(x) = \sum_{i=0}^{n} p_i(x) y_i \tag{4}$$

2. Cubic Spline

Spline theory is a relatively new field in matematics. It was originally introduced by I. J. Schoenberg in 1946 and has since developed greatly as a mathematical interpolation method[6]. The cubic spline interpolation method used in this paper is the same method laid out by Arlinghaus[7]. It approximates a set of data consisting of

$$(s_1, H(s_1)), \ldots, (s_n, H(s_n)) \tag{5}$$

164

The cubic spline fit piecewise approximates the data using a series of n-1 third-order polynomial equations of the form

$$a_1(s-s_1)^3 + b_1(s-s_1)^2 + c_1(s-s_1) + d_1$$
$$a_2(s-s_2)^3 + b_2(s-s_2)^2 + c_2(s-s_2) + d_2$$
$$\cdots$$
$$a_{n-1}(s-s_{n-1})^3 + b_{n-1}(s-s_{n-1})^2 + c_{n-1}(s-s_{n-1}) + d_{n-1}$$

(6)

The coefficients are found using the equations

$$a_i = (M_{i+1} - M_i)/6 \tag{7}$$
$$b_i = M_i/2 \tag{8}$$
$$c_i = \left(H(s_{i+1}) - H(s_i)\right) - \left((M_{i+1} + 2M_i)/6\right) \tag{9}$$
$$d_i = H(s_i) \tag{10}$$

where i = 1,2,…,n-1 and M_i is found using the following matrix equation

$$
\begin{bmatrix}
1 & 0 & 0 & 0 & \cdots & 0 & 0 & 0 \\
1 & 4 & 1 & 0 & \cdots & 0 & 0 & 0 \\
0 & 1 & 4 & 1 & \cdots & 0 & 0 & 0 \\
& & & \cdots & & & & \\
0 & 0 & 0 & 0 & \cdots & 1 & 4 & 1 \\
0 & 0 & 0 & 0 & \cdots & 0 & 0 & 1
\end{bmatrix}
\times
\begin{bmatrix}
M_1 \\ M_2 \\ M_3 \\ \cdots \\ M_{n-1} \\ M_n
\end{bmatrix}
= 6 \times
\begin{bmatrix}
0 \\
H(s_1) - 2H(s_2) + H(s_3) \\
H(s_2) - 2H(s_3) + H(s_4) \\
\cdots\cdots\cdots\cdots\cdots\cdots\cdots \\
H(s_{n-2}) - 2H(s_{n-1}) + H(s_n) \\
0
\end{bmatrix}
$$

(11)

With this method, the curve ends up being and continuous and smooth across all the data points.

3. Cauchy Method:

The Cauchy approximation method was laid out by A.L. Cauchy in the nineteenth century. It has been widely used as a method of interpolating frequency-domain data of different kinds ([8],[9]). This paper uses the method modelled by Adve et al.[8]. The interpolated signal, referred to as H(s) is defined by

$$H(s) \cong \frac{A(s)}{B(s)} = \frac{\sum_{k=0}^{P} a_k s^k}{\sum_{k=0}^{Q} b_k s^k} \qquad (12)$$

H(s) is formed by the division of two polynomials, one of order P with P+1 coefficients, and the other of the order Q with Q+1 coefficients. In our model, $a_0=1$ was arbitrarily chosen as it only affects the scaling factor on the other coefficients in H(s). Another point to be noted is that the points need not be equally spaced[9].

For notation purposes, let N = the number of data points being analyzed. The numerator and denominator coefficients can be written in the following form:

$$[a] = [1, a_1, a_2, \cdots a_P]^T \qquad (13)$$
$$[b] = [b_0, b_1, b_2, \cdots b_Q]^T \qquad (14)$$

The equation can then be written as

$$[A]a = [B]b \qquad (15a)$$

or

$$[B \quad -A] = \begin{vmatrix} b \\ a \end{vmatrix} \qquad (15b)$$

where [A] and [B] are N x (P+1) and N x (Q+1) respectively such that

$$A = \begin{vmatrix} s_1^0 & s_1^1 & \cdots & s_1^P \\ s_2^0 & \ddots & & \vdots \\ \vdots & & \ddots & \vdots \\ s_{P+Q+1}^0 & \cdots & \cdots & s_{P+Q+1}^P \end{vmatrix} \qquad (16)$$

$$B = \begin{vmatrix} H(s_1) * s_1^0 & H(s_1) * s_1^1 & \cdots & H(s_1) * s_1^Q \\ H(s_2) * s_2^0 & \ddots & & \vdots \\ \vdots & & \ddots & \vdots \\ H(s_{P+Q+1}) * s_{P+Q+1}^0 & \cdots & \cdots & H(s_{P+Q+1}) * s_{P+Q+1}^Q \end{vmatrix} \qquad (17)$$

166

For notational simplicity define

$$C \equiv \begin{bmatrix} B & -A \end{bmatrix}$$ (18)

Values for P and Q must then be chosen to get a high enough order approximation without returning a singular matrix. As stated in Adve et. al[8], For the system to be stable, P must be larger than Q. As an initial step, P and Q were chosen so that the equation P + Q + 1 = N. With a_0 preset at 1, this leaves one coefficient for each data point. As in Adve et al.[8], the singular value decomposition was used to obtain

$$[U][\Sigma][V]^H \begin{bmatrix} a \\ b \end{bmatrix} = 0$$ (19)

where U and V are unitary matrices and V is a diagonal matrix with the unitary values of C. The rank of Σ was calculated using a tolerance setting such that any singular value less than ten orders of magnitude below the maximum value were taken to be 0. For ease of notation define R ≡ rank of Σ. P and Q are then redefined so that

$$P+Q+1=R$$ (20)

For even values of R, P and Q were chosen so that P = Q + 1. For odd values, they were chosen so that P = Q + 2. Finally, the system was solved using the method of Total Least Squares (TLS). For an in-depth evaluation of the method of TLS, see the appendix of Adve et al.[8].

These three approximation methods were applied to three different sets of FDTD data, each with a different electron density profile. The first set of data was generated using the electron density profile to be zero at all points within the cavity between the earth and the ionosphere. The second and third sets of data used generalized daytime and nighttime electron density profiles, respectively. The profiles used were from the exponential two-parameter profile laid out by Cummer[3]. The model profile used is as follows:

$$N_e(h) = 1.43 \times 10^{13} \exp(-0.15h') \exp[(\beta - 0.15)(h - h')]$$ (21)

For the daytime profile, the values used for the two parameters were $\beta=0.3km^{-1}$ and h'=73km. For the nighttime profile, the parameters used were $\beta=0.5km^{-1}$ and h'=85km. Figure I gives a graphical view of the two profiles using a semilog plot.

167
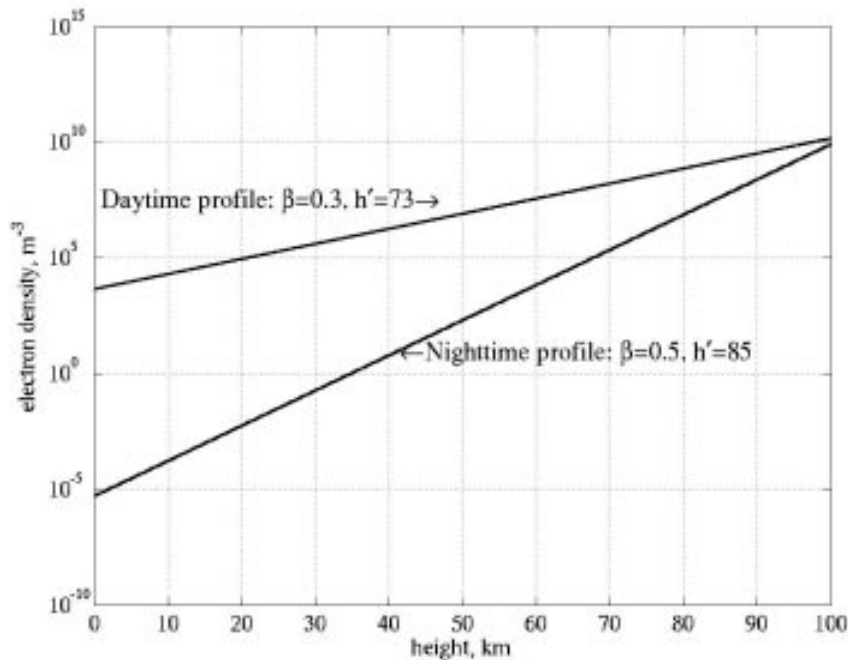
Figure I: Exponential electron density profile models for daytime and nighttime from Cummer[3].

RESULTS

In order to test out the different approximation methods, three different sets of FDTD data were analyzed. The first set of data was generated using the assumption that there was no conductivity in the cavity between the earth and the ionosphere. The results of the three approximations can be seen Figure I. The second and third sets of data were generated using daytime and nighttime electron density profiles, respectively, using the exponential equations from Cummer[3]. The approximation results of the daytime profile can be seen in Figure II, the results from the nighttime profile can be seen in Figure III. The constant values used for the daytime were $\beta = 0.3$ and h' = 73km. The nighttime values used were $\beta = 0.5$ and h' = 85km.

As noted in the experimental description, three different sets of generated data were examined, and the data was interpolated separately by all three approximation methods. Figure II shows the results of the interpolation on the zero-conductivity data set. Figure III shows the results of the daytime profile data set and figure IV shows the results from the nighttime profile data set.

168

Figure II: Results of the three approximation methods to the first set of data with a zero-conductivity electron density profile.

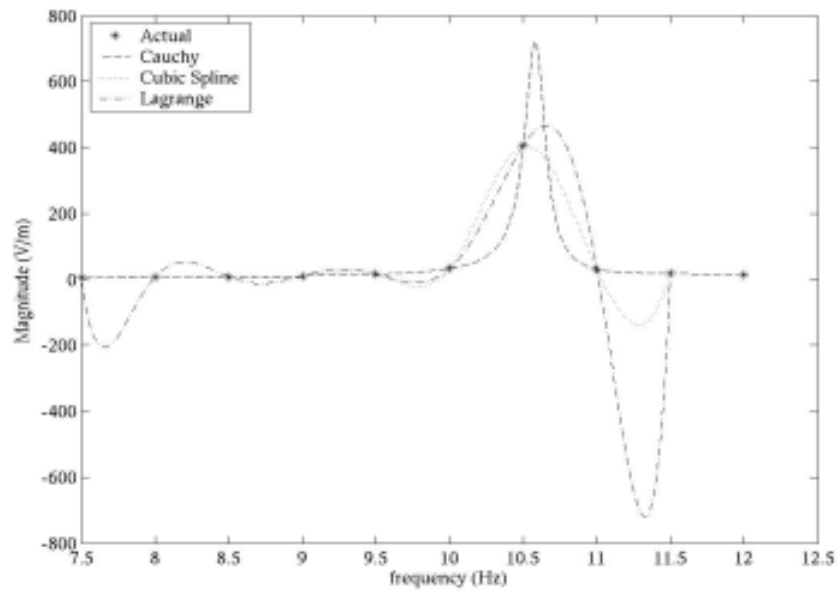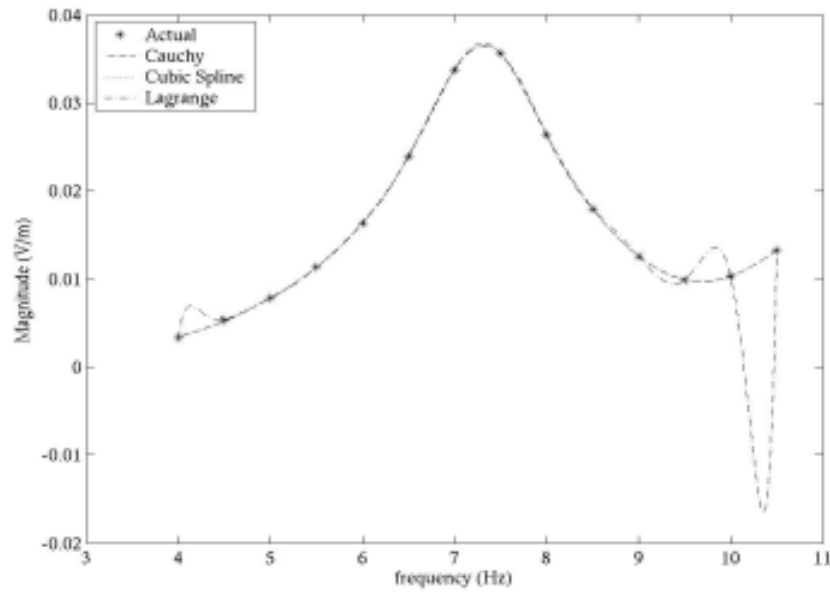Figure III: Results of the three approximation methods to the second set of data with a daytime electron density profile.

169
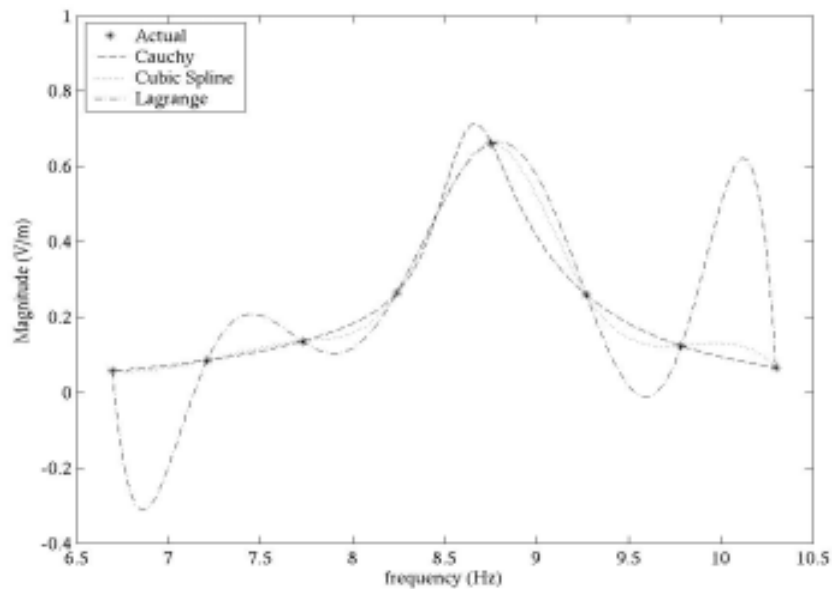
Figure IV: Results of the three approximation methods to the third set of data with a nighttime electron density profile.

In each model, the three approximations were each used to calculate the experimental Schumann frequency. These results are found in Table I.

Approximation Method	Electron Density Profile		
	No conductivity	Daytime	Nighttime
Cauchy	10.585 Hz	7.321 Hz	8.652 Hz
Cubic Spline	10.518 Hz	7.340 Hz	8.749 Hz
Lagrange	10.660 Hz	7.315 Hz	8.794 Hz
Theoretical	10.551 Hz	---	---

Table I: Calculated Schumann frequencies with Three Different Electron Density Profiles and Three Approximation Methods for Each Profile

DISCUSSION

In searching for an accurate way of finding the Schumann resonance given a set of discrete data with relatively poor resolution, we must first understand what the general shape of the data should be. With this, we can then generate the approximations and compare them to what we expect the actual data to look like. We can use this assumed picture from our mind to compare to the approximation methods because we know enough about the system and the variables affecting the system to get a general idea of what the shape of the graph should be. In fact,

170

most people could probably look at the actual data and make an estimate of the SR frequency with an accuracy at least twice the resolution of the data set. However, in this paper we are looking for a mathematical method that can approximate the data for us accurately and efficiently.

The first method tried was the Lagrange method. It is a classically popular and well-noted interpolation method that can be found in any good mathematical interpolation book (see Arlinghaus 1994, Booth 1966, Kvasov 2000). It is a polynomial type of approximation which, for this application, caused it to have poorer and poorer results as more data points were interpolated. The case where the conductivity was considered to be zero in the cavity was a very idealized and basic model of the earth, causing the data to be rather flat approaching the SR frequency. It would then have a quick spike in magnitude as it reached the SR frequency and quickly dropped back down to a relatively flat portion again. The polynomial manner of the Lagrange approximation did not allow it to follow the flat areas around the Schumann frequency, making the Lagrange approximation much different from what we assume the general shape of the actual data to take. However, the Lagrange approximation improved somewhat on the daytime and nighttime models due to the increased fluidity of the data points. In the end, it was decided that this method was not going to be able to give us the reliable accuracy we are looking for when finding the SR frequency from this data.

The cubic spline approximation was tried next as a means of approximating the frequency data. This is also a polynomial-based method. However, it is a combination of third order polynomials. The fact that it is broken up into many small order polynomial pieces allows it more ability to adapt to the changing features of the data than the Lagrange method could. It showed much improved results with all three sets of data in that it followed much more closely the general flow of the data. However, this method again had trouble following the data from the zero-conductivity data set as it dropped off and approached zero magnitude. This method showed definite improvement over the Lagrange method, but it still leaves room for more improvement with approximating this data.

The final method used to interpolate the data was the Cauchy approximation. This approximation differs from the other two in that it has both zeros and poles. Polynomial approximations such as the first two methods used in this paper tend to oscillate when trying to approximate flat unchanging data such as is found surrounding the peak of the SR frequency in these data sets. They also have trouble approximating sharp peaks. The Cauchy approximation is not limited in these ways because the poles in the denominator can make up for these weaknesses. For these reasons, and as Figures II, III, and IV obviously show, the Cauchy method gives very good interpolation results with the three sets of data examined. It especially sticks out in Figure II with the no-conductivity profile where the other two methods were obviously lacking.

It should be noted, though, that with the daytime and nighttime profiles, the Cauchy method and the Cubic Spline method were extremely similar and,

over certain stretches of the daytime data set, almost impossible to tell apart from one another by merely looking at the figures presented. From this, it can be assumed that, for real-world data, the Cubic Spline method has similar interpolating capabilities to the Cauchy method

SUMMARY

Three different methods were used to interpolate data in the ELF spectrum of electromagnetic fields in the earth-ionosphere waveguide. After thorough analysis of the methods themselves and the results of the interpolation data, some final conclusions were drawn. While the Lagrange method is a simple and popular approximation method, for the frequency data presented in this lab it makes a poor interpolation. The Cubic Spline method shows great improvements over the basic Lagrange method in all the data sets examined. However, we feel that the Cauchy approximation was the best method analyzed due to the fact that it was the most versatile, consistent and precise of the three methods analyzed. With the accurate Schumann resonance measurements obtained from the Cauchy approximation method, improved electron density profiles can be made of the lower ionosphere and improved meteorological profiles can be found.

This, of course, does not mean that the Cauchy approximation is the absolute best interpolation method in existence, and given more time it would be interesting to investigate the matter further to investigate how other interpolation methods hold up against these three. Further investigation could also include an analysis of the error functions of the different approximations. Also, data with differing shapes could be looked at to see which methods of interpolations best approximate which general forms of data.

REFERENCES
1. A. Tran and C. Polk, "Schumann resonances and electrical conductivity of the atmosphere and lower ionosphere—I. Effects of conductivity at various altitudes on resonance frequencies and attenuation," *Journal of Atmospheric and Terrestrial Physics*, vol. 41, pp. 1241-1248, (1979).
2. A. P. Nickolaenko, "Modern aspects of Schumann resonance studies," *Journal of Atmospheric and Solar-Terrestrial Physics*, vol. 59-7, pp. 805-816, (1997).
3. S. A. Cummer, "Lightning and ionospheric remote sensing using VLF/ELF radio atmospherics," Ph.D. dissertation, Department of Electrical Engineering, Stanford University, 1997.

4.   H. Rishbeth and O. K. Garriott, Ionospheric Measurements, pp. 48 and 58, *Introduction to Ionospheric Physics*, J. Van Mieghem, Academic Press, New York, 1969.
5.   B. P. Demidovich and I. A. Maron, The Interpolation of Functions, pp. 539-40, *Computational Mathematics*, Mir Publishers, Moscow, 1981.
6.   G. Micula and S. Micula, p. xi, *Handbook of Splines*, M. Hazewinkel, Kluwer Academic Publishers, Boston, 1999.
7.   S. L. Arlinghaus, Ed., p. 10, *Practical Handbook of Curve Fitting*, first edition, CRC Press, Anne Arbor, 1994.
8.   R. S. Adve, T. K. Sarkar, S. M. Rao, E. K. Miller and D. R. Pflug, "Application of the Cauchy Method for Extrapolating/Interpolating Narrow-Band System Responses," *IEEE Transactions on Microwave Theory and Techniques*, vol. 45-5, pp. 837-845, (1997).
9.   K. Kottapalli, T. K. Sarkar, Y. Hua, E. K. Miller and G. J. Burke, "Accurate computation of wide-band response of electromagnetic systems utilizing narrow-band information," *IEEE Transactions on Microwave Theory and Techniques*, vol. 39-4, pp. 682-687, (1991).

AN INVESTIGATION INTO THE MICROWAVE DIELECTRIC PROPERTIES OF HIGH-LOSS AND HIGH PERMITIVITY MATERIALS

Calvin A. Leiter*
(Michael T. Lanagan, Faculty Mentor)
Department of Electrical Engineering
Center for Dielectric Studies, Materials Research Laboratory
The Pennsylvania State University
University Park, PA 16802

*Undergraduate Student of
Chemical Engineering
The Pennsylvania State University
University Park, PA 16802

ABSTRACT

This study examined the dielectric loss of several commercially available RF absorbing materials in addition to some locally prepared thick films at 2.45 GHz, the common operating frequency of commercial microwave ovens. Microwave absorbing materials are important for shielding, heating and stealth applications. Power loss measurements were made indirectly in the form of thermal energy radiated from the dielectric material when mounted to a glass microscope slide. In addition, a vector network analyzer was used to collect scattering parameter data necessary for the calculation of dielectric properties and to verify the thermal data. The goal of this set of experiments was to find a low cost, widely available substance suitable for mass production in a disposable package. It was also desirable to discover a substantially lossy material in order to minimize the power necessary for heating and to avoid the possible breakdown of the biological substances concerned.

INTRODUCTION

Microwave measurements performed on a vector network analyzer provide a convenient method of obtaining key electrical properties of materials such as dielectric constant, dielectric loss and quality factor. Additionally, microwave

circuits are becoming increasingly popular due to miniaturization of electronic hardware and low power considerations within the biological and medical

communities. Rapid advancements in electronic circuitry and materials along with recent discoveries in the bio-medical field have prompted an interest in the microwave dielectric properties of both conventional and unconventional dielectric materials.

This study is two-fold; initially temperature measurements were recorded to determine which dielectric yielded the largest temperature ramp under an applied microwave field. The temperature rise, which is related to tan δ, or the loss of the material, is caused by conversion of microwave energy to thermal energy. The heating capability of the materials was of primary concern in this study, due to the intended application. A vector network analyzer was used to measure scattering parameters in accordance with the technique proposed by Lanagan et al[1] for high permitivity materials in order to obtain more substantial dielectric properties of the materials in the microwave region.

The intention of this study was to find a low-cost, high loss, widely available substance suitable for mass production in a disposable thick-film type package.   The commercial materials were suspected of being nearly identical in an unknown chemical composition, differing primarily in film thickness. Several other films were prepared from materials known to be very absorbent.

Principle of Measurement
Microwave dielectric properties are determined from transmitted and reflected electromagnetic waves measured using a vector network analyzer. The sample is a discontinuity for traveling waves, multiple reflections occur at the air-dielectric boundaries. A schematic representation is shown in Figure 1. The incident wave is, in fact, perpendicular to the sample; Figure 1 portrays the wave at an angle for a more convenient representation.

FIGURE I   An electromagnetic wave passing through a dielectric slab surrounded by air.
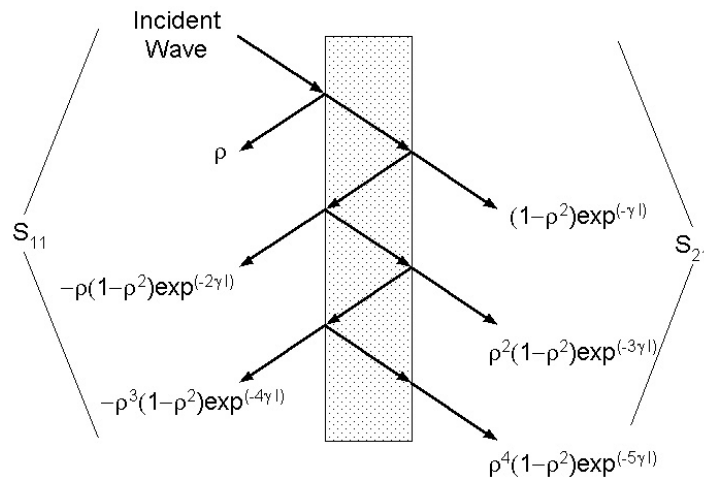
The reflected and transmitted waves are expressed in terms of a reflection coefficient, ρ, and a transmission coefficient, γ, the incident wave's amplitude is defined as unity.

The first reflected wave can be described in terms of the complex reflection coefficient:

$$\rho = \frac{1 - \sqrt{\varepsilon_r^*}}{1 + \sqrt{\varepsilon_r^*}} \tag{1}$$

Where ε_r^* is the relative complex permitivity of the dielectric material. The remainder of the incident wave is transmitted through the dielectric material until the next dielectric discontinuity is reached. The magnitude and phase of the transmitted wave are a function of the propagation coefficient, γ, which can also be expressed in terms of the real and imaginary parts of the permitivity. The relevant equations are shown below.

$$\varepsilon_r^* = \varepsilon_r' - j\varepsilon_r'' \tag{2}$$

$$\gamma = \alpha + j\beta = j\sqrt{\mu^* \varepsilon^*} \tag{3}$$

$$\alpha = \pi\sqrt{\varepsilon_r'} \frac{\tan\delta}{\lambda_0} \tag{4}$$

$$\tan\delta = \frac{\varepsilon_r''}{\varepsilon_r'} \tag{5}$$

$$\beta = \frac{2\pi\varepsilon_r'}{\lambda_0} \tag{6}$$

$$\lambda_0 = \frac{c}{\nu} \tag{7}$$

In Equations (2), (3), (4), (5), (6), and (7) ε_r' is the real part of the relative permitivity and is equivalent to the dielectric constant. λ_0 is the free space wavelength in meters, c is the speed of light in meters per second, ν is the frequency in Hertz, $\tan\delta$ is the dielectric loss and μ^* is the complex permeability.

The reflected and transmitted waves can be expressed in terms of the scattering parameters S_{11} and S_{21}, which characterize two port devices such as a waveguide connected on both ends. The scattering parameters are complex numbers, and are represented as a magnitude and phase as indicated by Equation (8).

176

$$S_{21} = |S_{21}| e^{j\theta} \tag{8}$$

The internal reflections shown in Figure 1 are accounted for by an infinite geometric series, and relationships for S_{11} and S_{21} are shown below.

$$S_{11} = \rho \frac{1 - \exp(-2\gamma l)}{1 - \rho^2 \exp(-2\gamma l)} \tag{9}$$

$$S_{21} = \frac{(1 - \rho^2) \exp(-\gamma l)}{1 - \rho^2 \exp(-2\gamma l)} \tag{10}$$

The solution of Equations (9) and (10) is non-trivial. Graphical solutions are generally required to determine the dielectric constant and loss since both equations are complex and transcendental. Another complication that may arise is that the solution of Equations (9) and (10) may yield more than one result, requiring that an approximate value of permitivity be known before the calculation is carried out.

A simplifying assumption may be made in the case of high dielectric constant and high loss materials. The series of internal reflections in Figure 1 is assumed to be negligible for such materials making only the first reflection, ρ, of any importance. In mathematical terms, $\rho^2\exp(-2\gamma l)$ is assumed to be significantly less than unity, which leads to the following simplification of Equation (10).

$$S_{21} = (1 - \rho^2) \exp(-\gamma l) \tag{11}$$

A plot of log S_{21} versus frequency is linear for Equation (11), which makes it possible to express the dielectric constant and loss in terms of the slopes of S_{21} phase and magnitude respectively.

$$\varepsilon_r' = \left(\frac{\Delta\theta}{\Delta v} \frac{c}{2\pi l} \right)^2 \tag{12}$$

$$\tan\delta = \frac{\Delta|S_{21}|}{\Delta v} \frac{8.686 \cdot c}{\pi l (\varepsilon_r')^{3/2}} \tag{13}$$

The difference between the guide thickness and the sample thickness may be accounted for by using the following equations to correct the phase of S_{21}:

$$\omega = 2\pi v \tag{14}$$

$$k = \omega \sqrt{\mu_0 \varepsilon_0} \tag{15}$$

$$k_c = \frac{n\pi}{d} \qquad (16)$$

$$\beta = \sqrt{k^2 - k_c^2} \qquad (17)$$

$$\lambda_g = \frac{2\pi}{\beta} \qquad (18)$$

$$\phi = \beta \cdot \Delta l \qquad (19)$$

$$\theta' = \theta - \phi \qquad (20)$$

In the preceding equations ω is the radian frequency, μ_0 is the permeability constant and ε_0 is the permitivity constant. In Equation (16), n =1 due to the propagation mode of the transverse electric wave, TE_{10}, and d is the height of the waveguide in the same direction as the amplitude of the traveling wave. λ_g is the wavelength of the dielectric material in the guide. ϕ is the phase shift due to the dielectric sample not completely filling the length of the waveguide in the direction of the traveling wave and θ' is the corrected phase shift of the sample, due only to the dielectric material.

The power reflected and transmitted by any element in the analyzer circuit is given by the magnitude of S_{11} and S_{21} respectively. Thus, the percentage of power absorbed by an element in the circuit may be calculated by applying the following equations:

$$\left| S_{21,linear} \right| = 10^{\frac{\left| S_{21,dB} \right|}{20}} \qquad (21)$$

$$\left| S_{11,linear} \right| = 10^{\frac{\left| S_{11,dB} \right|}{20}} \qquad (22)$$

$$PercentPowerAbsorbed = \left(1 - \left| S_{21,linear} \right|^2 - \left| S_{11,linear} \right|^2 \right) \cdot 100 \qquad (23)$$

EXPERIMENTAL DESCRIPTION

Film Preparation
Three films were prepared from base powders of various materials that were known to be highly absorbent of RF transmissions[#]. Microscope slides were masked using three layers of ordinary masking tape to create a rectangular well with an area equal to that of the commercial samples (15mm wide by 38 mm long). The various powders were combined with an organic solvent[#] and

---

[#] Materials and their composition will remain unnamed to do confidentiality and disclosure agreements with the client

178

thoroughly mixed using a mortar and pestle until a peanut butter like consistency was achieved. The pastes were then applied to the well on the slide with a metal spatula and spread evenly throughout the well using a small rubber squeegee. Once the pastes were applied to the slides, the slides were placed in a box oven at 105º C to volatilize the solvent. The slides were removed from the oven after 1 hour and the masking tape was removed leaving dried films of roughly 0.012 inches. An identical procedure was used to fill the waveguide sample holder with material for measurement.

FIGURE II   From left to right: Masked slide of area 15mm wide by 38 mm long, prepared slide with locally manufactured thick film, prepared slide with commercial RF absorbent, container of paste used to prepare the thick film.
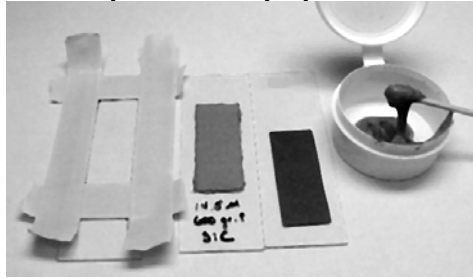
Thermal Ramp Measurements

Four commercially available RF absorbing materials[†] were affixed to glass microscope slides using the adhesive backing present on the materials. A standard sized area 15 mm wide by 38 mm long of the absorber material was used. A slot designed to hold the microscope slides upright was cut into a 1" thick Styrofoam block. The Styrofoam block was placed horizontally in the center of a microwave oven[††] glass carousel plate. The samples were loaded into the fixture with the absorbing material facing the rear of the oven and the initial temperature was recorded using an infrared thermometer[†††]. Temperature measurements were taken from the glass side of the slide opposite from the dielectric. After recording the temperature, the door to the oven was closed and the samples were microwaved on high power for 10 seconds, which also corresponded to one full revolution of the carousel. Upon hearing the first tone indicating that cooking was finished, the door to the microwave was opened and the final temperature of the sample was recorded, coinciding with the second warning tone produced by the oven. A series of ten measurements of each of the three prepared films, a blank control slide, and the four commercial substances was performed. The temperature ramp of each sample was determined by

---

[†] Exact products will remain unnamed due to confidentiality and disclosure agreements with the client
[††] 600 Watt General Electric Microwave Oven, Model Number JE635
[†††] Raytek Raynger non-contact thermometer, model number ST80

179

subtracting the initial temperature from the final temperature. The mean temperature ramp and standard deviation for the series of measurements was calculated.

FIGURE III   Photo of the experimental equipment used to take thermal measurements including the microwave oven, infrared thermometer and Styrofoam block with sample.

Network Analyzer Measurements

A network analyzer[*] was employed for the measurement of the dielectric samples. A standard X-band waveguide calibration kit[**] was used to account for false reflection due to the transmission lines. The equipment setup and calibration consisted of 7mm coaxial transmission lines connected to the two ports of the analyzer, coax-waveguide adapters, two offset shorts, a matched load, a sliding load and a through connection. The reference plane of the calibration was the terminal end of the coax-waveguide adapters. New samples of the dielectrics were cut and or prepared to fill the cross section of a rectangular waveguide sample holder. The waveguide sample holder was inserted between the two waveguide adapter reference planes. The frequency, log magnitude and phase of S_{21} was acquired by a personal computer using a GPIB data acquisition card and a LabVIEW program previously written for that purpose. Measurements were taken for the frequency range of 8.2 GHz to 12.4 GHz.

---

[*] Hewlett-Packard 8510C Vector Network Analyzer
[**] Maury Microwave Corporation Calibration Kit, model number X7005E

FIGURE IV   Schematic detail of the waveguide sample holder. The waveguide thickness is t, the sample thickness or path length is l and the free space within the waveguide is Δl.
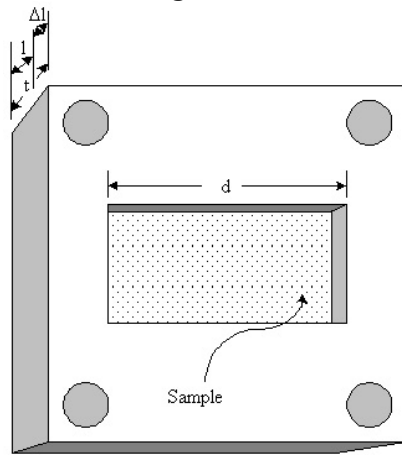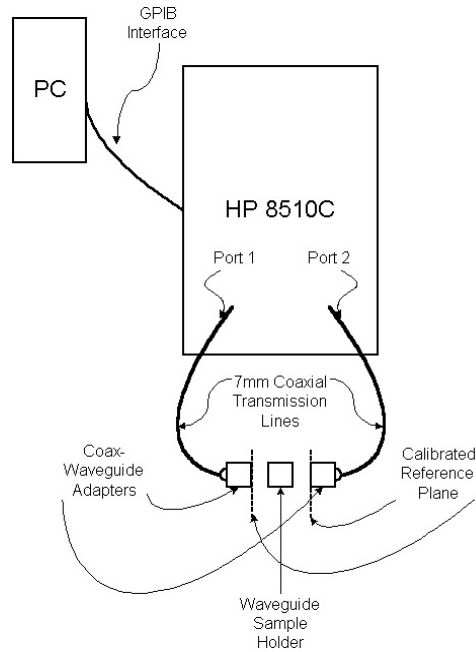

FIGURE V   Schematic representation of the equipment used to make microwave measurements.

Microwave Dielectric Properties Calculation

The acquired data was imported into MathCAD in order to perform calculations. The frequency was in units of Hertz, the log magnitude in dB and the phase in radians. The raw data for log magnitude and phase as a function of frequency was plotted and a median fit linear regression carried out. The equation of the regressed data for log magnitude was plotted on the same graph as the raw data for visual comparison. The phase shift was corrected using Equations (14)-(20) and then plotted on the same graph as the raw and regressed data for the phase as a function of frequency.

The dielectric constant and loss of the samples were calculated using Equations (12) and (13). The value obtained for the real part of permittivity from Equation (12) was substituted into Equation (10) in addition to a guessed value for the loss tangent. A calculated value for S_{21} was subsequently generated. The calculated value of S_{21} as a function of frequency was plotted in conjunction with the raw S_{21} data for visual comparison. This process was to be carried out iteratively using MathCAD until a reasonable match between the calculated value(s) and the raw data for S_{21} was obtained.

181

The results of the dielectric constant and loss tangent calculation were suspect; no good correlation between the measured and calculated scattering parameter (S_{21}) could be obtained. The results of the calculations are included in this paper for posterity.

The power absorbed by the sample was calculated using Equations (21)-(23) and compared with the observed trends from the thermal measurements.

RESULTS

TABLE I   Sample identification key

Sample Name	Abbreviated Identifier
Blank 'control' slide	B
Commercial Sample #1	C1
Commercial Sample #2	C2
Commercial Sample #3	C3
Commercial Sample #4	C4
Prepared Sample #1	P1
Prepared Sample #2	P2
Prepared Sample #3	P3

Thermal Data

TABLE II   Results of thermal measurements of the commercially obtained RF absorbing materials and locally prepared thick films.

	B	C1	C2	C3	C4	P1	P2	P3
Initial Temperature	24.52	24.41	24.84	24.64	25.02	24.28	24.38	24.2
Final Temperature	27.73	33.85	37.9	53.47	60.69	39	44.37	44.37
Temperature Change	3.21	9.44	13.06	28.83	35.67	14.72	19.99	20.17

TABLE III   Film thickness and temperature ramp data for all samples.

	B	P1	C1	P2	P3	C2	C3	C4
Thickness (mm)	0.000	0.279	0.330	0.330	0.406	0.864	1.016	1.168
Temp. Ramp (ºC/s)	0.321	1.472	0.944	1.999	2.017	1.306	2.883	3.567
Norm. Temp. Ramp (ºC/mm-s)	0.321	5.268	2.859	6.054	4.963	1.512	2.838	3.053

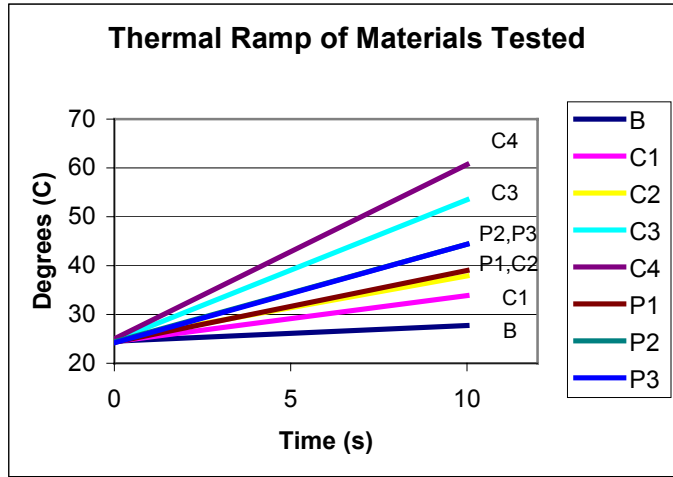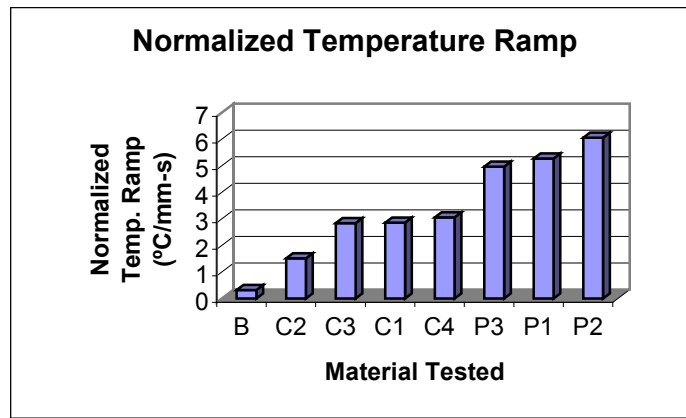**FIGURE VI   Graphical representation of thermal ramp of materials.**

**FIGURE VII   Graphical representation of temperature ramp per 1mm thickness.**

Dielectric Properties

TABLE IV   Calculated values for the dielectric constant – ε', the quality factor – Q, and dielectric loss – tan δ and absorbed power for the materials tested.

	C1	C2	C4	C3	P3	P2	P1
ε'	419.805	75.315	78.14	67.435	3.35	2.8	1.7
Q	32.335	4.665	4.195	2.14	0.032	0.026	0.026
tan δ	0.031	0.2145	0.2385	0.4675	31.22	38.15	38.205
Absorbed power	12.50%	21%	39.80%	35.70%	20%	24.50%	19%

FIGURE VIII   Graphical comparison of the thickness and power absorbed by the materials tested.

183

Absorbed Power vs. Material Thickness
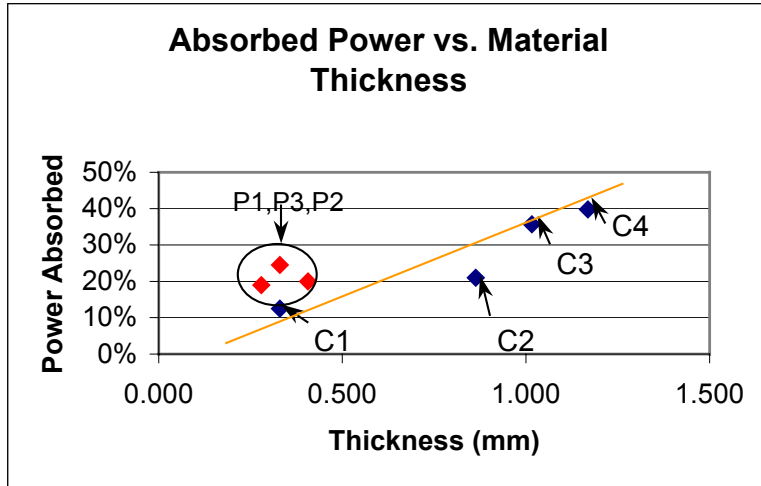
DISCUSSION

The commercial samples followed the expected trend with respect to material thickness in both thermal measurements and absorption calculations. The prepared samples fared well compared to the commercial samples. The maximum temperature reached by the prepared samples was not as high as some of the commercial samples, but the temperature achieved by the prepared samples per unit thickness exceeded that of all the commercial samples. As previously stated, the temperature rise of the material is directly related to the dielectric loss of the material. The materials ranked in order from lowest to highest, in terms of maximum temperature reached, were: B<C1<C2≈P1< P2≈P3<C3<C4 (FIGURE VI, TABLE II). However, in terms of the maximum temperature reached per unit thickness, the materials ranked thus: B<C2<C3≈C1≈C4<P3<P1<P2 (FIGURE VII, TABLE III). The calculated dielectric loss, based on microwave measurements, was expected to mirror this trend.

Several problems were encountered with the calculation of the dielectric properties of the materials. The technique used is known to be troublesome when calculating the loss of the material, and hence the quality factor also. In addition, sample size is important when using this method. If the sample is too thin, then the approximation made in Equation (11) no longer holds true; however, if the sample is too thick, then the accuracy of the network analyzer in measuring transmission data may be questionable. All samples measured in this study were considerably thinner (by a factor of at least 5) than samples of known dielectric properties used as a reference and verification of the validity of the technique and calculations.

 The results of the loss calculations did not coincide with the results of the thermal measurements. Using the procedure described above, it was impossible

184

to correlate the measured and calculated transmission data. If the dielectric constant was altered, a poor match could be obtained, but this would reduce the experiment to a guessing exercise and produce questionable results. As TABLE IV shows, the materials ranked in order of ascending loss were: C1<C2<C4<C3< P3<P2<P1. The calculated loss for the three prepared samples was at least two orders of magnitude greater than the calculated loss of the commercial samples. This fact, coupled with the problems in obtaining a match between the measured and calculated transmission data, prompted the calculation of absorbed power in order to validate the thermal measurements.

The materials, ranked in order of ascending power absorption, as indicated in TABLE IV, were: C1<P1≈P3≈C2<P2<C3<C4. This trend very closely matched the observed trend for maximum temperature. There were minor differences in the region where the four materials, P1, P2, P3 and C2, had roughly equivalent values; but these differences are well within the margin of error.

FIGURE VIII represents two key findings of this study very nicely. First, the assumption that the commercial samples were possibly constructed of the same material is given validity by the apparent linear dependence of power absorption on sample thickness as evidenced by the line drawn through the data set. Secondly, the prepared films were much more absorbent per unit thickness than the commercial samples. They present themselves as real possibilities for incorporation into low-cost, mass-produced microwave absorbing materials.

CONCLUSION
The microwave measurement technique used in this experiment was proven to be ineffective for these particular samples. It is believed that the samples were too thin, making the approximation that this technique is based on invalid in this circumstance.
Although no reliable values for the dielectric properties of these materials were calculated, the experiment still proved to be successful in its primary goal. Thermal data was successfully gathered and verified by the use of a vector network analyzer to collect the scattering parameter data necessary for performing calculations of absorbed power.

The prepared samples were made from a readily obtainable, low cost medium and proved to be superior in terms of their heating value per unit thickness, or volume. The medium used is capable of being cast in thick films to provide better-quality heating value in the same manner as the commercial samples now used in the process, or being integrated into other materials for the purpose of consolidation and miniaturization.

ACKNOWLEDGEMENTS

REFERENCES

M. T. Lanagan et al, "A Microwave Dielectric Measurement Technique for High Permitivity Materials," *Ferroelectrics,* Vol. 82, pp. 91-97, 1988.

BZT:MgO COMPOSITES FOR TUNABLE FILTER APPLICATIONS

George Y. Li
(Edward Alberta, Ph.D., A.S. Bhalla, Prof., Faculty Mentors)
Department of Electrical Engineering and Materials Research Laboratory
Pennsylvania State University, University Park, PA 16802

Undergraduate student of:
Department of Electrical and Computer Engineering
Rutgers University, Piscataway, NJ 08854

ABSTRACT

The figure of merit for the tunable dielectric resonator materials is defined as

$$\text{K-factor} = \text{tunability} * \text{electrical quality factor} \qquad (1)$$

In that context, the behavior of $Ba(Zr_xTi_{1-x})O_3$-BZT (x=0.25 and 0.3) ceramic is currently studied. The effect of electric field on the dielectric properties of BZT ceramics with a ferroelectric–relaxor behavior is observed. The permittivity, dielectric loss, and tunability information are obtained for BZT ceramic at temperatures in the range of 14 to 300K and under electric field ranging from 0-30kV/cm, using a cryogenic dielectric measurement system. The results obtained indicate that this lead-free perovskite material is a promising candidate for tunable materials in a range of temperatures, including space ambient temperatures, because of the exhibited high tunability and low dielectric loss.

INTRODUCTION

Electric field tunable materials have been studied extensively in recent years due to their potential applications in tunable filters, antennas, phase shifters, etc. These applications require a material that demonstrates high tunability, low dielectric loss, and desired permittivity. Electric tuning is defined by using an external electrical field to alter the RF characteristics of the material, such as its capacitance.[1] One example of an application of this technology is, by using the tunable characteristic of BZT ceramics, one can potentially replace multiple filterbanks with a single tunable filter. As a result, there has been great interest in materials that are tunable with an electric field.

$BaTiO_3$ is a well-known ferroelectric material that has been widely

studied, but when used as a microwave material suffers from high dielectric constant, temperature dependence of dielectric constant, high dielectric loss, a destructive phase transition near room temperature, and is difficult to have reproducible performance (due to large thermal hysteresis.) Partially substituting Zirconium, Zr, in place of Titanium, Ti, yields a material referred to as BZT, a solid-solution system, in which the phase transition temperatures vary with the Zr/Ti ratio. [1,2] Using Zr to replace Ti in the solid solution yields a pinched phase transition, which lowers the permittivity, and helps the material's dielectric properties become less temperature dependent by obtaining the paraelectric phase at room temperature. Manipulating the Zr concentration in BZT yields different and controlled properties, which are in turn, useful in an array of different applications.

To further enhance the properties of BZT it can be made into a composite by mixing it with MgO, a well-known microwave material with low absorption. [3] This is done to modify the high dielectric constant and loss characterized by BZT to levels suitable for microwave devices. With the introduction of MgO, and its low dielectric constant and loss, a suitable permittivity (100-400) can be obtained by following a dielectric mixing rule:

$$\log \kappa_{eff} = \log v_1 \kappa_1 + \log v_2 \kappa_2 + \cdots + \log v_N \kappa_N \qquad (2)$$

where κ_{eff} is the effective permittivity of the composite, κ_N is the permittivity of the component N, and v_N is the volume fraction of component N.

We are particularly interested in the composite's cryogenic properties which will help determine its feasibility in space and its integration with super conductor device applications. This composite has yielded low losses and high tunability in the −145 to -100°C range (for both x=0.25 and 0.3).

BZT is also of high interest because it is a lead-free compound. Environmental concerns are a contributing factor driving the exploration for lead-free piezoelectric and dielectric materials.

EXPERIMENTAL PROCEDURE

The BZT-MgO composites were prepared using conventional ceramic processing methods as described in Ref. 4. [4] The compositions studied were Ba(Zr$_{0.25}$Ti$_{0.75}$)O$_3$:50wt%MgO [BZT25] and Ba(Zr$_{0.30}$Ti$_{0.70}$)O$_3$:50wt%MgO [BZT30].

The composite is then polished (12um diamond paste) to create a parallel plate- the ideal capacitor configuration. Gold is then deposited by sputtering, to form the electrodes. Silver wire is attached to each electrode, allowing the connection to the leads.

Dielectric constant and loss (and also pyroelectric coefficient) measurements are made using an automated measurement system. This system consists of an LCR meter (HP-4284, Hewlett-Packard Inc.), closed–cycle helium cooled cryostat (HC-2, APD Cryogenics Inc.), temperature controller (model 330,

Lakeshore Inc.), vacuum pump (Drytel 31, Alcatel), and a desktop computer. The LCR is connected to the vacuum chamber which holds the sample. The chamber is connected to the cryostat, temperature controller, and pump. The temperature controller monitors the temperature, and the temperature within the cryostat. The pump creates a vacuum in the chamber, which allows cryogenic temperatures to be reached by reducing the thermal conductivity between the sample and the outside environment. A radiation shield within the vacuum chamber further insulates the system by preventing heat transfer by radiation. (see figure 1 below for experimental set up)
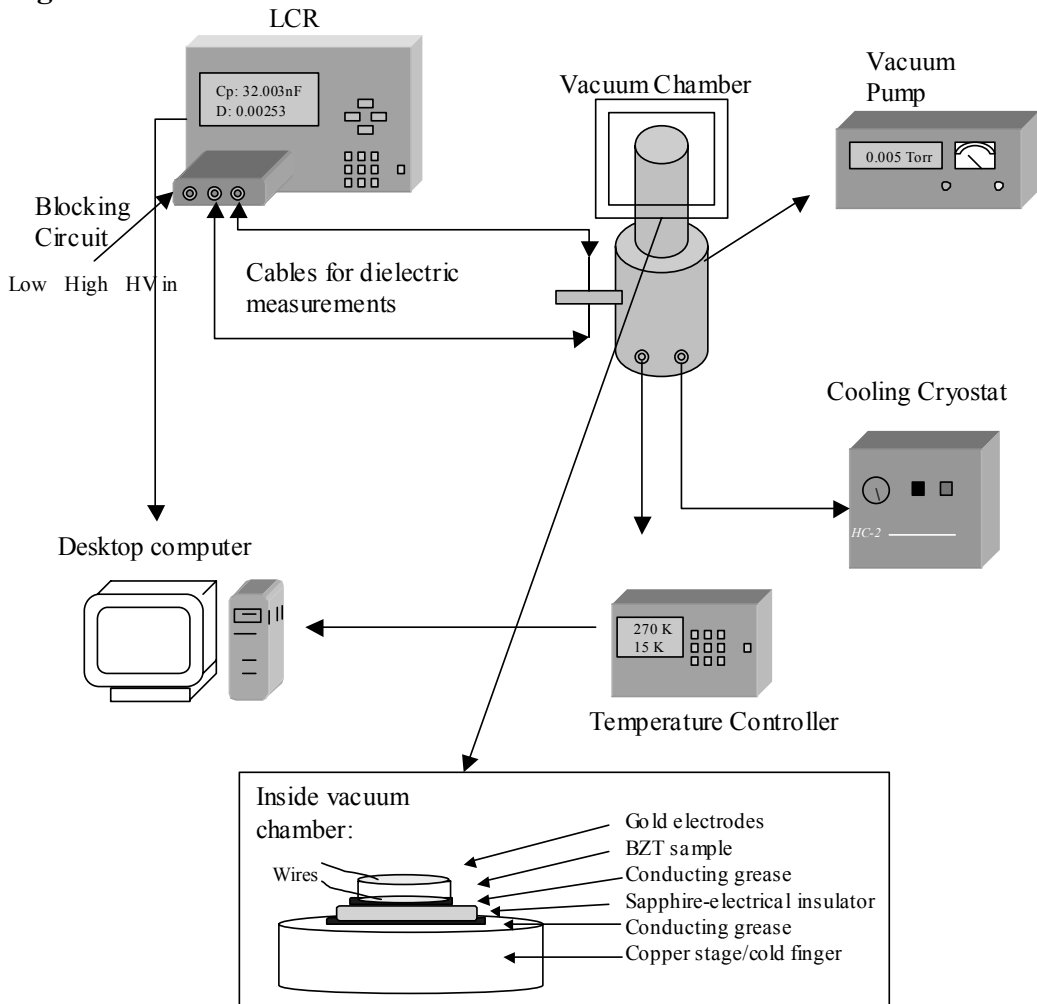
Figure 1

Figure1 The setup for the experiment is shown, with the vacuum chamber holding the sample. Refer to text for description.

Inside the chamber, we place a piece of sapphire on the copper stage (sometimes referred to as a cold finger). Thermally conductive grease is then applied above and below the sapphire, and the sample is placed on the grease.

189

The sapphire acts as an electrical insulator. The sample is then wired to the two leads. After a vacuum level is reached, the temperature is set, and the measurements are ready to start.

Dielectric measurements are made at cryogenic temperatures up to room temperature in the range of 13K to 300K at a rate of 2K/min, for discrete frequencies of 0.1 to 1MHz. Tunability is measured by measuring the dielectric constant of a sample under an applied electric field using a voltage source (TREK 610, Trek Inc.) and a high voltage blocking circuit, which effectively separates the LCR meter from the voltage (0 to 2kV) applied to the sample. The tunability is determined by finding the change in dielectric constant at zero-field compared to those dielectric values when there is an applied electric field at a given temperature, using the equation:

$$\text{Tunability} = -(\kappa(E) - \kappa(0)) / \kappa(0) \qquad (3)$$

where $\kappa(0)$ is the zero-field dielectric constant and $\kappa(E)$ is the dielectric constant that results from an applied electric field of E. The tunability is most commonly expressed as a percentage.

The dielectric loss data is also collected at each condition of temperature and field. By using equations (1) and (3), and the values of loss tangent, the K-Factor was determined and plotted as a function of temperature.

RESULTS AND DISCUSSION

1.Dielectric Behavior without Electric Field

The dielectric properties were measured for the BZT composites containing Zr concentration of 25% and 30% in the broad range of 100Hz to 1MHz. The temperature dependence of dielectric properties was observed (figure 1). The dielectric constant peaks were broad and occurred at progressively high temperatures as the measurement frequency is increased. This phenomenon is typical   for   ferroelectric-relaxor   behavior.
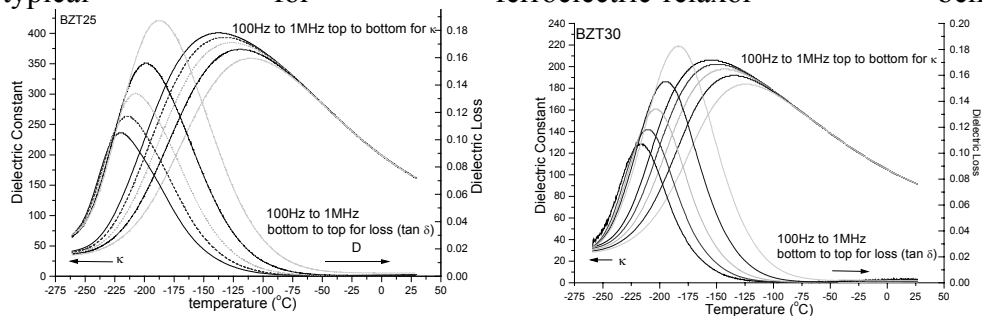

fig 1. Temperature dependence of dielectric constant and loss for BZT25 at 100Hz to 1MHz. Frequency dispersion can also be seen. For loss, 100Hz to 1MHz from bottom to top. For constant, from top to bottom.

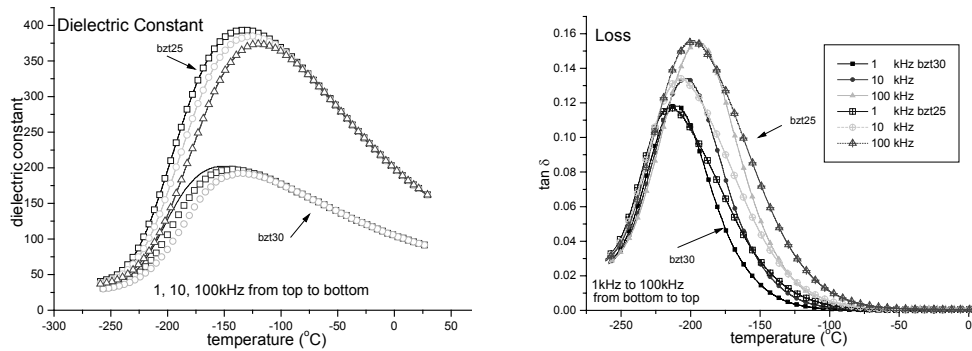fig1.1 BZT30 frequency and temperature dependence

190

fig2. BZT25,30 dielectric properties are compared.

By increasing the amount of Zr that is substituted at the Ti sites, the phase transition is shifted to lower temperatures. At 10kHz, the dielectric constants for BZT25 and BZT30 reached a high of 374 at −120°C and 192 at −134°C, respectively. Frequency dispersion can be seen, but above −125°C, dielectric constant of BZT30 is nearly independent of frequency. This also occurs for BZT25, at above −100°C.

With increasing Zr content, it can be seen that the loss peak is moved towards higher temperatures, as the transition point for permittivity is moved toward lower temperatures. The loss peaks for BZT25 and BZT30 were at −199°C and −195°C, respectively. (see figures 2 and 3) This data agrees with that found in papers by A. Chen and A.S. Bhalla (see reference 5.)
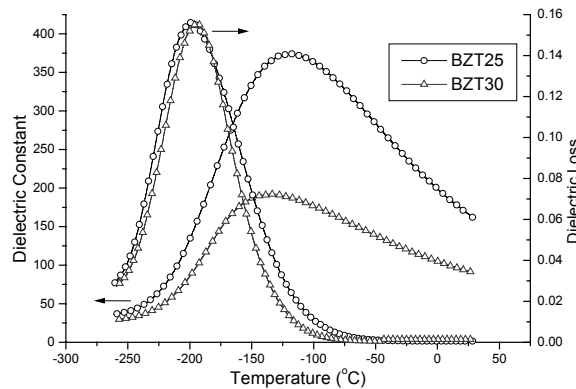

fig3. BZT 25 and 30 at 100kHz with comparison of dielectric constant, and dielectric loss changes. Note the shifting of loss peak and maximum permittivity.

2. Dielectric Behavior with An Applied Electric Field

The temperature was held steady at specified temperatures, and the electric field is manipulated, 1) increasing from 0 to 30kV/cm, 2) decreasing to 0kV, 3) switching polarity and decreasing to −30kV/cm, increasing to 0kV, and back up to 30kV/cm.
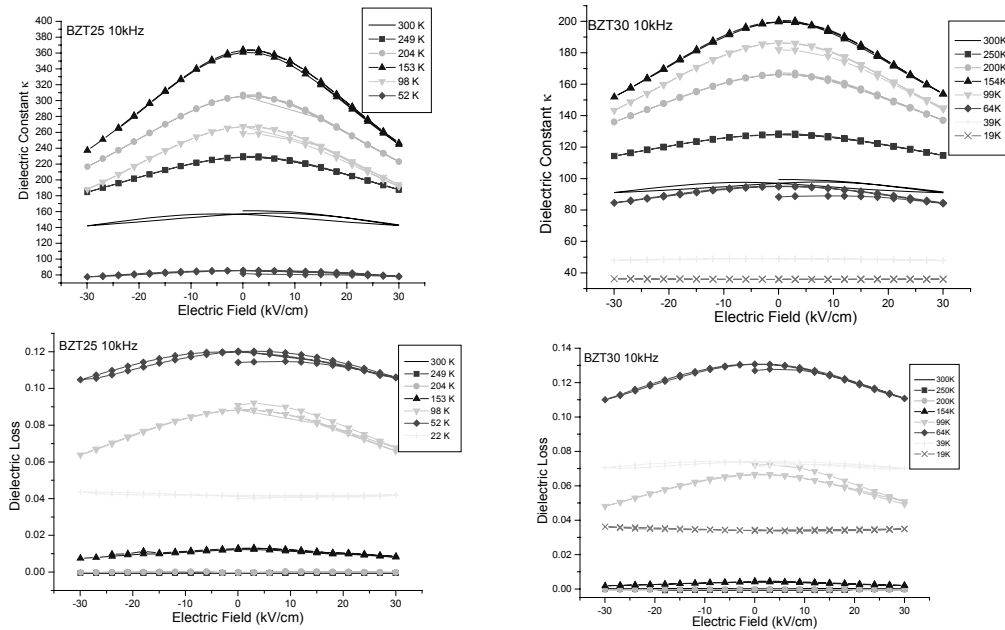
fig4. comparison of dielectric constant and loss for BZT25 on left and BZT30 on right under varying levels of electric field

The dependence of dielectric properties on electric field can be seen in figure 4, in general the dielectric constant and loss values decrease with increasing field magnitude. The effect of electric field is noticeably stronger near the phase transition temperature, in the -175°C to -50°C temperature range. (100K to 220K) The tunability is highest between -120°C and −145°C, and reaches 32.3% and 24.2% for BZT25 and BZT30, respectively at 30kV/cm (see fig 5.)
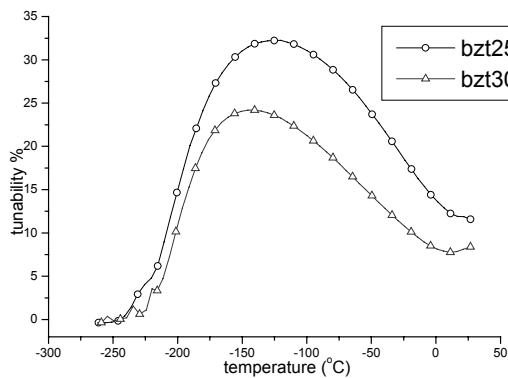

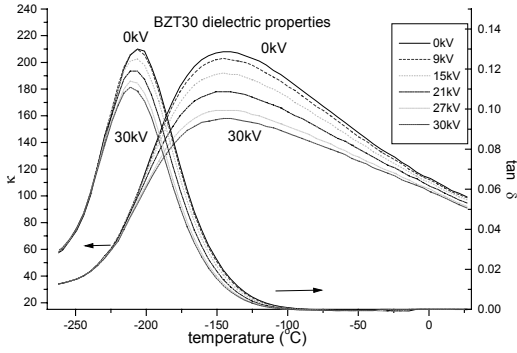fig 5 Tunability comparison at 100kHz. Highest tunabilty can be seen in −145°C to −120°C range.
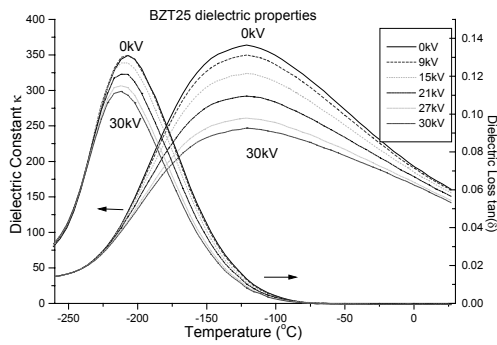
fig6 dielectric constant, loss under different electric fields at 10kHz for BZT25 and BZT30
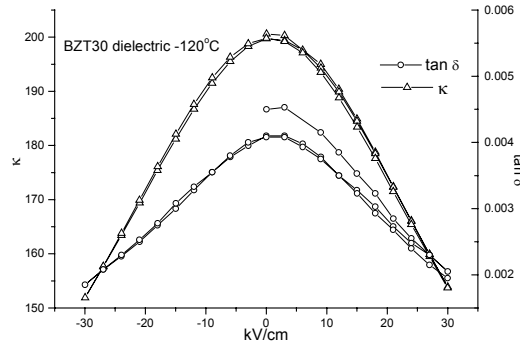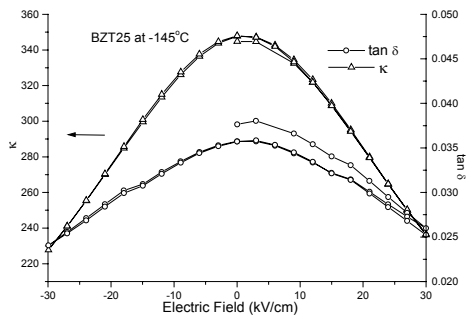

fig7 dielectric properties at max tunability temperature for BZT25 and BZT30, at -145°C and -120°C respectively. (10kHz)
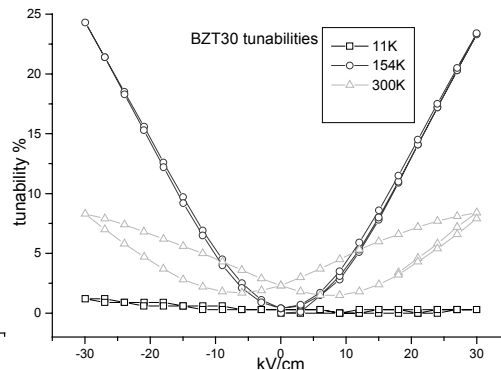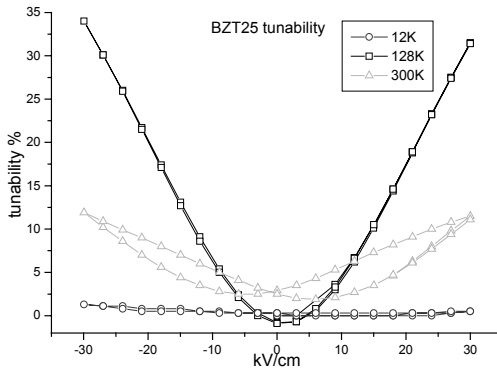

fig8 BZT25 and BZT30 tunability dependent on field and temperature at 10kHz

The dielectric properties of BZT30 are similar to that of BZT25 when under electric field. Losses are lower, but tunability is also lower. The calculated K-factor (figure of merit) can be found in figure 9. The K-factor was found to reach maximum values of 645 and 484 for BZT25 and BZT30 respectively.
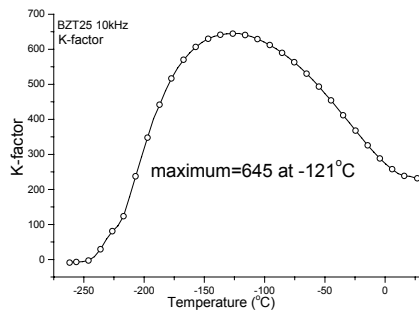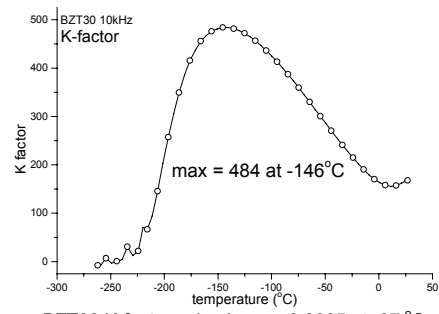
fig9 K-factor for BZT25 using loss=.0005 at -80°C

BZT30 K-factor using Loss = 0.0005 at -67 °C

fig9. Temperature dependence of the K-factor for BZT-25 and BZT-50 composites

Scanning electron microscope (SEM) study showed that the MgO was randomly dispersed in the BZT matrix (see figure 10). The tendency of MgO to absorb water has been observed in other composite ceramics and is known to impact on the conductivity of the composite material. However, we believe that water absorption was not a problem in our measurements because minimal leakage currents were observed during the high-field dielectric measurements.
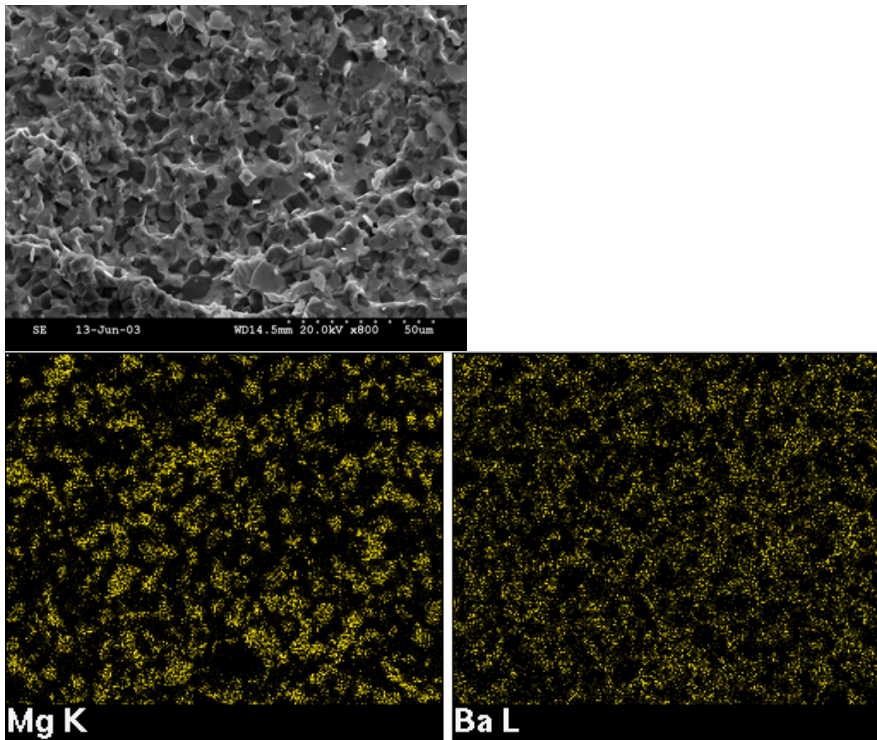

fig 10. Microstructure of a BZT25 composite. (Top) SEM image (bottom) Distribution of Mg and Ba as determined by EDS (energy dispersive spectroscopy).

CONCLUSION

The ferroelectric and dielectric properties of BZT25 and BZT30 have been studied. The field dependence of dielectric constant yields high tunability, characteristic of BZT, and decreasing dielectric constant due to MgO additive. The results show that BZT is a promising material that can be used in applications ranging from tunable filters to antennas. As a lead-free material, it is environmentally friendly, and can be useful in current attempts to reduce usage of lead containing piezoelectric materials.

There are many applications of this technology, such as tunable filters and phased array antennas. Current radar technology requires use of switched filterbanks that turn on and off according to the frequency of the received signal. With a single tunable filter, one can shift the filter's passband to match the incoming signal frequency. Having a single tunable filter instead of multiple switched filterbanks results in reduced weight of the RF device, and allows the smooth transition from each passband with the use of electric field.

In conclusion, the dielectric behavior of BZT 25 and 30 shows high tunability in the -145°C to -120°C range, and has losses lower than 0.001 at temperatures above -50°C, indicating that BZT:MgO composites are indeed promising tunable materials. In future work, by varying the x value in $Ba(Zr_xTi_{1-x})O_3$-BZT ceramics, one will be able to control the transition temperature as desired.

ACKNOWLEDGEMENT

REFERENCES

[1] Zhi Yu, C. Ang, R. Guo, and A.S. Bhalla. Applied Physics Letters, V.81number 7, August 12 2002

[2] Zhi Yu, C. Ang, R. Guo, and A.S. Bhalla. Journal of Applied Physics, V.92 number 3, August 1 2002

[3] E.F. Alberta, R. Guo, and A.S. Bhalla. Novel $BZT:MgTiO_3$ Composites for frequency agile applications, Ferroelectrics, V.268 p169 2002.

[4] Zhi Yu, R.Guo, and A.S. Bhalla, Applied Physics Letters, V.77, 1535 (2000).

[5] A. Chen and A.S. Bhalla, Journal of Applied Physics (to be published).

PROPERTIES OF NICKEL RING RESONATORS IN THE MICROWAVE FREQUENCY RANGE

Lance Haney*
(Dr. Michael Lanagan, Faculty Mentor)
Department of Electrical Engineering and Materials Science
Pennsylvania State University, University Park, PA 16802

*Undergraduate Student of
The Department of Electrical and Computer Engineering
Mercer University
Macon, GA 31207

ABSTRACT

Ring resonators deposited with nickel ink with screen-printing techniques were compared with ring resonators that have silver ink deposited on them. The electrical properties of nickel ring resonators were explored, while the silver ring resonators were used as a base case to compare with previous experiments. The ring resonators were placed on a substrate of alumina (Al_2O_3) by a screen-printing process.

Microwave analysis was performed on the ring resonators using the Hewlett Packard Network Analyzer 8510. The dielectric constant (ε_r) for the alumina substrate was determined using the split cavity approach. Next, the experimental Q values at different peak frequencies for the nickel ring resonators were obtained. At different frequencies an effective dielectric constant (ε_{eff}), skin depth (δ_s) and surface resistivity (R_s) were calculated. Also, theoretical calculations were made for the attenuation and Q values of the ring resonators and these values were then compared to the experimental results.

INTRODUCTION

Resonators are a very important part of digital devices for the telecommunications industry. They are widely used to form a basic part of both band-pass filter (BPF) and voltage controlled oscillator (VCO) circuits [1]. The frequency range that is explored in this research project is the microwave frequency, which ranges from 300 MHz to 300 GHz. With these high frequencies, the electromagnetic waves do not penetrate deep into the metal in which they travel and thus the current travels on the surface of the conductor. This effect is called the skin effect [2].

Investigating the properties of nickel, one of the three main ferromagnetic materials, could provide interesting future applications. One of fascinating applications that studying the properties of nickel as a ring resonator comes from the fact that once a ferromagnetic material is exposed to an external magnetic field, it is capable of staying in that state for an extended period of time [3]. This tendency, called hysteresis, makes nickel and other ferromagnetic materials a very useful material for computer memory devices built with thin films of electromagnetic materials [4].

With ferromagnetic material each atom has a relatively large dipole moment, caused by uncompensated electron spin moments [3]. Iron, nickel, and cobalt are the only elements that are ferromagnetic at room temperature. These elements all exhibit the ferromagnetic behavior up to what is called the Currie temperature (T_C). At the Curie temperature the thermal energy of lattice vibrations in the crystal can overcome the potential energy of the exchange interaction and destroy the spin alignments [5].

Ferromagnetic metals and alloys with large relative permeability values, offer higher attenuation values at low frequencies. At higher frequencies, greater than 100 kHz, the permeability values degrade for most of the ferromagnetic materials [6]. Another factor that is known to cause permeability to decrease is the amount of porosity present within the sample [7].

EXPERIMENTAL DESCRIPTION

The major purpose of this experiment was to perform microwave analysis on the nickel ring resonators in order to determine the values for various electrical properties. The dielectric constant (ε_r) for the alumina substrate was determined using the split cavity approach. Next, the experimental Q values at different peak frequencies for the nickel and silver ring resonators were obtained. At different frequencies an effective dielectric constant (ε_{eff}), skin depth (δ_s) and surface resistivity (R_s) were calculated. Theoretical calculations were then made for the attenuation and Q values of the ring resonators and these values were compared to the experimental results.

In addition, finite difference time domain modeling was utilized to demonstrate the flow of the electromagnetic energy through the ring resonator structure in the time domain. A perfect electric conductor (PEC) was assumed and this was used as a best case model of how a ring resonator performs in frequency range of 3.5 GHz to 15.5 GHz. With this frequency range, the first four resonant peaks were observed.

EXPERIMENTAL PROCEDURE
A. Dielectric Measurements of Alumina (Al_2O_3) Substrate

To obtain the dielectric constant of the alumina substrate that the ring resonator structures were printed on, a Gordon Kent (GDK) resonant mode dielectrometer was used. The software used to determine the dielectric constant and tan δ values of this substrate was RMDSFT V7.5. For this software, the

dimensions of the substrate are entered in. Also the peak frequencies as well as the Δf determined from the 3dB roll-off points are entered. This measurement structure can be seen in figure III.A.

Figure III.A Resonant Mode Dielectrometer
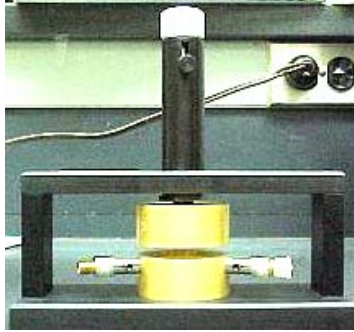

B. Production of Ring Resonators

To place the ring resonator structure on the alumina (Al_2O_3) substrate a screen-printing technique was used. With this technique, a mesh screen that has the ring pattern in it was used to place the pattern of conductive material onto the substrate. The patterns for the ring conductive plate and the base plate were already available in the lab. The substrate was placed underneath the pattern and a good amount of ink was poured in front of the squeegee. When using the squeegee, the ink was forced through the mesh screen and the ring pattern is formed on the substrate. The nickel ink used was NLP-68050 Nickel paste for inner electrodes. The silver ink used was manufactured by Dupont and was 6160 post-fire silver.

C. Heat Treatment of Ring Resonators

Once the ring patterns and the base plate were printed on the substrate, the nickel samples were heated in a furnace with a controllable atmosphere. A controlled atmosphere furnace, figure III.C.1, was used for heating the nickel ring resonators. The silver samples were heated in a Radiant Technology Company (RTC) infrared belt furnace. For the silver ring resonators, a temperature of 850° C for 15 minutes was used since the Q values for this temperature were available for comparison.

The controlled atmosphere for the heat treatment of the nickel ring resonators was needed because at high temperatures nickel is very easily oxidized. The atmosphere that was successfully used when the ring resonators were heated was 99.5% nitrogen and 0.5% hydrogen. The flow rate of the nitrogen was set to 100 standard cubic centimeters per minute.

Figure III.C.1 Controlled Atmosphere Furnace

199
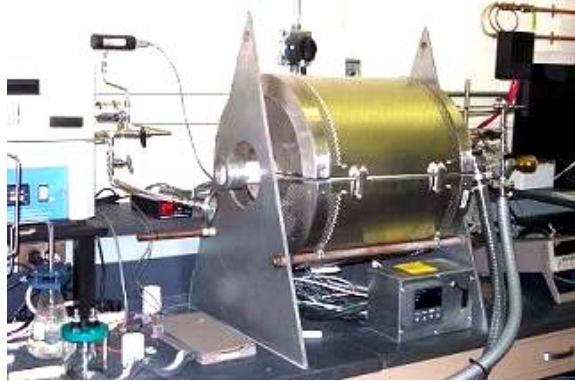
The heating process for the nickel ring resonators was set up as four stage process. In the first process the temperature was increased at a rate of 3° C per minute from the initial temperature of 66° C until the maximum heating temperature was reached. The maximum temperature was held for one hour and then a cool down phase was set to decrease the temperature at a rate of 3° C per minute. The final step was for the ring resonators to go through a soak phase at 66° C for 10 minutes. Figure III.C.2 shows a nickel ring resonator that has been fired at 1250° C.

Figure III.C.2 Nickel Ring Resonator Fired at 1250° C
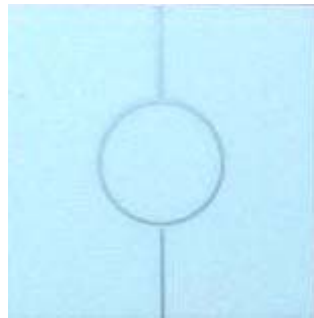
D. Observation of Microstructure within Ring Resonators

To ensure that the bonds were complete within the ring resonator structure a Hitachi S-3500N scanning electron microscope (SEM) was used. The main purpose of using the SEM was to observe the surface topography of the ring resonators and to ensure that proper bonding had occurred during the heat treatment process. The accelerating voltage was set to 20 kV to obtain the best image quality with a working distance of 5.7 mm. The image, figure III.D, as well as additional images were produced by bombarding the ring resonator with secondary electrons in a vacuum chamber.

Figure III.D Nickel Ring Resonator fired at 1300° C (x5k)

Nickel Ring Resonator
1300 C

SE 02-Jul-03 Ni1300 WD 5.7mm 20.0kV x5.0k 10um
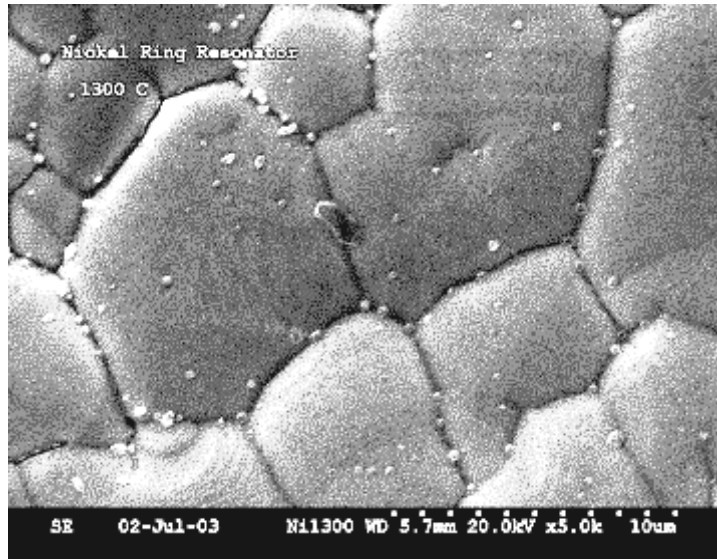
E. DC Resistivity of Nickel Ink

To determine the actual value of resistivity of the nickel ink used for the ring resonator structure a four point probe process was used, figure III.E. Samples were manufactured that had a strip of ink around the surface and had four pads that leads were connected to. At two pads a current was applied and then the voltage was measured at the other two pads. This was done to ensure that there would be an elimination of contact resistance and to obtain a more accurate value for the resistance of the nickel ink. The resistance value was calculated from the voltage measured and the current applied. The length and the cross sectional area was then measured so that resistivity (ρ) for these samples could be determined. The cross sectional area is the product of the strip conductor width and the thickness of the ring resonator structure.

Figure III.E Resistivity
Measurement Structure
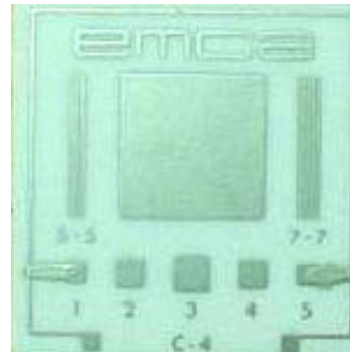
F. Microwave Analysis

The Hewlett Packard 8510 Microwave network analyzer, figure III.F.1, was the specific network analyzer used in this research to perform microwave analysis. A network analyzer is used to characterize the behavior of electronic circuits by comparing signals that come out of the circuit to the signal that went in. The frequency range that this network analyzer is capable of is 45 MHz to 26.5 GHz.

Figure III.F.1 Hewlett Packard 8510 Microwave Network Analyzer

The fixture that was used while electromagnetic energy was sent through the ring resonators was a universal substrate test fixture manufactured by Inter-Continental Microwave, figure III.F.2. This fixture is capable of testing substrates from 0.24 to 4.75 inches long and up to 75 mils thick. In order to calibrate this fixture before use, the TRL-304D Substrate (Alumina) calibration kit was used.

Figure III.F.2 Inter-Continental Microwave Fixture

EXPERIMENTAL CALCULATIONS

The dimensions of the ring resonators play a crucial role in determining the electrical properties. The diameter of the ring (D) is found by taking the average of the inner and outer diameters of the ring structure. The width of the strip conductor (W) is constant throughout the structure. The height of the alumina substrate (h) is fairly constant from sample to sample while the thickness of the ink (t) for the ring structure on the alumina substrate varies significantly within each structure and from sample to sample. To measure the thickness of the ink, a profilometer was used and a range of points were tested and then an average thickness was computed. A diagram of this ring resonator structure can be seen in figure IV.1.

Figure IV.1 Ring Resonator Structure with Dimensions
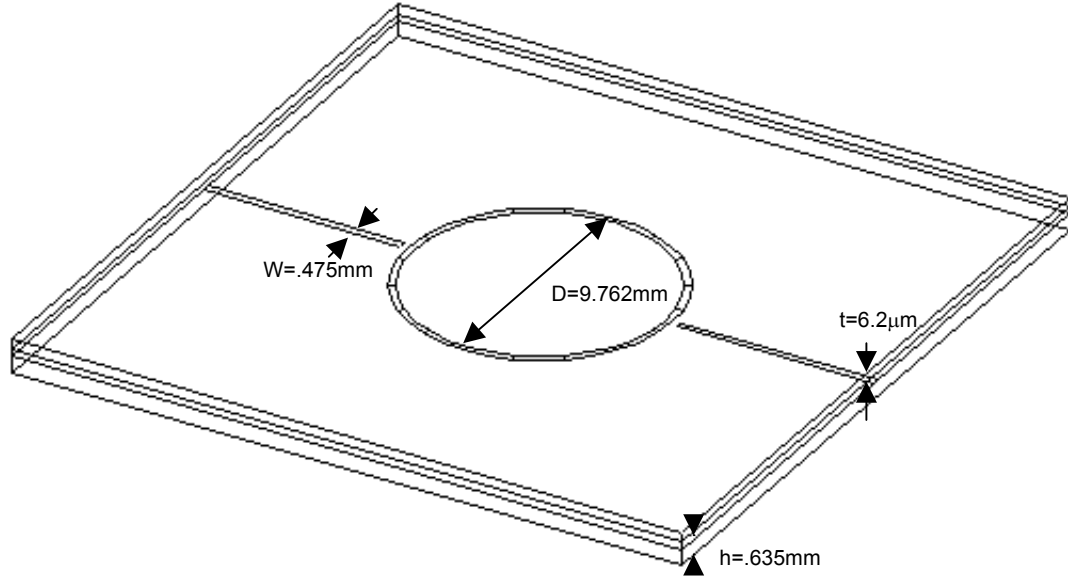
The experimentally obtained values for this experiment were the conductivity of the nickel ink used (σ), dielectric constant of the alumina substrate (ε_r), dielectric loss (tan δ), resonant frequencies (f_{Rn}), the 3dB roll off frequencies (Δf), and the S_{21} value in dB. The conductivity was found by taking the inverse of the resistivity measured, equation IV.1.

$$\sigma := \frac{1}{\rho}$$

(IV.1)

The effective dielectric constant, equation IV.2, was determined for different resonant frequencies. In this equation C_0 is the speed of light in a vacuum (299,792,458 m/s), n is the nth resonant frequency which is related to the number of wavelengths around the ring circumference, D is the ring diameter, and f_{Rn} is the resonant frequency value.

$$\varepsilon_{eff} := \left[\frac{(C_0 \cdot n)}{(\pi D \cdot f_{Rn})} \right]^2$$

(IV.2)

To calculate skin depth (δ_s) equation IV.3 was used. The fundamental units for skin depth are meters. In this equation, σ is a material property which represents the conductivity. The conductivity value (σ) for nickel used was 1.499 x 10^7 S/m and for the silver ink used was 3.125 x 10^7 S/m. The value of μ is the magnetic permeability of the medium, which is the product of the absolute permeability, μ_0, and the relative permeability, μ_r. The values are $\mu_0 = 4\pi$ x 10^{-7} H/m, for nickel μ_r varies significantly for different frequencies and for silver μ_r = 1.

$$\delta_s := \frac{1}{\sqrt{\pi \cdot f_{Rn} \cdot \mu \cdot \sigma}}$$

(IV.3)

Next, the value of surface resistivity (R_s) for nickel was determined using equation IV.4. The units for resistivity are ohm meters, Ω m.

$$R_s := \sqrt{\frac{(\pi \cdot f_{Rn} \cdot \mu)}{\sigma}}$$

(IV.4)

From surface resistivity, theoretical values can be calculated for the attenuation of the conductor, α_c, equation IV.5. The units for attenuation are Nepers per meter. This equation is used to obtain the theoretical values for Q and then to compare them to the actual values obtained in the experiment. W_e, equation IV.6, is the effective width of the resonator and Z_0, equation IV.6, is the characteristic impedance. Equations IV.5 – IV.7 are taken from Losses in Microstrip [8].

$$\alpha_c := \frac{R_s}{2\pi \cdot Z_0 \cdot h} \cdot \left[1 - \left(\frac{W_e}{4 \cdot h} \right)^2 \right] \cdot \left[1 + \frac{h}{W_e} + \frac{h}{\pi W_e} \cdot \left[\ln\left[\frac{(4\pi W)}{t} + 1 \right] - \frac{\left(1 - \frac{t}{W} \right)}{1 + \frac{t}{4\pi W}} \right] \right]$$

(IV.5)

$$W_e := W + \frac{t}{\pi} \cdot \left[1 + \ln\left[\frac{(4\pi \cdot W)}{t} \right] \right]$$

(IV.6)

$$Z_0 := \frac{60}{\sqrt{\varepsilon_{eff}}} \cdot \ln\left[\frac{(8 \cdot h)}{W} + \frac{W}{4 \cdot h} \right]$$

(IV.7)

Next, the attenuation (α_d) and the Q of the dielectric material (Q_d) are found, equations IV.8, IV.9.

$$\alpha_d := \frac{\pi \sqrt{\varepsilon_r}}{\lambda_0} \cdot \tan\delta$$

(IV.8)

$$Q_d := \frac{1}{\tan\delta}$$

(IV.9)

From these values, the Q of the conductor (Q_c) can be determined using equation IV.10.

$$Q_c := \frac{Q_d \cdot \sqrt{\varepsilon_{eff}} \cdot \pi}{Q_d \cdot \lambda_0 \cdot (\alpha_c + \alpha_d) - \sqrt{\varepsilon_{eff}} \cdot \pi}$$

(IV.10)

With both the values for the both the conductor and the dielectric material, a theoretical value for unloaded Q can be calculated as well as a theoretical attenuation, equations IV.11, IV.12.

$$\alpha_{theo} := \alpha_c + \alpha_d$$

(IV.11)

204

$$Q_{theo} := \frac{(Q_c \cdot Q_d)}{Q_c + Q_d}$$

(IV.12)

With the unloaded Q value, a theoretical loaded Q value can be calculated, equation IV.13. This theoretical value will be used to compare to the experimental results that are found for the Q values. This theoretical value should be higher than the actual value because surface roughness is not taken into effect. Also the S_{21} value entered into this equation should be in the linear scale.

$$Q_{L.theo} := Q_{theo} \cdot (1 - |S_{21}|)$$

(IV.13)

To experimentally determine the loaded Q value ($Q_{L.exp}$), the resonant frequency (f_{Rn}) values were obtained from the graph produced by the HP network analyzer after the electromagnetic wave was sent through the ring resonators. The width of these peaks (Δf_{Rn}) were then calculated by taking the frequency value at a 3db roll off to the right of the peak and subtracting from that the frequency value at a 3bd roll off to the left of the peak. With the values for f_{Rn} and Δf_{Rn} determined, equation IV.14 was used to calculate the Q value.

$$Q_{L.exp} := \frac{f_{Rn}}{\Delta f_{Rn}}$$

(IV.14)

To determine the unloaded Q (Q_{exp}) value equation IV.15 is used. In this equation, S_{21} is the transmission value of the signal sent from input 1 and received by input 2 obtained from the network analyzer. Again, S_{21} is the linear scale value.

$$Q_{exp} := \frac{Q_{L.exp}}{1 - |S_{21}|}$$

(IV.15)

The next calculation that was performed was to determine the experimental attenuation loss (α_{exp}) for the dielectric substrate, using equation IV.16. The units for attenuation are Nepers per meter.

$$\alpha_{exp} := \frac{\pi \sqrt{\varepsilon_{eff}} \cdot f_{Rn}}{C_0 \cdot Q_{exp}}$$

(IV.16)

FINITE DIFFERENCE TIME DOMAIN (FDTD) MODELING

The modeling was performed in order to show how the electromagnetic energy travels through the ring resonator structure in the time domain. The initial pulse of energy is applied and at certain frequencies resonance occurs. The frequency range that was used in the model was from 3.5 GHz to 15.5 GHz. The first, second, third, and fourth peaks are shown in figures V.1 through V.4 respectively. The peaks are symmetrical and with each higher resonance the number of peaks increases. There are two maximum peaks at the first resonance, four at the second resonance, six at the third resonance, and eight at the fourth resonance, which correspond to 1, 2, 3, and 4 wavelengths, respectively.

Figure V.1 First Resonant Peak

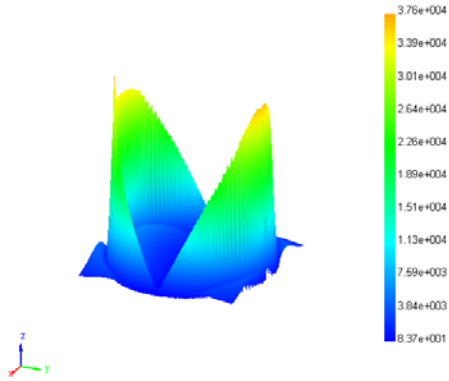3D Frequency Domain Field Magnitude First Resonant Peak 3.8 GHz

Figure V.2 Second Resonant Peak

3D Frequency Domain Field Magnitude Second Resonant Peak 7.3 GH

Figure V.3 Third Resonant Peak
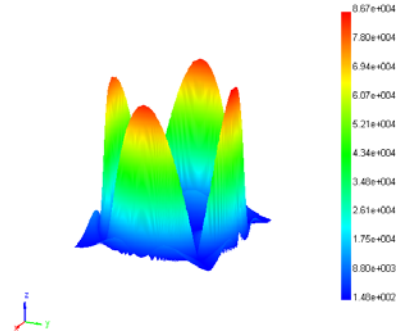
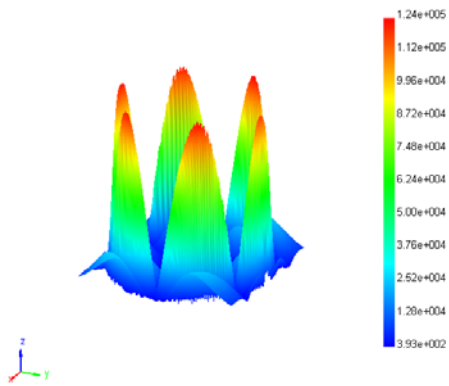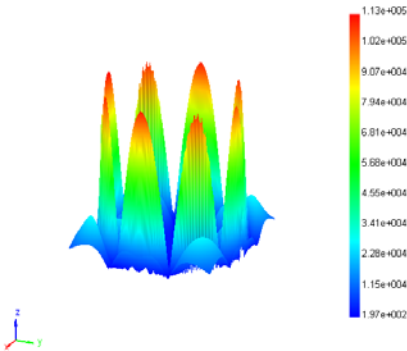3D Frequency Domain Field Magnitude Third Resonant Peak 11 GHz

Figure V.4 Fourth Resonant Peak

3D Frequency Domain Field Magnitude Fourth Resonant Peak 14.6 GH

RESULTS

A. Silver Ring Resonators

Table VI.A.1 Silver Ring Resonator Sample Fired at 850° C

Sample #2	n	Center Frequency (GHz)	reference value (dB)	Δf (MHz)	Loaded Q-value

206

	1	3.919349	-26.05	42.903	91.35373
	2	7.760094	-23.03	54.873	141.4192
	3	11.52658	-21.09	78.748	146.373

Table VI.A.2 Silver Ring Resonator Skin Depth

Sample #2	f (GHz)	skin depth δ_s (µm)	Surface Resistivity R_s (Ωm)
	3.919	1.438	0.022
	7.760	1.022	0.031
	11.527	0.839	0.038

B. Nickel Ring Resonators

Table VI.B.1 Nickel Ring Resonators Fired at 1200° C

	n	f (GHz)	reference value (dB)	Δf (MHz)	Loaded Q value	Unloaded Q value
Sample #10	1	3.9493	-31.83	133.616	29.557	30.334
	2	7.8272	-31.72	176.531	44.339	45.520
	3	11.657	-22.14	166.416	70.044	75.984
	4	15.41	-26.34	151.315	101.840	106.997
Sample #11	1	3.9346	-31.7	141.1	27.885	28.629
	2	7.8111	-31.74	165.088	47.315	48.572
	3	11.633	-21.97	127.133	91.504	99.430
	4	15.388	-25.44	121.164	127.000	134.172

Table VI.B.2 Nickel Ring Resonators Fired at 1250° C

	n	f (GHz)	Reference value (dB)	Δf (MHz)	Loaded Q value	Unloaded Q value
Sample #7	1	3.976	-32.82	123.42	32.214	32.968
	2	7.933	-33.82	163.533	48.507	49.516
	3	11.775	-22.22	153.573	76.674	83.111
	4	15.594	-26.72	160.29	97.283	101.988
Sample #13	1	3.9612	-31.58	115.673	34.245	35.173
	2	7.8457	-32.02	168.701	46.507	47.702
	3	11.727	-21.71	167.636	69.955	76.215
	4	15.484	-25.756	144.172	107.397	113.234

Table VI.B.3 Nickel Ring Resonators Fired at 1300° C

	n	f (GHz)	Reference value (dB)	Δf (MHz)	Loaded Q value	Unloaded Q value

	n					
Sample #9	1	3.985	-33.31	144.342	27.608	28.218
	2	7.9475	-33.91	147.5	53.881	54.990
	3	11.844	-22.79	159.511	74.251	80.058
	4	15.637	-25.74	115.067	135.891	143.291
Sample #12	1	3.9616	-31.82	126.236	31.382	32.208
	2	7.8456	-31.82	167.324	46.889	48.123
	3	11.731	-21.51	164.158	71.461	78.018
	4	15.484	-24.55	146.529	105.670	112.322

Table VI.B.4 Nickel Experimental and Theoretical Q Value Comparison

	n	f (GHz)	Loaded Q value	Theoretical Loaded Q value	Approximate Relative Permeability
Sample #7	1	3.976	32.214	29.250	7.2
	2	7.933	48.507	44.060	6.2
	3	11.775	76.674	69.637	3.1
	4	15.594	97.283	89.086	2.6
Sample #9	1	3.985	27.608	25.097	9.9
	2	7.948	53.881	48.904	5
	3	11.844	74.251	67.668	3.35
	4	15.637	135.891	123.64	1.25
Sample #10	1	3.949	29.557	26.97	8.5
	2	7.827	44.339	40.252	7.3
	3	11.657	70.044	63.362	3.75
	4	15.410	101.840	91.817	2.4

Table VI.B.5 Nickel Ring Resonator Skin Depth and Surface Resistivity

Sample #5	f (GHz)	Skin Depth δ_s (μm)	Surface Resistivity R_s (Ωm)
	3.937	1.656	0.154
	7.779	1.178	0.217
	11.645	1.138	0.225

DISCUSSION
A. Silver Ring Resonators

The values for the silver ring resonators on alumina substrate fired in the furnace at a temperature of 850° C obtained from my experiment can be seen in experimental results section. Values used for comparison are taken from the thesis paper of Christie Skrip dealing with fabrication and testing of microwave materials [9]. These values served as the base comparison for the nickel ring resonator experiment. Since the steps to produce the silver ring resonators were almost identical to the steps taken to produce the nickel ring resonators, obtaining values relatively close to the known values suggest that the experimental process was done correctly.

B. Nickel Ring Resonators

The measured resistance was 5.3 Ω and the length over which this resistance was measured was 6.1 cm. To determine the cross sectional area, the thickness, 6.2 μm, and the width, .475 mm, were multiplied for an area value of 2.945×10^{-9} m^2. Resistivity for the nickel ink used was found to be 2.559×10^{-7} Ωm, which gives a conductivity of 3.908×10^6 S/m.

The nickel ring resonators provided higher Q values than what was initially expected. This can be attributed to the permeability of nickel dramatically decreasing once a frequency greater than 100 KHz is reached as well as porosity within the sample. The approximate permeability values used in the theoretical calculations were found by determining what permeability value at a certain frequency would give less than a 10% error between the theoretical Q values and the experimental Q values.

The skin depth decreases as the frequency is increased. This shows that at a higher frequency, the current is not traveling uniformly throughout the structure. Also, it should be noted that the surface resistivity is increased as the frequency increases. For the nickel ring resonators, the skin depth is higher than that of the silver ring resonators. In addition, the surface resistivity for nickel is much higher in comparison to the silver.

CONCLUSION

The exploration of the properties of nickel as a ring resonator provides a simplified model of multilayered capacitors. Once the losses and the behavior of the nickel conductor are known, the multilayered capacitor structure can be better understood. A future study should be used to determined exact values for the permeability of nickel at high frequencies (> 100 KHz). This would help in obtaining more realistic and plausible theoretical Q values for the nickel ring resonators. The experimental results obtained along with theoretical calculations help show that there are factors affecting the permeability of nickel and causing the value to decrease significantly.

REFERENCES
1. Okomoto, Akira. Miniaturization and Integration of Passive Components by Multilayer Ceramic Technology. 1994.
2. Vasudevan, S. The Effect of Processing Parameters and Surface Roughness of Conductor Traces on the Microwave properties of LTCC Structures.
3. Hayt, William H., Buck, John A. Engineering Electromagnetics. 6th edition: 290-291; 2001.
4. Johnson, Mark. Magnetoelectronic memories last and last…, *IEEE Spectrum*. 37(2): 33-40; February 2000.
5. Kasap, S.O. Electronic Materials and Devices. 2nd edition: 608; 2000.
6. Neelakanta, Perambur S. Handbook of Electromagnetic Materials: monolithic and composite versions and their applications. 454; 1995.
7. Ramesh, A, Govindaraju, M.R., Jiles, D.C., Biner, S.B. Magnetic Property Variations in Nickel Caused by Non-Magnetic Inclusions. *IEEE Transactions of Magnetics*. 32(5): September 1996.
8. Pucel, Robert A, Masse, Daniel J., Hartwig, Curtis P. Losses in Microstrip. *IEEE Transactions on Microwave Theory and Techniques*. 16(6): June 1968.
9. Skrip, Christie. Fabrication and Testing of Microwave Materials, *Thesis in Materials Science and Engineering*; 2003.

PYROOPTIC RESPONSE OF PMN-PT CRYSTAL UPON NEAR-IR RADIATION

Elric Von Eden*
(Ruyan Guo, Faculty Mentor; Hongbo Liu and Dr. Edward Alberta, Mentors)
Department of Electrical Engineering and Materials Research Institute
Pennsylvania State University, University Park, PA 16802

*Undergraduate student of
Department of Electrical Engineering and Mathematics
University of Maryland College Park
College Park, MD 20742

ABSTRACT
       Dynamic (Chynoweth) pyroelectric measurements were carried out on PMN-PT (solid solution of 66 percent Lead Magnesium Niobate with 33 percent Lead Titanate) to determine its pyroelectric coefficient under both clamped (approximately constant strain) and free boundary (approximately constant stress) conditions. These results were compared against each other. In the experiments, a programmable temperature controller with a cryogenic optical stage was used to control the temperature, and the depolarization current and voltage were measured with a current-voltage lock-in amplifier and oscilloscope. The experiment and data acquisition were automated via HPIB microprocess or interface.

INTRODUCTION
       Pyroelectric effect is of fundamental importance in thermal detection and imaging within a variety of applications.[1] Certain materials, pyroelectric materials, exhibit the pyroelectric effect as a result of a change in temperature. Detection and imaging applications are based on this property of pyroelectric materials and aided by other desirable features such as their low cost, light weight, low power consumption, and relatively high damage threshold. There also exists the possibility for using pyroelectric materials in an array to increase

the potential of thermal imaging systems.[2]   As a result, studying the different characteristics of various pyroelectric materials is becoming increasingly important. Although a number of pyroelectric materials have been studied, there still remains a great amount to learn about other pyroelectric materials.

Research has been devoted to the determination and the understanding of the response of various pyroelectric materials to different temperature and heating conditions. The pyroelectric coefficient is a valuable part of understanding a certain material's response to heating or a change in temperature.   The pyroelectric coefficient is a substance's change in polarization with respect to temperature. Various methods have been used to characterize the pyroelectric coefficient of pyroelectric materials. However, since these materials would most likely be employed in systems using chopped or modulated radiation, e.g. light, the optimum method of measuring the pyroelectric coefficient should also employ chopped or modulated radiation.

Lead Magnesium Niobate with Lead Titanate (PMN-PT) is a pyroelectric and ferroelectric crystal whose cryogenic pyroelectric properties are not well known. Although research has been done on it using the Byer and Roundy technique[3] (a method of measuring the pyroelectric coefficient using a continuous heating rate of the substance), there has not been much done on PMN-PT using the pyrooptic Chynoweth[4] method (a method of measuring the pyroelectric coefficient using modulated radiation absorption). Also, results from the Byer and Roundy technique do not always match results from the Chynoweth method, as the former cannot distinguish discharge current from thermally stimulated processes. Measurements obtained by the Chynoweth method may give more vital information on the feasibility of using PMN-PT in detector or imaging systems that employ modulated optical radiation.   The Chynoweth method does need to account for the types of radiation that a certain material can absorb. For example, PMN-PT readily absorbs infrared (IR) light (especially the 1550nm light used in communications systems), and Chynoweth measurements are more easily done using IR light.

EXPERIMENTAL SETUP
Description

The sample was placed on a MMR Technologies cryogenic optical stage. The sample was allowed to achieve thermal equilibrium with its contingent surroundings using thermal grease.   The thermal grease was also chosen to minimize surface scattering of light on the sample and help the sample absorb heat more efficiently. The base of the sample had an electrical contact to the copper plate of the optical stage aided by silver paint, and it was grounded using a specially insulated wire from the copper plate to the shell of the cryogenic stage. A silver wire connected to the top of the sample by conductive epoxy was also connected to an electrode allowing the voltage to be measured by a lock-in amplifier. Figure 1 shows a picture of the sample on the copper plate.

The optical stage has a sapphire window that is transparent to the incident light. A MMR Technologies programmable temperature controller was used to control the temperature of the cryogenic stage. The lock-in analyzer has a built-in amplifier that allowed the filtered waveform of the depolarization voltage (and current) signal from the sample to be displayed to an oscilloscope as well to be measured as an RMS voltage (and current) of the fundamental voltage (and current) signal phase-locked to the modulating signal.

The infrared laser source has a continuous wave (CW) output of 1550 nm with a power level between 0 and 2.0 mW. A standard multimode fiber-optic cable with input from the infrared laser source was held above the sample. Special care was taken to make sure that the laser was shining directly onto the sample by moving the stage until the lock-in amplifier showed the greatest voltage signal. The infrared light was modulated using an external DCH-61 chopper held by a stage between the multimode fiber and a lens that focused the light onto the sample. The frequency of the chopper was monitored using the lock-in amplifier and was used as the phase-locked reference signal. The data acquisition was automated via HPIB interface.

There were two different samples used for experiment. A fully electroded but partially illuminated crystal of (2:1) PMN-PT was used for the purpose of studying the material under clamped boundary conditions. Then, a fully electroded and fully illuminated sample of (2:1) PMN-PT was used to study the material under free boundary conditions. Both samples were tested between room temperature and 80 Kelvin as well as under a vacuum. Figure 2 shows the schematic of the instruments used in the experiment and their configuration.

Determination of Pyroelectric Coefficient

Since the lock-in amplifier outputs the RMS value of the phase-locked fundamental voltage (and current) signal, the oscilloscope and the program, Origin 6.0, was helpful in determining the actual waveform of the signal and converting the RMS value to a peak-to-peak value. Using the peak-to-peak value of the current, one could calculate the pyroelectric coefficient using the following equation[1]:

$$p = \frac{dP}{dT} = \frac{mcI}{\eta WA} \tag{1}$$

where p is the pyroelectric coefficient, dP/dT is the change in polarization with respect to temperature, m is the mass of the sample, c is the specific heat of the sample, I is the depolarization current, η is the emissivity of the sample, W is the incident radiation power onto the sample, and A is the area of the sample that absorbs the incident radiation. The power incident on the sample, W, was measured using a Melles Griot universal optical power meter with a Germanium

sensor.   The emissivity of the sample, however, had to be assumed since emissivity cannot be calculated directly.
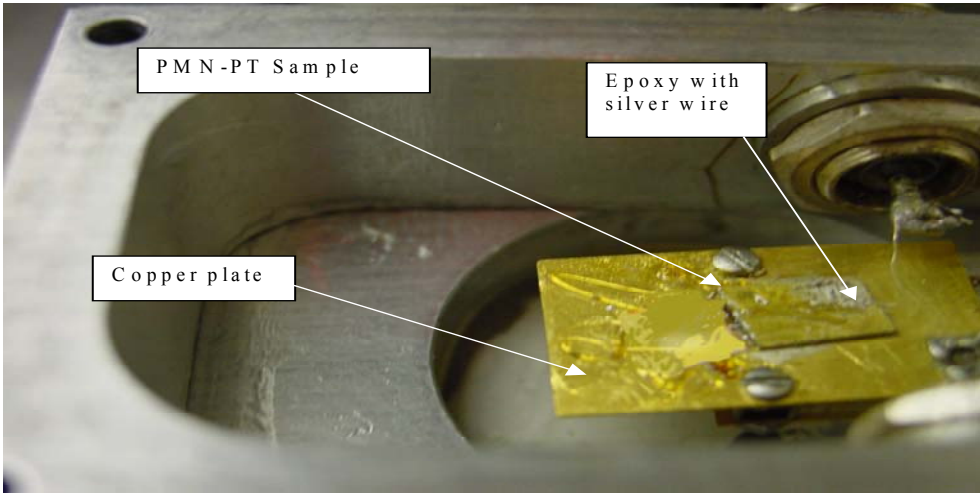

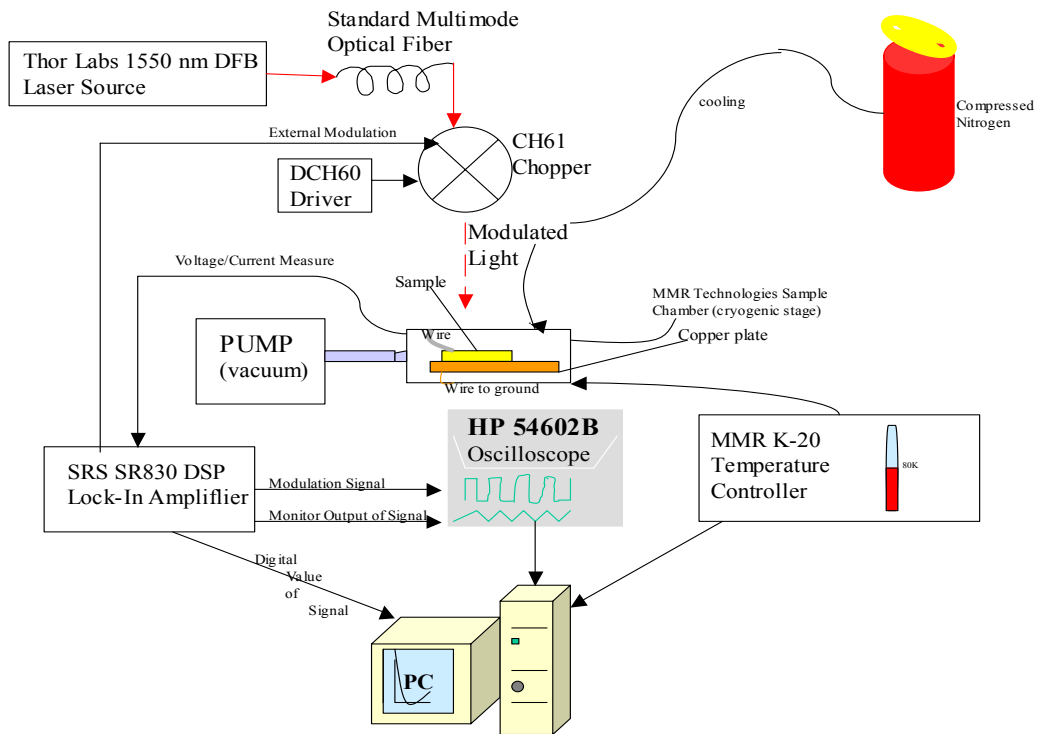Figure 1: Picture of Larger PMN-PT Sample in Cryogenic Stage

Figure 2: Diagram of Experimental Setup

RESULTS
Shortcomings of Research

      Because of a limited amount of time and some necessary adjustments made to modify the initial experimental design to the current one, my research on the pyrooptic response of PMN-PT was not completed in as much detail as I had wanted. Initially, I wanted to test a reference material, specifically Lithium Tantalate, along with both samples of PMN-PT. The results obtained from the Lithium Tantalate sample could then be compared to the results done from previous research on Lithium Tantalate. However, time limitations did not allow me to do this. Therefore, I could not test nor verify the quantitative merit of my research.

      Also, the measurement of certain figures, such as the illumination area of the laser, needed for the calculation of the pyroelectric effect was not very accurate. Other values, such as the emissivity and specific heat of the PMN-PT solution, had to be assumed.

Measurements and Data

      Measurements: The table below lists the calculated mass, the measured illuminated area, the measured incident light power, the assumed emissivity, and the assumed specific heat of each sample.

Table I. Specifics for both PMN-PT Samples

|	Fully Illuminated PMN-PT (free boundary)	Partially Illuminated PMN-PT (Clamped Boundary)
Emissivity (η):	0.98	0.98
Specific Heat (c):	307.73 J/kg*K[5]#	307.73 J/kg*K[5]
Incident Light Power (W):	12.3 to 12.4μW	12.12 to 12.32μW
Illuminated Area (A):	0.51 to 0.54mm^2	0.7 to 0.9mm^2
Mass (m)	2 to 2.4mg	170 to 200mg

      Using these numbers, the pyroelectric coefficient can be determined for a particular temperature if the current response as a function of temperature is known.

This value only refers to the specific heat of a modified PT ceramic instead of the specific heat of PMN-PT. The specific heat of PMN-PT was difficult to find and therefore it was assumed that the specific heat of the PT ceramic was not that much different than the specific heat of PMN-PT.

Data: The two graphs below show the general shape of the pyroelectric coefficient for free and clamped boundary conditions in the range between 90K and 300K at a modulation frequency of 4.5Hz.


Pyroelectric Coefficient of PMN-PT with Free Boundary (4.5Hz)

Pyroelectric coefficient for PMN-PT with clamped boundary (4.5 Hz)
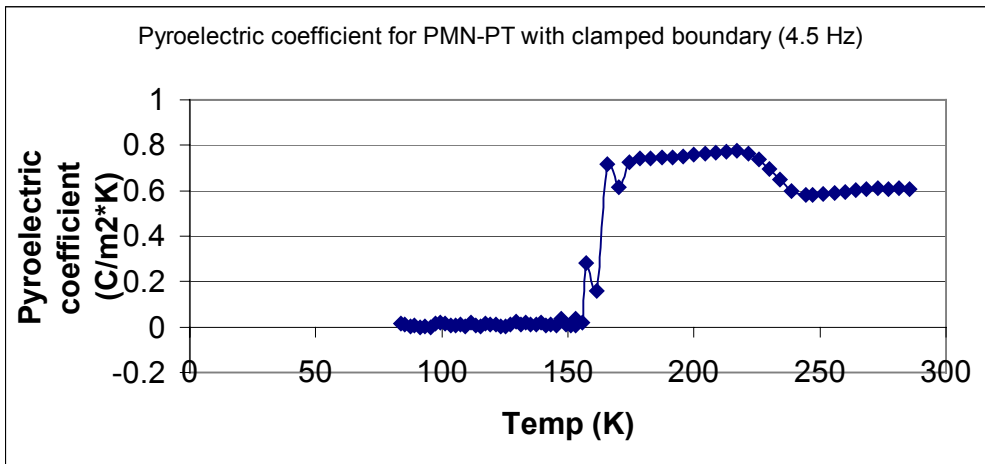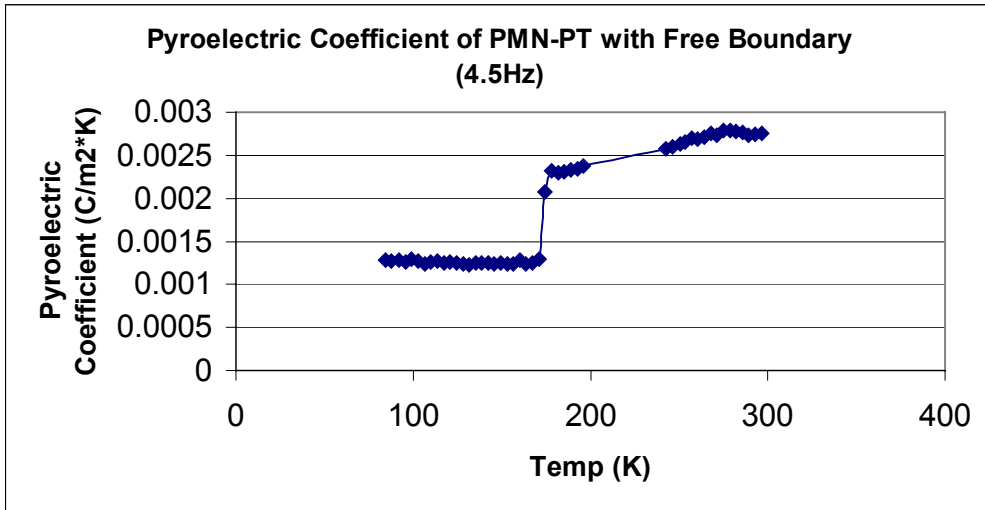
In order to test the relationship between frequency and the pyroelectric response, four different frequencies were chosen for the larger PMN-PT sample to induce a certain depolarization voltage waveform. These waveforms are shown below.

Low Frequency

Square Wave Response

216
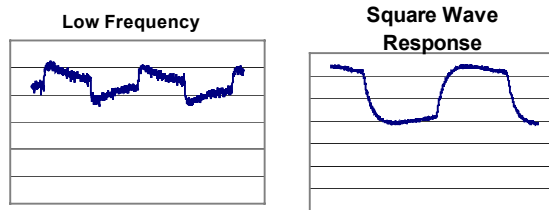
Triangularlike Wave with Flat Top
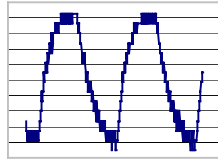
Triangular Wave (Hi freq.)
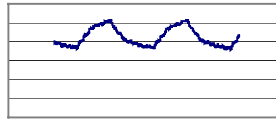
The frequencies corresponding to each waveform are given below.

_____

Table II. Frequency and Waveform Relationship for Clamped Boundary PMN-PT

	Low Frequency	Square Wave Response	Triangular-like Wave with Flat Top	Triangular Wave (High Frequency)
Frequency	0.45 Hz	1.4412 Hz	4.5 Hz	12 Hz

DISCUSSION

Although nothing quantitative can be confirmed by my results, a number of things are worth noting. No real measurements were taken on the frequency-waveform relationship for the free boundary PMN-PT; however, the free boundary PMN-PT was observed to have a square wave response at the same frequency as well as higher frequencies than the large PMN-PT. This is expected because the free boundary PMN-PT has a significantly smaller area and its temperature can increase at a faster rate.

Both samples of PMN-PT show a similar trend in pyroelectric response with respect to temperature. At a temperature between 130 and 180K, both samples of PMN-PT experience a dramatic increase in its pyroelectric coefficient. This may be due to either saturation of pyroelectric response at lower temperatures or some type of phase transition in the crystal. However, this is more evident in the clamped boundary condtion where the depolarization voltage (which is ten million times the depolarization current, but about ten thousand times smaller than the pyroelectric coefficient) goes from just about zero to half of a millivolt in a short temperature span.

From the graphs above showing the pyroelectric coefficient at 4.5Hz for both samples, it can easily be seen that the larger sample has a higher pyroelectric response. This can be explained by arguing that the larger sample has a larger area to allow for more charge to accumulate on its surface. However, the larger sample has a very poor pyroelectric response below 130K and has an unreliable response between 130K and 180K. A reason for this observation may be that the most of the relatively large surface of the PMN-PT is being kept at a very low temperature and not being illuminated or heated by the infrared light. As a result,

a large depolarization voltage and current cannot be achieved. However, the smaller PMN-PT sample (free boundary condition) is completely illuminated by the infrared light and continues to show an appreciable signal. The trend for the free boundary PMN-PT is that below a certain temperature around 170K, the depolarization current is only cut in half. On the other hand, the depolarization current for the clamped boundary PMN-PT decreases more than a hundredfold as the temperature decreases from 180K to 130K.

Pyroelectric response at a certain temperature can therefore be maximized by the size of the pyroelectric material and illumination frequency. For low temperature applications, it may be very advantageous to use a smaller pyroelectric sensor whose area allows it to heat up very quickly. For other applications, a larger area may be preferable.

For future research, it may be useful to study the thermal properties of this substance as well as find the specific temperature when the pyroelectric response decreases dramatically. PMN-PT is sensitive enough to infrared light to be able to use it in thermal detection and imaging systems. Also, depending on the size of PMN-PT and IR laser used, PMN-PT may be used for low temperature applications. However, more quantitative research needs to be done in order to completely understand the material.

Some inconsistencies that may have devalued the quantitative merit of the research include fluctuations in lock-in voltage reading, temperature fluctuations, inaccurate measurement of laser area, and incomplete illumination of the sample. Inaccurate measurement of laser area may cause the calculated pyroelectric effect for the larger PMN-PT sample to be too high, while incomplete illumination of the smaller PMN-PT sample may result in the pyroelectric coefficient being reported three times smaller than it actually is. Another thing that may have affected the results of the experiment is the actual starting temperature of the PMN-PT before it was heated or cooled to a certain temperature. Since the PMN-PT crystal is hysteretic, its behavior may noticeably vary because of how it is heated and cooled. However, the results from this experiment do show the type of general behavior PMN-PT exhibits under clamped and free boundary conditions.

The pyrooptic Chynoweth method used to study PMN-PT shows the great ability in displaying a material's response at a certain background temperature as well as at a certain illumination frequency. However, an improvement in the Chynoweth technique may be needed in order to calculate pyroelectric coefficients accurately and easily. Also, this pyrooptic Chynoweth method could also be extended to study a material's response under background heating and illumination frequency. This could be very useful to understand how a pyroelectric substance will behave in an uncontrolled temperature environment.

CONCLUSION

The behavior of the fully illuminated PMN-PT sample under low temperature does show the potential of PMN-PT and its possible use in future detection and imaging systems employing pyroelectric materials. However, more

research has to be done in order to completely understand the behavior of PMN-PT at certain illumination frequencies and temperatures. Since PMN-PT was able to show such a strong response to 1550 nm light and does not respond to visible light, it may be of great use in communications systems and fiber-optic technology.

This experiment shows also that the dynamic Chynoweth method can be of great use in understanding a material's response to modulated light at various temperatures. However, the Chynoweth method can be improved in order to ensure better accuracy in measuring the pyroelectric effect of different materials.

ACKNOWLEDGEMENTS

REFERENCES:

[1] M.H. Lee, R.Guo, and A.S. Bhalla, "Pyroelectric Sensors," *Journal of Electroceramics* **2** (4), 229-42, 1998.

[2] J.A. Sopko, "Introduction"; p. 1 in *A quantitative method for determining dynamic response characteristics of pyroelectric materials,* M.S. Thesis, The Pennsylvania State University, University Park, 1987.

[3] R.L. Byer and C.B. Roundy, "Pyroelectric Coefficient Direct Measurement Technique and Application to a Nsec Response Time Detector," *Ferroelectrics* **3**, 333-38 (1972).

[4] A.G. Chynoweth, "Dynamic Method for Measuring the Pyroelectric Effect with Special Reference to Barium Titanate," *Journal of applied physics.* **27** (1), 78-84, 1956.

[5] R.W. Whatmore, "Pyroelectric Materials and Devices"; Chapter 54 in *The Electrical Engineering Handbook*, Edited by R.C. Dorf, CRC Press LLC, Boca Raton, 2000.